

Engineering Carbide Nanoparticles Coated with
Noble Metal Monolayers for Catalysis

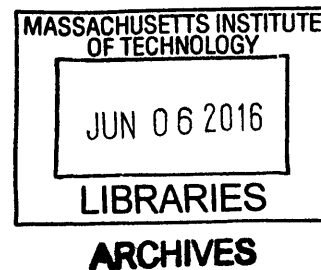
by

Sean Thomas Hunt

M.S., Massachusetts Institute of Technology (2013)

B.ChE., University of Delaware (2011)

B.S., University of Delaware (2011)



Submitted to the Department of Chemical Engineering
In Partial Fulfillment of the Requirements for the Degree of

Doctor of Philosophy

at the

MASSACHUSETTS INSTITUTE OF TECHNOLOGY

June 2016

© 2016 Massachusetts Institute of Technology. All rights reserved.

Signature of Author.....

Signature redacted

Department of Chemical Engineering

May 9th, 2016

Certified by.....

Signature redacted

Yuriy Román-Leshkov

Associate Professor of Chemical Engineering

Thesis Supervisor

Accepted by.....

Signature redacted

Richard D. Braatz

Edwin R. Gilliland Professor of Chemical Engineering

Chairman, Committee for Graduate Students

Engineering Carbide Nanoparticles Coated with
Noble Metal Monolayers for Catalysis

by

Sean Thomas Hunt

Submitted to the Department of Chemical Engineering
On May 9th, 2016 in Partial Fulfillment of the
Requirements for the Degree of Doctor of Philosophy in
Chemical Engineering

Abstract

The noble metals (NMs) comprise ruthenium (Ru), rhodium (Rh), palladium (Pd), silver (Ag), osmium (Os), iridium (Ir), platinum (Pt), and gold (Au). Together, these corrosion-resistant elements serve as nature's universal catalysts by binding reactant molecules neither too strongly nor too weakly. This allows for rapid catalytic transformations of reactants into useful products. Modern society, its current technologies, and its emerging renewable energy technologies are underpinned by precious metal catalysts. However, the noble metals are the least abundant elements in the lithosphere, making them prohibitively scarce and expensive for future global-scale technologies. Furthermore, the traditional catalyst engineering toolkit is ill-equipped to optimize the reactivity, stability, and loading of NM catalysts.

The technologies developed in this thesis have two overarching implications. First, a method is developed to engineer non-sintered and metal-terminated transition metal carbide (TMC) nanoparticles. Featuring "noble metal-like" surface reactivity, TMCs are earth-abundant and exhibit many useful catalytic properties, such as carbon monoxide and sulfur tolerance. By designing TMC nanoparticles with controlled surface properties, this thesis offers new avenues for replacing noble metal catalysts with inexpensive alternatives. Second, a method is developed to synthesize TMC nanoparticles coated with atomically-thin noble metal monolayers. This offers new directions for improved catalyst designs by substantially enhancing reactivity and stability while reducing overall noble metal loadings. These synthetic achievements in nanoscale core-shell catalyst engineering were guided by computational quantum chemistry, model thin film studies, and advanced spectroscopic techniques. Examination of the catalytic utility of these new materials was performed in the context of water electrolysis, proton exchange membrane fuel cells, direct methanol fuel cells, and high temperature thermal reforming.

Thesis Supervisor: Yuriy Román-Leshkov
Title: Associate Professor of Chemical Engineering

Acknowledgements

This thesis would not have been possible without the help and encouragement of many people. First, I would like to thank my innumerable predecessors, such as Svante Arrhenius and Paul Sabatier who laid the foundations for the study of heterogeneous catalysis. My work is most indebted to the inventors of transmission electron microscopy, Max Knoll and Ernst Ruska. Second, I would like to thank my undergraduate advisor, Prof. Jingguang Chen, Prof. Dan Esposito, and the rest of the Chen group at the University of Delaware. This thesis is the direct translation of my undergraduate thesis to a high surface area catalytic system. I would like to thank my advisor, Yuriy, and the rest of the Román group for making these past five years an awesome and fun experience. Dr. Tarit Nimmanwudipong and Dr. Maria Milina have been especially integral in helping me carry out my research. I am particularly grateful to Yuriy for being so positive and encouraging about my research each week, but mostly for financing this little adventure.

I would like to thank the members of my thesis committee – Prof. Martin Bazant, Prof. Fikile Brushett, and Prof. T. Alan Hatton – for their thoughtful comments and expert advice on my main project and sub-projects. I would also like to thank all of my friends at MIT in particular Mickey Wildman, the Chairman, K-\$, T-bone, the Don, Nasty D, Helldog, Falty, Lionel, Steven, Eric, and Rosanna. I would also like to thank all of my other friends for always being there: Cory, Arjun, Zack, Chris, and Eric.

I would like to thank my Mom and Dad for supporting my education and my entire family for being way too positive and encouraging all the time. Emily, our conversations always give me a great escape, and you always keep it real! Josh, you are the editor-in-chief, and I thank your idiosyncrasies for making me look normal and super kewl.

Most importantly, I would like to thank my wonderful wife, Wenly. Without this extremely tight leash, I would never have gone to grad school in the first place, and I certainly would not have remained focused on my research. You are BAMF, and I love you. Thank you for being super supportive, super understanding, and super kewl.

Table of Contents

Abstract	3
Acknowledgements	5
Chapter 1. Introduction	9
Chapter 2. Computational Quantum Chemical Modeling of Noble Metal Monolayers on Transition Metal Carbides	27
Chapter 3. Model Thin Film Studies	39
Chapter 4. Engineering Non-Sintered, Metal-Terminated Tungsten Carbide Nanoparticles for Catalysis	63
Chapter 5. Characterization of Bimetallic Carbide Nanoparticles and Electrocatalytic Study of $Ta_{0.3}W_{0.7}C$	115
Chapter 6. Self-Assembly of Noble Metal Monolayers on Transition Metal Carbide Nanoparticle Catalysts	145
Chapter 7. Applications of NM/TMC Core-Shell Nanoparticles in Thermal and Electrocatalysis	179
Chapter 8. Conclusions and Outlook	225
References	231
Appendix A. List of Publications and Patents	251
Appendix B. List of Presentations	255
Appendix C. About the Author	257

Chapter 1

Introduction

1. The Role of Noble Metals in Catalysis

The noble metals (NMs) comprise ruthenium (Ru), rhodium (Rh), palladium (Pd), silver (Ag), osmium (Os), iridium (Ir), platinum (Pt), and gold (Au). While the noble gases are chemically inert, the noble metals are not. Each can form innumerable stable organometallic molecules for many industrially-relevant applications as homogeneous catalysts. Instead, nobleness here refers to the “bulk nobleness” exhibited by these elements when in the metallic state. These properties include corrosion-resistance and an impediment to forming ceramic compounds, e.g. oxides, carbides, nitrides, borides, and phosphides. For this reason, they are often found in nature as the pure elements and not in oxide ores. Their bulk nobleness is the primary reason that they are popular in currencies and jewelry.

As with any metal surface, the surfaces of noble metals feature uncoordinated electron density. For non-noble metals, such coordinatively unsaturated sites are highly reactive and extremely unstable. For instance, freshly reduced and metal-terminated early transition metals like molybdenum and titanium will explosively passivate with a strongly bound oxide layer on exposure to air. This is because the early transition metals bind strongly to oxygen. By contrast, Au does not form a passivation layer while the other NMs form weakly and reversibly passivated surfaces. This weak binding to molecular oxygen extends to small hydrocarbons of various functionalities and even to large, complex hydrocarbons.

Currently, the origin of this weak binding is best explained by d-band theory as popularized by Hammer and Nørskov.^[1,2] Briefly, extended transition metal lattices feature valence s-band and d-band electron states. The molecular orbitals of adsorbing molecules mix with these bands and split into bonding and anti-bonding states. Generally, mixing with the s-band always results in a strong interaction, even for Au.^[1] For early transition metals, the anti-bonding states reside far above the fermi level, and the interactions of molecules with these surfaces is extremely strong and often irreversible. By contrast, the first moment of the d-band density of states (DOS) for Au is far below the

fermi level, and the resulting anti-bonding states are partially occupied for many molecules. This results in an extremely weak interaction. There is also an orthogonalization energy penalty for mixing adsorbate-metal d states that increases with the magnitude of the coupling matrix element, V_{sd} , which increases down a group in the periodic table. For these two reasons, Au is the noblest metal. Just one group over from Au is Pt, which has a slightly higher first moment d-band DOS (i.e. d-band center) than Au, and the anti-bonding states formed with adsorbed molecules tend to reside immediately above the fermi level.

As a result, Pt exemplifies Sabatier's famous principle: the best catalysts bind neither too strongly nor too weakly to reactant molecules.^[3] Here, binding refers to adsorption enthalpies. If binding is too strong (i.e. in the case of W), desorption of products becomes rate-limiting. Alternatively, if binding is too weak (i.e. in the case of Au), then reactant adsorption becomes rate-limiting. As a consequence of its intermediate binding, the surface of Pt is extraordinarily reactive, capable of dissociating molecules at low temperatures and rapidly inserting and withdrawing electron density. Consequently, Pt is nature's universal catalyst. For many commercially relevant reactions, there simply are no alternatives to Pt and the other NMs. Examples include the three-way catalytic converter, oil reforming, fuel cells, electrolyzers, and Li-Air batteries.

While the NMs are nature's universal catalysts, they are the least abundant elements in the lithosphere,^[4] making them prohibitively expensive and scarce for future global-scale renewable energy technologies. Their scarcity can be attributed to two properties. First, their nobleness and density means that they sink to deep within the interior of the earth, unimpeded by common mineral alloying. This makes them extremely scarce in the upper lithosphere. Second, they comprise the least abundant elements in the universe. Main sequence nucleosynthesis stops at iron fusion, which is an endothermic rather than exothermic process. The conditions sustained by supernovae nucleosynthesis are not sufficient to synthesize late 5d transition metals. Instead, nearly all of the Au and Pt in the observable universe can be accounted for by extremely rare short gamma ray burst "kilonova" brought on by the collision of binary neutron stars as they radiate away their orbital energy in the form of gravitational waves.^[5,6]

2. Noble Metal Catalyst Design: The Case for Core-Shell Architectures

The ultimate goal in catalytic design is to have complete synthetic control of the material properties that determine reactivity, selectivity, and stability.^[7-9] However, the traditional noble metal catalyst engineering toolkit is ill-equipped to optimize the reactivity and stability of NM catalysts while minimizing costs. Many envisioned catalyst designs remain synthetically inaccessible even on small scales. Furthermore, the design of NM catalysts is constrained by entailing high dispersions of surface NMs to maintain commercial viability. Large NM structures have intrinsically low surface dispersions and are simply not relevant catalyst designs.

The problem is illustrated visually in **Figure 1.1**, which shows (drawn to scale, from left to right) singly dispersed Pt atoms, a 10 atom Pt cluster, a 2 nm Pt nanoparticle, and a 5 nm Pt nanoparticle supported on a graphite slab. Because Pt is an expensive and precious resource, singly dispersed Pt atoms appear to be the optimal catalyst as this formulation achieves 100% Pt dispersion. However, such a configuration is intrinsically unstable and will readily sinter on heating or leach from the support and into the reactant media over time. Even with the 10 atom cluster, there is an interior atom that cannot participate in catalysis, making the dispersion only 90%. In addition, this formulation

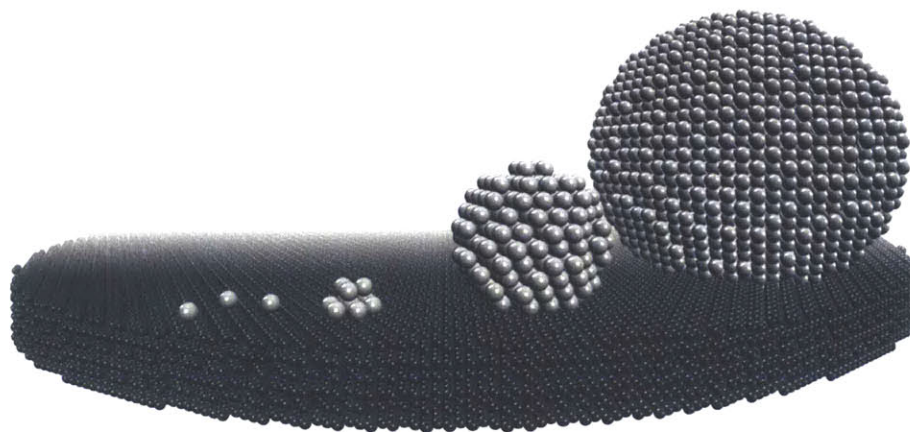


Figure 1.1. Traditional Supported NM Catalyst Designs (Drawn to Scale)

(From left to right) singly dispersed Pt atoms, a 10 atom Pt cluster, a 2 nm Pt nanoparticle, and a 5 nm Pt nanoparticle supported on a graphite slab.

exclusively has high index edge sites, which have high surface free energies, making sintering and leaching a critical issue. Finally, both of these formulations lack long-range order and facets with extended sites. Consequently, the d-band is completely discretized into molecular orbitals. Both the catalytic properties and reaction pathways are fundamentally altered compared to bulk Pt surfaces. When normalized by surface sites, these formulations are often less active than larger nanoparticles, despite the extremely high dispersions.

The 2 nm Pt nanoparticle shown in **Figure 1.1** is the most common structure used in commercial catalysts as it strikes a balance between reactivity, dispersion (ca. 50%), and stability. Larger nanoparticles, such as the 5 nm Pt nanoparticle tend to be drastically more stable,^[10] but this enhanced stability is offset by its poor dispersion (ca. 10%). For reactions such as oxygen reduction (ORR), 30 nm Pt black tends to be more intrinsically active and stable than smaller nanoparticles because it features low-index, contiguous facets. However, with a dispersion of less than 1%, Pt black is not a commercially viable fuel cell electrocatalyst architecture.

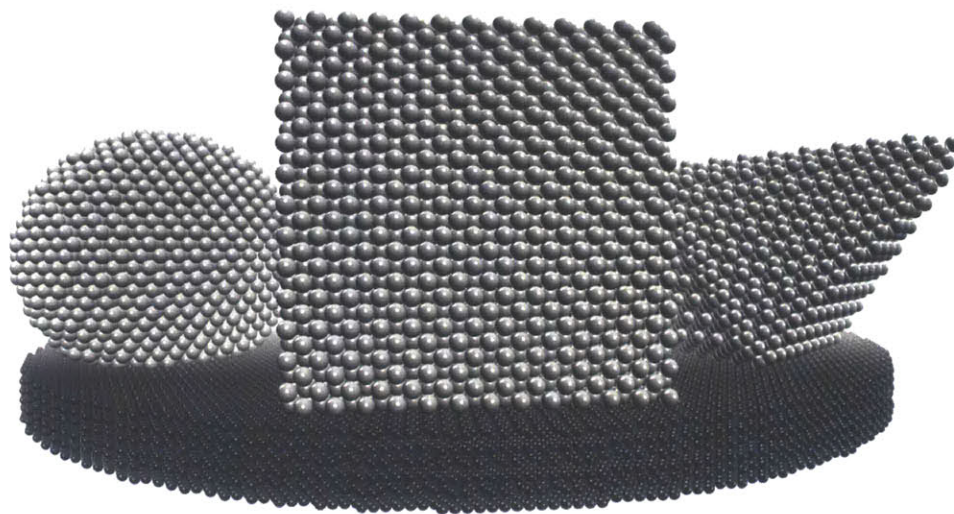


Figure 1.2. Shape-Specific NM Catalyst Designs (Drawn to Scale)

(From left to right) a 5 nm Pt nanoparticle, a 5 nm Pt cube showing only facets, and a 6 nm Pt octahedron supported on a graphite slab.

Recently, much work has been done on engineering non-traditional NM catalyst architectures. The first include shape-selective designs meant to preferentially expose one facet, such as shown in **Figure 1.2**. Oftentimes, certain crystalline planes, such as the 111 or the 100 will show better reactivity than the other planes. For these reactions, shaped nanoparticles with preferentially exposed facets demonstrate improved reactivity. However, the long-term durability for such designs remains unproven. They are especially unstable in high temperature catalytic reactions where the thermal energy would cause the shapes to evolve into traditional spherical particles, which exhibit the minimum in surface free energies.

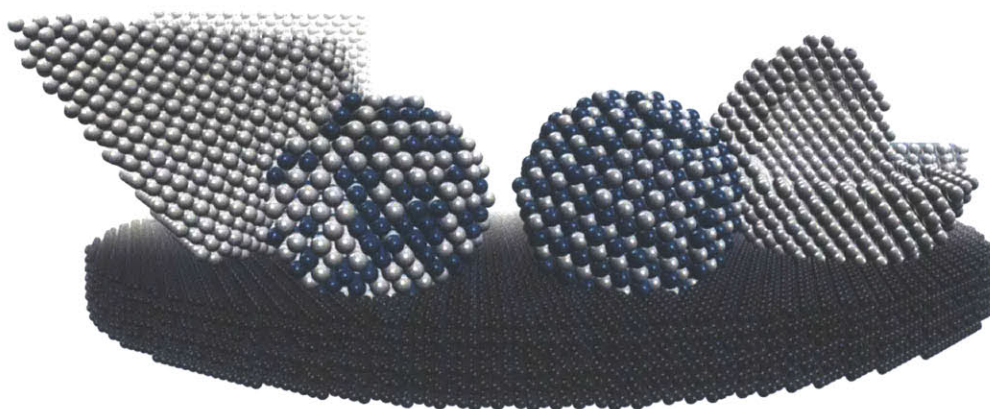


Figure 1.3. Bimetallic and Hollow NM Catalyst Designs (Drawn to Scale)

(From left to right) a 6 nm Pt octahedron, a 3 nm bimetallic Pt-Pd random alloy, a 3 nm bimetallic Pt-Pd intermetallic alloy, and a hollow 4 nm Pt nanoparticle supported on a graphite slab.

Bimetallic nanoparticles can be synthesized in two forms depending on the elements used and the synthesis conditions: random alloys and ordered intermetallic alloys (**Figure 1.3**). These architectures feature high metal dispersion and design pathways for achieving bifunctional surfaces and/or more stable catalysts. By alloying with earth-abundant materials, the catalyst cost can also be reduced. Hollow nanoparticles, shown in **Figure 1.3** feature high dispersion and extended surface sites, but the overall dispersion is still low because thick shells are needed to prevent collapse

into a standard nanoparticle. Even with thick shells, such formulations are not thermally stable.

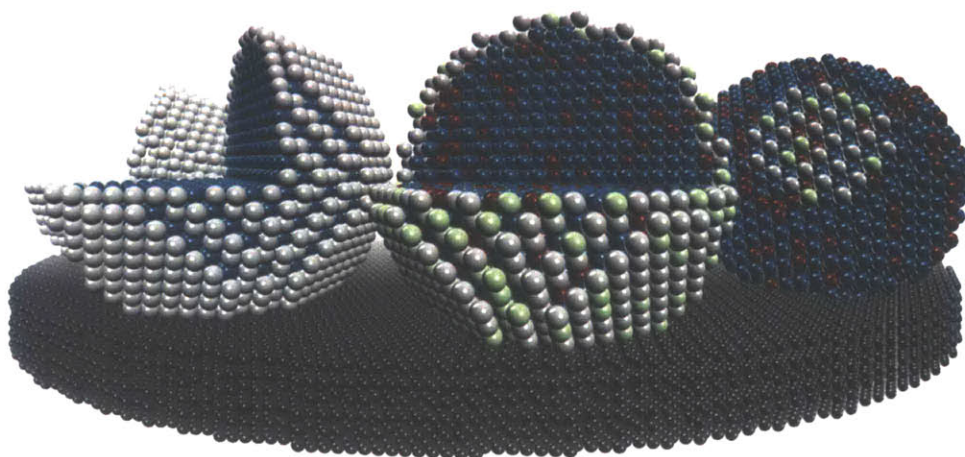


Figure 1.4. Core-Shell Nanoparticle Designs (Drawn to Scale)

(From left to right) a 5 nm 1 ML Pt/Pd (shell/core) core-shell nanoparticle, a 5 nm heterometallic 1 ML PtRu/PdRh core-shell nanoparticle, and a 5 nm heterometallic 0.1 ML PtRu/PdRh core-shell nanoparticle supported on a graphite slab.

Core-Shell nanoparticles (examples shown in **Figure 1.4**) offer the most design flexibility while maximizing NM dispersion.^[7] In fact, all of the previous architectures (**Figure 1.1** to **Figure 1.3**) are subgroups of the core-shell architecture. For instance, core-shell nanoparticles can be tuned by size, shape, heterometallic core composition and structure, heterometallic shell composition and structure, as well as shell thickness, ranging from single atoms to several monolayers (MLs). Each formulation could be optimized for specific reactions, dispersion, stability, selectivity, etc. However, while it is easy to envision the graphics in **Figure 1.4**, this level of control is not synthetically realizable even with NM shells on NM cores. Furthermore, NM cores are not commercially relevant because the overall NM dispersion would remain low. There are very few methods to synthesize core-shell nanoparticles, and none of the available methods provide the level of control needed to engineer the structures shown in **Figure 1.4**.

Instead, the cores must be properly engineered from earth-abundant materials while satisfying several other rigorous requirements.

3. Constraints on the Core Material

While core-shell nanoparticles offer highly tunable pathways for realizing the ultimate goal in catalytic design, they are both exceptionally challenging to engineer, and the core material design is rigorously constrained. There are currently no synthetically viable core materials that satisfy all of the constraints tabulated below in **Table 1.1**.

Table 1.1. Constraints on Core Material Design

i.	Earth-abundant and inexpensive
ii.	Metallic electrical conductivity and corrosion resistance
iii.	Melting point > 2000 °C
iv.	Core material insoluble in the core lattice
v.	Noble metal monolayer formation is favorable and binding is strong
vi.	Minimal or favorable modifications to NM work function and d-band
vii.	Readily engineered and independently tunable core-shell architectures

The constraints listed above are critical to achieving a commercially relevant core-shell architecture. First, the core must be earth-abundant and inexpensive to minimize NM loadings and cost by maximizing NM dispersion in the shell. Second, the core must be electrically conductive and corrosion-resistant in both acidic and alkaline media for use as an electrocatalyst. Otherwise, overpotentials associated with ohmic losses will be exacerbated and the core could leach and dissolve over time, respectively. Third, nanoparticle sintering at elevated temperatures is the main driver of irreversible loss of active surface area.

Whereas coked catalysts can be regenerated via *in situ* high temperature heat treatments, sintered catalysts cannot currently be redispersed *in situ*, instead requiring complete recovery and re-synthesis. Sintering becomes appreciable above the Tammann temperature for a material, which is roughly one third of the melting point. Many reactions

require temperatures of above 600 °C, requiring catalysts with melting points beyond 2000 °C for sintering to be mitigated. For instance, while Au nanoparticles are a growing area of research for selective hydrogenations, Au has a melting point of ca. 1060 °C, meaning Au nanoparticles sinter readily above only 300 °C. This makes them highly unstable catalysts.

Late 3d transition metals, such as Fe, Co, Ni, and Cu are common core materials for supporting NM monolayers. These core-shell structures are still very difficult to synthesize, but some success has been achieved. However, none of these materials are corrosion resistant in both acidic and alkaline media. Furthermore, their melting points are well below 2000 °C. In addition, none of these materials satisfy constraint iv in **Table 1.1**. Satisfying this constraint is absolutely critical for core-shell structures to maintain long-term durability at high temperatures and even at low temperatures. The problem of shells being soluble in the core lattice is well-known in the literature^[11] and is illustrated qualitatively below in **Figure 1.5**

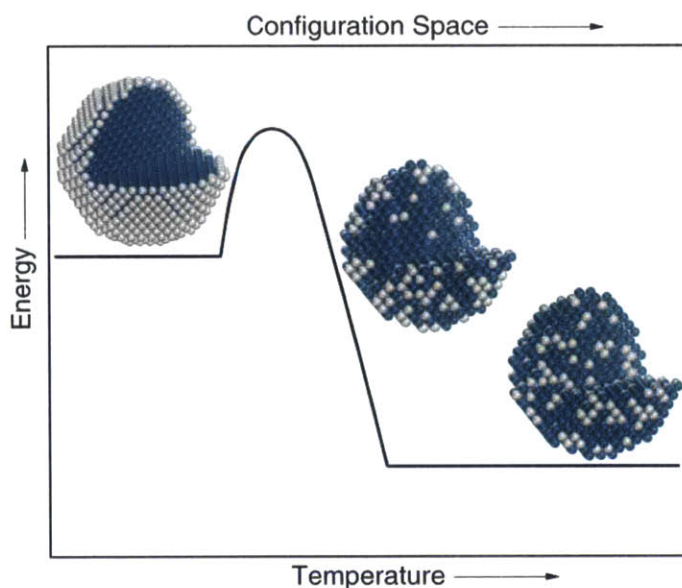


Figure 1.5. Core-Shell Structures are Metastable if the Shell is Soluble in the Core Lattice.

As shown in **Figure 1.5**, a core-shell nanoparticle occupies a very specific configuration and is therefore in a low entropy state. If the shell is soluble in the core lattice, then the structure is metastable. Even at ambient temperatures, the kinetics of solid state diffusion

of the shell into the core is non-zero, resulting in long-term loss of the active shell into the bulk of the earth-abundant core simply because there are more configurational states for the shell to be in the bulk than at the surface. This process is accelerated at elevated temperatures, making current core-shell catalysts infeasible for use in thermal catalysis. If the shell were insoluble in the core lattice at catalytically relevant temperatures, then a thermodynamically stable core-shell architecture could be engineered.

However, this presents a seeming contradiction. To satisfy both constraints iv and v in **Table 1.1**, the noble metal shell must both be insoluble in the core lattice (an unfavorable interaction) but also exhibit a strong, favorable interfacial binding interaction between the shell and the core. If this interfacial interaction is weak, the shell could leach from the surface or phase-separate at high temperatures to form a Janus particle. Strong interfacial binding also implies charge transfer of electron density between the shell and the core. However, to maintain catalytic activity of the NM shell, especially at only a single monolayer of coverage or lower, the work function (fermi level for a metal) of the shell and the d-band must have minimal modifications. As described in Section 1.1, these electronic parameters are strongly correlated with reactant binding and therefore observed catalytic reactivity via Sabatier's principle. The ideal core should in fact offer tunable pathways for favorably modulating the d-band structure and work function of the NM shell to boost reactivity beyond what the parent NM can normally achieve.

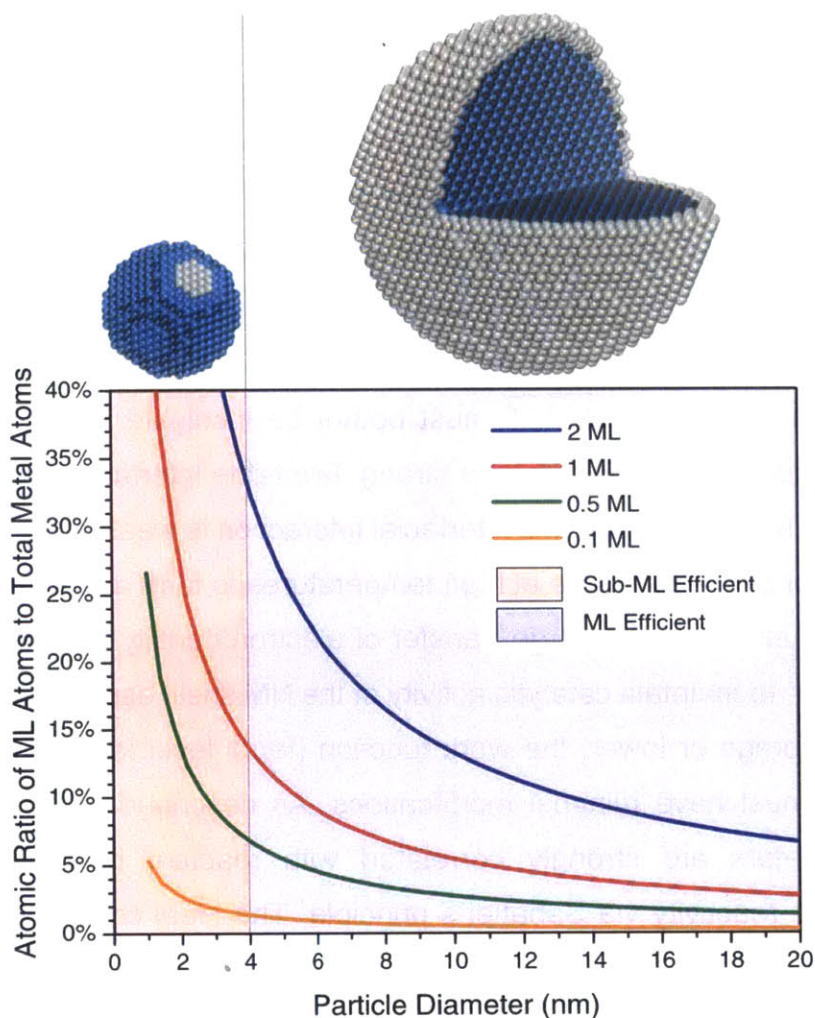


Figure 1.6. Core-Shell Nanoparticle Design Space

Atomic ratio of surface ML coverage to the total number of metal atoms in the NP versus total NP diameter. Small core-shell NPs with sub-ML NM surface coverages offer complete NM dispersion while also offering bifunctional surfaces with exposed NM sites and core sites accessible for catalytic transformations. However, small core-shell NPs with complete ML NM coatings cannot offer substantial NM loading reductions. As such, this regime is designated as “Sub-ML Efficient.” For large NPs, complete ML and multilayer NM surface coverages can still result in substantial reductions in NM loadings and are more appropriate for applications in electrocatalysis where durability is a significant challenge. As such, this regime is designated as “ML Efficient.”

Finally, for the structures envisioned in **Figure 1.4** to become a reality, the entire core-shell architecture must be independently tunable. To have complete control over the material properties that govern reactivity, we must be able to manipulate the shell thickness and its heterometallic composition, as well as the core diameter and its

heterometallic composition. This is also critical if core-shell nanoparticles are to be rationally designed, with small cores and sub-monolayer coverages and large diameter cores with multilayer coverages being the most rational designs (**Figure 1.6**).

Unfortunately, no material currently satisfies this final constraint. For instance, Ni nanoparticles are readily engineered at low temperatures via solution-processable routes, but depositing controlled quantities of Pt onto Ni surfaces is nontrivial due to the passivating oxide layer making the interaction unfavorable.^[12] In the following sections, **Chapter 2**, and **Chapter 3**, early transition metal carbides (TMCs) are introduced and investigated as ideal core candidates that could potentially satisfy each of the first six core constraints outlined in **Table 1.1**. However, this class of materials certainly does not satisfy the final, seventh constraint. Early TMCs require high temperatures and a carburizing atmosphere to drive carbon into the metal lattice. Such harsh conditions are incompatible with the synthesis of finely controlled nanoscale structures, requiring the development of novel high temperature synthetic processes. These will be explored in **Chapter 4**, **Chapter 5**, and **Chapter 6**.

4. Early Transition Metal Carbides are Earth-Abundant Alternative Catalysts to Noble Metals as well as Ideal Core Candidates for Supporting Noble Metal Monolayers

Early transition metal carbides (TMCs) comprise elements from Groups 4, 5, and 6 on the periodic table where carbon is intercalated into the interstitial sites of the parent element. The resulting ceramic compounds feature metallic electrical conductivity while possessing an amalgam of useful properties specific to both ionic solids and covalent solids.^[13] As a result, there is already widespread commercial use of early TMCs in a variety of market segments due to their favorable optical, electronic, mechanical, and chemical properties.^[13-15]

While these current applications exploit the favorable bulk properties of TMCs, the surfaces of TMCs exhibit unique catalytic properties. The investigation of TMC surfaces began in the 1970s with the discovery that tungsten carbide (WC) can perform catalytic

reactions specific to platinum while metallic tungsten exhibits no reactivity.^[16-18] This finding was later extended to Mo₂C, which was shown to have ruthenium-like reactivity. It was conjectured that the intercalation of carbon into the tungsten lattice alters the d-band structure to resemble that of Pt.^[18] Studies of the atomic structure have confirmed that WC is “Pt-like” in the occupied portion of the d-band,^[19] that WC⁻ ions are isoelectronic with Pt ions,^[20] but that in the unoccupied portion of the d-band, WC is very dissimilar to Pt.^[21] More recent studies have confirmed that WC and other early TMCs are a unique class of catalysts, and reactions proceed under very different pathways than on Pt, especially when oxygen moieties are present in the reactants.^[14,15,22,23]

The unique catalytic properties of TMC surfaces stem from the hybridization of carbidic carbon sp states with the metal d-band. While it was thought previously that carbon is just a spectator, recent studies have indicated that the carbon states themselves may play a major role in the surface reactivity.^[14,24] The surface behavior becomes even more complex when considering the different facets, some of which are metal-terminated, carbidic carbon-terminated, or feature both species. Unlike the NMs, early TMCs also passivate with an oxide layer, adding an additional layer of surface complexity. Depending on the procedure used, this can result in a clean sub-monolayer metal oxide surface, a thin oxycarbide film with varied stoichiometry MC_xO_{1-x}, or (if the passivation is uncontrolled) a thick oxide layer can form via the liberation of carbidic carbon as CO₂. Taken together, these unique surfaces result in TMCs “breaking” the traditional adsorbate-metal scaling relations explained by standard d-band theory in Section 1.1 and shown below in **Figure 1.7**, reproduced from R. Michalsky, et al.^[24]

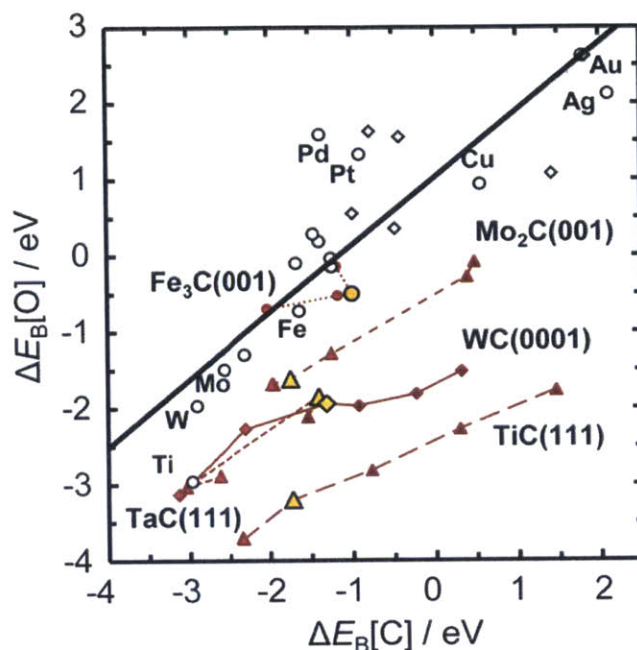


Figure 1.7. Details of the binding energies of carbon and oxygen on several carbide surfaces and their comparison to transition metal surfaces. The yellow symbols indicate the stoichiometric carbide surface, whereas the red symbols connected to this indicate the oxidized (typically weaker binding) and reduced (typically stronger binding) surfaces. The open symbols represent bonding on transition metal close-packed (diamonds) and stepped (circles) surfaces, taken from the literature.^[25-27] This figure was reproduced from R. Michalsky, et al.^[24]

As shown in **Figure 1.7**, the traditional adsorbate-metal scaling relations follow the path of the thick black line whereby oxygen binding energies are correlated with carbon binding energies. Notably, Pt and Pd deviate from the scaling relations because of their high degree of oxophilicity. By contrast, TMCs such as WC are much more oxophilic than their parent metals but substantially more carbophobic. These deviations can help in explaining why even simple reactions can proceed along radically different mechanisms on TMC surfaces than on NM surfaces. They can also explain why TMCs such as WC are extremely CO tolerant and sulfur-resistant whereas Pt is rapidly poisoned by strong binding to these species.^[13] These unique reaction pathways and tolerance to common poisons have resulted in the investigation of TMCs in several thermo- and electro-catalytic reactions, such as biomass conversion/reforming,^[14,28,29] CO₂ reduction,^[30] hydrogen evolution and oxygen reduction,^[31-35] and alcohol electrooxidation.^[36,37] In some

instances, such as biomass reforming and CO₂ reduction (i.e. reverse water-gas shift), TMCs are actually more active than Pt and the other NMs. However, in most instances, the apparent rate of reactions on TMCs are orders of magnitude slower than on NM catalysts. In addition, the propensity towards over-oxidation often renders TMC surfaces catalytically inert over long times on stream.

While TMCs have remarkable catalytic properties in their own right, in this thesis, it is proposed that they could also serve as ideal core candidates based on the constraints in **Table 1.1**. WC will be used as a representative TMC candidate. First, WC is both earth-abundant and inexpensive, as shown from publicly available data in **Figure 1.8**.^[38-40] It can be seen that W is one of the least abundant early transition metals, but is still ca. 1000 times more abundant than Pt in the lithosphere. On a \$ g⁻¹ basis, reagent-grade ammonium paratungstate is ca. 100,000 times less expensive than Pt, and substantially less volatile. As a core material, WC-based cores satisfy the first constraint of **Table 1.1**.

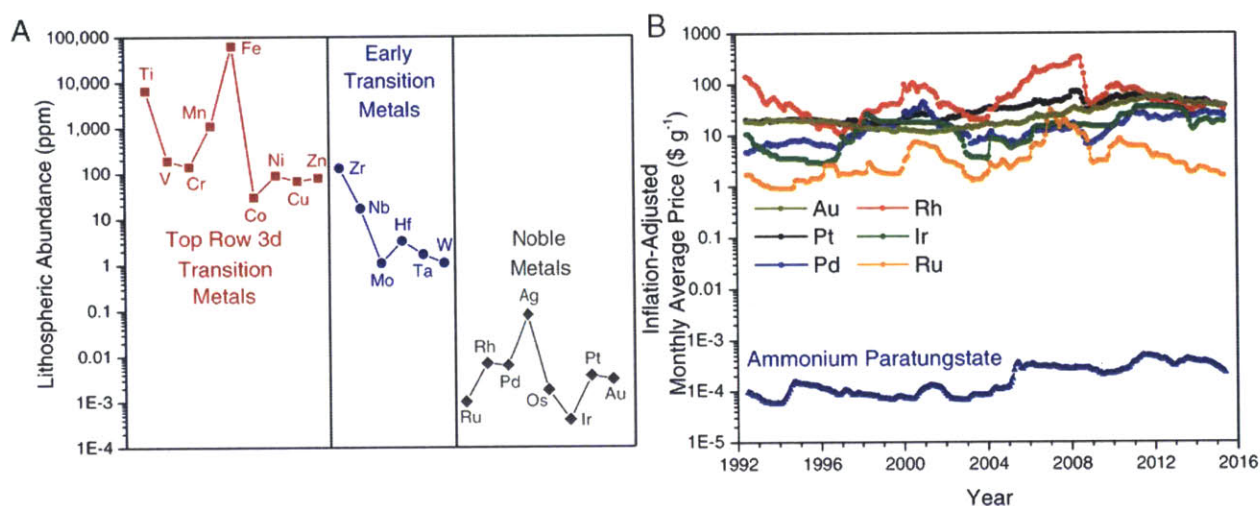


Figure 1.8. (A) Average Lithospheric Abundance of the Transition Metals and (B) Inflation-Adjusted Monthly Average Price of the Noble Metals Compared to Reagent-Grade Ammonium Paratungstate Precursor

The early TMCs are known as the “cermets” because they are ceramic materials that exhibit metallic electrical conductivity. Furthermore, TMCs have the highest melting

points among binary compounds, and all of the early TMCs have melting points above 2000 °C. While WC has a melting point of ca. 2800 °C (a Tammann temperature of ca. 900 °C), TaC has a melting point of nearly 4000 °C (a Tamman temperature of over 1300 °C).^[13] Once synthesized, TMCs are exceptionally sinter-resistant materials. The corrosion-resistance of TMCs is also well-studied in both alkaline and acidic media.^[41-43] While WC remains stable in acidic media at all potentials below +0.8 V vs. RHE (reversible hydrogen electrode), TiC and ZrC are the most electrochemically stable carbides, remaining stable at all potentials below +1.5 V vs. NHE (normal hydrogen electrode) in acidic media and below +1.0 V vs. NHE in alkaline media. As such, TMCs can satisfy the second and third constraints of **Table 1.1**.

Whereas the noble metals are at least partially miscible with all of the parent transition metals, the noble metals cannot form carbide compounds under catalytically relevant conditions.^[44-46] For instance, the synthesis of sub-stoichiometric PtC_x requires 80 GPa (over 780,000 atm) and over 2500 °C.^[45] Under these conditions, argon is a face-centered-cubic crystalline solid. Because the noble metals cannot form carbides under typical laboratory conditions, they are also insoluble in carbide lattices. In addition to satisfying the fourth constraint of **Table 1.1**, this useful physical property was discovered to be the key to synthesizing core-shell NM/TMC architectures in **Chapter 6**.

The fifth and sixth constraints of **Table 1.1** are critical to achieving a stable and active core-shell catalyst. However, it is difficult to know whether TMCs satisfy these constraints *a priori* without first synthesizing the materials and examining their catalytic reactivity. The determination of whether or not TMCs satisfy these two constraints is a central tenet of this thesis. Before attempting to synthesize monolayer coverages of noble metals on carbide surfaces, quantum chemical modeling in the form of density functional theory (DFT) coupled with molecular dynamics (MD) was used to examine the nature of the interfacial bond between noble metal monolayers and TMC surfaces in **Chapter 2**. The nature of this interfacial interaction was then probed experimentally. This was done first with noble metal monolayers which were deposited on TMC thin films as low surface area model catalysts in **Chapter 3**. Then, this interfacial interaction was examined experimentally once core-shell nanoparticles became synthetically realizable entities in **Chapter 6** and **Chapter 7**.

TMCs do not satisfy the final constraint of **Table 1.1** because it is exceptionally difficult to synthesize non-sintered and metal-terminated TMC nanoparticles of controlled sizes in their own right, let alone with controlled monolayer coverages of noble metals. The synthesis of TMCs requires high carburization temperatures (greater than ca. 700 °C) to overcome thermodynamic and kinetic barriers to carbon activation and intercalation into the metal lattice. This induces uncontrollable particle sintering, generating particles with exceedingly low surface areas that are not commercially relevant, and certainly cannot compete with state-of-the-art NM catalysts. Furthermore, to obtain stoichiometric carbide materials, excess carbon is needed at the surface to create a driving gradient for mass transfer. This results in surfaces that are covered in excess graphitic carbon (called coke) that blocks the access of reactant molecules to the catalytic surface sites. Finally, TMCs passivate with an oxide layer. If not properly controlled, this too can dramatically reduce catalytic reactivity. Current nanoparticle synthesis methods cannot simultaneously prevent TMC nanoparticle sintering while also mitigating surface impurity deposition. As a result, nearly all catalytic studies of TMCs are performed on low surface area model surfaces (i.e. thin films) where the complex surface properties can be controlled and finely characterized. Thus, despite the promising catalytic properties of model TMC surfaces, the lack of synthesis methods to produce metal-terminated TMC NPs of controlled sizes has prevented their wide-spread use as earth-abundant catalysts.^[13,14,31,47]

Therefore, engineering carbide nanoparticles coated with noble metal monolayers requires overcoming two technological hurdles. First, a new and general method must be developed to engineer non-sintered and metal-terminated TMCs. This will open the door to both TMCs as alternative earth-abundant catalysts to the noble metals. It will also open the door to using TMCs as potential core candidates. Second, a new and general method must be developed to assemble noble metal monolayers onto TMC cores with fine control over the final architecture. This will open the door to minimizing noble metal loadings while optimizing catalytic reactivity and stability for the myriad of commercial reactions today and the myriad of emerging renewable energy technologies of tomorrow.

5. Outline of the Thesis

The results of this thesis are presented in six chapters (**Chapter 2** to **Chapter 7**) followed by the Conclusions and Outlook in **Chapter 8**. In **Chapter 2**, computational quantum chemistry coupled with molecular dynamics is used to study the nature of the interfacial bond between noble metal monolayers and transition metal carbide surfaces. This is used to make predictions about whether noble metal monolayer formation is favorable on transition metal carbide surfaces and how the d-band structure and work function of the noble metal will be altered. Model catalysts are then examined by depositing noble metal monolayers on finely controlled transition metal carbide thin film surfaces using ultrahigh vacuum systems in **Chapter 3**. These model catalysts are used to show that single noble metal monolayers on transition metal carbides can achieve similar catalytic reactivity of bulk noble metal thin films.

In **Chapter 4**, a new method is developed to engineer transition metal carbide nanoparticles of controlled sizes that are both non-sintered and metal-terminated. A supported WC nanoparticle catalyst is shown to be highly active and stable for electrochemical hydrogen evolution (HER) and methanol electrooxidation (MOR). The developed method is then extended to the synthesis of both bimetallic transition metal carbide as well as nitride nanoparticles in **Chapter 5**. The structures of this new class of materials is then probed in detail using X-ray Absorption Spectroscopy (XAS), specifically Extended X-ray Absorption Fine Structure (EXAFS). It is shown that bimetallic $\text{Ta}_{0.3}\text{W}_{0.7}\text{C}$ nanoparticles are significantly more stable than WC nanoparticles while maintaining catalytic reactivity due to the highly compressed nature of the bimetallic lattice.

The finding that noble metal monolayers will self-assemble onto transition metal carbide nanoparticles at high temperatures is presented in **Chapter 6**. Through controlled engineering, it is shown that the entire core-shell architecture can be finely controlled despite synthesis temperatures exceeding 900 °C. Because this is the first demonstration that noble metal monolayers on transition metal carbide core nanoparticles are a synthetically achievable core-shell architecture, the new class of materials is probed in detail using aberration-corrected high angle annular dark field scanning transmission electron microscopy coupled with energy dispersive x-ray spectroscopy mapping (STEM-EDX). The developed method is then used to engineer bimetallic $\text{Ti}_{0.1}\text{W}_{0.9}\text{C}$

nanoparticles coated with 2 monolayers of Pt as well as 2 monolayers of a bimetallic $\text{Pt}_{0.67}\text{Ru}_{0.33}$ shell for use in electrocatalytic applications in **Chapter 7**. These materials are shown to be exceptionally CO-tolerant hydrogen oxidation (HOR) anode electrocatalysts and highly active and stable methanol electrooxidation (MOR) anode electrocatalysts for use in proton exchange membrane fuel cells (PEMFCs) and direct methanol fuel cells (DMFCs), respectively. Next, the catalytic activity versus monolayer coverage was examined to develop hydrogen evolution (HER) and HOR electrocatalysts with reduced Pt loadings. A techno-economic analysis reveals that sub-monolayer core-shell nanoparticles are several times less expensive than either fully earth-abundant alternatives or traditional Pt nanoparticles. Finally, the thesis concludes by demonstrating the sub-monolayer 0.25 ML Pt supported on $\text{Ti}_{0.1}\text{W}_{0.9}\text{C}$ nanoparticles are sinter-resistant with the core-shell structure staying intact after various heat treatments in several different atmospheres.

Chapter 8 summarizes the main results of the research introduced throughout this thesis, elaborates on strategies for the design of better core-shell nanoparticles, and identifies the challenges that lay ahead.

Each chapter of this thesis was written based on one or more separate publications^[32,33,48-54] and can be read independently. See Appendix A. Accordingly, some overlap between the chapter introductions occurs.

Chapter 2

Computational Quantum Chemical Modeling of Noble Metal Monolayers on Transition Metal Carbides

1. Introduction

The rapid advances in computational power, the scalability of massively parallel calculations, and the improved accuracy of the latest functional and pseudopotential packages enables the theoretical investigation of heretofore intractable metal catalyst systems. The ubiquity of self-contained packages now renders Paul Dirac's famous quote debatable: "The amount of theoretical ground one has to cover before being able to solve problems of real practical value is rather large...".^[55] These developments have allowed for the high-throughput screening of catalytic materials,^[56] saving time and resources, while also offering insights into how catalytic reactivity arises from the electronic structure of materials.^[1,2,57] The latter is critical for understanding how to design new and better catalysts for renewable energy technologies and for improving the efficiency of the world's existing processes.

The electronic structure of metallic lattices is difficult to model because of the high number of electron-electron interactions, the non-zero density of states (DOS) at the fermi level, and the smearing of orbital symmetry states that arises from periodic crystal lattices. The problem is best summarized by examination of the time-independent Schrödinger equation for multiple electrons interacting with multiple nuclei (with spin neglected) in **Equation 2.1** and **Equation 2.2** below.

$$H\psi = E\psi \quad 2.1$$

$$\left[-\frac{\hbar^2}{2m} \sum_{i=1}^N \nabla_i^2 + \sum_{i=1}^N V(\mathbf{r}_i) + \sum_{i=1}^N \sum_{j<i}^N U(\mathbf{r}_i, \mathbf{r}_j) \right] \psi = E\psi \quad 2.2$$

Above, ψ (the electronic wavefunction) is shown as a function of each of the spatial coordinates for all N electrons, i.e. $\psi = \psi(\mathbf{r}_1, \dots, \mathbf{r}_N)$. E is the ground-state energy of the electrons, and H is the Hamiltonian operator that we have chosen. H has three terms, which (from left to right) include the kinetic energies of the N electrons, the electron-nuclei interactions (V), and the electron-electron interactions (U). Sholl and Steckel offer a succinct picture of the complexities of the Hamiltonian operator in the context of catalysis.^[58] CO_2 is typical of the structure of simple reactant molecules, but with 22 electrons over three dimensions, the full wave function is already a 66-dimensional function. An incredibly small Pt cluster of 100 atoms would have a full wave function of more than 23,000 dimensions (3 dimensions \times 100 atoms \times 78 electrons).^[58] The intractability of solving **Equation 2.2** outright is comically apparent for real catalyst systems.

Based on the two fundamental mathematical theorems of Hohenberg and Kohn and the resulting Kohn-Sham equations,^[59] density functional theory (DFT) greatly simplifies the Hamiltonian by re-expressing it as a unique functional of electron density in just three spatial dimensions. Kohn-Sham equations have the form of **Equation 2.3** below.

$$\left[-\frac{\hbar^2}{2m} \nabla^2 + V(\mathbf{r}) + V_H(\mathbf{r}) + V_{XC}(\mathbf{r}) \right] \psi_i(\mathbf{r}) = \varepsilon_i \psi_i(\mathbf{r}) \quad \mathbf{2.3}$$

While the true functional remains unknown, the myriad of accurate, efficient, and tested approximations allows practical applications of DFT to the modeling of periodic, solid state materials, such as metal catalysts. The exact computational details used are described in the following sections.

At present, DFT is of practical value for understanding the nature of carbide surfaces, whose catalytic properties deviate substantially from those of the base metals as described in **Chapter 1**, Section 1.4. In this chapter, DFT is coupled with molecular dynamics (MD) to examine the nature of interfacial binding between noble metal monolayers and transition metal carbide (TMC) surfaces. Specifically, we are interested in using theory to make three predictions. First, we want to develop a method to model

the non-idealized structure of noble metal monolayers on TMC surfaces after thermal annealing. Second, we want to characterize the strength of the interfacial NM-TMC bond compared to the standard NM-NM bond. Ideally, for the fifth constraint to be satisfied in **Table 1.1**, the NM-TMC interfacial bond must be stronger than the NM-NM interfacial bond. Finally, we want to use DFT to make predictions about the reactivity of NM monolayers on TMC surfaces. How is the d-band center shifted? Are the work functions aligned? These are the questions that computational quantum chemical modeling can seek to provide answers before embarking on a lengthy journey through synthesis phase space. In accordance with the optimal carbide core used in **Chapter 6** and **Chapter 7**, this section focuses on characterizing NM Monolayers on WC and $\text{Ti}_{0.1}\text{W}_{0.9}\text{C}$ (denoted as TiWC) substrates.

2. Computational Methods

All calculations were performed within the DFT construct as implemented in the Vienna *ab initio* Simulation Package (VASP).^[60] Starting with the experimentally determined crystallographic structure of fcc-WC, the lattice parameters and atomic positions were optimized using the PBEsol functional,^[61] with a Gamma point-centered $10\times 10\times 10$ k-mesh and a 500 eV planewave cutoff. These criteria resulted in energies converged to at least 0.01 eV per atom. The [111] surface was then cut from this optimized structure. The most suitable material was determined by successive iterations to be a stoichiometric polar construction, in contrast to non-stoichiometric surface reconstructions known for other fcc materials^[62] and non-polar terminations for semiconductors.^[63] Although this termination results in a dipole across the cell, the effect is only non-trivial in semiconductors; the metallic nature of TiWC permits the use of such topology (**Figure 2.1**).

The slab was then expanded to a $2\times 2\times 1$ supercell with a 15 Å vacuum layer. Ti substitutions were then made to the crystalline slab at 10 wt% loading in W lattice sites. The slab, shown in **Figure 2.1**, was then relaxed with respect to atomic positions using a $2\times 2\times 1$ Gamma point-centered k-mesh and the same energetic cutoffs as the bulk material. The Pt layer was then built by the addition of a layer of [111] Pt on the W-terminated surface. The initial Pt positions occupied the next layer C sites. This lattice

spacing was a reasonable starting point as it resulted in similar Pt-Pt distances to bulk Pt [111]. To achieve sub-monolayer loading, random Pt atoms were removed from the perfect [111] surface coating. Multilayers were constructed in a similar fashion, through the addition of a second depleted Pt [111] layer.

To provide a description of the surface topology of the Pt at synthetically relevant temperatures, *ab initio* molecular dynamics was used to introduce heat (nuclear kinetic energy) to the slab. Heating was performed from 0 to 700°C in 0.1°C per 5 fs time steps. The structure was then held at the terminal temperature to reach a steady-state structure. 700°C was determined a sufficient final temperature from studies up to 1700°C, which did not alter the 700°C steady-state structure.

The standard state for Pt was obtained by full optimization of the experimental crystal structure, using 500 eV cutoff and an 8×8×8 k-mesh. Slabs of Pt were constructed in the same fashion as WC and TiWC. Surface binding energies were computed using a method developed from the literature.^[64] Workfunctions were aligned using a code freely available online.^[65] Electronic d-band centers were aligned through the integral of the partial density of states for relevant atoms.^[66]

3. Results and Discussion

3.1 Simulated Annealing Reveals a More Accurate Model for Monolayer Formation of Noble Metals on TMC Surfaces

Typically, bimetallic surfaces are modeled using DFT at 0 K and perfect vacuum by populating the admetal into the interstitial surface sites of the substrate surface with a 1:1 correspondence, as shown in **Figure 2.1a**.^[33,48] While several surface configurations are often tested, this simple method still assumes perfect lattice matching *a priori*, which is an assumption that cannot be rigorously justified. If this classical monolayer structure is subjected to simulated annealing using MD, the resulting thermally-equilibrated slab model becomes sub-monolayer, as shown in **Figure 2.1c**. Instead, to achieve full monolayer coverage, the packing density has to be increased, and the resulting monolayer structure is not in an idealized 1:1 correspondence as shown in **Figure 2.1b**.

This lattice mismatch was also found after performing simulated annealing on 1.33 ML coverage slabs and 2 ML slabs.

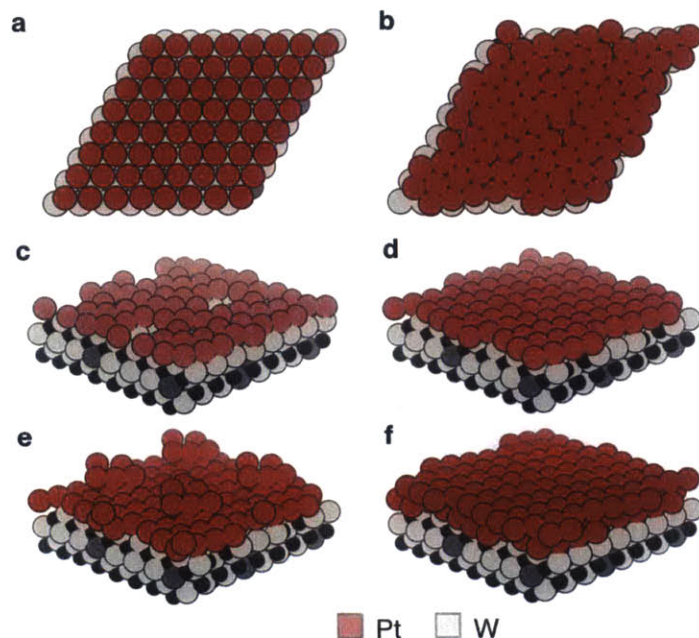


Figure 2.1. Model Surfaces Obtained from High Temperature DFT Equilibration.

The [111] terminated TiWC slab model with various surface concentrations of Pt. **(a)** The classical ML structure assuming perfect lattice matching. **(b)** A realistic ML structure obtained after simulated annealing. **(c)** Simulated annealing of the classical ML structure from **(a)** results in a sub-monolayer coverage. **(d, e, and f)**: side-view of 1 ML, 1.33 ML, and 2 ML Pt on TiWC.

TiWC crystallizes in an fcc lattice with two predominantly exposed facets: the 111 and the 100 plane. As shown in **Figure 2.1**, the Pt matches the 111 TiWC surface in a 111 orientation. Surprisingly, it was also found that Pt orients along the 111 direction even on the 100 TiWC surface, as shown below in **Figure 2.2**. This has interesting implications in catalysis where the close-packed (111) facet of Pt is known to be substantially more active than the (100) facet for many relevant reactions, such as oxygen reduction.^[67,68]

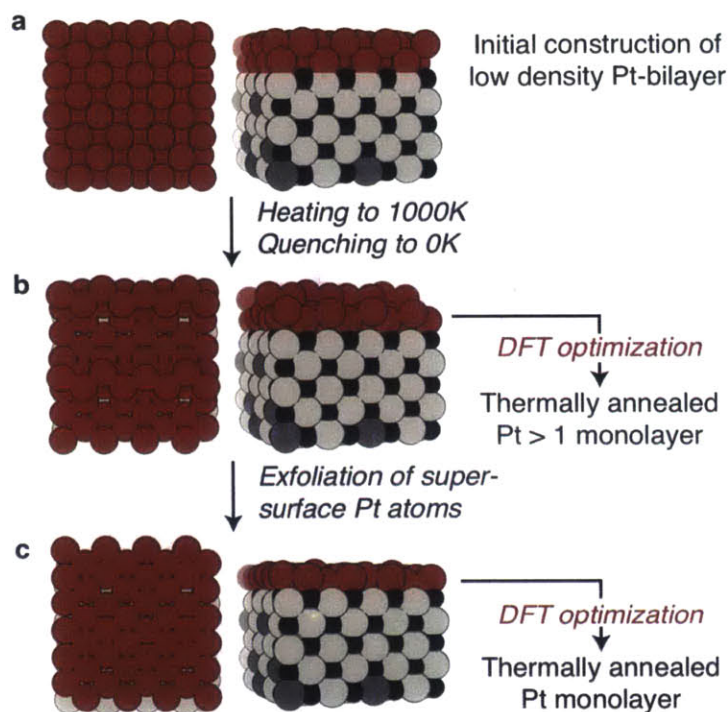


Figure 2.2. Examination of Pt annealing on the (100) TiWC Surface.

3.2 Investigation of the Thermodynamics of Interfacial Bonding between Noble Metal Monolayers and Transition Metal Carbide Surfaces

The interfacial binding energy between monolayers of different noble metals and different TMC surfaces was examined using **Equation 2.4** below. The energies were referenced versus the computed ground state energy of a non-interacting noble metal gas, E_{gas} . Here, n refers to the number of adsorbed metal atoms in the equilibrated monolayer, while X refers to the substrate surface. Two substrate surfaces were used in order to normalize the binding energies. We are interested in the relative difference in binding energy for a NM ML binding to a TMC surface versus the parent noble metal surface. This was performed by using **Equation 2.5**. By this convention, $\Delta[B.E.]$ is equal to zero for all noble metal monolayers bound to their parent noble metal surfaces. If $\Delta[B.E.]$ is negative, then the interfacial binding energy of NM-X is stronger than NM-NM. In this instance, monolayer wetting is thermodynamically favorable. Likewise, if it is

positive, then the interfacial binding energy of NM-X is weaker than NM-NM binding and monolayer wetting is thermodynamically unfavorable.

$$B.E._{NM/X} = \frac{1}{n} (E_{slab+adsorbate}(X + nNM) - E_{slab}(X) - nE_{gas}(NM)) \quad 2.4$$

$$\Delta[B.E.] = B.E._{NM/NM} - B.E._{NM/X} \quad 2.5$$

This interfacial binding energy was studied for various noble metal monolayers supported on different surface substrates, shown in **Figure 2.3**. As a control, the $\Delta[B.E.]$ was found to be positive for a ML of Pt on a graphite (0001) substrate. It was also found to be positive for a ML of Pt on an oxide-terminated WC. This is consistent with i) atomic layer deposition (ALD) studies of Pt on high surface area graphitic carbon supports where Pt does not grow layer by layer but instead forms nanoparticles^[69] and ii) the observations that Pt does not wet WC surfaces which are passivated or coated in graphitic carbon, but instead form separate fcc Pt crystallites.^[70,71] The propensity of Pt to not form monolayers on oxide surfaces and even on oxide-terminated metal nanoparticles is well-known.^[12] Interestingly, monolayer formation is also unfavorable if the interstitial surface sites are populated with carbidic carbon. Such a configuration would require the noble metals to be in a partially carburized state, which is not thermodynamically favorable, as discussed in **Chapter 1**.

In contrast, it was found that noble metal monolayer formation is strongly thermodynamically favorable for a variety of noble metals supported on a variety of *metal-terminated* TMC surfaces. The inability of previous research endeavors to achieve noble metal monolayer formation on TMC surfaces can therefore be largely attributed to the difficulty in obtaining finely controlled TMC surfaces while maintaining a well-defined nanoscale architecture. TMC surfaces must be free of graphitic coke, a passivation layer, and even a carbidic carbon layer. In addition to making ML formation theoretically achievable, obtaining such finely controlled surfaces on the nanoscale would also improve activity as carbon layers have been found to greatly diminish the reactivity of TMC surfaces.^[72] Fortunately, chemical vapor deposition (CVD) using CH_4/H_2

atmospheres has been shown to achieve metal-terminated surfaces. This can be achieved by a “scavenging” step after carburization whereby the surface is held in a pure H₂ atmosphere for several minutes. This treatment can both remove slight excesses of graphitic surface carbon while also partially decarburizing the surface to obtain metal-termination as opposed to a mixture of C-terminated and metal-terminated sites.^[48]

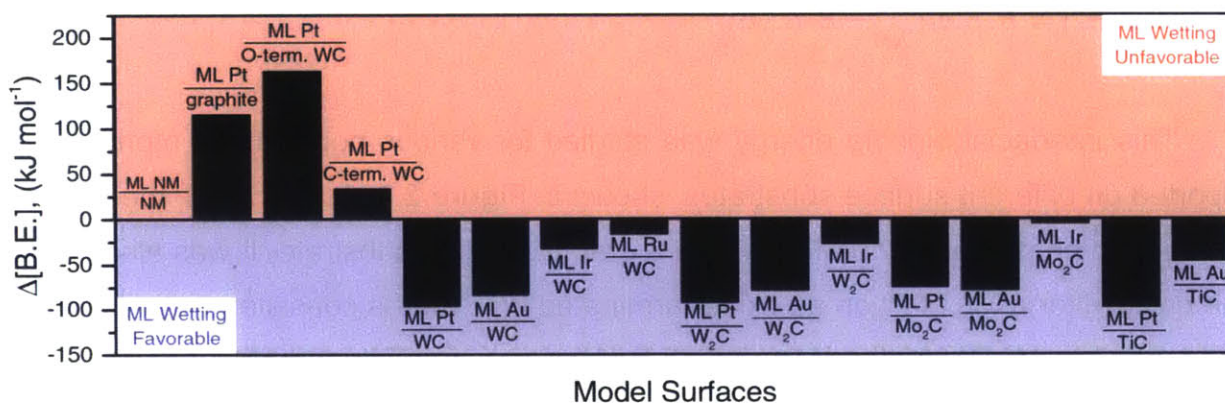


Figure 2.3. Interfacial Binding Energy Difference of Various Noble Metal Monolayers on Various Substrate Surfaces.

3.3 Survey of Various ML NM/TiWC Combinations to Predict Reactivity from Electronic Structure Calculations

Based on the developed models, the vacuum-aligned work functions were compared, and the d-band local density of states (DOS) was obtained by integration of the valence electron density over k space. For metals, the work function corresponds to the fermi level, which describes the electrochemical potential of surface electrons. In addition to the d-band structure, the work function is particularly important in electrocatalytic applications. The work function is the minimum thermodynamic energy needed to remove a surface valence d electron to a vacuum region immediately above the surface. It can vary widely from surface to surface even on the same material. Because the electrostatic potential at the surface, ϕ , is equal to the applied voltage minus the local work function (divided by the elementary charge), the local electrostatic potential will always be lower

than the actual applied voltage. Thus, there will be a built in electric field in the space between two dissimilar conductors, even in equilibrium (electrically shorted and at same temperature). This will result in band-bending of the surface monolayer and is critical in understanding both electrocatalytic reactivity and in understanding how a core, just by the very nature of being a different material, can modify the electrostatic potential at an electrode surface. Ideally, the core should favorably modify the d-band structure while maintaining the surface work function intrinsic to the parent noble metal, even at sub-monolayer coverages. In **Figure 2.4**, it is seen that the Pt work function varies from 5.39 eV to 5.82 eV depending on the exposed facet. Addition of Ti to the WC lattice, downshifts the work function by 0.1 eV. While there is some alterations in the Pt work function with monolayer coverage, varying from 5.41 eV to 6.10 eV, the alterations are not dramatic. This indicates electrocatalytic reactivity will be preserved in the monolayer architecture.

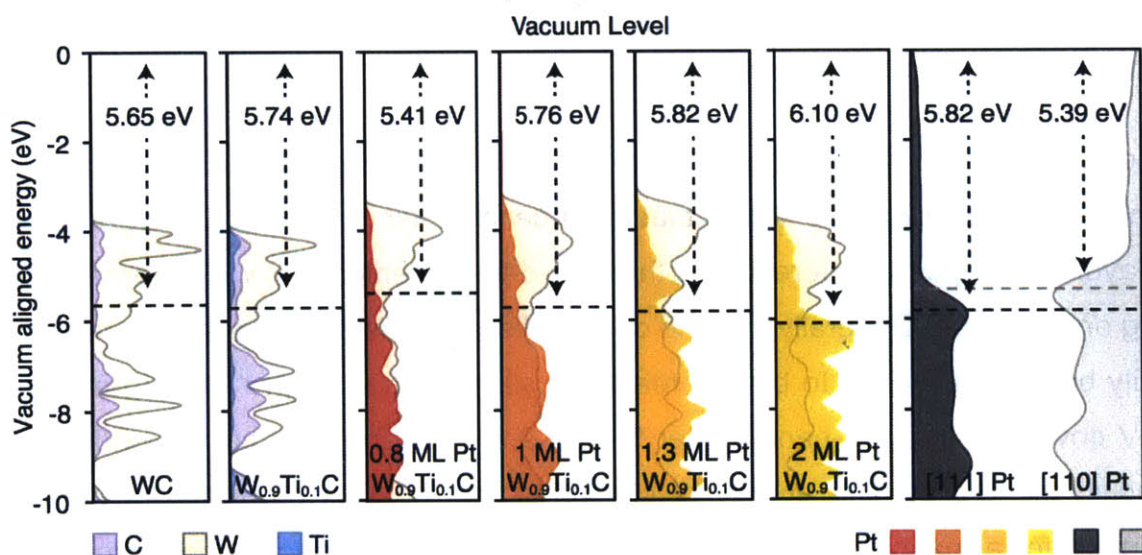


Figure 2.4. Elemental Projected Density of States Aligned to the Vacuum Level.

The elemental projected density of states (Fermi level depicted in dotted lines) for the materials examined herein. The rightmost DOS arise from the pure [111] and [110] surface terminated bulk Pt. The low loading of Pt results in low density, similar to the [110] Pt surface, whereas increased loading provokes the surface Pt to obtain a workfunction nearer to bulk [111] Pt. The decrease in workfunction beyond bulk [111] observed in the 2 ML loading is attributed to the increase in Pt-Pt packing density (91% more dense), which is favored in both the high temperature kinetic modeling and from DFT.

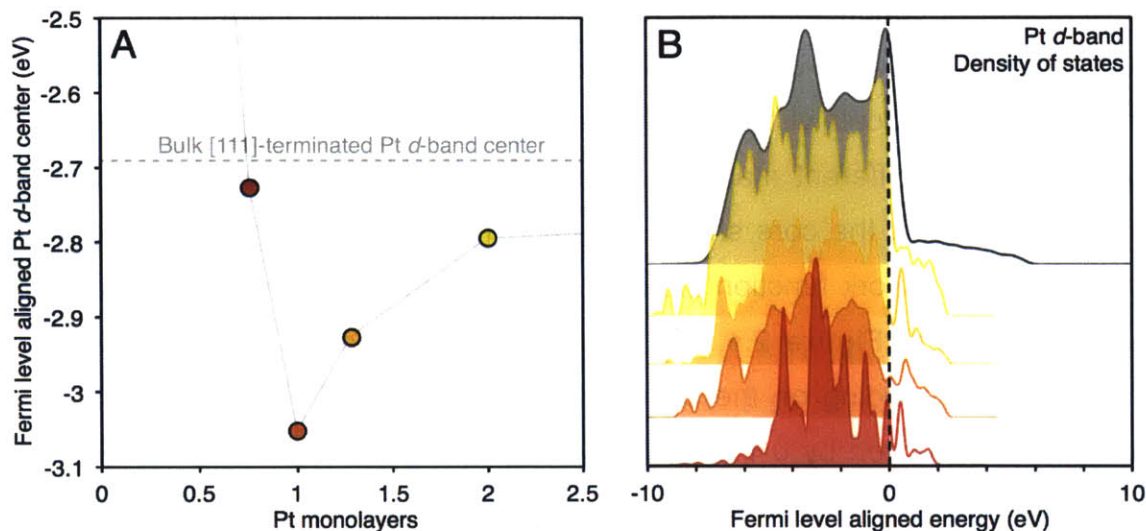


Figure 2.5. Comparison of Pt d-band Centers from Projected Density of States

The Pt d-band can be directly correlated to the CO binding.^[73] The d-band center, as obtained by the mean of the integral of the pDOS, is Morse-like: at low loading levels, the Pt acts highly localized and the d-band descriptor breaks down. At monolayer and greater loading the d-band center progresses to that of bulk [111] Pt.

The first moment of the d-band structure (the d-band center) and the projected DOS is shown in **Figure 2.5**. It is shown that the d-band center of Pt shifts downwards for all monolayer coverages of interest, but that the d-band center can vary dramatically depending on coverage. Generally, d-band downshifts for Pt result in favorable increases in reactivity because Pt tends to bind to reactants slightly too strongly.^[23] In **Figure 2.5**, the 0.1 eV downshift in the d-band center for the 2 ML configuration corresponds to a weakening in the CO binding energy of ca. 40 kJ mol⁻¹.^[73] This prediction is probed experimentally for a real catalyst system in **Chapter 7**. MD-DFT calculations also show that this downshift in the d-band center is not unique to just Pt on TiWC. With the exception of Ru on TiWC, it appears that NM monolayers on TiWC surfaces tend to result in noticeable downshifts in the d-band center as shown in **Figure 2.6**. This can be attributed to an increase in lattice compression at the surface, increasing d-band orbital overlap, which downshifts the d-band center.^[23] This is a well-known and common effect

for monolayer bimetals that appears to extend even to monolayers of metals supported on more exotic carbide substrates.

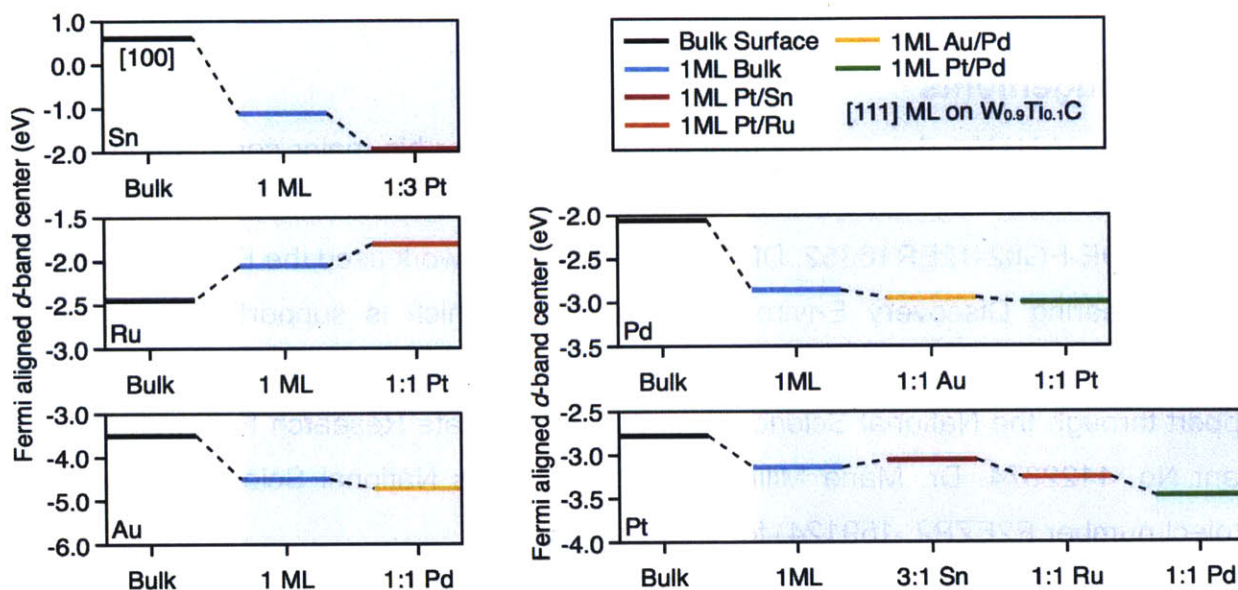


Figure 2.6. Theoretical Survey of d-band center shifts for various monometallic and heterometallic NM monolayers on (111) TiWC

4. Conclusions

Density Functional Theory coupled with Molecular Dynamics is a useful construct for probing complex metal surface structures. Simulated annealing studies show that all prior models of noble metal monolayer formation on TMC surfaces have been idealized and over-simplified. Using the new simulated annealing method, it was predicted that noble metal monolayer formation is thermodynamically favorable on TMC surfaces. However, the TMC surface must be metal-terminated, an exceptionally challenging constraint to meet when synthesizing real TMC materials. A theoretical survey shows that TiWC is an excellent TMC substrate that results in minimal alterations to both the work function of the noble metal monolayer and the d-band structure. These simulations actually predict a favorable downshift of the d-band center in many cases. While this suggests TMCs, in particular TiWC, could satisfy the fifth and sixth constraints of **Table 1.1**, these calculations also suggest TiWC could actually improve the reactivity of noble metals in

addition to minimizing noble metal loadings. The predictions made in this chapter are investigated experimentally for several relevant reactions in **Chapter 7**.

Acknowledgements

Dr. Christopher H. Hendon is gratefully acknowledged for his major contribution to this chapter. This work was supported by the Department of Energy, Office of Basic Energy Sciences (DE-FG02-12ER16352, DE-SC0014058). This work used the Extreme Science and Engineering Discovery Environment (XSEDE), which is supported by National Science Foundation (ACI-1053575). I thank the National Science Foundation for financial support through the National Science Foundation Graduate Research Fellowship under Grant No. 1122374. Dr. Maria Milina thanks the Swiss National Science Foundation (Project number P2EZP2_159124) for financial support.

Chapter 3

Model Thin Film Studies

1. Introduction

Polycrystalline thin films allow for the systematic investigation of new catalytic systems via reproducible and well-characterized surfaces. While the materials developed are not relevant to commercial devices due to their low surface area, the investigation of new materials via fundamental surface science gives fundamental insights into the structure-property relations governing reactivity and stability. In this chapter, TMC thin films were synthesized using chemical vapor deposition (CVD) with well-defined, metal-terminated surfaces. Noble metals were then deposited on the thin films in monolayer (ML) amounts using physical vapor deposition (PVD). Using X-ray photoelectron spectroscopy (XPS), the monolayer coverage could be accurately calculated. Furthermore, the oxidation state of the surface could be characterized. The ML NM/TMC thin films were then analyzed for hydrogen evolution (HER) as a probe reaction, and the long-term durability was examined. Before embarking on the design of a true core-shell catalytic architecture, these studies were paramount to examining the fundamental interactions between a NM ML and a TMC substrate, demonstrating that such a ML configuration could even be achieved. Furthermore, the durability of the NM-TMC interface was confirmed under real electrochemical cycling.

2. Materials and Methods

Synthesis of WC, W₂C, and Mo₂C thin films

Polycrystalline tungsten foil (99.95% pure, Alfa Aesar) was used as the substrate for all W_xC samples. W_xC thin films were deposited using a Torus 3 Magnetron sputtering source in a UHV chamber with base pressure of 5×10^{-8} Torr and connections to argon (Grade 5), hydrogen (Grade 5) and ethylene (99.5 % pure) gas cylinders. A WC target (99.9% pure, Williams Advanced Materials) was used as the source material for the thin films. Quartz lamp heaters were used to preheat the foils to 400°C. Before deposition,

an Ar gas flow rate of 2.0 sccm was delivered at the base of the magnetron assembly and the partial pressure of the chamber adjusted to 22.5 mTorr by throttling a gate valve between the chamber and the turbo pump. For both WC and W₂C, DC sputtering at 70 W power was conducted while holding the substrate temperature at 400°C. For W₂C synthesis, sputtering was conducted in a pure Ar environment. For WC synthesis, reactive sputtering was conducted by leaking an additional 1 mTorr H₂ and ½ mTorr C₂H₄ into the chamber. Prior to deposition, pre-sputtering was conducted for 10 minutes with a shield positioned between the target and the substrate. Deposition was then carried out for three hours. Upon removal from the PVD chamber, samples underwent a post anneal processing step in a Lindberg 55035 quartz tube furnace. WC samples were annealed to 1000 C, where they were held for 1 hr, while W₂C samples were annealed to a maximum temperature of 825°C, where they were held for 2.5 hrs. Flow rates of 122 sccm of H₂ and 33 sccm of CH₄ were used during the annealing process. Upon conclusion of the high-temperature annealing step, WC/W₂C samples were cooled to 850/825°C and the CH₄ flow rate shut off while the temperature was maintained constant for 15/30 minutes to ensure that excess surface carbon was removed from the samples. Longer annealing times were used for W₂C samples during the high temperature steps because of the strong temperature dependence of C-diffusion rates and surface carbon removal. Once an annealed sample had cooled to room temperature, the hydrogen flow rate was turned off and replaced by 20 sccm of 1% O₂/ 99% N₂ for 1 hour to slowly passivate defects on the sample.

Mo₂C thin films were synthesized by directly carburizing polycrystalline molybdenum foil (99.95% pure, Alfa Aesar) in the quartz tube furnace described above. The same gas flow rates were used as in the W_xC post anneal procedure, while the maximum temperature was held at 850°C for 3.5 hours before shutting off the CH₄ flow for 0.5 hours to remove excess surface carbon.

Deposition of Pt Overlayers

Pt deposition was carried out using a hot filament Pt source in an XPS/UHV chamber with a base pressure of 5x10⁻¹⁰ Torr. The Pt source consists of Pt wire (99.99% pure, Alfa Aesar) wrapped tightly around a resistively heated W wire filament, as often used for deposition of metal overlayers with monolayer thickness.^[74] For Pt overlayer growth

experiments, the substrate was positioned in front of the Pt source for a set amount of time before being transferred to the main chamber where XPS measurements were conducted, as described below. Alternating Pt deposition and XPS measurements were carried out until a total deposition time of ~ 20 minutes was reached. For HER measurements, ~ 1 ML Pt overlayers were deposited on W_xC substrates for ~5 minutes.

Characterization Techniques

Scanning Electron Microscopy (SEM) images were taken using a JSM 7400f SEM with an accelerating voltage of 3 KeV and a probe current of 10 μ A. Symmetric XRD was conducted using a Phillips X'Pert PW3040-MPD X-ray diffractometer, operated with a Cu K α x-ray source at 45 kV and 40 mA. GIXRD was performed using a Rigaku D/Max 2200 diffractometer with a Cu K α source operated at 40 mA and 40 kV, with the incidence angle set at 1.0, 2.0, or 5 degrees.

A Phi 5600 XPS system with a multi-channel hemispherical analyzer and Mg anode X-ray source was used to monitor the growth of Pt overlayers, determine overlayer thickness, and investigate the electrode stability during electrochemical measurements. The XPS was calibrated using the reported binding energies^[75] for the strongest photoelectron lines of Au, Ag, and Cu reference foils.

Electrochemical Measurements

0.5 M H₂SO₄ (Fisher Scientific, assay 96 w/w %) solutions were freshly prepared from deionized water prior to all electrochemical measurements. For quantitative measurement of HER activities in Ar-saturated 0.5 M H₂SO₄, electrodes having areas of 0.75-1.0 cm² were assembled with a 1.0 mm thick Teflon sheet epoxied to the backside of the electrodes. Electrochemical measurements were performed in a standard electrochemical cell using a PARSTAT 2273 potentiostat, saturated calomel reference electrode (SCE, -0.241 V vs. NHE), and a 10 cm² Pt gauze auxiliary electrode. Prior to experiments, H₂SO₄ solutions were purged with high purity Ar for at least 45 minutes, and a slow flow of Ar was maintained above the solution during measurements. Upon submersion in the electrolyte, electrodes were conditioned by conducting 25 cycles of potential cycling between 0.0 and +0.3 V with a scanning rate of 50 mV/s. Linear sweep

voltammograms (LSV) were then conducted at a scan rate of 2 mV/s from a starting potential of +0.14 V to a final potential of -0.4 V vs. SCE. The stability of ML Pt-W_xC was evaluated with chronopotentiometric (CP) cycling conducted in H₂-purged 0.5 M H₂SO₄ in a standard two-neck electrochemical cell.

Density Functional Theory Calculations

Hydrogen binding energies (HBE) and metal-metal (M-M) binding energies were calculated for the close packed crystal structures of all surfaces using the Vienna ab initio Simulation Package (VASP) as described previously.^[76] TMC surfaces comprised of six layers of atoms and twelve layers of vacuum, while all other surfaces contained four layers of atoms and ten layers of vacuum. In all cases, the bottom layers were fixed while the top two layers were allowed to relax. A 3 x 3 x 1 Monkhorst-Pack automatic k-point mesh and a plane wave cutoff of 396 eV were used. From DFT results, HBE values were calculated as defined by Norskov et al.^[77] M-M binding energies were calculated in the same manner as HBE values, but treating the top metal ML as the adsorbate layer. For both HBE and M-M binding energies, the value corresponding to the most stable binding site was used.

3. Results and Discussion

3.1 Using Sabatier's Principle to Predict Active ML NM/TMC HER Catalysts

One of the fundamental concepts of heterogeneous catalysis is Sabatier's principle, whereby those metals that bond reactive intermediates with moderate strength are generally observed to be the most active catalyst towards the reaction.^[78] For simple reactions such as the HER that have one key reactive intermediate (adsorbed H), this principle manifests itself in the form of a volcano relationship between catalytic activity and reactant/surface bond strength. The significance of such a correlation is that the catalytic activity of a given catalyst can often be predicted based on the binding energy of the adsorbed intermediate, which can be calculated using DFT. Tremendous advances in the computational capabilities of quantum mechanical modeling based on DFT have enabled researchers to quickly and accurately achieve this goal in a variety of reaction

systems. For example, Greeley and co-workers utilized DFT-calculated hydrogen binding energies (HBE) to computationally screen over 900 combinations of ML-bimetallic and intermetallic catalysts for the purpose of identifying active HER electrocatalysts.^[79] While that study and several others have successfully demonstrated this computational approach to the design of HER catalysts, they have not identified a ML bimetallic surface with non-precious metal substrate that matches the activity and stability of the standard HER catalyst, Pt. One possible reason for the lack of identifiable non-precious metal supports for ML Pt-group metals is that the latter generally need to bond to a substrate having similar electronic structure in order to maintain its high catalytic activity and stability. Conversely, it can be expected that a ML Pt-group metal bonded to a substrate with substantially different electronic structure would experience a large perturbation in its original electronic structure, leading to large deviation in activity and stability compared to the parent metal. From this reasoning, it follows that the similar electronic properties of many TMCs to Pt-group metals make the former excellent candidates to be low-cost supports for the latter.

Table 3.1. DFT-Calculated Binding Energies for Hydrogen (HBE) on Various Metal, TMC, and ML NM/TMC Surfaces

Class	Surface	HBE (eV)
Carbides	α -WC (0001)	-0.99
	W ₂ C (0001)	-0.67
	Mo ₂ C (0001)	-0.79
Metals	Pt (111)	-0.46
	Au (111)	0.13
	Pd (111)	-0.50
ML NM/TMC	1 ML Pt/WC	-0.43
	1 ML Pt/W ₂ C	-0.24
	1 ML Pd/Mo ₂ C	-0.46
	1 ML Pd/WC	-0.40
	1 ML Au/Mo ₂ C	0.30
	1 ML Au/WC	-0.06

In **Table 3.1**, DFT-calculated hydrogen binding energy (HBE) values for several unmodified and ML metal-modified TMC surfaces are shown in comparison to the precious metals Pt and Pd, two of the most commonly explored HER electrocatalysts whose HBEs are located at the center of the HER volcano curve. Although the unmodified TMC surfaces are all predicted to bind hydrogen too strongly compared to Pt and Pd, it is seen that the HBE values of several ML surfaces are located in the optimal HBE range of the volcano curve, approximately $-0.1/+0.2$ eV less/greater than the HBE of Pt.^[77] The finding of similar HBE values, such as between ML Pt-WC and Pt, can be attributed to minimal strain and ligand effects on the Pt ML due to the general similarity between bulk Pt and WC. Also included in **Table 3.1** are the HBE values of several Au surfaces. Although Au is not a prominent HER catalysts, the weak HBE values of the Au surfaces make them useful for analyzing surfaces on both sides of the volcano curve.

In addition to predicting catalytic activity from the binding energies of reactive intermediates, DFT can also be used to gauge the relative stability of ML bimetallic catalysts.^[79,80] In this chapter, the relative stability of various ML NM/TMC surfaces is compared by calculating the differences in binding energies of a ML metal with its bulk parent metal (M-M) and with the TMC substrate (M-TMC). In general, the larger the M-TMC binding energy compared to the M-M binding energy, the more favorable the ML configuration should be. Conversely, it can be expected that ML systems with M-M binding energies greater than that of the corresponding M-TMC binding energies should experience a driving force towards agglomeration into bulk-like metal particles.^[81] While this methodology does not provide absolute determination of thermodynamic stability, it can provide a good indication of relative stability when the difference in M-TMC and M-M binding energies are compared for several surfaces. In **Table 3.2**, DFT-calculated M-M and M-TMC binding energies are provided for Pt, Pd, and Au MLs. Also included is the calculated ML Pt binding energy for 1 ML of Pt on a model graphite C(0001) surface to represent the relative stability of commonly used carbon supports. While all calculated M-TMC binding energies are 15-35% greater than the corresponding M-M binding energies, the binding energy of ML Pt on the graphite C(0001) surface is seen to be 24% less than ML Pt on Pt(111). The disparity in binding energies between the Pt-C and Pt-

W_xC surfaces predicts that the W_xC surfaces should serve as a more stable support for ML Pt than conventional carbon.

Table 3.2. DFT-Calculated Binding Energies for 1 ML of Pt, Pd, or Au on Close Packed Surfaces of the Parent Metals, Three Different TMC Surfaces, and on Graphite

ML Surface Atoms	Substrate	Binding Energy (eV)	ΔB.E. (eV)
Pt	Pt (111)	-5.43	0.00
	C (0001)	-4.12	1.31
	WC (0001)	-6.59	-1.16
	W ₂ C (0001)	-6.51	-1.08
Pd	Pd (111)	-4.68	0.00
	C (0001)	-3.27	1.41
	Mo ₂ C (0001)	-5.46	-0.78
	WC (0001)	-5.59	-0.91
Au	Au (111)	-2.91	0.00
	C (0001)	-1.60	1.30
	Mo ₂ C (0001)	-3.90	-1.00
	WC (0001)	-3.69	-0.78

3.2 Characterization of Pt/W_xC Thin Films

WC and W₂C thin films used in this study were deposited on smooth, polycrystalline W foil substrates by reactive and nonreactive magnetron sputtering, respectively. Pt overlayers were deposited on the W_xC substrates by evaporation of Pt wire wrapped around a resistively heated W filament, a technique that is commonly used for synthesis of ML overlayers under UHV conditions.^[74] Descriptions of the synthesis procedures are provided in the Materials and Methods section.

Thin Film Morphology

On a macroscopic scale, the as-synthesized W_xC thin film surfaces display a shiny metallic luster and uniform, flat appearance. In **Figure 3.1**, the microscopic surface morphology is shown in SEM images at two different resolutions for each sample. The

thin film surfaces are observed to be flat at the micron length scale, with the exception of randomly-spaced striations directed vertically in **Figure 3.1**. These striations are most likely artifacts of milling lines in the W foil substrate, features that are common in the manufacture of metal foils.^[82] On the nanoscale, the WC and W₂C thin films appear to have a similar roughness and are characterized by small, barely discernable grains.

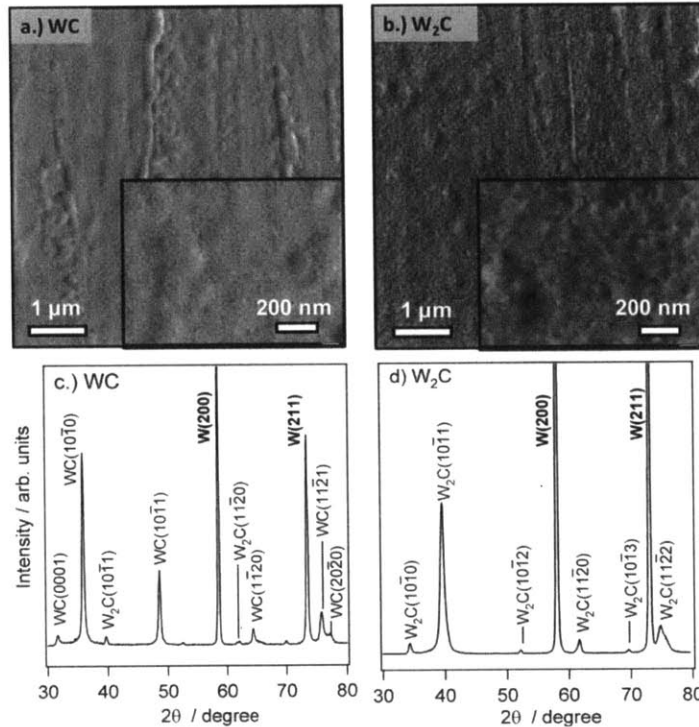


Figure 3.1. SEM Images of As-Synthesized PVD Thin Films.

(a) WC and (b) W₂C deposited onto polycrystalline W foil. Symmetric XRD patterns for as-synthesized (c) WC and (d) W₂C thin films.

Crystal Structure of W_xC Thin Films

Symmetric X-ray diffraction (XRD) and glancing incidence XRD (GIXRD) were used to verify the bulk crystal structure of as-synthesized thin films, with XRD patterns for the as-synthesized WC and W₂C thin films provided in **Figure 3.1c** and **d**, respectively. For both thin films, the primary diffraction peaks of the W foil substrate are detected at $d = 2.238\text{\AA}$ ($2\theta = 40.3^\circ$), $d = 1.582\text{\AA}$ ($2\theta = 58.6^\circ$), and $d = 1.292\text{\AA}$ ($2\theta = 72.8^\circ$), corresponding to the W (110), W (200), and W (211) crystal planes of unstrained cubic W [ICDD 04-0806]. In **Figure 3.1c**, the XRD pattern of the annealed, reactively sputtered thin film is seen to be consistent with hexagonal WC [ICDD 03-065-4539]. Phase-purity is observed with the

exception of very minor $W_2C(10\bar{1}1)$ and $W_2C(10\bar{2}0)$ peaks, which arise from a small amount of W_2C located at the interface between the W foil substrate and WC thin film, as previously shown for carburized WC foils.^[83] In **Figure 3.1d**, the diffraction pattern for the annealed, non-reactively sputtered thin film is shown, with the peaks corresponding to hexagonal W_2C with space groups P-31m [ICDD 01-079-0743] and P-3m1 [ICDD 00-035-0776]. Glancing incidence XRD (GIXRD) patterns for WC and W_2C thin films confirm the single-phase nature near the surface.

Characterization of W_xC Surface Stoichiometry

Of great importance to this study is the characterization of the TMC surface stoichiometry, which is known to have a profound effect on the catalytic behavior of TMC surfaces.^[84-86] For example, excess surface carbon has commonly been observed on as-synthesized W_xC surfaces, and generally has a prohibitive effect on the catalytic properties of a catalyst.^[72] In this study, build-up of excess surface carbon was avoided by shutting off the flow of CH_4 during a post deposition annealing step, which has previously been used to eliminate excess surface carbon in the synthesis of WC powder catalysts.^[87] **Figure 3.2a** contains XPS C 1s spectra for WC and W_2C thin films for which the CH_4 flow rate was turned off towards the end of the post anneal process. At lower binding energies, the characteristic carbidic carbon peak for WC is clearly visible at 282.8 eV, while that for W_2C , which is expected to be lower in intensity and higher in binding energy than WC,^[86] is located near 283.7 eV. For both W_xC surfaces, C 1s peaks at 284.7 eV are also observed, which originate from adventitious carbon adsorbates from atmosphere. This is confirmed by the location and similar magnitude of the C 1s peak measured on a cleaned 99.99% pure W.

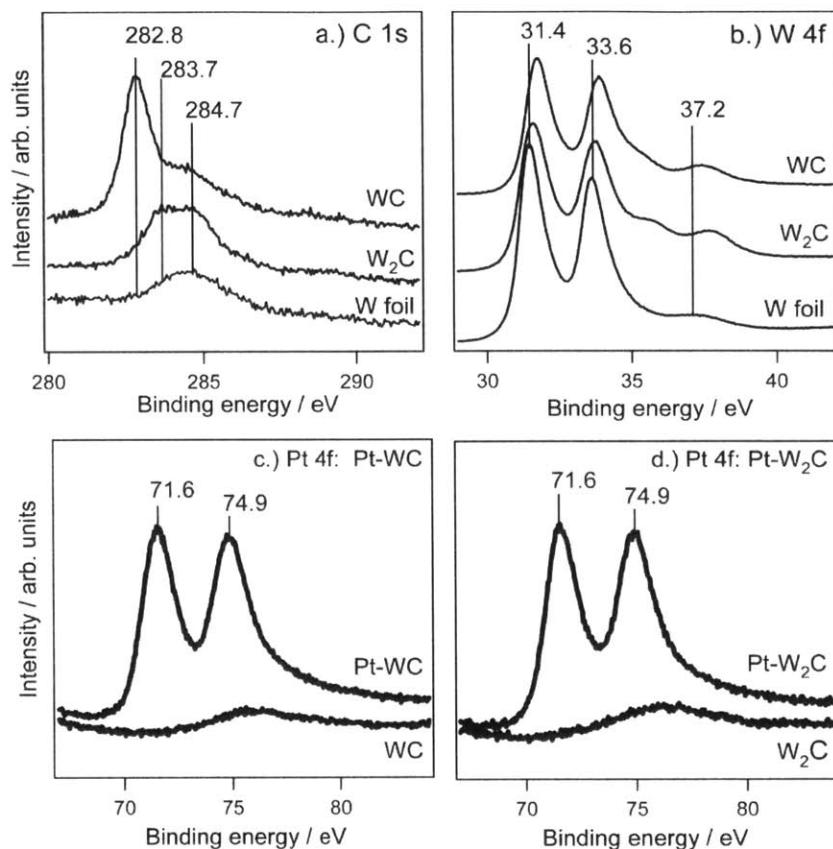


Figure 3.2. XPS C 1s peaks for (a) PVD WC and (b) PVD W₂C thin films. Spectra for an NaOH-cleaned W foil (bottom spectra) are shown for reference. XPS Pt 4f spectra for 1 ML of Pt deposited on (c) WC and (d) W₂C thin films. Background spectra for unmodified carbide surfaces are also included.

Figure 3.2b contains the W 4f spectra of as-synthesized WC and W₂C thin films alongside that of a reference W foil stripped of oxides with NaOH. The W 4f signals for the W foil sample are located at 31.45 and 33.7 eV, in agreement with literature.^[75] The relatively weak and broad peak centered at 37.1 eV is the W5p^{3/2} signal, not from the W 4f signal originating from W_xO_y species. For all W_xC samples, the W 4f peak locations are observed to be shifted +0.2 to 0.4 eV higher in binding energy compared to metallic W. Weak W_xO_y W 4f signals are observed for the W_xC samples, likely due to exposure to air during sample transfer from synthesis to XPS measurements. The carbidic W:C atomic ratio of the WC thin film is around 1.0 and that of W₂C around 2.0, which is expected for stoichiometric W-carbides.

Quantification of Pt Overlayer Thickness

In **Figure 3.2c** and **d**, XPS of Pt 4f peaks are shown for one ML of Pt deposited on WC and W₂C, respectively. The Pt 4f region for each sample before Pt deposition is also included for comparison, which shows the presence of a broad peak centered at ~ 75.7 eV that corresponds to signal from a W 4f satellite peak originating from the W_xC substrate. Based on the integrated peak areas of the Pt 4f and W 4f features of as-deposited Pt-W_xC samples, the thickness of the Pt overlayers was estimated using overlayer equations based on the Beer-Lambert law, as described previously.^[76] After deposition of 1 ML of Pt on the W_xC thin films, neither the carbidic C 1s spectra nor atomic W:C ratio of either W_xC sample was observed to change significantly.

Evidence of ML Pt Formation on W_xC Surfaces

In order to investigate the structure of the Pt overlayers deposited on W_xC surfaces, Pt overlayer growth experiments were performed in which the Pt 4f and W 4f spectra were periodically measured during overlayer growth. **Figure 3.3a** and **b** contain integrated Pt 4f and W 4f peak area intensities as a function of Pt deposition time on WC and W₂C thin films, respectively. For both substrates, changes in the slopes of the Pt 4f and W 4f signals are observed around 5 minutes of cumulative deposition time. This distinct break in slope is caused by self-screening of successive MLs and is indicative of layer-by-layer overlayer growth.^[88] This result is consistent with a similar Pt growth experiment on carburized polycrystalline W surface, in which it was found that layer-by-layer growth persisted for the first two MLs of evaporated Pt.^[89]

Further evidence of the ML character of the as-deposited Pt overlayer is the core level shift (CLS) of the Pt 4f ⁷/₂ peak center position relative to that of bulk Pt. CLS values are commonly observed for ultra thin metal overlayers, and are well known to be depend on the structure of the metal overlayer.^[90] In **Figure 3.3c**, the Pt 4f ⁷/₂ peak center position during Pt-WC and PtW_xC growth experiments is plotted against deposition time, showing a positive CLS compared to bulk Pt. For both samples, the Pt 4f ⁷/₂ CLS is observed to be around 1.0 eV at the lowest Pt coverage and decreases most sharply over the first 5 minutes. At a deposition time of 5 minutes, corresponding to about 1 ML of Pt deposited,

a shift of ~ 0.45 eV is observed for both samples, consistent with that reported for one pseudomorphic layer of Pt evaporated onto a W(110) substrate.^[91]

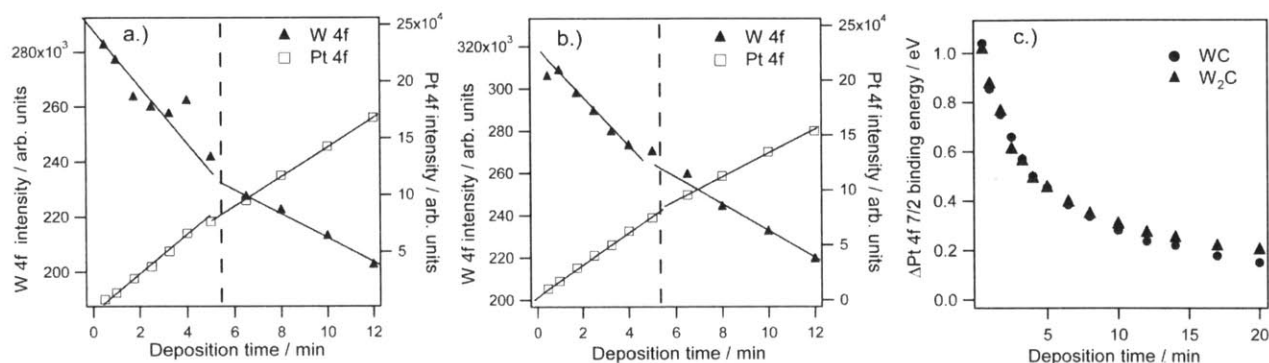


Figure 3.3. W 4f and Pt 4f intensities versus deposition time for (a) WC and (b) W_2C substrates. (c) XPS Pt 4f_{7/2} peak position as a function of time. Peak positions are shown relative to that of a clean Pt foil.

The origin in CLS in thin metal overlayers has been attributed to a variety of factors, including (i) inter-atomic charge transfer between the overlayer and the substrate, (ii) intra-atomic charge transfer between orbitals in the overlayer atoms, (iii) charge redistribution, and (iv) differences in final state effects caused by relaxation of electrons around the core-hole.^[90] All of these factors result directly or indirectly from bonding between the overlayer atoms and the substrate. Although the presence of the Pt 4f_{7/2} CLS in **Figure 3.3c** is not direct proof of a Pt ML, it does provide strong evidence that a majority of the deposited Pt atoms are in intimate contact with the W_xC substrate. Supporting this statement is the observation that the notable change in the slope of the CLS curve is located at around 5 minutes, which corresponds well with the break in the growth curves of **Figure 3.3a** and **b**. This change in slope in **Figure 3.3c** can be explained by a decrease in the influence of the factors (i-iv) cited above that can be expected once the first ML is completed.

Because the core level binding energy reflects the electronic and structural states of the Pt overlayer, the Pt 4f_{7/2} peak position can serve as an important metric for detecting changes in the Pt overlayer structure resulting from a chemical or electrochemical

treatment. For this reason, changes to the Pt $4f_{7/2}$ peak position and line shape were closely monitored following extended HER stability tests presented below.

3.3 Evaluation of W_xC and Pt/ W_xC HER Activity

The HER activity of Pt, WC, W_2C and Pt- W_xC electrodes was determined by conducting LSV measurements in 0.5 M H_2SO_4 at room temperature. From LSV measurements, the log of the current density was plotted versus the electrochemical potential to obtain Tafel curves (**Figure 3.4**), commonly used for quantitative kinetic analysis of HER catalysts. From the linear region of the Tafel plots, the exchange current densities (j_0) and Tafel slope (b) were determined for each sample and are provided in Table 3. Comparison of the Tafel plots for single phase electrodes in **Figure 3.4** reveals that the W_xC surfaces display HER overpotentials that are 200-300 mV greater than the Pt foil. The Tafel parameters obtained for Pt foil are consistent with those reported in literature for polycrystalline Pt in H_2SO_4 .^[77] For the WC thin film, j_0 and b values are slightly lower than those reported for smooth, sintered WC electrodes.^[92] These differences likely arise from differences in electrode surface areas. No reported Tafel parameters could be found for smooth W_2C electrodes. Despite similarities in the HER overpotentials of the WC and W_2C samples, the Tafel slopes are substantially different (91 mV/dec. for WC and 69 mV/dec. for W_2C). This deviation in HER behavior may reflect differences in the rate limiting step on each surface,^[93] but more advanced electroanalytical techniques are needed to verify this possibility. Nonetheless, it can be concluded from **Figure 3.4** that single-phase WC and W_2C catalysts having comparable real surface areas display similar HER overpotentials.

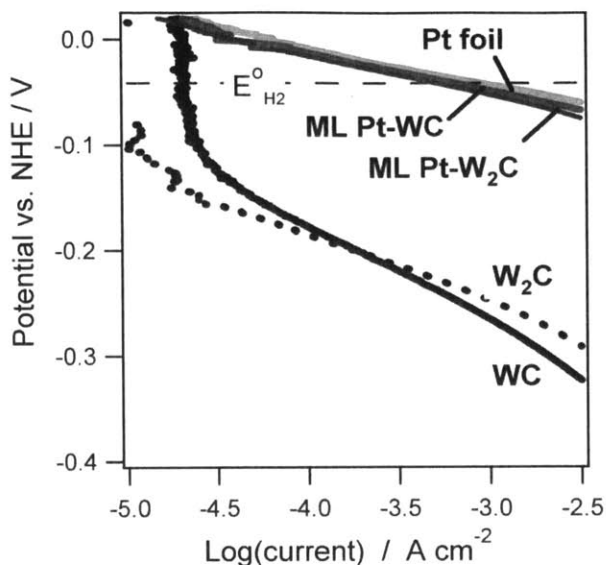


Figure 3.4. Tafel curves of bare and Pt-modified WC and W₂C thin films in Ar-purged 0.5 M H₂SO₄ at room temperature. For comparison, the Tafel plot for polycrystalline Pt foil is also included.

As shown in **Figure 3.4**, ML Pt-WC and Pt-W₂C surfaces were found to exhibit significant enhancement in HER activity compared to unmodified W_xC, with Tafel curves being nearly identical to bulk Pt. From **Table 3.3**, the Tafel parameters for Pt foil are slightly better than ML Pt-W_xC surfaces, although this minute difference could be caused by differences in crystal orientation, as strong dependence on HER j_0 values has been found for the various crystal faces of Pt.^[94] Regardless, both ML Pt-W_xC surfaces show very high HER activity, consistent with predictions based the DFT-calculated HBE values of these surfaces. On the basis of HER activity, both WC and W₂C are effective supports for ML Pt, although there do not appear to be a synergistic effect on HER activity as claimed for W_xC-supported Pt particles.^[95] It is possible that W_xC supported Pt nanoparticles could have higher HER activity than the ML Pt-W_xC films studied in this work, although such an enhancement must be quite large to out-weigh the cost-benefit of using ML amounts of Pt. The great importance of **Figure 3.4** is that one ML of Pt on W_xC surfaces can provide HER activity that is comparable to bulk Pt, indicating that Pt loadings in water electrolysis applications may be drastically decreased without compromising efficiency.

Table 3.3. Tafel Parameters Obtained for Different Thin Films from LSV Measurements in Ar-purged 0.5 M H₂SO₄ Solutions at Room Temperature

Model Catalyst	$-\log(j_0, \text{A cm}^{-2}_{\text{geo}})$	$-b \text{ (mV dec}^{-1}\text{)}$
Pt foil	-3.1	33
W ₂ C	-6.7	69
WC	-5.6	91
ML Pt/WC	-3.2	34
ML Pt/W ₂ C	-3.3	35

3.4 Stability of W_xC and Pt/W_xC Surfaces under HER Conditions

For ML electrocatalysts, the most important characteristic is the monolayer stability under appropriate operating conditions. Stability is especially critical for sub-nm Pt particles or films, which can be expected to agglomerate into larger, more thermodynamically stable particles in the absence of strong Pt-substrate interactions.^[96] Currently, the most common PEM support material is carbon, usually in the form of carbon black.^[96] Carbon can be an inexpensive, high surface area support material, but it is relatively inactive towards the HER, and its slow degradation in acidic environments has been cited as a primary reason for Pt loss in fuel cells.^[96,97] In alkaline water electrolysis, it has similarly been found that the low adhesion of Pt to graphite leads to loss of Pt particles during hydrogen evolution.^[98] In contrast to carbon, W_xC phases have displayed comparably better stability as support materials in fuel cell applications for Pt nanoparticles^[99-101] and Pt ML.^[102,103] These findings are consistent with the strong DFT-calculated binding energies between Pt and W_xC in **Table 3.2**, and lead to the expectation that ML Pt is stable on the W_xC substrates.

For bulk W_xC and Pt electrocatalysts, a primary concern in electrochemical applications is their oxidation to oxides or dissolved solution species. Fortunately, the negative potentials of a HER cathode are generally not conducive to electrooxidation of these materials. Pt is one of the more stable electrocatalyst materials, with Pt oxidation/dissolution typically not observed for potentials < 0.85 V RHE in acidic conditions.^[104] Although W_xC phases do not possess the same superb corrosion resistance as Pt, both W₂C and WC display oxidation onset potentials that are significantly more positive than RHE,^[105] meaning neither carbide should be susceptible to sustained

corrosion under HER operating potentials. As expected, XPS scans of the W 4f region for both unmodified W_xC surfaces following chronopotentiometry (CP) measurements under HER conditions reveal negligible W 4f oxide features.^[48]

Although the very positive standard reduction potential for Pt ensures that ML Pt is not vulnerable to anodic dissolution under HER conditions, there is concern that poor adhesion of the Pt ML to a given substrate will lead to detachment and/or agglomeration of Pt. Because all Pt atoms in a ML structure are exposed to the electrolyte, minor detachment or agglomeration of small portions of the Pt ML is likely to result in significant loss of active surface area and a corresponding decrease in HER activity. DFT-calculated binding energies for ML Pt on $W_xC(001)$ and Pt(111) indicate that ML Pt should be stable on W_xC surfaces (**Table 3.2**), but these DFT calculations do not take into account the possible influences of the interaction with the aqueous electrolyte and H_2 bubble formation/cavitation.

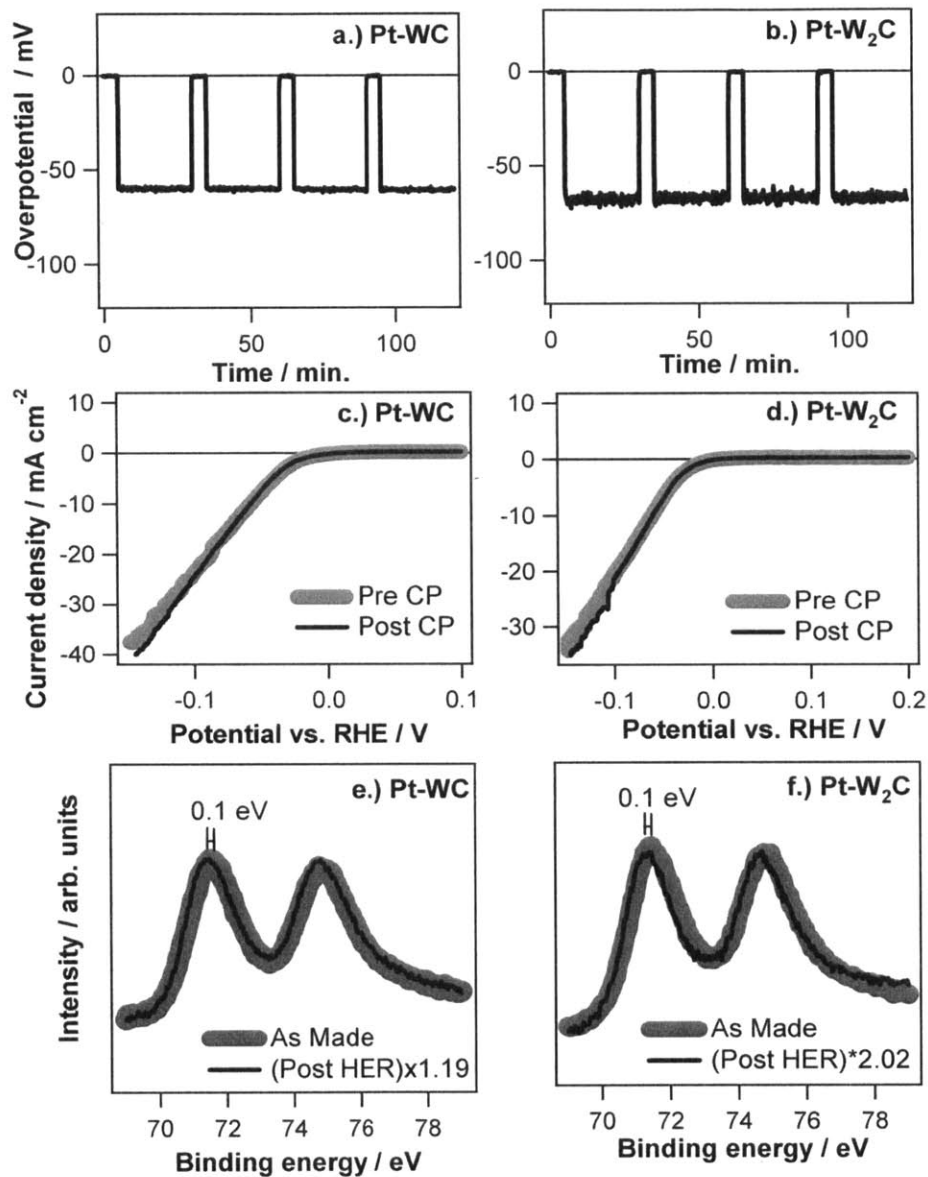


Figure 3.5. Results of stability tests for ML Pt/WC and ML Pt/W₂C thin films. (a, b) CP stability tests performed in H₂-purged 0.5 M H₂SO₄ at room temperature over 2 h. The current was alternated between 0.0 and 10 mA cm⁻²_{geo} to simulate electrolyzer operation. (c, d) LSV measurements taken before and after the CP measurement. (e, f) Pt 4f region following extended stability tests conducted in H₂-purged 0.5 M H₂SO₄ at room temperature.

In order to test the stability of ML Pt-W_xC surfaces in this work, LSV measurements were recorded before and after a series of CP measurements to simulate on/off operation in a real electrolysis cell. CP measurements consisted of alternating induced current densities of 0.0 mA cm⁻² (5 min.) and -10.0 mA cm⁻² (25 min.) over 2 h. During CP

measurements, the overpotential of the working electrode was monitored as a function of time, as shown for ML Pt-WC and Pt-W₂C surfaces in **Figure 3.5a** and **b**, respectively. For both electrodes, constant HER overpotentials of ~ 60 mV were recorded during the current withdrawing steps and the potential assumed the value of the reversible hydrogen electrode (RHE) during the open circuit steps. The constant overpotential in this CP measurement is characteristic of stable cathodic operation,^[98] which suggests that the structure of the Pt ML has not changed. In **Figure 3.5c** and **d**, stable HER activity is verified by the observation that LSV measurements recorded before and after CP measurements are essentially identical.

XPS and SEM measurements of the ML Pt-W_xC surfaces were conducted before and after the CP measurements to further verify the stability of the Pt overlayer. XPS scans following HER measurements confirmed the absence of any contaminants on the Pt-W_xC surfaces, which can have a strong influence on HER behavior. In **Figure 3.5d** and **e**, the Pt 4f spectra of the ML Pt-W_xC surfaces taken following CP/LSV measurements are superimposed to those of the as-synthesized samples. For both Pt-WC and Pt-W₂C, the normalized Pt 4f spectra are nearly identical in shape and position, indicating no change in the electronic properties of the Pt overlayer as discussed in Section 3.2. This in turn infers no change in the structure of the Pt overlayer. Equally important is the finding that the Pt 4f / W 4f peak ratios taken before and after extended stability tests do not change for either catalyst (not shown). If there were a loss of Pt from the surface or agglomeration of Pt to form particles, the Pt/W ratio would be expected to decrease.

3.5 Investigation of Other ML NM/TMC Model Electrocatalysts

In addition to the ML Pt-W_xC surfaces, the HER activity was also investigated for the following metal-TMC surfaces whose HBE values span a wide range of the HER volcano curve: Mo₂C, ML Pd-Mo₂C, ML Pd-WC, ML Au-Mo₂C, and ML Au-WC. The DFT-calculated HBE values for these surfaces are listed in **Table 3.1**. Among these new materials, Mo₂C is an interesting TMC surface to investigate as a substrate for ML HER catalysts because Mo₂C powders can be synthesized at much lower temperatures than W_xC, allowing for synthesis of smaller Mo₂C particles with much higher surface areas than

W_xC.^[13] Furthermore, the onset for oxidation of single-phase Mo₂C thin films is not observed until +0.4 V NHE,^[106] a potential that is well positive of HER operating potentials. For overlayer metals, Au was selected for the purpose of investigating catalysts located on the low HBE side of the volcano curve (Au-WC and Au), while Pd was chosen due to reported high HER activity of previously studied ML Pd bimetallic surfaces.^[107,108] Furthermore, the price of Pd is currently less than 50% that of Pt,^[109] making ML Pd HER catalysts especially attractive from a cost standpoint.

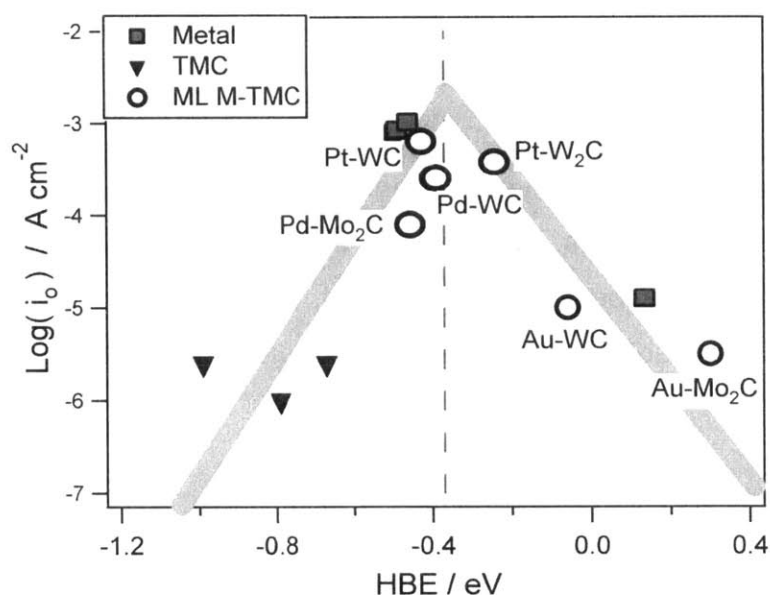


Figure 3.6. Volcano Relationship between HER activity (j_0) and hydrogen binding energy (HBE) for all metal, TMC, and ML NM/TMC thin films studied in this chapter. The j_0 values were obtained from Tafel analysis of linear sweep voltammograms performed in H₂-purged 0.5 M H₂SO₄ at room temperature. HBE values are taken from **Table 3.1**. Thick gray lines are included to guide the eye while the dashed gray line marks the center of the volcano curve, located 0.09 eV more positive than the HBE of Pt (111) according to Nørskov et al.^[77]

The HER activity of each of the surfaces was measured in identical conditions as already described for the ML Pt-W_xC surfaces. In **Figure 3.6**, the j_0 values determined from the Tafel plots for these surfaces are plotted versus the corresponding DFT-calculated HBE. Also included are the data points for W_xC, Pt, and Pt-W_xC surfaces. It is apparent that a volcano relationship is observed for the surfaces studied in this work,

reflecting Sabatier's Principle as discussed earlier. Previous DFT studies have shown that both pure metals^[77] and ML bimetallic surfaces^[107] display volcano relationships for the HER with the peak center located around an HBE of -0.38 eV. **Figure 3.6** provides evidence that TMC and metal-modified TMC surfaces also obey a similar volcano relation for the HER. As discussed in Section 3.1, the importance of this finding is that other ML-TMC surfaces may be effectively screened for HER activity based on their DFT-calculated HBE values.

Of the additional surfaces studied, the ML Pd-WC and ML Pd-Mo₂C thin films showed the most promise as HER electrocatalysts. Although their measured HER activity was not as high as Pt or Pd, their relatively high activity, potential for synthesis of high surface area structures (for Mo₂C), and the lower cost of Pd compared to Pt warrant further development of these catalysts. Slightly lower HER activity may be tolerated for low-current density electrolysis applications such as photoelectrochemical cells or photovoltaic electrolysis, especially if a low-cost, high surface area substrate material such as Mo₂C can be used. This possibility is explored further below in **Figure 3.7** and **Figure 3.8**.

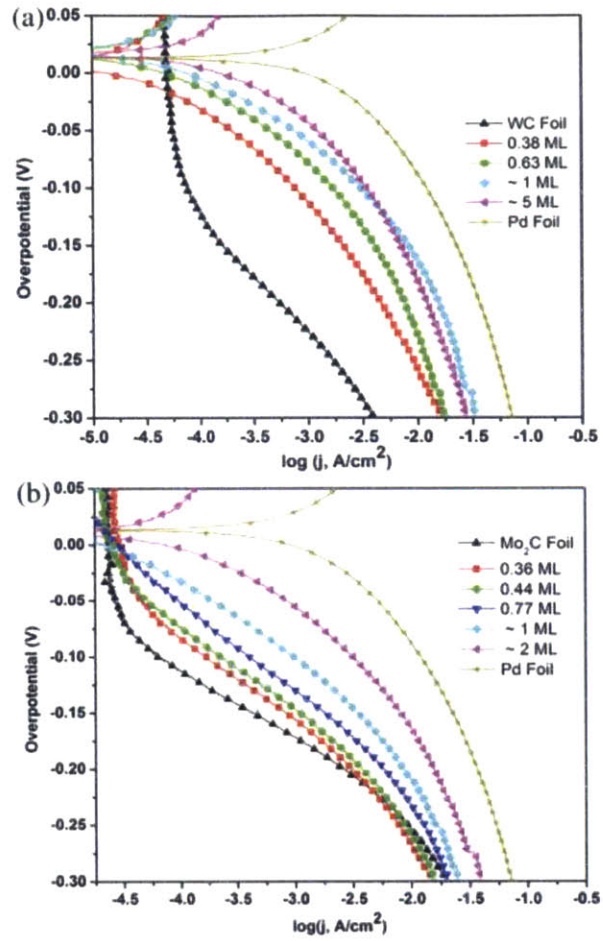


Figure 3.7. Tafel plots for (a) WC and Pd-modified WC and (b) Mo₂C and Pd-modified Mo₂C LSV data

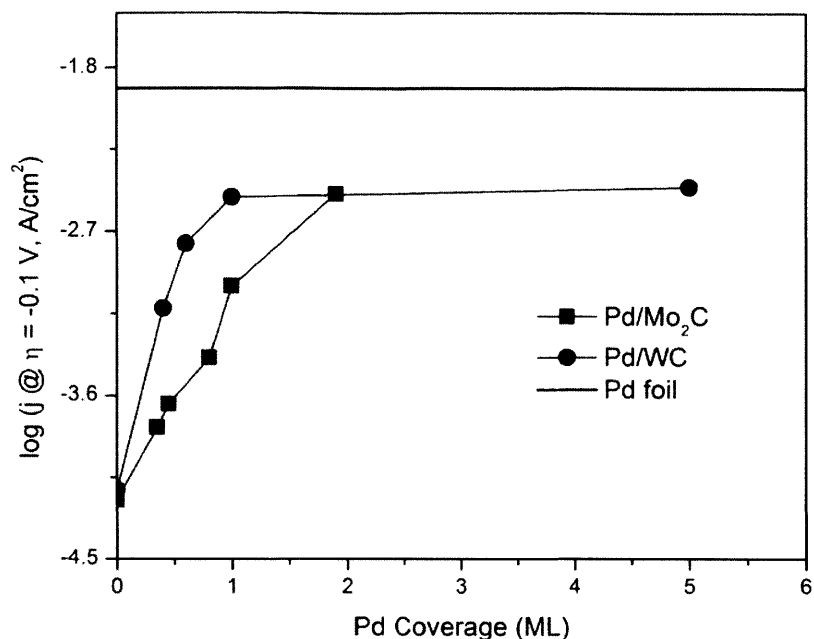


Figure 3.8. Log of the current density at an overpotential of 0.1 V vs. Pd coverage on WC and Mo₂C. Solid black line represents the current density on Pd foil.

4. Conclusions and Insights for Real Core-Shell Catalyst Design

We have studied well-characterized, single-phase WC and W₂C thin film electrodes as a platform for comparing the utility of these materials as supports for ML-thick Pt HER catalysts. In electrochemical measurements, both W_xC surfaces were shown to be excellent supports for ML amounts of Pt, with demonstrated HER activities that are comparable to bulk Pt, consistent with predictions based on DFT-calculated hydrogen binding energies for ML Pt-W_xC. More importantly, a combination of electroanalytical, XPS, and SEM measurements were used to show that these ML Pt-W_xC catalysts are stable over two hours of HER operation at an HER current density of 10 mA cm⁻². Additionally, it has been shown that multiple combinations of ML metals supported on TMC substrates obey the commonly observed volcano relationship between HER activity and HBE. In future research efforts, the single-phase TMC thin films studied here can serve as a useful experimental platform for elucidating the roles of defects, surface carbon, and oxide species on the metal ML-TMC interface. Such investigations will lead to a better understanding of the interactions of metal overlayers with TMC surfaces,

allowing for the optimization of catalyst activity/stability while enabling translation of that knowledge to high surface area mesoporous and particulate catalysts for high current density electrolysis applications.

Although this study has focused on well-controlled ML metal-TMC thin film surfaces, the thin film electrode geometry is not suitable for electrolysis applications besides low-current density photoelectrochemical and PV electrolysis cells. For high rates of water electrolysis in a PEM electrolyzer, high surface area particulate or mesoporous materials with a ML NM/TMC core-shell structure are needed. However, synthesis of such core-shell structures presents several challenges, including deposition/synthesis of uniform metal shells, achieving good control of the metal-TMC interface, and synthesizing TMC structures with high surface areas. Thermal evaporation on TMC thin films was suitable in this work, but vacuum processing steps are generally not conducive to scaled up production processes and line-of-site deposition techniques are not capable of uniformly coating 3-dimensional materials. For these reasons, alternative synthesis methods, including but not limited to atomic layer deposition, reverse microemulsion synthesis, and chemical vapor deposition must be explored. Through careful design of processing steps and knowledge gained from thin film studies, such techniques should be capable of producing low-cost ML NM/TMC core-shell catalysts which are suitable for high current density electrolysis applications. The steps needed to realize such a system are taken in the subsequent chapters.

Acknowledgements

We acknowledge Brian McCandless for assistance with XRD and GIXRD, Irene Hsu for assistance with thin film synthesis, and Kevin Dobson for invaluable discussion. We acknowledge financial support from the Department of Energy (DE-FG02-00ER15104). DVE acknowledges partial support from the NSF Solar Hydrogen IGERT Program (DGE-0549399) and the NASA Delaware Space Grant College and Fellowship Program (NASA Grant NNG05GO92H).

Chapter 4

Engineering Non-Sintered, Metal-Terminated Tungsten Carbide Nanoparticles for Catalysis

1. Introduction

Early transition metal carbides (TMCs) are earth-abundant materials with established commercial use in a variety of applications due to their favorable optical, electronic, mechanical, and chemical properties.^[13-15] Tungsten carbide (WC) has garnered much attention for its catalytic similarities to the platinum group metals^[18] (PGMs) in several thermo- and electro-catalytic reactions, such as biomass conversion,^[14,28,29] hydrogen evolution and oxygen reduction,^[31-35] and alcohol electrooxidation.^[36,37] The reactivity of WC has been partially attributed to the intercalation of C to the W lattice, which gives rise to a “Pt-like” d-band electronic density states (DOS).^[19] Peppernick et al. demonstrated that WC⁻ ions exhibit isoelectronic correspondence with Pt⁻ ions.^[20] Because WC exhibits high thermal and electrochemical stability while resisting common catalyst poisons such as carbon monoxide and sulfur,^[13-15] it has been identified as a suitable candidate to replace PGM catalysts in emerging renewable energy technologies such as fuel cells and electrolyzers.^[31-35,48,70,110]

While there are many methods to synthesize WC nanoparticles (NPs), none of the current methods can simultaneously prevent sintering of the WC nanoparticles while also mitigating surface impurity deposition. Thus, despite the promising catalytic properties of model WC surfaces, the lack of synthesis methods to produce metal-terminated WC NPs of controlled sizes has prevented its wide-spread use as an earth-abundant catalyst.^[13,14,31,47] The high carburization temperatures (> ca. 700 °C) required to overcome the thermodynamic and kinetic barriers for carbon incorporation into the metal lattice induce uncontrollable particle sintering, generating particles with exceedingly low surface areas that are not suitable for commercial applications (**Figure S4.5**).^[13,14] Although alternative synthesis methods with unconventional heating^[111-114] and carbon sources^[35,47,70,115,116] have been developed to mitigate sintering, the resulting particles are extensively coked and do not feature metal-terminated surfaces. Current methods either

partially mitigate sintering while generating thick surface oxide layers with excess surface carbon or fully mitigate sintering by embedding carbides within high excesses of carbon. Minute quantities of surface impurities block reactants from accessing active sites and have been shown to greatly reduce or eliminate the catalytic activity of WC.^[37,72]

Consequently, catalytic studies with WC are often restricted to model materials (e.g., thin films or bulk particles) where metal-terminated active sites are synthetically achievable. To date, the encouraging catalytic results obtained with these model materials have not been translated to analogous metal-terminated nanoscale formulations. For instance, surface science studies have shown that planar, metal-terminated polycrystalline α -WC foils are more active than comparable planar Pt foils for anodic methanol electrooxidation (MOR),^[36,37] but W_2C microparticles and α -WC nanowires containing synthesis-inherent surface carbon impurities are inactive towards MOR.^[117,118] Accordingly, the unique electrocatalytic properties arising from high degrees of coordinative unsaturation and quantum size effects for WC NPs continue to be known only theoretically^[119] and remain experimentally unexplored. To bridge this “materials gap” and translate the promising surface science studies for replacing PGMs with WC in commercial devices, it is critical to develop new synthetic methods capable of generating non-sintered, metal-terminated TMC NPs.^[14,31]

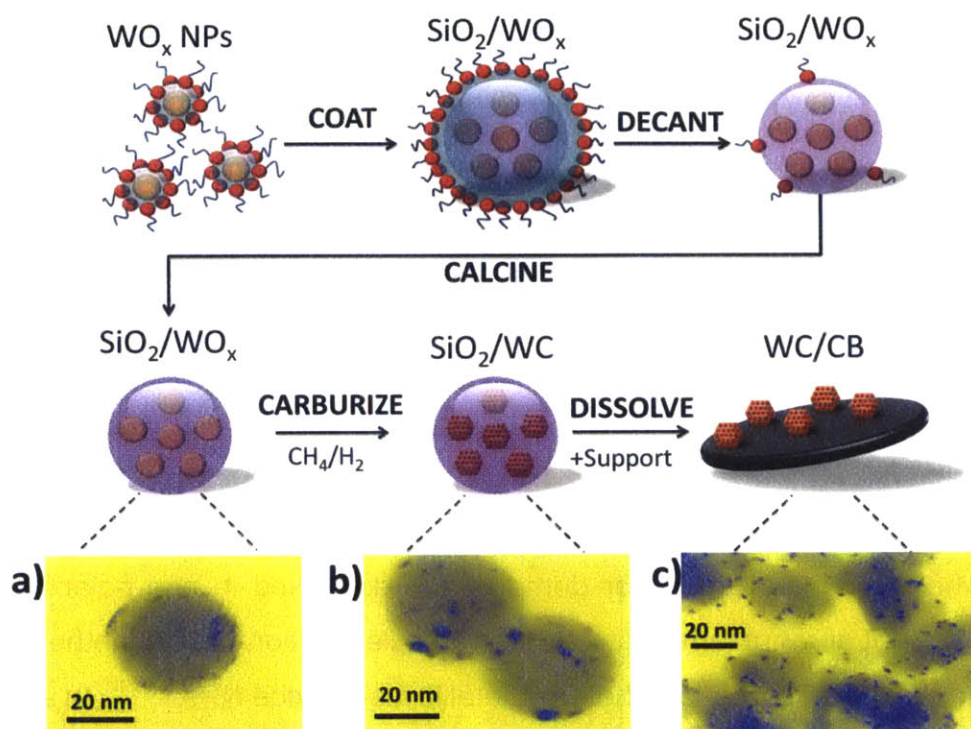


Figure 4.1. Schematic representation of the “removable ceramic coating method” for the synthesis of WC/CB. [a] STEM image of silica-coated tungsten oxide NPs. [b] STEM image of silica-encapsulated WC NPs. [c] STEM image of WC NPs supported on carbon black

Here, we demonstrate a method to produce mono- and multi-metallic TMC NPs with tunable size, composition, and crystal-phase. This synthesis method is versatile, allowing for the deposition of well-dispersed, metal-terminated TMC NPs in the range of 1–4 nm on a high surface area support with loadings exceeding 40 wt%. The three-step process is depicted in **Figure 4.1**. First, a reverse microemulsion (RME) is used to create transition metal oxide NPs encapsulated within silica (SiO₂) nanospheres. The resulting composite particles are subjected to a high temperature carburization process, wherein the SiO₂ coating serves as a hard template to prevent NP sintering while allowing the diffusion of carburization gases onto the metal oxide surfaces (**Figure 4.1b**). Next, a liquid dispersion of naked TMC NPs is obtained by dissolving the SiO₂ shell, and supported NPs are obtained by mixing a high surface area solid with the dispersion (**Figure 4.1c**). The method is general, being applicable to virtually any metal oxide

formulation that can be transformed into a carbide. We exemplify the method here through the synthesis of monometallic tungsten carbide (WC) and bimetallic molybdenum tungsten carbide ($\text{Mo}_x\text{W}_{1-x}\text{C}$) NPs. Using hydrogen evolution (HER) and methanol electrooxidation (MOR) as probe reactions, we show that these TMC NPs supported on Vulcan® XC-72r carbon black (CB) are highly stable and attain capacitances and catalytic activities that are orders of magnitude higher than those obtainable with analogous carbides synthesized with current methods, approaching the activities of PGM-based electrocatalysts.

2. Synthesis and Characterization

An RME, wherein nano-sized water domains are dispersed in non-polar media via a nonionic surfactant at room temperature, is a versatile solution-based method to tune the size and composition of mono- and hetero-metallic metal oxide NPs.^[120-122] In a single step, ca. 100 ultrasmall (1–2 nm) WO_x NPs were encased within ~40 nm silica nanospheres (Figure 1a) at metal loadings of ca. 20 wt% when using a nonionic Brij-L4@/*n*-heptane/water RME system (see **Figure S4.6-Figure S4.10** and **Figure S4.12-Figure S4.22** for a survey of synthesis space). High angle annular dark field scanning transmission electron microscopy (STEM) images show that controlled temperature treatments of the encapsulated WO_x NPs with sequential oxidizing (air, 450 °C), reducing (21% CH_4/H_2 mixture, 590 °C), and carburizing (21% CH_4/H_2 mixture, 835 °C) conditions result in the formation of carbide NPs in the 1–4 nm range (**Figure 4.1b**). An H_2 treatment at 835 °C followed by exposure to 1% O_2/N_2 at 25 °C scavenges residual surface carbon and forms a surface-passivating oxide layer that allows handling in ambient conditions.^[33,48] We hypothesize that the heat treatment promotes the formation of micropores on the silica shell allowing H_2 and CH_4 to reach the surface of the oxide, while diminishing particle migration and coalescence (see **Figure S4.11**). This phenomenon is consistent with recent reports showing sintering reduction during high temperature catalytic reactions (up to ca. 750 °C) is achieved by coating noble metals with microporous and mesoporous ceramic overlayers.^[123-125] Measured particle-size distributions (PSD, **Figure 4.2c**) indicate that sintering is largely mitigated within these silica nanospheres

even after prolonged exposure to carburizing conditions at 835 °C and as high as 950 °C (see **Figure S4.9**, **Figure S4.14**, and **Figure S4.15**). The slight increase in PSD after carburization is attributed to the lateral diffusion of surface-bound NPs on the silica nanospheres.

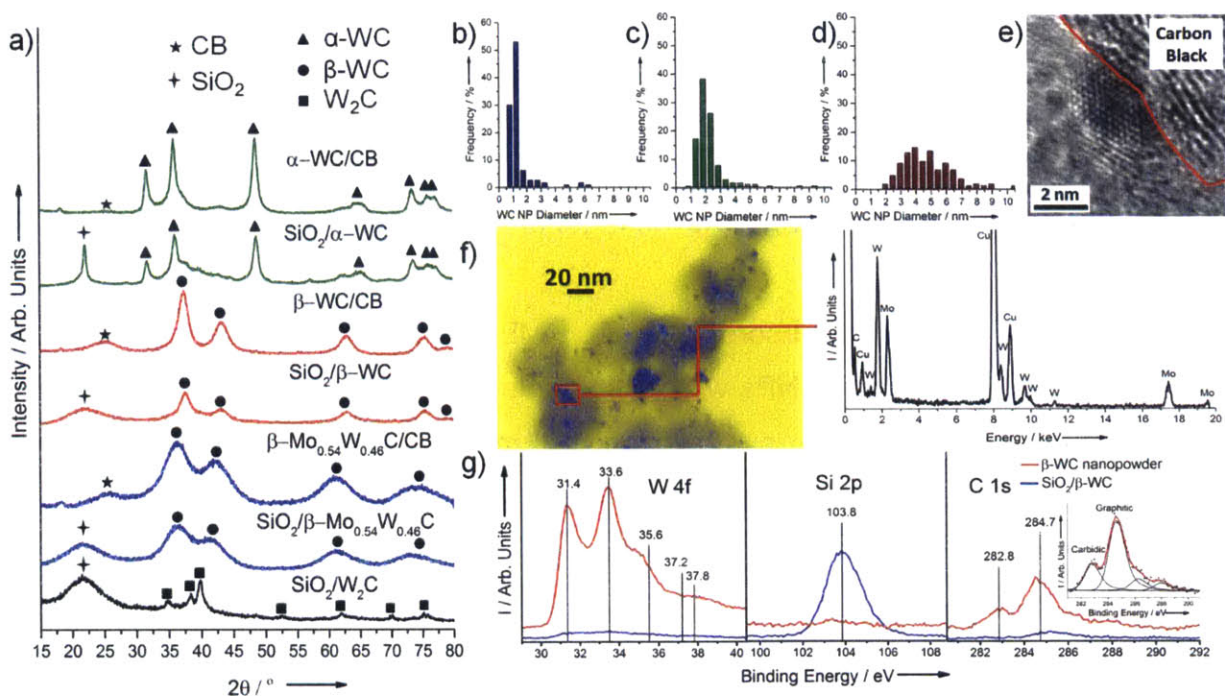


Figure 4.2. Characterization of Non-Sintered, Metal-Terminated WC Nanoparticles [a] PXRD diffractograms (in ascending order) of silica-coated and CB-supported W_2C , β - $Mo_{0.54}W_{0.46}C$, β -WC, and α -WC. [b] PSD for β -WC tuned for 1 nm NPs. [c] PSD for 1-3nm β -WC tuned for 2 nm NPs. [d] PSD for 3-6nm α -WC. [e] HR-TEM image of a 2nm β -WC NP. [f] STEM image of a 25 wt% β - $Mo_{0.54}W_{0.46}C/CB$ and the corresponding EDX spectra for a single NP showing the presence of both W and Mo (The presence of the Cu background arises from the TEM grid material). [g] XPS spectra of SiO_2/β -WC and the β -WC nanopowder obtained post-ABF-dissolution for W, Si, and C signals.

The PSD, crystal phase, and composition of TMC NPs can be tuned by altering synthesis parameters. Powder x-ray diffractograms (PXRD) diffractograms shown in Figure 2a confirm the presence of phase-pure face-centered cubic (fcc) WC particles (β -WC or WC_{1-x}) when using standard RME and heat treatment protocols (*vide supra*). Increasing the size of silica nanospheres from 40 to 50 nm resulted in a decrease in the PSD of WC NPs from 1–3 nm to 1–2 nm (**Figure 4.2b**). Lowering the carburization temperature to 775°C and decreasing the CH_4/H_2 ratio to 18%, resulted in the formation

of phase-pure tungsten semicarbide (W_2C) NPs (**Figure 4.2a**). While β -WC is typically considered a high temperature phase,^[126] both β -WC and the traditional hexagonal phase (α -WC) were synthesized under identical carburization conditions (835 °C, 21%CH₄/H₂). α -WC was obtained when lowering the methanol:heptane ratio used for precipitation prior to carburization (**Figure 4.2a**). The resulting α -WC NPs were larger (3–6 nm) than the β -WC NPs and featured quartz-like domains within the silica spheres (**Figure 4.2a, c**). Although no experimental methods had been reported before for the synthesis of β -WC NPs in the 1–4 nm range, recent density functional theory (DFT) studies have predicted that both the fcc β -WC lattice and the hexagonal α -WC lattice are stable phases for ultras-small NPs.^[119]

Combining metal precursors at the RME stage allows the synthesis of heterometallic “double” carbide NPs with a high degree of compositional control. In this respect, $Mo_xW_{1-x}O_y$ NPs were synthesized by mixing tungsten and molybdenum precursors (see **Figure S4.6-Figure S4.8** and **Figure S4.18-Figure S4.21**). These heterometallic oxides were subjected to similar encapsulation and carburization protocols as those used for mono-metallic carbides to generate double carbides either in a β -WC phase (**Figure 4.2a**) or in an α -WC phase (**Figure S4.21**). A separate molybdenum carbide (Mo_2C) phase was not observed, which is consistent with reports showing the formation of double carbide microparticles.^[127] STEM with energy-dispersive X-ray spectroscopy (EDX) analysis confirmed the presence of both W and Mo within single NPs (**Figure 4.2f** and **Figure S4.24**). The exact compositions were determined using inductively coupled plasma (ICP) analysis. The compositions synthesized range from $Mo_{0.02}W_{0.98}C$ to $Mo_{0.54}W_{0.46}C$ (**Figure S4.24**).

Silica and other hard template materials are electrically insulating; therefore, the resulting composite materials are not amenable for electrocatalysis. For this reason, syntheses methods using hard templates, such as SBA-15,^[128] have not been geared towards producing electrocatalytically active WC. Moreover, such hard templating methods suffer from being synthetically complex, having low metal loadings, and lacking control over crystal phase and particle size. Critical to our method, we show that the silica shell can be fully removed under acidic (20 wt% ammonium bifluoride [ABF]) or alkaline (0.5 M NaOH) conditions to yield solutions containing dispersed, non-sintered naked

carbide NPs (see **Figure S4.23**). Although WC dissolves in strong alkaline media,^[41] PXRD diffractograms show that both α -WC, β -WC, and β -Mo_{0.54}W_{0.46}C are stable in ABF (**Figure 4.2a, f**). Notably, re-dispersing α - and β -WC NPs in water or ethanol showed no signs of sedimentation after 20 days (see **Figure S4.23**). In contrast with other methods,^[129] neither sonication nor polymeric agents are required to disperse the WC NPs. Targeted loadings (even in excess of 40 wt%) are obtained simply by mixing specific amounts of CB directly with the SiO₂/WC/ABF solution or the waterborne dispersion. STEM images confirm that highly dispersed TMC NPs on CB are obtained following this procedure (**Figure 4.1c, Figure 4.2f, and Figure S4.16**). Decoupling carburization from support deposition is important because it allows dispersing the TMC NPs on a variety of supports, including those that would be damaged during the harsh carburization conditions.

X-ray Photoelectron Spectroscopy (XPS) analyses on passivated β -WC nanopowders post ABF-dissolution revealed that the carbide NP surfaces are free of impurities, with undetectable quantities of Si, minimal graphitic surface carbon, and indiscernible bulk oxidation formation (**Figure 4.2g**). Specifically, strong W 4f signals are found at 31.4 and 33.6 eV, which correspond to reduced metallic W. The small peaks at 36.2 and 38.3 eV correspond to WO_x in a surface passivating layer. These surface oxides can be easily removed prior to catalytic testing by in-situ treatment in H₂ or by quick alkaline rinses without impacting the bulk carbide structure.^[13,33,41,48] A carbidic C 1s signal at 282.8 eV indicates that the NP surfaces are carbide-terminated and that surface graphitic impurities are largely mitigated (**Figure 4.2g**). The locations and relative intensities are in agreement with previous literature for pristine WC thin films.^[37,48] High-resolution TEM images confirm that graphitic carbon is not present in detectable amounts on the surface of the NPs (**Figure 4.2e and Figure S4.17**). In contrast, reported TEM characterization data for conventional TMC synthesis methods show extensive surface carbon overlayers surrounding each nanoparticle, which obfuscate the carbidic C 1s signal.^[35,47,70,115]

3. Electrocatalytic Evaluation

HER is a well-established probe reaction for comparing WC materials. HER electrocatalytic activities of α -WC/CB and β - $\text{Mo}_{0.06}\text{W}_{0.94}\text{C}/\text{CB}$ materials were compared to conventional WC catalysts (using commercial WC microparticles and NPs synthesized using the “urea glass” method)^[47] and commercial 40 wt% Pt/CB. To obtain consistent power density comparisons across all catalysts, all working electrodes were loaded with 50 μg of catalyst by total weight uniformly dispersed on a 0.071 cm^2 glassy carbon disk (surface areas obtained from N_2 adsorption isotherms provided in **Table S4.2**). The catalysts were subjected to capacitance measurements at room temperature in Ar-saturated 0.5 M H_2SO_4 . The capacitances of the supported β -carbides were similar to Pt/CB and over 1.6 orders of magnitude higher than bare CB or the carbide controls (see **Figure S4.27** and **Figure S4.28**). These data indicate that 40 wt% WC/CB and 40 wt% Pt/CB with equivalent masses and geometric surface areas have similar electroactive surface areas, and they also suggest that supported β -carbides can serve as high power density supercapacitors with similar capacitances as supported amorphous RuO_2 nanoparticles prepared using a standard method (see **Figure S4.29** and **Figure S4.30**).^[130]

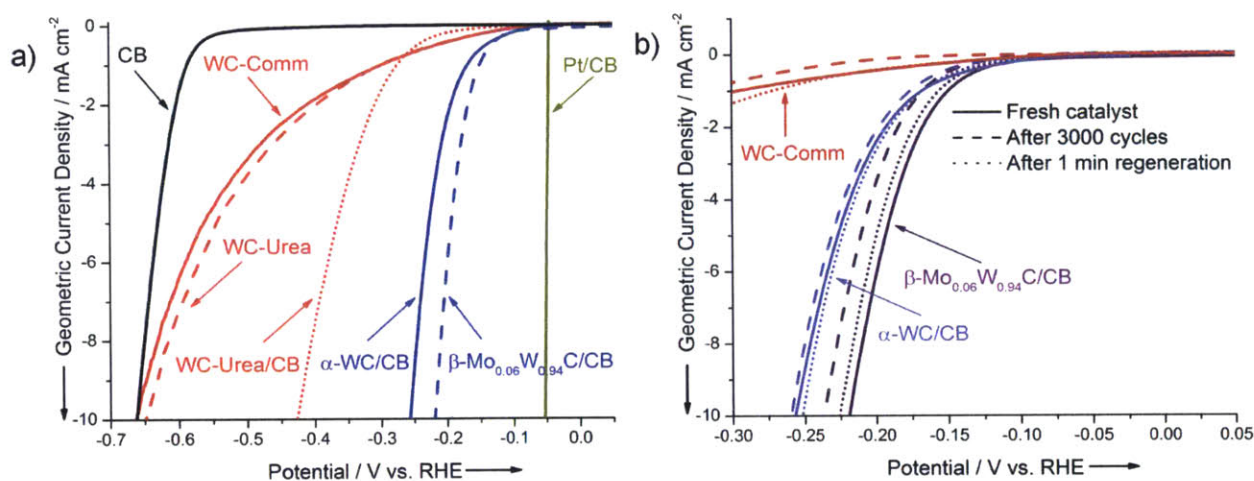


Figure 4.3. HER Activity, Stability, and Catalyst Regeneration. [a] Initial HER LSVs at 2 mV/s in H_2 -saturated 0.5M H_2SO_4 at RT. [b] LSVs at 2 mV/s in H_2 -saturated 0.5M H_2SO_4 at RT showing initial HER activity, the final activity after 3000 cycles between -0.3 and $+0.6$ V vs. RHE at a scan rate of 50 mV/s, and the regenerated activity after dipping the spent electrodes in 0.1 M NaOH for one minute. All CB-supported catalysts are loaded at 40 wt%.

Linear sweep voltammograms (LSVs) for each material under HER conditions show that TMC NPs synthesized with our method are highly stable and easily regenerated, achieving substantially higher HER currents at lower overpotentials when compared to the commercial or the “urea glass” WC (**Figure 4.3a**). We note that the large slope of the 40% Pt/CB control catalyst can be attributed to its high loading and the low pH of the electrolyte, while its offset from 0 V vs. RHE can be attributed to the use of a static working electrode (**Figure S4.31**).^[131] Chronoamperometry (CA) and chronopotentiometry (CP) measurements (**Table 4.1**) show that α -WC/CB and β - $\text{Mo}_{0.06}\text{W}_{0.94}\text{C}/\text{CB}$ exhibit current densities that are 1.4 orders of magnitude higher than either of the carbide controls. To drive 1 mA cm^{-2} of cathodic current, α -WC/CB and β - $\text{Mo}_{0.06}\text{W}_{0.94}\text{C}/\text{CB}$ required an overpotential that was lower by more than 100 mV than either of the carbide controls (**Table 4.1**). While $\text{Mo}_2\text{C}/\text{CB}$ and MoS_2 have been shown to be active HER electrocatalysts,^[132,133] we demonstrate the superior stability of both the CB-supported α and β -carbide NPs as well as a facile electrode regeneration method. After 3000 cycles between -0.3 V and $+0.6 \text{ V}$ vs. RHE, both the α and β carbides exhibited minimal deactivation (**Figure 4.3b**), showing an increase in overpotential of ca. 10 mV to drive 1 mA cm^{-2} (**Table 4.1**). Notably, the catalysts can be easily regenerated by dipping the electrode for 1 min in a 0.1 M aqueous NaOH solution to remove surface oxides (**Figure 4.3b, Table 4.1**).

Table 4.1. HER Activity, Stability, and Regeneration Comparison

Catalyst ^[a]	Initial j ^[b]	Initial η ^[c]	Final η ^[d]	Regenerated η ^[e]
	$j_{\alpha} = 290\text{mV}^*$ [mA cm ⁻²]	$\eta_i @ j_{\text{cat}} = 1$ [mV]	$\eta_f @ j_{\text{cat}} = 1$ [mV]	$\eta_r @ j_{\text{cat}} = 1$ [mV]
Pt/CB	-150	44	44	-
β -Mo _{0.06} W _{0.94} C/CB	-27	156	166	161
α -WC/CB	-21	165	175	165
Commercial WC	-1	290	311	281
WC-Urea/CB	-1.3	280	-	-
WC-Urea	-1.1	270	-	-
Vulcan CB	-0.1	360	-	-

[a] All CB-supported catalysts are loaded at 40 wt%. [b] Initial cathodic current density at a fixed overpotential of $\eta = 290\text{mV}$ vs. RHE. [c] Initial overpotential at 1mA cm^{-2} of cathodic current. [d] Overpotential at 1mA cm^{-2} after 3000 cycles between -0.3 and $+0.6\text{V}$ vs. RHE. [e] Overpotential at 1mA cm^{-2} after regeneration of the spent working electrode by dipping it in 0.1M NaOH solution for one minute.

PXRD diffractograms of the spent and subsequently regenerated catalysts indicate that both the α and β -carbides are stable after 3000 cycles (see Figure S28). Intrinsically, WC has a stronger hydrogen binding energy than Pt, which translates to a higher onset potential of HER.^[33,48] This inherent thermodynamic limitation is largely offset by WC's substantially lower cost and higher abundance in comparison to PGMs,^[31] as well as its higher activity, stability, conductivity, and ease of regeneration in comparison to other earth-abundant alternatives. We attribute the higher activity of the bimetallic β -Mo_{0.06}W_{0.94}C relative to α -WC to its smaller PSD (**Figure 4.2c** and **Table S4.3**), its higher surface area (see **Table S4.2**), as well as a bimetallic effect. Thin film studies have shown that pristine Mo₂C is more active towards HER than pristine WC,^[32] but Mo₂C features lower electrochemical stability than WC.^[42] A bimetallic Mo_xW_{1-x}C allows us to achieve a compromise between the activity of Mo₂C and the stability of WC in a single material. Insertion of Mo heteroatoms compresses the WC lattice due to the larger Wigner-Seitz radius of Mo, potentially giving rise to new catalytic activities via modulation of the d-band surface electronic density of states (DOS).

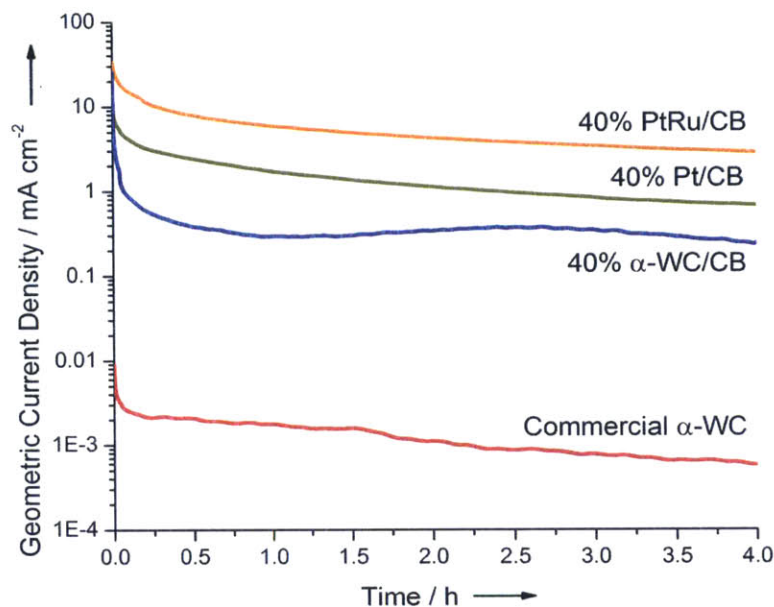


Figure 4.4. MOR Electrochemical Activity Comparison. Chronoamperometric responses in Ar-saturated 0.5 M H₂SO₄ and 2.0 M CH₃OH at 40 °C held potentiostatically at +0.75 V vs. RHE over 4 h.

Unlike other earth-abundant materials, WC is unique in its “Pt-like” ability to catalyze a broad array of important thermal and electrochemical reactions. However, activating WC for more complex reactions such as MOR requires pristine metal-terminated surfaces that are free from surface carbon or thick oxide layers.^[37] Thus, MOR activity serves as a probe to test if the WC nanoparticles are metal-terminated and free of surface impurities. For the first time, we show that CB-supported α-WC NPs are highly active and stable electrocatalysts for MOR, with power densities approaching those of commercial Pt-based materials (see **Figure S4.33-Figure S4.40**). **Figure 4.4** shows CA responses under MOR conditions, wherein a strong oxidizing potential of +0.75 V was chosen to verify that the measured currents were catalytic in nature, as reported in prior studies,^[117,118] and to highlight the remarkable long-term stability of the carbide NPs under harsh conditions. After 4 h, 40 wt% α-WC/CB was over 2.5 orders of magnitude more active than a commercial α-WC catalyst. Over the last 15 min of the 4 h experiments, the commercial WC drove an average current density of $0.58 \pm 0.01 \mu\text{A cm}^{-2}$, while α-WC/CB drove $235 \pm 8 \mu\text{A cm}^{-2}$. The “urea glass” WC was inactive, likely due to excessive surface carbon deposition during synthesis. We attribute the slight activity of commercial WC

from exposed metal-terminated sites achieved during the top-down ball-milling synthesis process. Remarkably, the activity of the α -WC/CB material was ca. 33% of that measured for a commercial 40 wt% Pt/CB catalyst ($696 \pm 6 \mu\text{A cm}^{-2}$), and approximately 1 order of magnitude less active than a bifunctional 40 wt% PtRu/CB ($2,850 \pm 15 \mu\text{A cm}^{-2}$). Further activity and stability improvements can now be achieved through alloying and/or surface admetal decoration as suggested by surface science studies.^[31,36] In **Figure 4.4**, integration of the charge under the CA response for the 40 wt% α -WC/CB catalyst indicates that the current is catalytic and cannot be attributed to capacitive discharging or bulk oxidation of WC to WO_3 (see **Figure S4.39**). Specifically, after 4 h at +0.75 V in 0.5 M H_2SO_4 at 40°C without methanol, the average final current for α -WC/CB was $6.0 \pm 1.7 \mu\text{A cm}^{-2}$ or 2.5% of the current density achieved in the presence of methanol.

4. Conclusions

This “removable ceramic coating method” is a versatile technique to synthesize non-sintered, ultrasmall, metal-terminated monometallic and heterometallic TMCs with strict control over composition, crystal phase, and PSD. The resulting NPs can be stored as a nanodispersion or deposited at any desired loading onto a high surface area support material. Importantly, this method is general and could be extended to synthesize not only other monometallic and heterometallic carbides, but also a variety of transition metal nitrides and phosphides by replacing methane with the corresponding reactive precursor. We envision that the metal-terminated TMC NPs open interesting avenues for synthesizing advanced TMC-PGM core-shell NPs that could substantially reduce noble metal loadings in catalysts using PGMs.^[31,48] While the PGMs are too scarce and expensive to support a global renewable energy economy,^[134] we demonstrate that earth-abundant TMCs engineered with finely controlled sizes and surfaces can achieve the required energy densities and stabilities for use in a variety of burgeoning renewable energy platforms.

Acknowledgements

Dr. Tarit Nimmanwudipong is gratefully acknowledged for his major contribution to this chapter. This work was sponsored by the Chemical Sciences, Geosciences and Biosciences Division, Office of Basic Energy Sciences, Office of Science, U.S. Department of Energy, grant no. DE-FG02-12ER16352. I thank the National Science Foundation for financial support through the National Science Foundation Graduate Research Fellowship under Grant No. 1122374.

5. Supporting Information

5.1. Synthesis of 10wt% WC/CB without the removable ceramic coating method

Using a reverse microemulsion, ultrasmall 1–2 nm WO_x NPs were made in a mixture of heptane/Brij-L4®/water. An appropriate mass of carbon black was then added to the reverse microemulsion to obtain 10 wt% WO_x /CB, shown below in **Figure S4.5**. The material was then carburized by heating in 21% CH_4/H_2 for 4 h at 835°C. **Figure S4.5** shows that after carburization, the 1–2 nm WO_x NPs sinter into 200–300 nm microparticles and that the support has degraded.

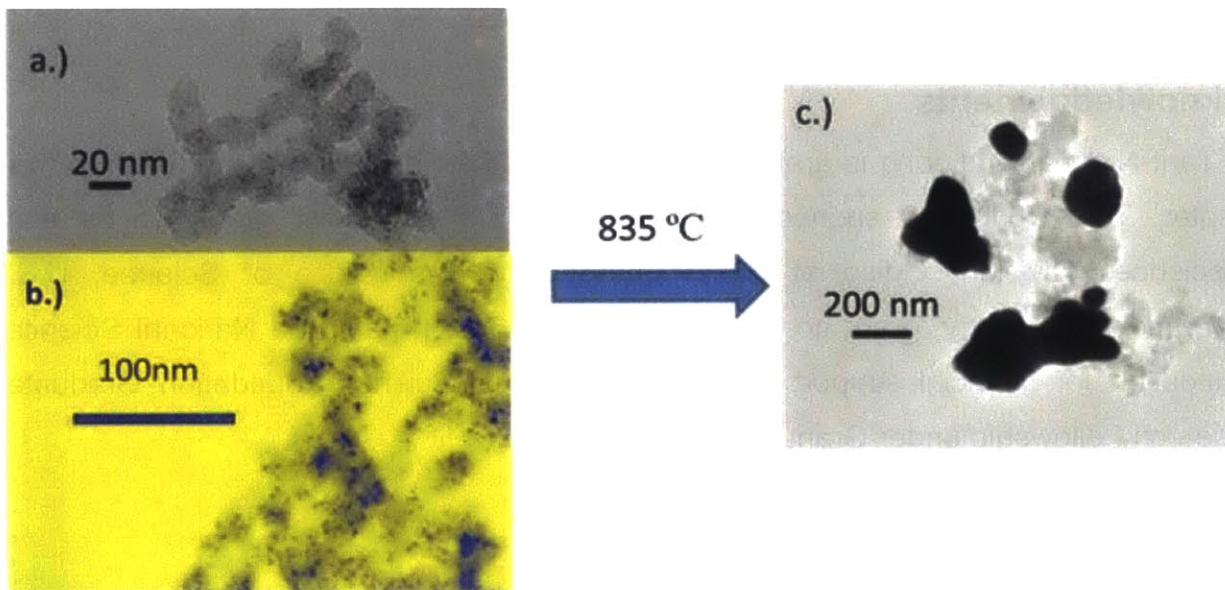


Figure S4.5. Direct Carburization of 10 wt% WO_x/CB at 835°C for 4 h. (A) TEM image of 10 wt% WO_x/CB as synthesized, (B) corresponding STEM image of 10 wt% WO_x/CB as synthesized, (C) TEM image of 10 wt% $\alpha\text{-WC}/\text{CB}$ after carburizing under a 21% CH_4/H_2 atmosphere for 4 h at 835°C . Extensive sintering has occurred along with degradation of the carbon black support.

5.2. The Removable Ceramic Coating Method Synthesis Details

Synthesis of SiO_2/WC and $\text{SiO}_2/\text{Mo}_x\text{W}_{1-x}\text{C}$ using metal alkoxides/Brij-L4®/heptane/water

A reverse microemulsion (RME) was prepared by room-temperature mixing of 240 mL of *n*-heptane with 54 mL of Brij-L4® surfactant followed by 7.8 mL of ultrapure deionized water to obtain a clear and colorless solution. For the synthesis of WO_x nanoparticles (NPs), 12 mL of a 5% w/v tungsten(VI) isopropoxide (WIPO) solution in isopropanol (IPA) was added to 120 mL of *n*-heptane in a separate flask and mixed at room temperature to form an alkoxide precursor solution.^[120] For the synthesis of $\text{Mo}_x\text{W}_{1-x}\text{O}_y$, the appropriate molar ratio of a 5% w/v molybdenum (V) isopropoxide (MoIPO) solution in isopropanol was added to 120 mL of *n*-heptane already containing an appropriate amount of WIPO necessary to form the alkoxide precursor solution. The MoIPO/WIPO alkoxide solution was then mixed thoroughly.

By means of a cannula, the desired alkoxide precursor solution was transferred to the RME and allowed to hydrolyze by room temperature mixing, over which time the solution remained clear and colorless in the case of WO_x or clear and purple in the case of $Mo_xW_{1-x}O_y$ at low molybdenum loadings (**Figure S4.6**). For higher molybdenum loadings, the RME would remain clear and a dark orange/gold (**Figure S4.6**). WIPO-based RMEs were allowed to hydrolyze for 4 h while MoIPO/WIPO-based RMEs were allowed to hydrolyze for 8 h. Once an appropriate reaction time had passed, 2.7 mL of reagent-grade ammonium hydroxide (NH_4OH , Sigma-Aldrich®, 28-30% NH_3 basis) (2 mL of NH_4OH for $Mo_xW_{1-x}O_y$ syntheses) was added drop-wise to the RME to raise the pH followed by 1.2 mL of reagent-grade tetraethylorthosilicate (TEOS). Stirring continued over 16.5 h, during which time the RME would slowly lose transparency, growing cloudy but remaining colorless for WO_x syntheses or slightly purple for $Mo_xW_{1-x}O_y$ syntheses.

The silica-encapsulated transition metal oxide (TMO) NPs were then recovered by adding 300 mL of methanol, stirring for 15 min, and then allowing the encapsulated NPs to settle over an hour. Addition of methanol would form two distinct liquid phases, an upper heptane-rich phase, and a lower methanol-rich phase that would contain the settling coated NPs. The coated NPs were then rinsed once by fully dispersing in 30 mL of acetone and centrifuging at 6000 rpm for 10 min. **Figure S4.6** depicts RMEs containing silica-encapsulated transition metal oxide NPs before and after precipitation with methanol.

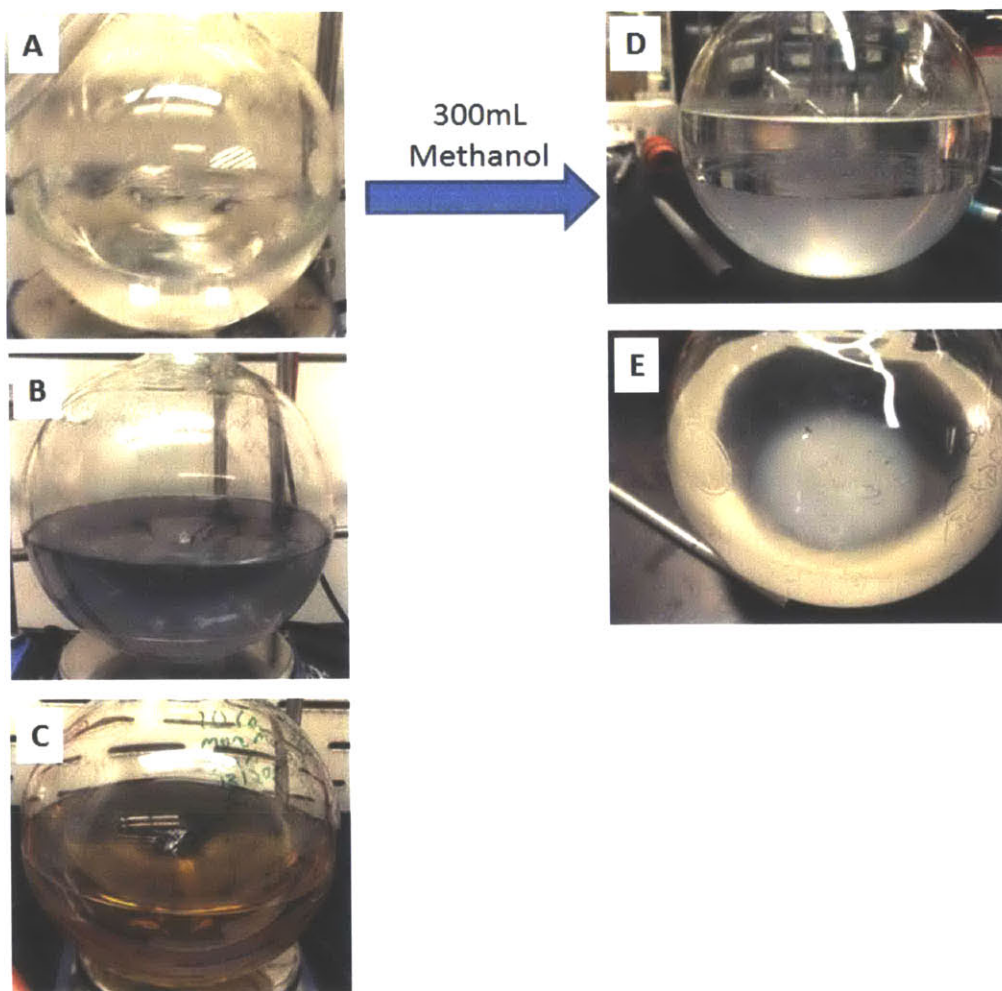


Figure S4.6. Photographs of RMEs containing silica-encapsulated TMO NPs. (A) a water/brij/heptane RME containing WO_x NPs encapsulated in silica nanospheres. (B) a water/brij/heptane RME containing $\text{Mo}_{0.06}\text{W}_{0.94}\text{O}_y$ NPs encapsulated in silica nanospheres. (C) a water/brij/heptane RME containing $\text{Mo}_{0.54}\text{W}_{0.46}\text{O}_y$ NPs encapsulated in silica nanospheres. (D) side-view of the RME from (A) after 300mL of methanol has been added; note the distinct phase-separation. (E) top-down view of the RME from (A) after 300mL of methanol has been added; note the SiO_2/WO_x precipitant settling on the bottom of the flask.

The as-synthesized powders were then allowed to dry overnight before being micronized with a glass rod and calcined at 450°C for 1 hour under 100 standard cubic centimeters per minute (sccm) of air using a $2^\circ\text{C}/\text{min}$ heating rate. After calcination, XRD analysis indicated the presence of a broad amorphous silica peak, but no tungsten oxide peaks were detected (spectra not shown). **Figure S4.12d** shows a TEM image of the SiO_2/WO_x material synthesized under these conditions. The material could be stored for

several weeks after calcination and before carburization with no noticeable changes in the results.

The material was then reduced at 590°C for one hour and carburized at 835°C for 4 h under 33 sccm CH₄ and 120 sccm H₂ using 2°C/min heating rates in a tube furnace. The material was then held under pure H₂ at 120 sccm for one hour at 835°C to scavenge residual surface carbon before being passivated at room temperature under 1% O₂/N₂ for 3 h. After carburization, the materials would be stored in ambient condition anywhere from days to weeks before dissolution in ABF with no noticeable changes in activity. The centerline temperature of the gases in the tube furnace was monitored using an exposed N-type thermocouple (Omega® Corp.) held at the center of the furnace within the quartz tube. The steady-state centerline gas temperatures are reported here. **Figure S4.7** depicts TEM images of the SiO₂/β-WC material post-carburization, clearly showing that the ~40nm silica nanospheres are non-sintered and contain ultrasmall β-WC NPs encapsulated within them with a minority of particles existing as larger NPs on the surface of the silica nanospheres.

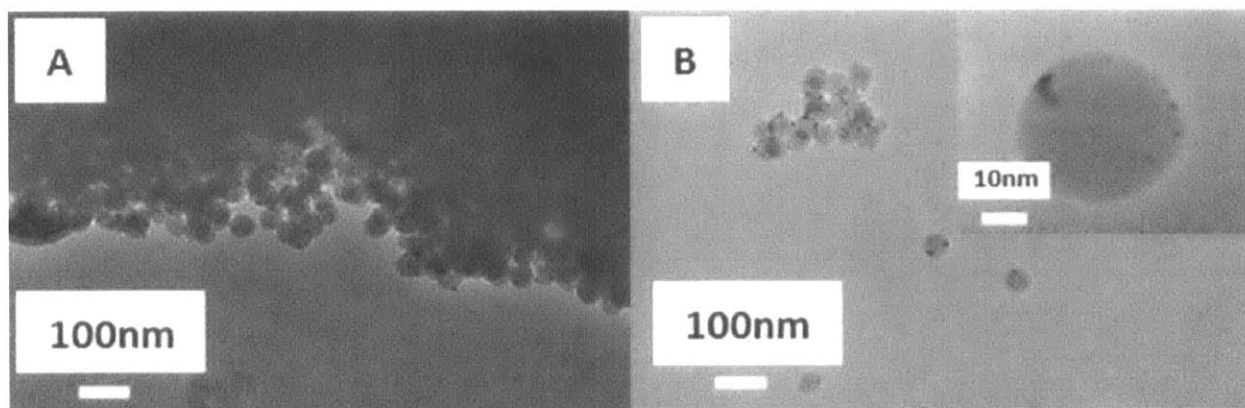


Figure S4.7. TEM images of SiO₂/β-WC synthesized at a pH of 11.1 using a methanol:heptane volumetric precipitation ratio of 0.83. Carburization was performed at 835°C for 4 h in a 21% CH₄/H₂ atmosphere. (A) depicts a low-magnification image of the edge of a macroscopic SiO₂/β-WC powder grain, showing that the primary particle size of the powder are discrete ~40nm particles. (B) depicts another low-magnification image of a cluster of ~40nm particles (the inset shows a high-magnification image that clearly shows the ultrasmall β-WC NPs encapsulated within the ~40nm silica nanosphere).

Figure S4.8 below depicts photographs of the powders at various stages in the “removable ceramic coating method.” Post-carburization, the powders were typically dark grey. This color is due the reduced nature of carbide nanoparticles rather than the deposition of graphitic carbon. Directly a carburizing bluish-white WO_x nanopowder also results in a black powder while directly carburizing a white silica powder also results in a white powder post-carburization (images not shown).

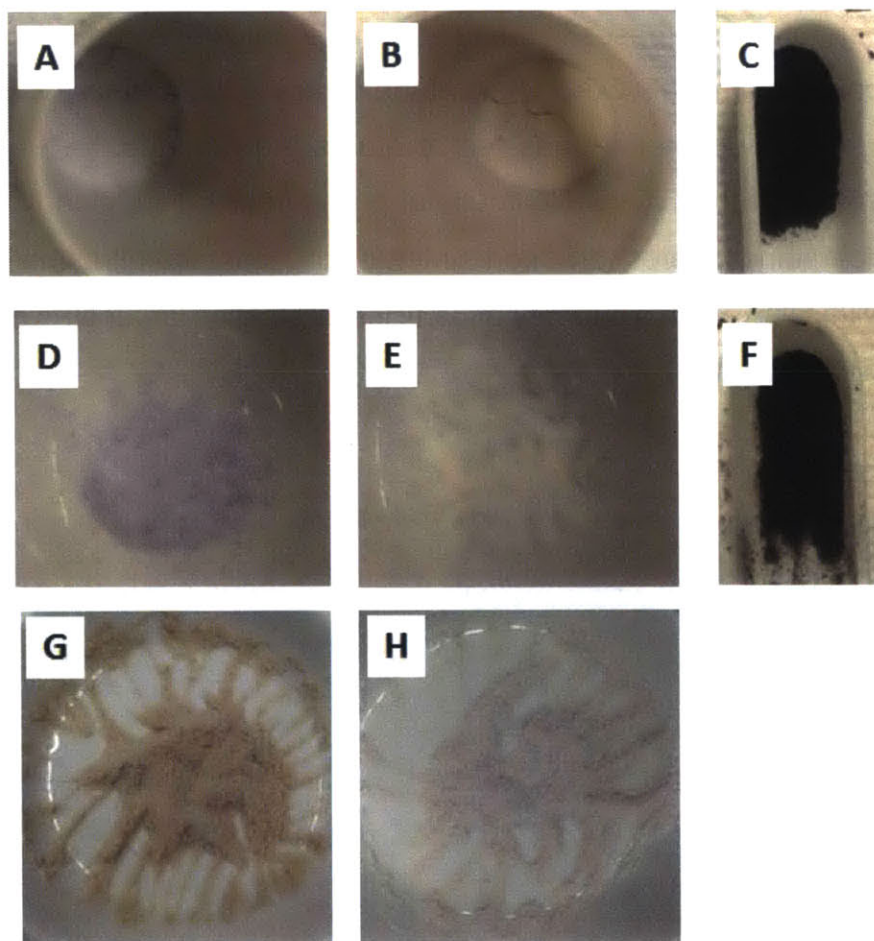


Figure S4.8. Photographs of the various synthesized materials at different stages in the “removable ceramic coating method.” (A) as-synthesized SiO_2/WO_x is a fine white powder. (B) calcined SiO_2/WO_x is a fine light-tan powder. (C) carburized $SiO_2/\beta-WC$ is a fine dark-grey powder. (D) as-synthesized $SiO_2/Mo_{0.06}W_{0.94}O_y$ is a fine light purple powder. (E) calcined $SiO_2/Mo_{0.06}W_{0.94}O_y$ is a fine white powder. (F) carburized $SiO_2/\beta-Mo_{0.06}W_{0.94}C$ is a medium-grey powder. (G) as-synthesized $SiO_2/Mo_{0.54}W_{0.46}O_y$ is a fine orange/tan powder. (H) calcined $SiO_2/Mo_{0.54}W_{0.46}O_y$ is a fine white powder. Once carburized, $SiO_2/Mo_{0.54}W_{0.46}C$ is black (not shown) as in panel (C).

The effect of temperature on carbide phase-purity and silica stability

Figure S4.9 shows the XRD spectra for the material synthesized using the alkoxide/Brij-L4®/heptane/water system after high temperature carburizations at 950°C and 1000°C. Even at 950°C, the β -WC phase is preferred. Some W_2C is also present, which could be due to either the lower porosity of silica at this temperature preventing complete carburization or due to the lower CH_4/H_2 ratio used for this specific study. Notably, the silica maintains a broad amorphous peak centered at $2\theta = 22^\circ$. Carbide NP sintering was largely mitigated at 950°C while the silica nanospheres were evidently sintered (images not shown). The powder was also much more difficult to disperse than the powder obtained after carburization at 835°C. At 1000°C, the amorphous silica transitions to quartz. The silica nanospheres were no longer discrete but part of a continuous silica matrix. The carbide NPs were also more sintered and consisted of an α -WC + W_2C mixture. The W_2C could be the result of incomplete carburization of interior tungsten NPs due to the lack of porosity in crystalline quartz.

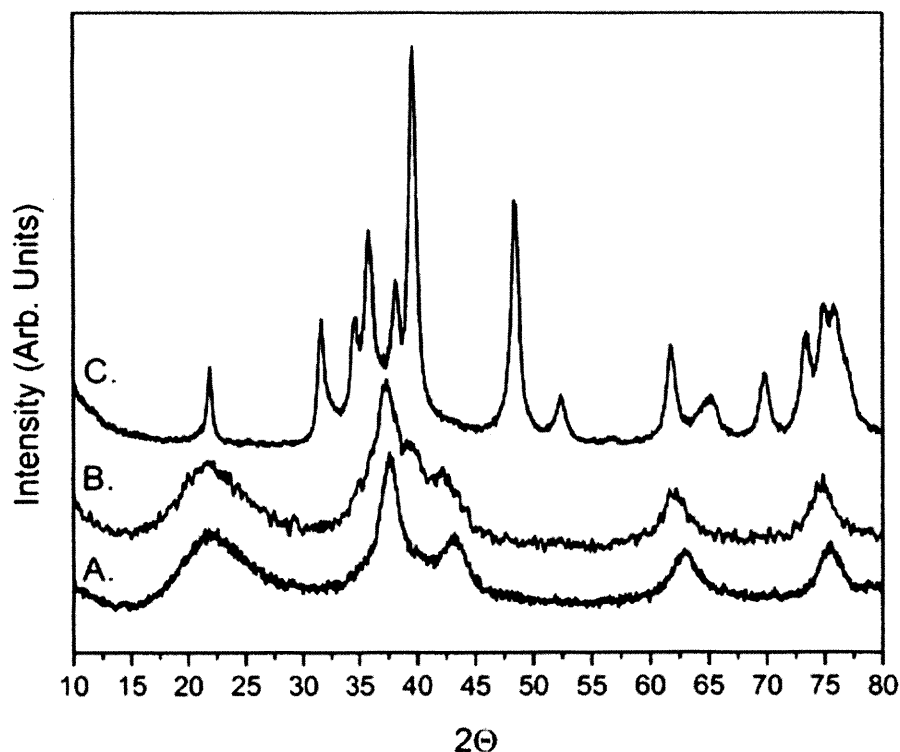


Figure S4.9. Temperature studies of SiO_2/β -WC by carburizing for 4 h under 21% CH_4/H_2 at (A) 835°C, (B) 18% CH_4/H_2 at 950°C, and (C) 21% CH_4/H_2 at 1000°C

The effect of precipitating solvent on the carbide phase-purity and silica stability

Studies were done to examine the effects of precipitating the water/brij/heptane RME using different solvents. **Figure S4.10** depicts the XRD spectra for materials precipitated in 300 mL of acetone, isopropanol, and methanol. Phase separation of the RME is not observed with acetone or isopropanol, and the silica-encapsulated NPs settle more rapidly. All materials in these studies were calcined at 450°C, reduced for one hour at 590°C, and carburized for 4 h at 835°C in a 21% CH₄/H₂ atmosphere. One can clearly see that the silica has formed quartz and the tungsten is incompletely carburized and in a three-phase mixture of α -WC, W₂C, and α -W for syntheses in which either acetone or isopropanol have been used to precipitate the RME. For these syntheses, the silica shells were sintered together with extensive sintering observed for the nanoparticles (images not shown). Notably, the SiO₂/WO_x ~40nm nanospheres were also much more compact post-synthesis whereas the nanospheres from syntheses precipitated in methanol are discrete and separated (images not shown).

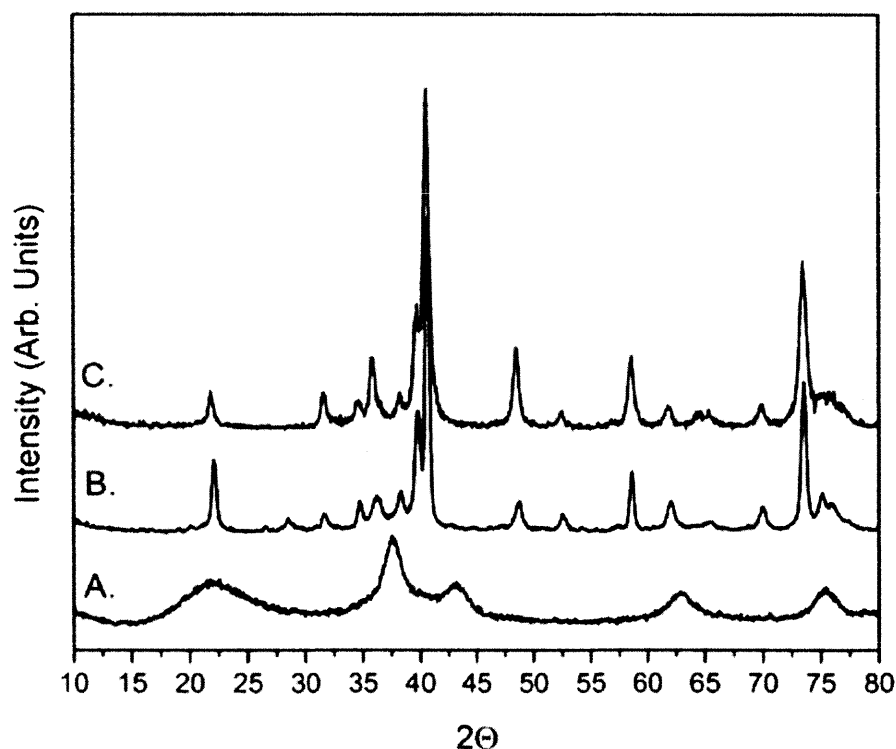


Figure S4.10. Solvent precipitation effect studies by precipitating SiO₂/WO_x or SiO₂/Mo_xW_{1-x}O_y with (A) Methanol, (B) Acetone, and (C) Isopropanol. All materials were rinsed with acetone. XRD Spectra are for the resulting materials post-carburization at 835 °C for 4 h under 21% CH₄/H₂.

Catalyst surface area and micropore volume determination using BET

Catalyst surface areas were analyzed using a Quantachrome® BET evaluated under liquid nitrogen conditions and using N_2 as the adsorbing species. BET was used to probe micropore generation and collapse during the removable ceramic coating process as shown in **Figure S4.11**, which depicts the BET adsorption isotherms of as-synthesized SiO_2/W_xO_y , calcined ($450^\circ C$) SiO_2/W_xO_y , and carburized ($835^\circ C$) $SiO_2/\beta-WC$. It is seen that the calcined material has the highest micropore volume, likely due to the calcination of the pore-blocking surfactants in the as-synthesized material. The carburized material has the lowest microporosity, which is expected due to the high temperatures required to carburize the material, which results in densification of the amorphous silica matrix. Likely, carburization occurs before and during collapse of the calcined micropores. This is especially the case for the synthesis of α -carbides, which results in the eventual formation of low-microporosity quartz domains. Once supported on carbon black, the surface areas were also determined using BET and are reported below in **Table S4.2**.

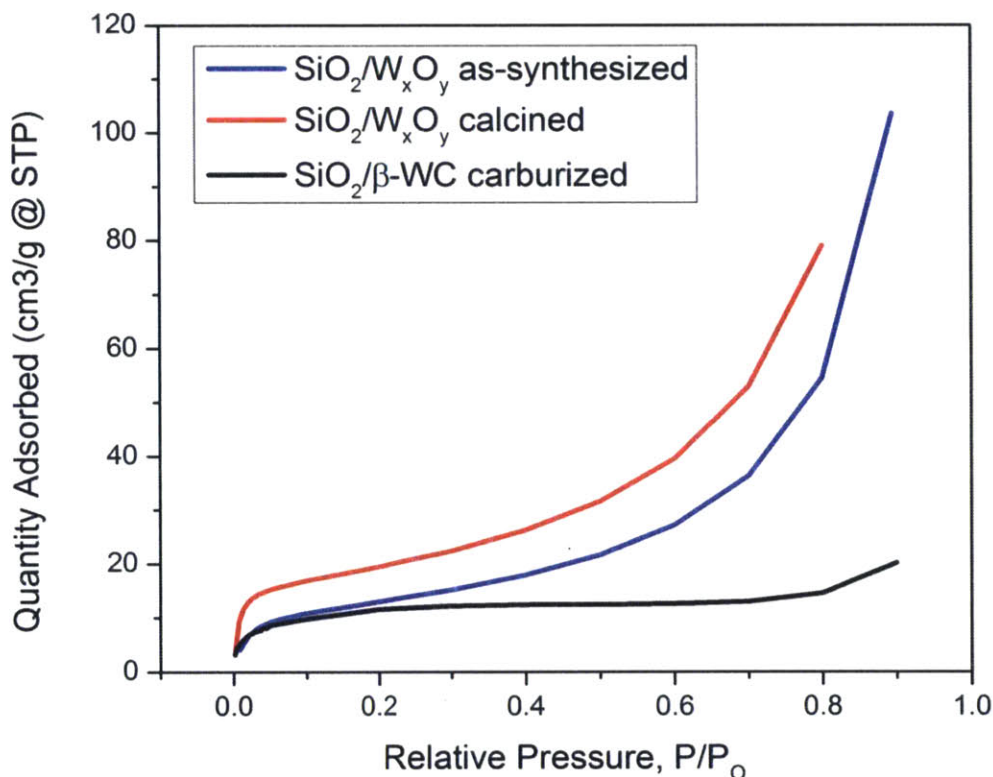


Figure S4.11. BET adsorption isotherms during various stages of the “removable ceramic coating” method

Table S4.2: BET Surface Areas

Catalyst	BET Surface Area (m ² /g)
40 wt% Pt/CB, commercial	126
40 wt% α -WC/CB, "rcc" method	90
40 wt% β -Mo _{0.06} W _{0.94} C/CB, "rcc" method	160
Acidified Vulcan® XC-72r	250

The effect of coating pH on the SiO₂/WO_x nanostructure, carbide phase-purity, and silica stability

The pH of the water nanodomains was adjusted by adding ammonium hydroxide after formation of the TMO NPs. Hydrolysis of TEOS to form the SiO₂ nanospheres is base-catalyzed. The pH was calculated based on the moisture loading in the RME system and the amount of NH₄OH added. A pH of 11.1 was obtained by slow injection of 2.7 mL of NH₄OH solution while pH values of 10.9, 10.5, and 10 were obtained by slow injection of 1.4 mL NH₄OH, 0.6 mL NH₄OH, and 0.16 mL NH₄OH, respectively. All syntheses were injected with 0.6 mL TEOS with the exception of the syntheses at pH 11.1, which were injected with 1.2 mL TEOS. All syntheses were also allowed to stir for 16.5 h before being precipitated with 300 mL of methanol. It was determined that coating at pH 10 did not produce silica nanospheres but rather large aggregates of WO_x NPs dispersed throughout a continuous silica matrix, as shown in **Figure S4.12a**. At a pH of 10.5, discrete ~15nm silica nanospheres can be seen with WO_x NPs encased inside. The coating process occurs more slowly at lower pH values and thus these powders contained a much higher ratio of W:Si and were more prone to sintering. At a pH of 10.9 and 11.1, the silica nanospheres are larger (~35nm and ~50nm, respectively), and the WO_x NPs are much more disperse within the nanospheres. If WO_x NPs are calcined directly at 450 °C, a black powder is obtained, indicative of WO₂. If the NPs are coated at a pH exceeding 11 within silica nanospheres, a light tan powder is obtained. If the NPs are coated at a lower pH, the W:Si ratio is much higher and a darker tan-brown powder is obtained after calcination (images not shown)

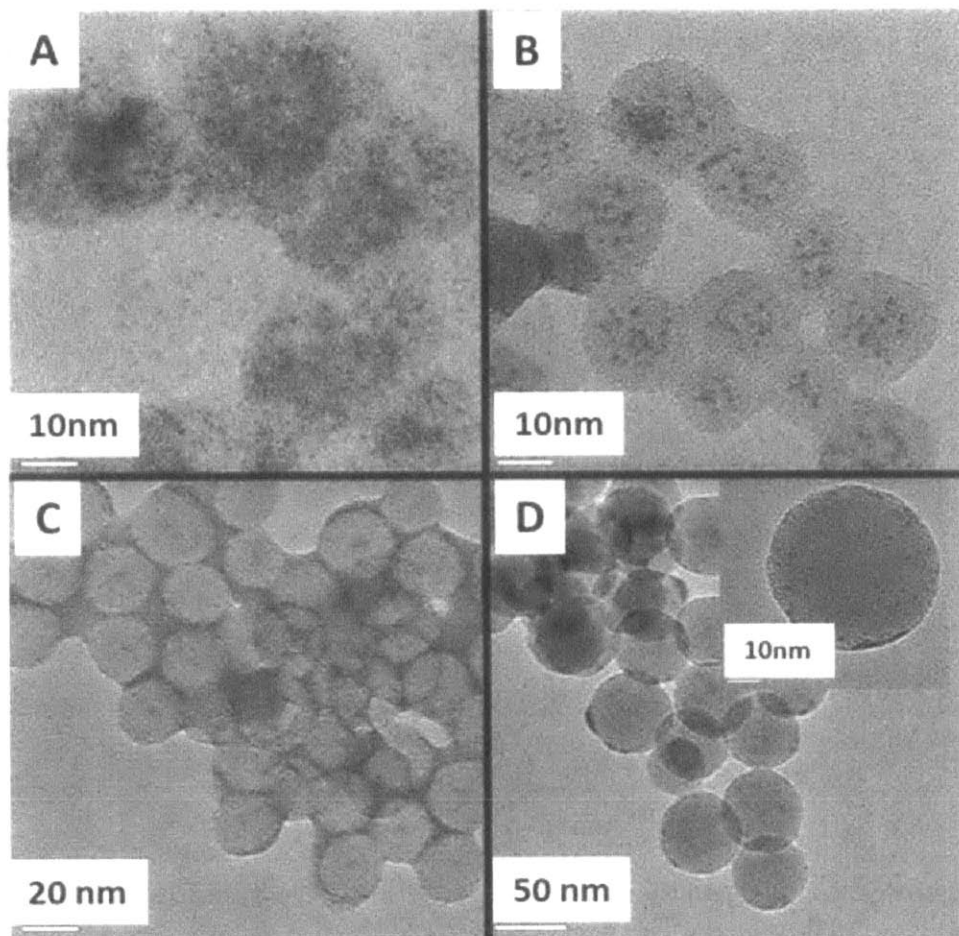


Figure S4.12. TEM images of SiO_2/WO_x obtained at pH values (calculated) of (A) 10.0, (B) 10.5, (C) 10.9, and (D) 11.1 (inset shows a close-up of a SiO_2/WO_x particle). The materials from Figure S4.12 were calcined at 450°C for one hour, reduced at 590°C for one hour, and carburized at 835°C for 4 h under a 21% CH_4/H_2 atmosphere. The resulting XRD spectra are shown in Figure S4.13 where it can be seen that at low pH values, quartz forms in addition to a $\alpha\text{-WC} + \text{W}_2\text{C}$ NP mixture. These materials were prone to more sintering (images not shown). At higher pH values, $\beta\text{-WC}$ forms, and the NPs were non-sintered.

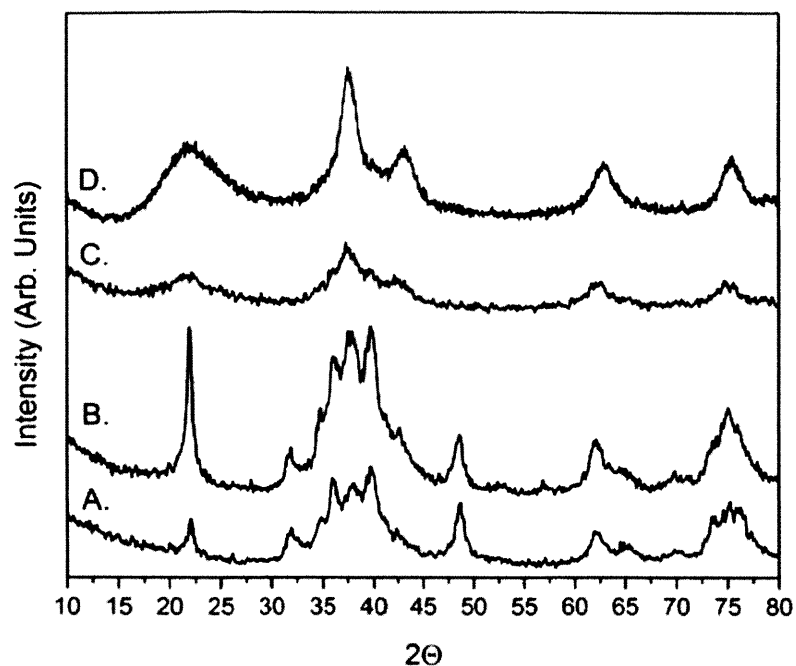


Figure S4.13. Post-carburization XRD spectra of the various SiO_2/WO_x materials coated at different pH values. Carburizations were conducted at 835°C for 4 h under 21% CH_4/H_2 and are shown for materials coated using a pH of (A) 10, (B) 10.5, (C) 10.9, and (D) 11.1.

Control of carbide phase-purity and carbide NP particle size distribution

Different carbide phases and particle sizes could be obtained by adjusting various synthesis parameters. To obtain 1–2nm cubic β -carbide NPs, a pH of 11.1 (11 for $\text{Mo}_x\text{W}_{1-x}\text{C}$ syntheses), and the emulsion was precipitated with 300mL of methanol (a volumetric methanol:heptane ratio of 0.83). A modified **Figure 4.1** is included below as **Figure S4.14** showing the synthesis results for the production of 1–2nm β -WC NPs supported at 25 wt% on carbon black in comparison to 1–3nm β -WC NPs. If instead, a volumetric ratio of 0.31 was used (i.e. 112mL of methanol), sintering of both the silica and the carbide NPs would occur, and 3–6nm hexagonal α -carbide NPs would be obtained. These 3–6nm α -carbides could be synthesized as monometallic WC (**Figure 4.2a**) or as a heterometallic $\text{Mo}_x\text{W}_{1-x}\text{C}$ (not shown). To obtain larger 1–3nm β -carbide NPs, a pH of 11 was used (10.9 for $\text{Mo}_x\text{W}_{1-x}\text{C}$ syntheses), and the emulsion was precipitated with 300mL of methanol (a volumetric methanol:heptane ratio of 0.83) (**Figure S4.15a–c**). The resulting carbides and their corresponding particle size distributions are shown below in **Figure S4.15**. The Scherrer equation was also utilized to determine the average particle size based on the

XRD diffractograms. For β -carbides, the peaks centered at $2\theta = 37.4^\circ$ and 43.3° were used in the analysis and found to be in close agreement. For α -carbides, the peak centered at $2\theta = 48.5^\circ$ was used in the analysis. Peaks were analyzed using standard deconvolution software employing the Stokes-Wilson integral breadth method. There was little quantitative difference between the 1–2 nm and 1–3 nm β -WC NPs using the Scherrer equation, likely because this method is only sensitive to $\sim \pm 1$ nm. The results of the Scherrer equation and the PSD obtained from TEM analysis is shown below in **Table S4.3**. To show the uniformity of the ultrasmall 1–2 nm β -WC NPs, a wide-view STEM image of 25 wt% β -WC/CB is included below in **Figure S4.16a**. To show the minimization of surface carbon and the crystal lattice of the ultrasmall 1–3 nm β -WC NPs supported on CB, several HR-TEM images are included in **Figure S4.17**.

Because the WC NPs are ultrasmall and non-sintered, they are not intended to be a catalyst support but rather the active material dispersed onto a support. **Figure S4.16b** shows a β -WC nanopowder without a dispersing solvent. Because there is no solvent or surface stabilizing species, the nanopowder aggregates by van der Waals attractions, which dominate at such small scales. This blocks WC active sites because WC NPs become embedded within the aggregate. This was confirmed by examining the HER activity of a WC nanopowder versus 40wt% WC/CB where the nanopowder had a lower HER activity (results not included).

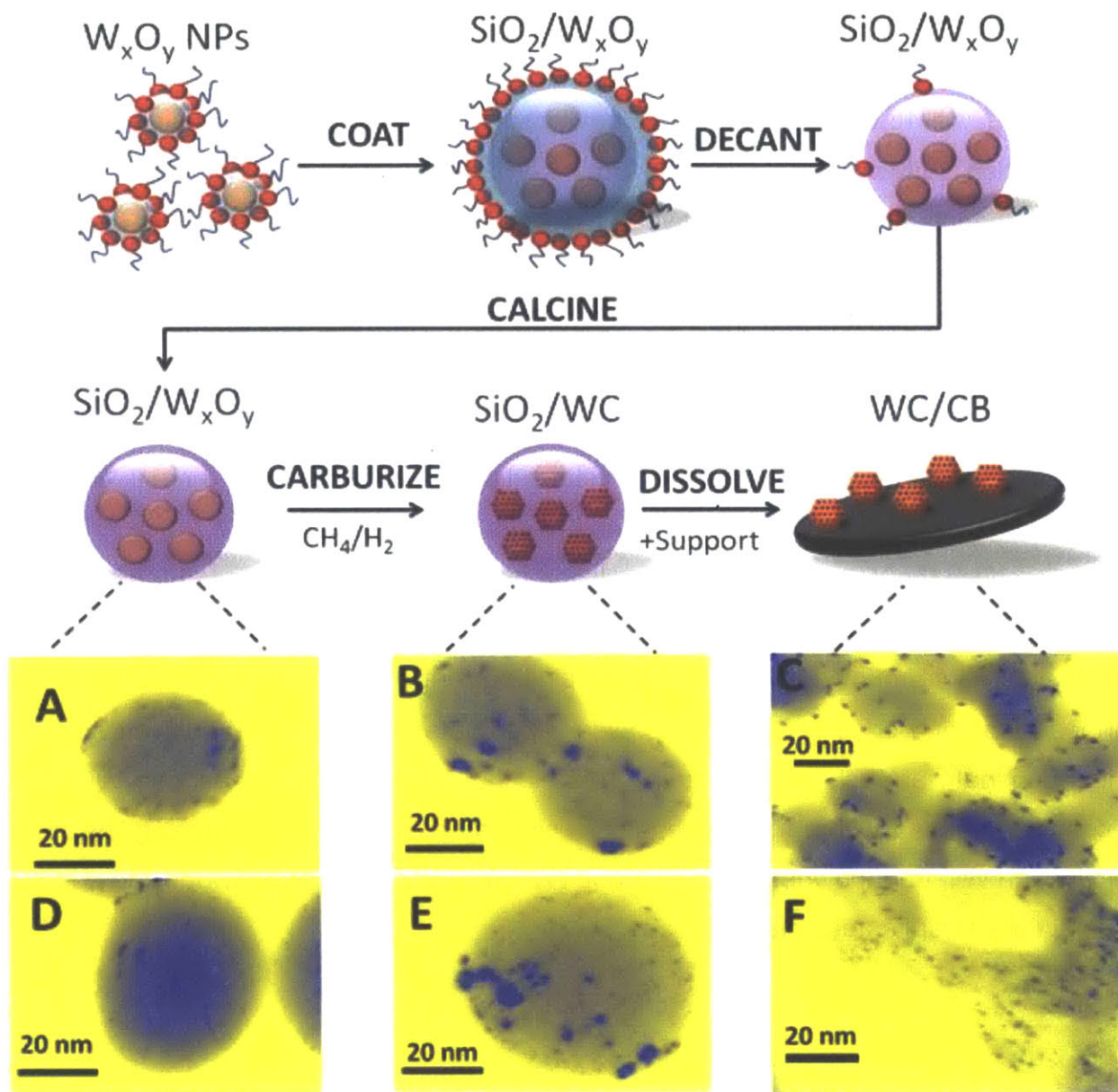


Figure S4.14. Synthesis of β -WC in two different sizes: (A,D) SiO_2/W_xO_y NPs, (B,E) SiO_2/W_xO_y NPs, (C) 25 wt% 1–3nm β -WC/CB, (F) 25 wt% 1–2 nm β -WC/CB

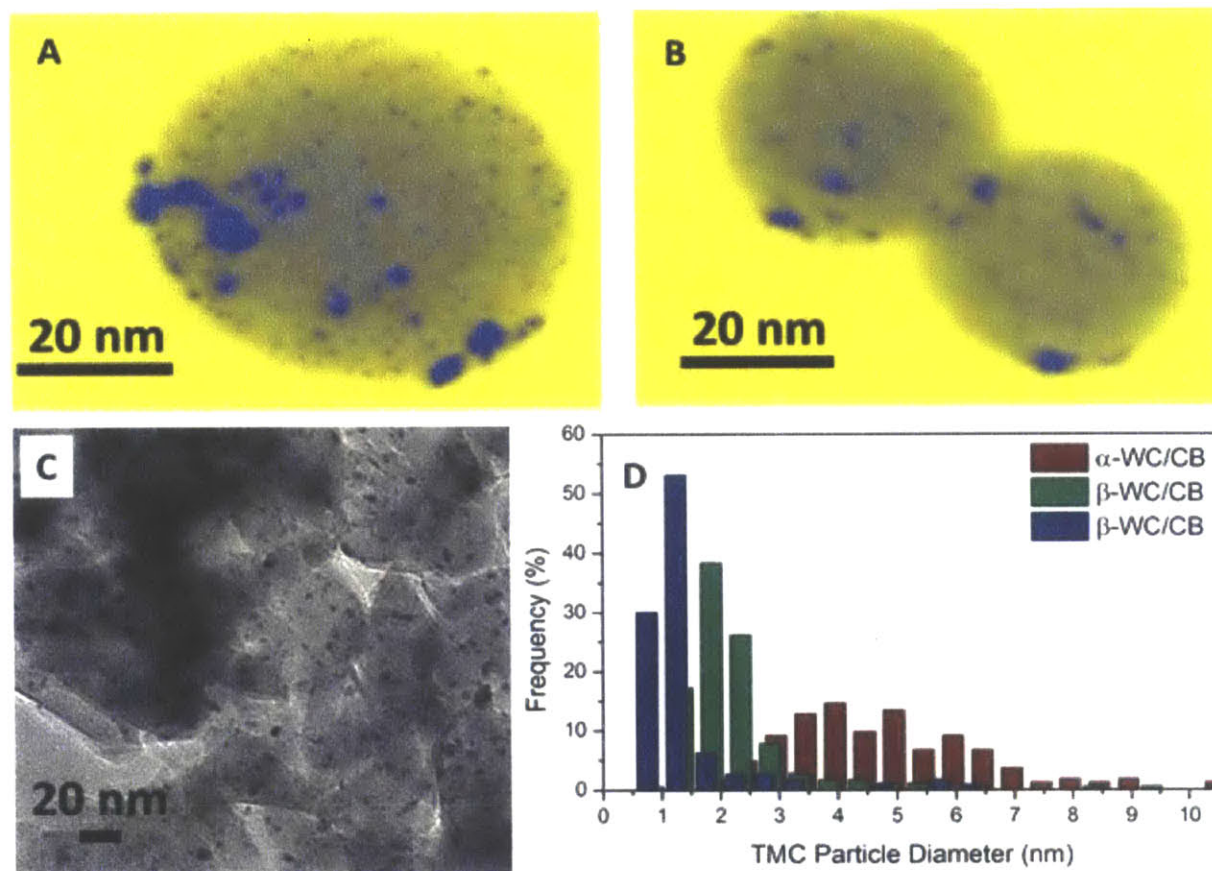


Figure S4.15. Carbide NPs of various phases and particle size distributions encapsulated in silica matrices. (A) STEM of ultrasmall 1–2 nm β -WC NPs encapsulated in a silica nanosphere. (B) STEM of ultrasmall 1–3 nm β -WC NPs encapsulated in two silica nanospheres. (C) TEM of 3–6 nm α -WC NPs encapsulated in a quartz-like matrix. (D) Corresponding particle size distributions (PSDs) for each of the three syntheses with at least 150 particles analyzed per distribution.

Table S4.3. PSD determined by XRD and TEM

Catalyst	PSD by XRD (nm)	PSD by TEM (nm)
1–2 nm β -WC	--	1.5 ± 0.9
1–3 nm β -WC	2.4	2.2 ± 1.1
3–6 nm α -WC	5.5	4.6 ± 1.7

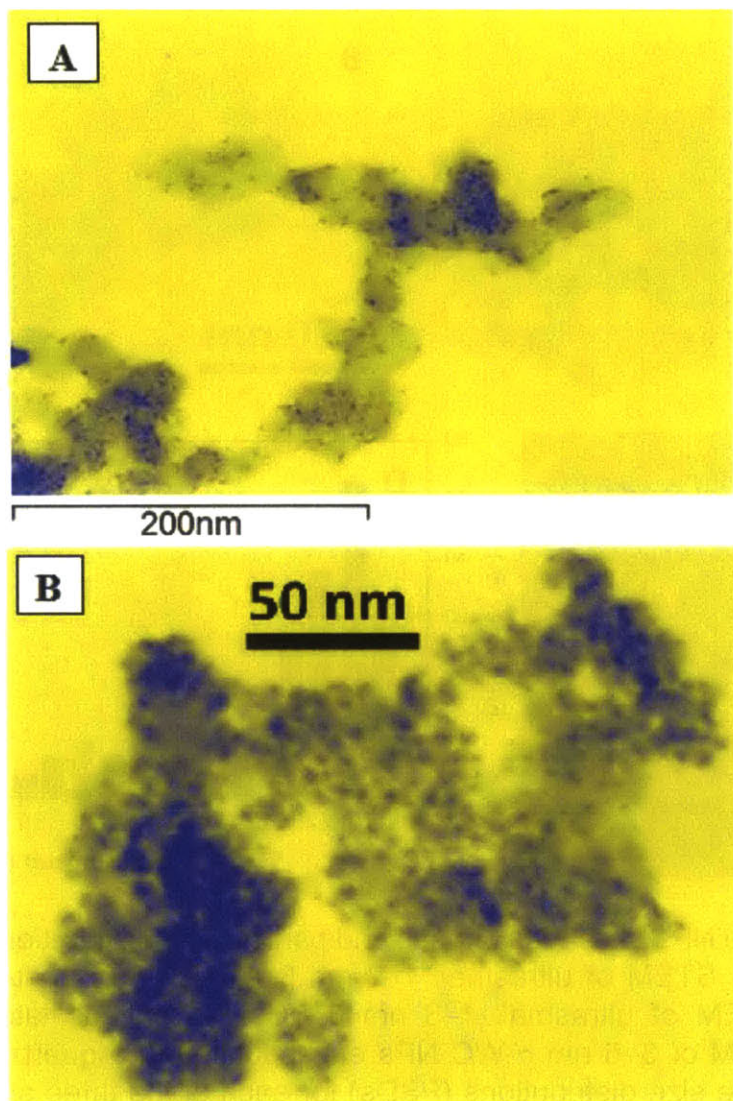


Figure S4.16. (A) Wide-view STEM image of 25 wt% 1–2 nm β -WC/CB (B) STEM image of a β -WC nanopowder

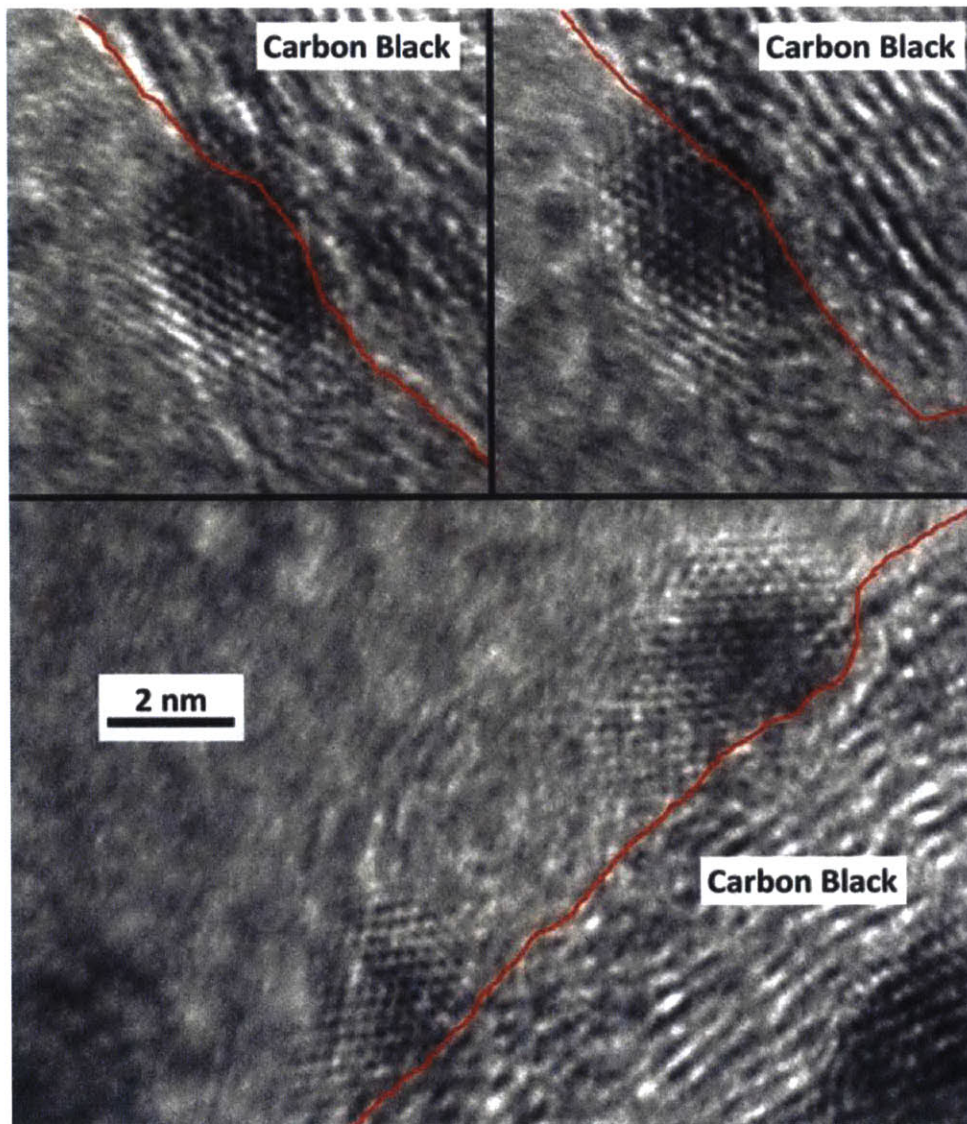


Figure S4.17. HR-TEM images of 1–3 nm β -WC/CB. The images are of WC NPs sitting at the edge of the carbon black support with the red line demarcating the transition from the carbon black surface (on the right) to the empty space of the background TEM grid on which the samples are sitting.

Synthesis of SiO_2/WC and $\text{SiO}_2/\text{Mo}_x\text{W}_{1-x}\text{C}$ using metal alkoxides/Igepal CO-520®/heptane/water

In addition to nonionic Brij-L4® surfactant, we also performed studies using the nonionic Igepal CO-520® surfactant. These syntheses were identical to those using Brij-L4® with the exception that 60 mL of Igepal CO-520® was used instead of 54 mL of Brij-L4® and a pH of 11 was used during the coating. Precipitation with 300 mL of methanol would also form two liquid phases. Using Igepal, the oxide nanoparticles are larger and singly-

coated at the center of each silica nanosphere (**Figure S4.18**). However, after carburization, the nanospheres lose their structure and sinter together. The resulting carbide was a mixed phase α -WC + W_2C (xrd spectra not shown).

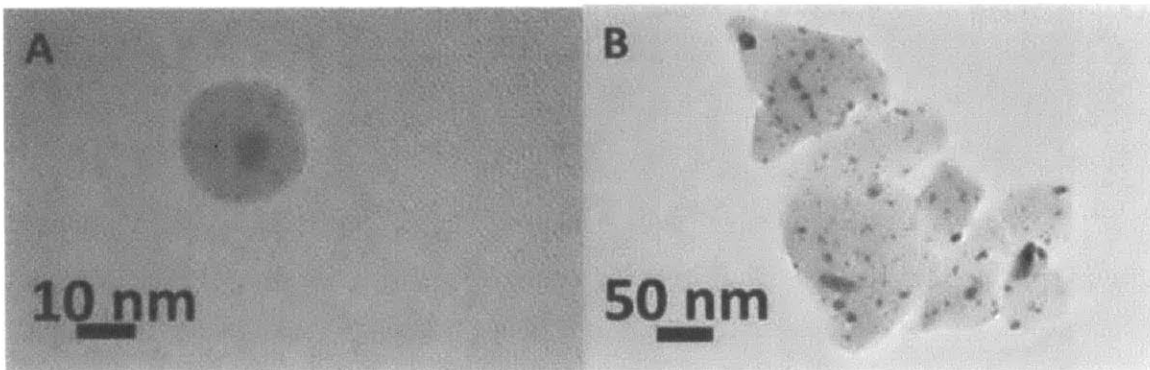


Figure S4.18. TEM Images of (A) SiO_2/WO_x prepared using WIPO/water/Igepal/heptane and (B) the same material post-carburization

Synthesis of SiO_2/H_2WO_4 and $SiO_2/H_2(Mo_x, W_{1-x})O_4$ using $Na_2WO_4/Na_2MoO_4/HCl/Igepal CO-520®/heptane/water$ and their subsequent carburization

Alternatively to metal alkoxide autocatalysis in water, the metal oxide nanoparticles could be synthesized using the stoichiometric reaction of metal salts with an acid.^[121] In a typical synthesis, 6.5 mL of a stock solution of 0.2 M HCl in water was added to a flask containing 53 mL of Igepal CO-520® and 300 mL of heptane to form the acid-RME. In a separate flask, 6.5 mL of a stock solution of 0.1M Na_2WO_4 in water was added to 53 mL of Igepal CO-520® and 300 mL of heptane to form the TMO-RME. The TMO-RME was then added to the acid-RME under continuous stirring over the span of 30 min. It was allowed to react for 6–8 h to form tungstic acid nanoparticles before 1.75mL of NH_4OH was added followed by 1.2 mL of TEOS. 16.5 h later, it was precipitated with methanol. To make the heterometallic molybdenum tungstic acid nanoparticles, a stock solution containing 0.8 M Na_2WO_4 and 0.2 M Na_2MoO_4 mixed together was used to form the TMO-RME. **Figure S4.19** shows a typical result for $SiO_2/H_2(Mo_{0.1}W_{0.9})O_4$ calcined and carburized to $SiO_2/Mo_{0.1}W_{0.9}C$. Again, extensive sintering of the silica nanospheres was observed after carburization.

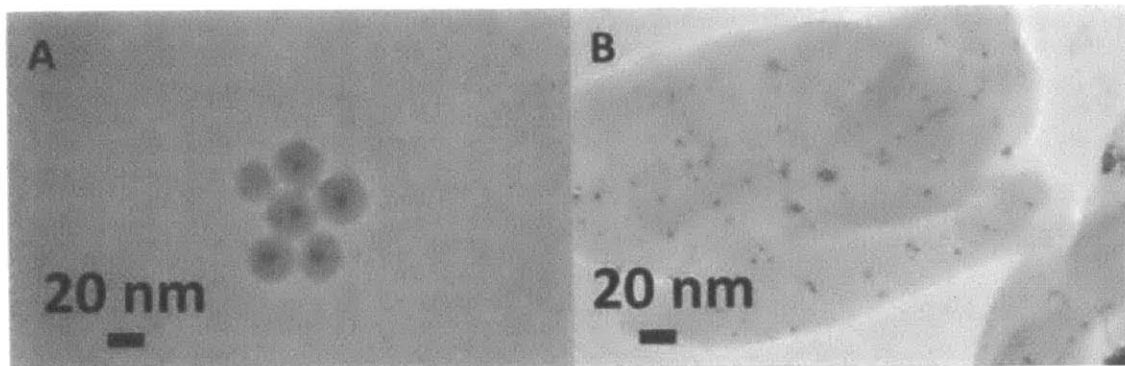


Figure S4.19. TEM Images of (A) $\text{SiO}_2/\text{H}_2(\text{Mo}_{0.1}\text{W}_{0.9})\text{O}_4$ synthesized using $\text{Na}_2\text{WO}_4/\text{Na}_2\text{MoO}_4/\text{HCl}/\text{water}/\text{Igepal}/\text{heptane}$ and (B) the same material post-carburization.

Synthesis of $\text{SiO}_2/\text{H}_2\text{WO}_4$ and $\text{SiO}_2/\text{H}_2(\text{Mo}_x\text{W}_{1-x})\text{O}_4$ using $\text{Na}_2\text{WO}_4/\text{Na}_2\text{MoO}_4/\text{HCl}/\text{Triton X-100}^\circledast/1\text{-hexanol}/\text{heptane}/\text{water}$ and their subsequent carburization

Triton X-100[®] is a more hydrophilic surfactant that requires a co-surfactant to solubilize it in the oil phase. The co-surfactant used in these studies was 1-hexanol. The double RME method was again used, with RMEs prepared by adding 70 mL of 1-hexanol to 200 mL of heptane followed by 55 mL of Triton X-100[®]. 3 mL of the aforementioned stock solutions were mixed with 3 mL of water and injected into the RMEs rapidly to form the TMO-RME and the acid-RME. The TMO-RME was then added continuously to the acid-RME over a span of 30 min and allowed to react for 6–8 h. The TMO-RME would slowly grow cloudy for these syntheses. Next, 0.34 mL of NH_4OH and 0.34 mL of TEOS was added and allowed to react for 16.5 h. These samples were notable for containing a high wt% of W relative to Si. They were dark brown after calcination and had extreme structural rearrangement on carburization as shown in **Figure S4.20**. While the synthesis resulted in large ~50 nm spheres of hybrid Si and W/Mo, the resulting carburized material resulted in ~20 nm carbide nanoparticles coated in ~8 nm of silica. The segregation of the silica from the carbide was confirmed using EDX (**Figure S4.20**). EDX was also used to confirm the presence of both W and Mo. The XRD is shown in **Figure S4.21**, confirming that the material is carbidic and predominantly in an α hexagonal lattice. Neither an amorphous silica nor quartz peak is apparent, possibly due to the low loading of silica.

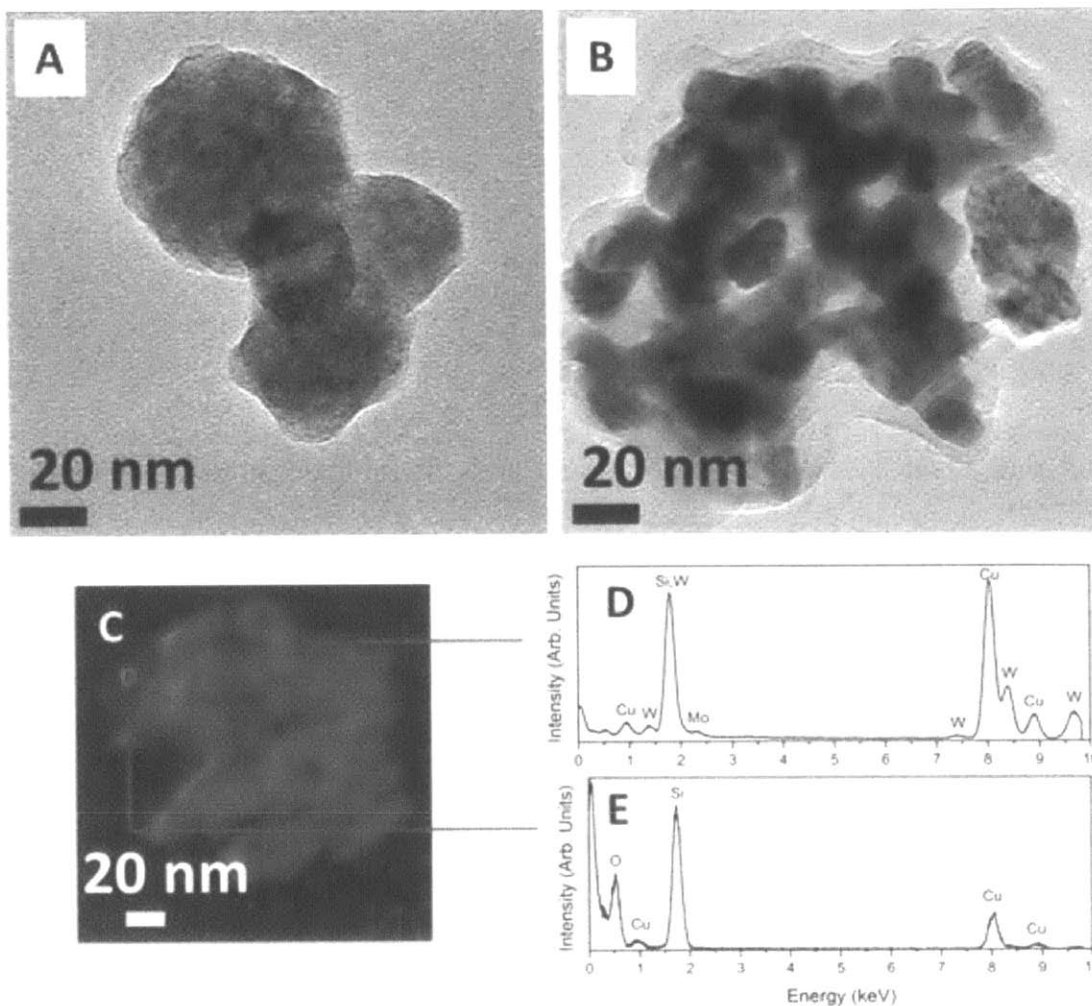


Figure S4.20. TEM, STEM, and EDX of calcined and carburized $\text{SiO}_2/\alpha\text{-Mo}_{0.1}\text{W}_{0.9}\text{C}$. **(A)** TEM of calcined $\text{SiO}_2/\text{H}_2(\text{Mo}_{0.1}\text{W}_{0.9})\text{O}_4$ prepared using $\text{Na}_2\text{WO}_4/\text{Na}_2\text{MoO}_4/\text{HCl}/\text{water}/\text{Triton}/\text{hexanol}/\text{heptane}$. **(B)** TEM of the same material after carburization for 4 h at 835°C in a 21% CH_4/H_2 atmosphere to form phase-pure hexagonal heterometallic $\text{Mo}_{0.1}\text{W}_{0.9}\text{C}$. **(C)** STEM of the same image shown in (B). **(D)** Analysis of 1 nm x 1 nm region of carbide showing the presence of both W and Mo. **(E)** Analysis of a 1 nm x 1 nm region of the silica shell showing only Si and O detectable with neither W or Mo detected.

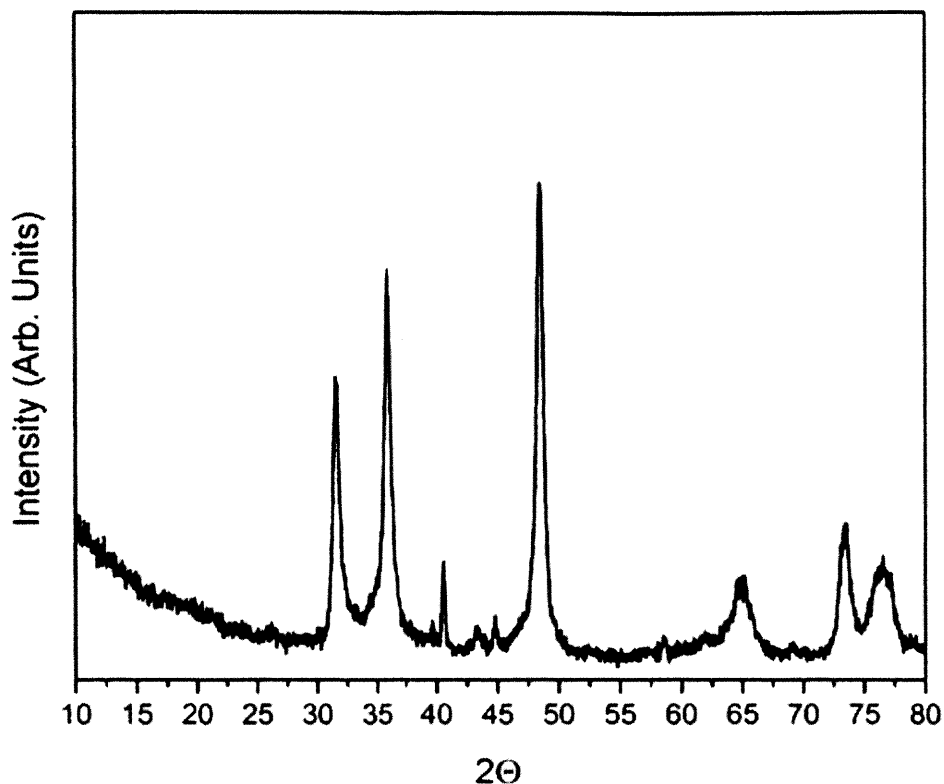


Figure S4.21. XRD of $\text{SiO}_2/\alpha\text{-Mo}_{0.1}\text{W}_{0.9}\text{C}$ prepared using $\text{Na}_2\text{WO}_4/\text{Na}_2\text{MoO}_4/\text{HCl}/\text{water}/\text{Triton}/\text{hexanol}/\text{heptane}$. Silica is undetectable by XRD because it is in such small quantities but was detectable by EDX and TEM in **Figure S4.20**

Dissolution of SiO_2/WC using a hot alkaline treatment

While WC and $\text{Mo}_x\text{W}_{1-x}\text{C}$ are both soluble in alkaline conditions, this dissolution procedure is facile, inexpensive, solution-processable, and applicable to other systems where the NPs that are encased in silica are stable in caustic conditions but not in ABF. When dispersed in 0.5 M NaOH for 12 h at 80°C, the initially black suspension becomes optically clear and pale yellow. Addition of methanol to an aliquot of the clear solution would induce precipitation of white flocs while the supernatant remained yellow. This was interpreted to be silica flocs while the yellow supernatant was caused by the presence of WO_4^{2-} . A study was performed by doing a controlled dissolution in 0.1 M NaOH at 40°C. TEM images were taken at various time intervals, which show uniform dissolution of the nanospheres from the surface to the center as being the primary mode of dissolution, further indication that the silica nanospheres are non-sintered post-carburization. This is

shown in **Figure S4.22**. For larger NPs, such as those prepared using Triton X-100®/hexanol or using less silica, were stable in 0.3 M NaOH at 50°C for at least 24 h (images not shown). If the sample developed a quartz-like character, it was not possible to remove the silica using the alkaline treatments attempted at present. Such alkaline dissolutions could be amenable to TMCs that are stable in alkaline conditions, such as TiC and TaC.

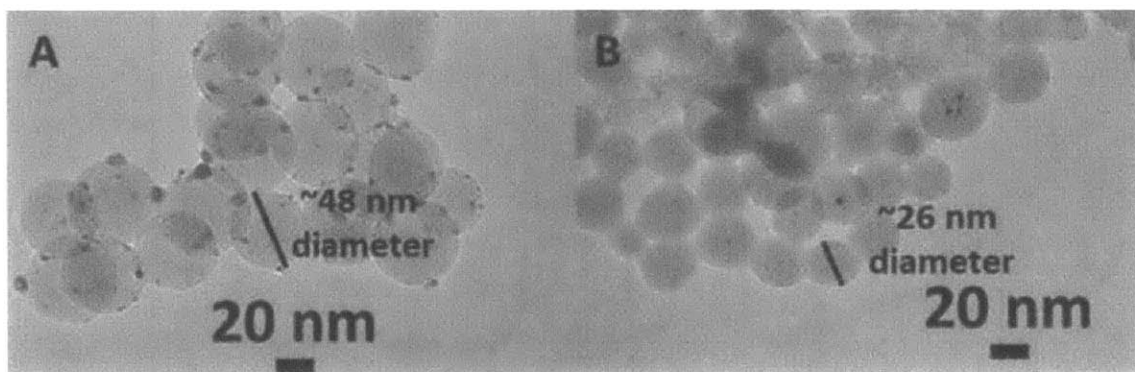


Figure S4.22. TEM images of (A) SiO₂/β-WC and (B) SiO₂/β-WC after stirring in 0.1M NaOH at 40°C for 10 h.

Dissolution of SiO₂/WC and SiO₂/Mo_xW_{1-x}C in aqueous ammonium bifluoride

It was found that both WC and Mo_xW_{1-x}C in either hexagonal or cubic phases were stable in aqueous ammonium bifluoride solutions for extended times. ABF was chosen because it is an inexpensive industrial glass etchant and can readily remove both amorphous silica and quartz in a solution-processable manner at room temperature. In a typical dissolution, 0.2 g of SiO₂/WC or SiO₂/Mo_xW_{1-x}C was added to 21 mL of DI water in a polypropylene container with a Teflon magnetic stir bar. If it was desired to support on carbon black, an appropriate mass of acidified-carbon black (acidified to ~pH 5 using 6 M HCl and rinsing with DI water) was added to the solution. Carbon black was not added if it was desired to obtain a nanodispersion or if it was desired to support on a material that is not stable in ABF such as alumina. Finally, ~5.25 g of ABF was added to make a 20 wt% ABF solution. Such a large excess of ABF solution was used to obtain good dispersion of the NPs on the CB support. Without sonication, the material would naturally disperse to form a black suspension by using mechanical stirring. The silica was fully removed with overnight stirring at room temperature, although STEM and EDX analysis

of an aliquot showed the silica to be fully removed after just 2 h (images not shown). On the opposite extreme, we were able to maintain a black suspension even after 20 h in 30 wt% ABF at 40°C (images not shown).

After a sufficient time had passed, the nanodispersion was neutralized with ~5.5 mL of NH_4OH to a pH of 7 (caution: moderately exothermic reaction). At this point, the nanodispersion, WC/CB, or $\text{Mo}_x\text{W}_{1-x}\text{C/CB}$ was obtained by centrifugation at 6000 rpm for 10 min. Alternatively, an appropriate amount of alumina could be added to the neutralized nanodispersion and stirred for 12 h to obtain WC/ Al_2O_3 (images not shown) before centrifuging. Once recovered, the material was rinsed twice with water. With each successive rinse, the nanodispersion became more difficult to recover by centrifugation possibly due to the decreasing solution ionic strength driving flocculation, eventually requiring 10,000 rpm or more for 30 min. A phase-pure α -WC nanodispersion dispersed in water at ~7.5 mg/mL is shown in **Figure S4.23** after initially dispersing it and after three weeks of sitting in stagnant conditions. No settling was observed. Ethanol could also be used as a dispersing agent with a similar effect (images not shown). While all carbide nanodispersions prepared were dark grey and nearly black, dispersing commercial WC was light-medium grey (images not shown).

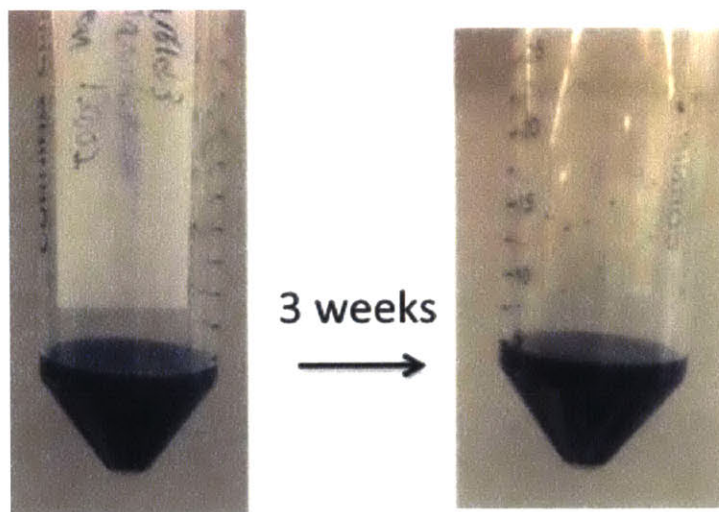


Figure S4.23. Photographs of an α -WC nanodispersion dispersed in water at 7.5 mg/mL before and after three weeks of sitting in stagnant ambient conditions. No settling was observed.

Once the silica coating was removed with ABF, the $\text{Mo}_x\text{W}_{1-x}\text{C}/\text{CB}$ material was particularly interesting to analyze to confirm that both W and Mo were not removed during the dissolution. **Figure S4.24** indicates that Mo and W are detectable post-ABF-dissolution. The ratios of the Mo to W EDX signals are also shown for various compositions for $\text{Mo}_x\text{W}_{1-x}\text{C}$. The actual compositions of the bimetallic carbides were determined using inductively coupled plasma atomic emission spectroscopy (ICP-AES).

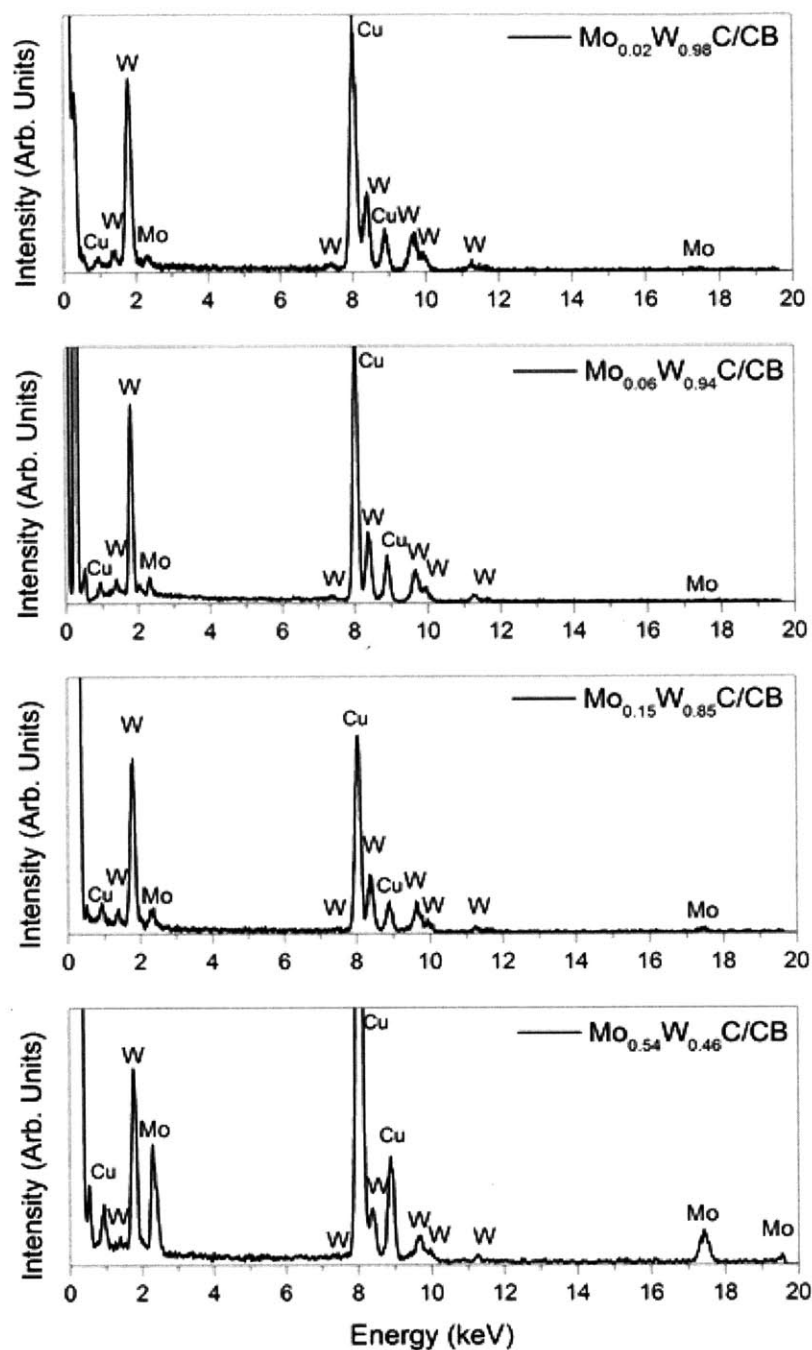


Figure S4.24. EDX comparison of single nanoparticle spectra for various $\text{Mo}_x\text{W}_{1-x}\text{C/CB}$ compositions post-ABF-dissolution using a 0.2 x 0.2 nm STEM probe and 10 s of exposure. Roughly 8–10 nm particles were analyzed to obtain good signal to noise.

Catalyst loading and composition determination for WC/CB and Mo_xW_{1-x}C/CB using ICP-AES and TGA-XRD

Two techniques were used to determine the catalysts loadings: Inductively Coupled Plasma-Atomic Emission Spectroscopy (ICP-AES) and thermogravimetric analysis (TGA) coupled with powder X-ray Diffraction (XRD). ICP-AES was used to determine the loading of elemental W within the silica nanospheres, whereas TGA-XRD was used to determine the wt% loadings of WC/CB and indirectly the loading of WC within the silica nanospheres through calculation. ICP-AES was also used to compute the exact compositions of the Mo_xW_{1-x}C bimetallic carbides.

To determine the loading of W within the silica-encapsulated carbides, calcined SiO₂/WO_x was instead used because it is easier to dissolve. Ostensibly, there is no loss of W on transforming WO_x to WC during the carburization process. The calcined SiO₂/WO_x powder was dissolved by dripping 48% HF solution onto the powder and letting the SiF₄ evaporate over 4 h. The WO_x also dissolved and was redispersed in 3 wt% nitric acid solution and diluted to various ppm concentrations for ICP-AES analysis. A 5 point calibration curve was performed using a W ICP standard. It was determined that the wt% loading of elemental W within the SiO₂/WO_x material is 20.5 wt% (W basis) for the optimal method presented used to make 1–3nm β-WC NPs.

To determine the loadings of the Mo_xW_{1-x}C bimetallic carbides, the carbides were dissolved in a 1:1 mixture of 48% HF and reagent grade nitric acid. The carbides do not readily dissolve in 48% HF even after several days. The addition of reagent grade nitric acid dissolves the carbides within a half hour, obtaining a clear and pale yellow solution. The solvent was then evaporated over 4 h and the solution was redispersed in 3 wt% nitric acid and diluted to various ppm concentrations for ICP-AES analysis. Five point calibration curves for a W ICP standard and an Mo ICP standard were used. The standards were used to first ensure that the selected elemental lines for each element did not have a large background signal from the presence of the other element.

To determine the approximate loading of the carbide NPs on the carbon black support and within the silica nanospheres, a combination of thermogravimetric analysis (TGA) and XRD was used. XRD spectra were taken before and after TGA. TGA was performed using 5°C/min heating until 800°C under 90 sccm of air and 10 sccm of N₂. As

the catalyst is heated, the carbon black support combusts to CO_2 , and WC is oxidized to WO_3 . After TGA, a greenish-yellow powder remains, indicative of WO_3 , that was then analyzed by XRD to confirm phase-pure WO_3 . The mass loss during the TGA was then corrected for the mass gain of all the WC being oxidized to WO_3 . For instance, in **Figure S4.25**, the final mass was 29.15% of the original mass, and the resulting powder was phase-pure green WO_3 . The molar mass of β -WC is 195.85 g/mol while the molar mass of WO_3 is 231.84 g/mol. Thus, the actual wt% loading of β -WC on the original CB support is $(195.85/231.84) \times 29.15\%$ or roughly 25 wt% β -WC on CB. By then back-calculating the mass of CB and mass of SiO_2/β -WC added at the start of the ABF dissolution, the wt% loading of WC within the silica nanospheres was found to be ~ 13 wt% (W basis). This is 7.5 wt% lower than the weight percent determined using ICP-AES and represents a 66% yield throughout the dissolution process for adhering β -WC onto the carbon black support.

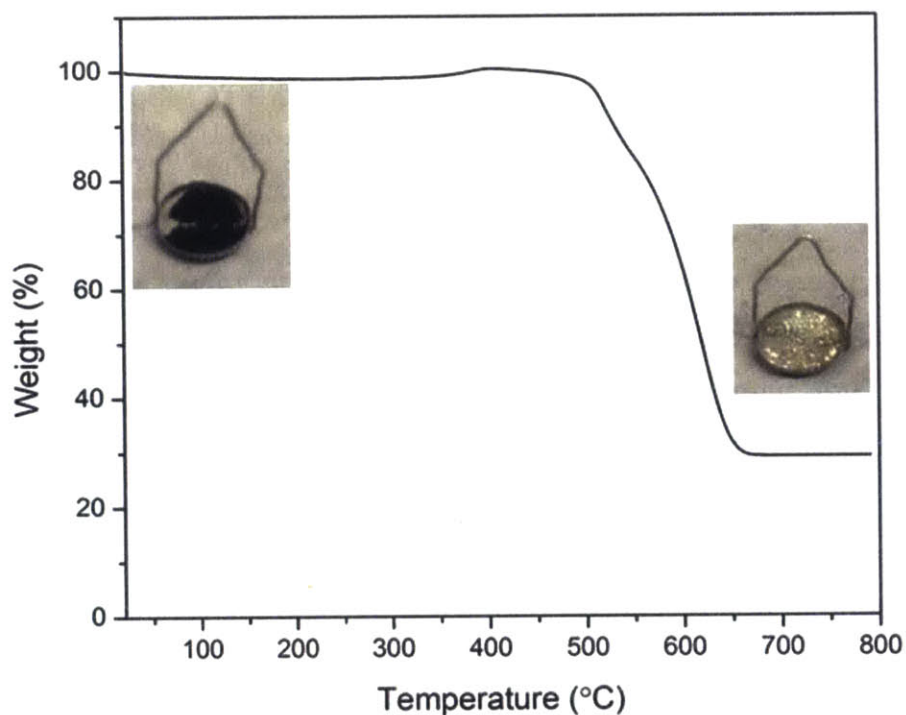


Figure S4.25. TGA of 25 wt% β -WC/CB in air with photographs showing the powder before and after TGA. The final weight percent was 29.15% WO_3 , indicating that the initial powder was 25 wt% β -WC/CB

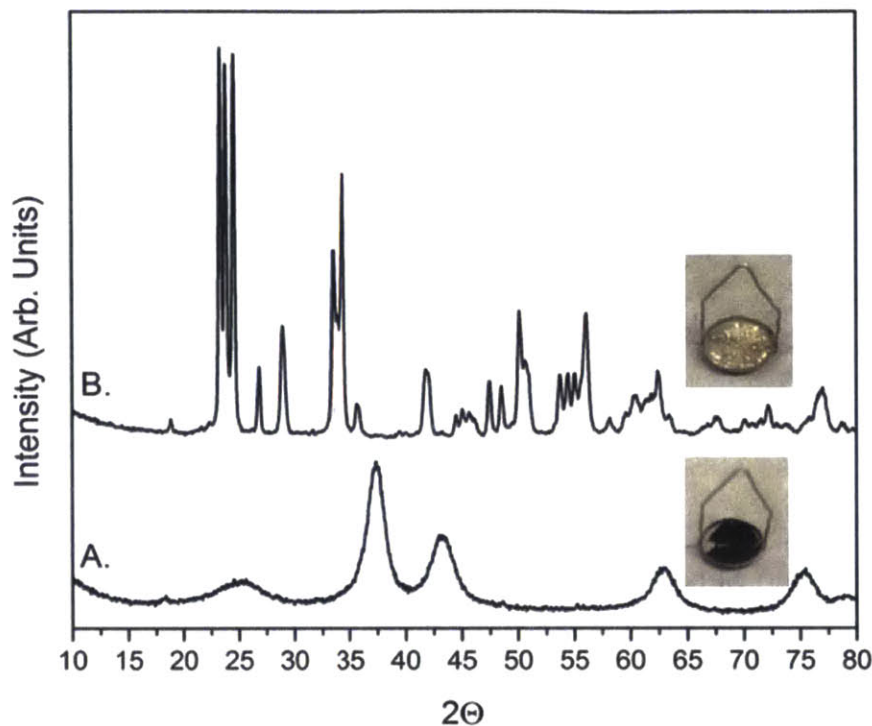


Figure S4.26. (A) XRD spectra of 25 wt% β -WC/CB before TGA and (B) XRD spectra of the resulting material after TGA at 800°C under Air. Carbon black has combusted while the remaining W is in the form of phase-pure WO_3 .

X-ray Photoelectron Spectroscopy (XPS) analysis of catalyst powders

XPS was performed by drying the carbide nanodispersions under vacuum in an argon atmosphere. They were then mounted on copper tape in an argon glovebox and transferred to the XPS side-chamber with less than 30 s of ambient exposure. XPS spectra were collected using a PHI Versaprobe II equipped with a multichannel hemispherical analyzer and a monochromatic aluminum anode X-ray source operating at 100 W with a 100 μm beam scanned over a 1.4 mm line across the sample surface. A dual-beam charge neutralization system was used with an electron neutralizer bias of 1.2 eV and an argon ion beam energy of 10 eV. A standard charge correction was applied to the adventitious C 1s signal to 284.7 eV.

5.3 Electrochemical Characterization of the Carbide Materials

Catalyst ink and working electrode preparation

All catalyst inks were prepared by dispersing 7.5 mg of catalyst in 1 mL of degassed ultrapure water using sonication. While sonicating, 20 μL of 5% Nafion® 117 solution (Sigma-Aldrich®) was added dropwise as a binding agent. Next, 7 μL of ink was dripped onto a 3 mm diameter glassy carbon disk electrode (CH Instruments) to obtain a working electrode geometric surface area of 0.071 cm^2 . Using this protocol, the catalyst loadings were also controlled by mass such that all working electrodes contained $\sim 50 \mu\text{g}$ of catalyst by total weight. The electrode was then dried for 1 hour in an argon atmosphere under vacuum. Before mounting the catalyst ink onto the glassy carbon electrode, the glassy carbon was polished to a mirror finish with 0.05 μm alumina powder (BASi, Inc.), wiped with lens paper, and rinsed thoroughly with ultrapure water. To prevent any possibility of cross-contamination, a separate glassy carbon working electrode was used for the Pt-based catalysts. Carbide-containing catalysts were never mounted on this working electrode.

Electrochemical Setup and Protocols

A standard ~ 12 mL glass electrochemical cell (CH Instruments) containing a Pt wire counter electrode (CH Instruments) and a 1 M KCl Ag/AgCl reference electrode (CH Instruments) with a Teflon cap was used for all experiments. The glass electrochemical cell was etched with reagent-grade sulfuric acid before experiments and rinsed thoroughly with ultrapure DI water. 10 mL of aqueous 0.5 M H_2SO_4 was used for the hydrogen evolution reaction (HER) studies while 10 mL of aqueous 0.5 M H_2SO_4 and 2 M methanol was used for methanol electrooxidation (MOR) studies. For all studies, these 10 mL aliquots were taken from the same stock solution and degassed for 30 min with ultra-high purity (Grade 5) hydrogen or argon (through a Teflon bubbler) prior to loading the cell with the electrodes. A continuous H_2 or Ar purge at 75 mL/min was used throughout the course of all experiments. A freshly-etched and thoroughly rinsed electrochemical cell and fresh electrolyte was used for each working electrode to prevent cross-contamination. Carbide catalysts were activated before use by swirling the dried electrode in 0.1 M NaOH for one

minute and rinsing thoroughly with degassed DI water to minimize surface oxides before use.^[41]

Capacitances of the catalysts

Once the working electrode was loaded, it underwent twenty cycles using cyclic voltammetry (CV) between 0 and +0.4 V vs. RHE at 50 mV/s to condition the electrode and remove any surface contaminants. Conditioning scans can provide insights into the capacitance of the electrodes and the relative electrochemical active surface areas. The twentieth scan for each catalyst in Ar-saturated room-temperature 0.5 M H₂SO₄ is shown below in **Figure S4.27** while a zoomed-in version is shown in **Figure S4.28** to depict the characteristic scans of materials with lower capacitances. It was observed that the capacitances of the β carbides were remarkable, and ~ 1.6 orders of magnitude larger than blank carbon black. To further explore its use as a supercapacitor, it was compared to amorphous 40wt% RuO₂/CB prepared using the optimal method reported in the literature.^[130] Over the span from 0 to +0.4 V in room temperature Ar-saturated 0.5 M H₂SO₄, 40 wt% β -Mo_{0.06}W_{0.94}C/CB and 40wt% RuO₂/CB have nearly identical capacitances as shown in **Figure S4.29**. Oftentimes, supercapacitors must operate over large potential windows. **Figure S4.30** depicts the capacitances for 40wt% β -Mo_{0.06}W_{0.94}C/CB and 40 wt% RuO₂/CB over a potential window from 0 V to +1.25 V vs. RHE. In this potential window, carbides are not stable but become thickly passivated in a core-protecting oxide layer. The capacitance of the carbides was observed to drop but the capacitance remained within an order of magnitude of the amorphous RuO₂/CB over this potential window.

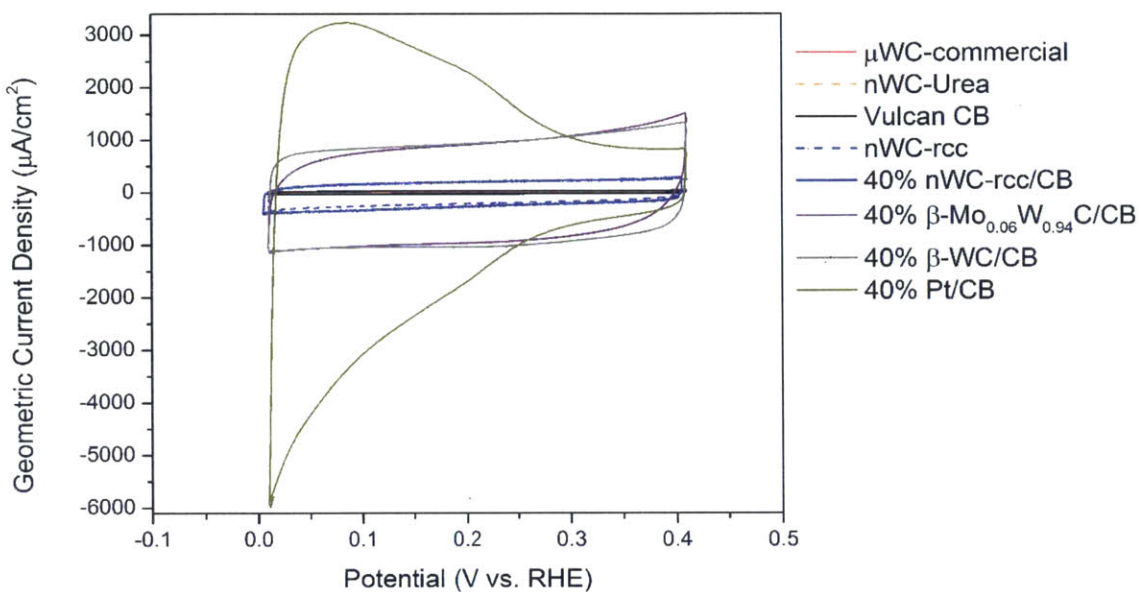


Figure S4.27. Capacitances of the various catalysts in room-temperature, argon-saturated 0.5 M H₂SO₄. The twentieth scan is shown. CV scan rate = 50 mV/s

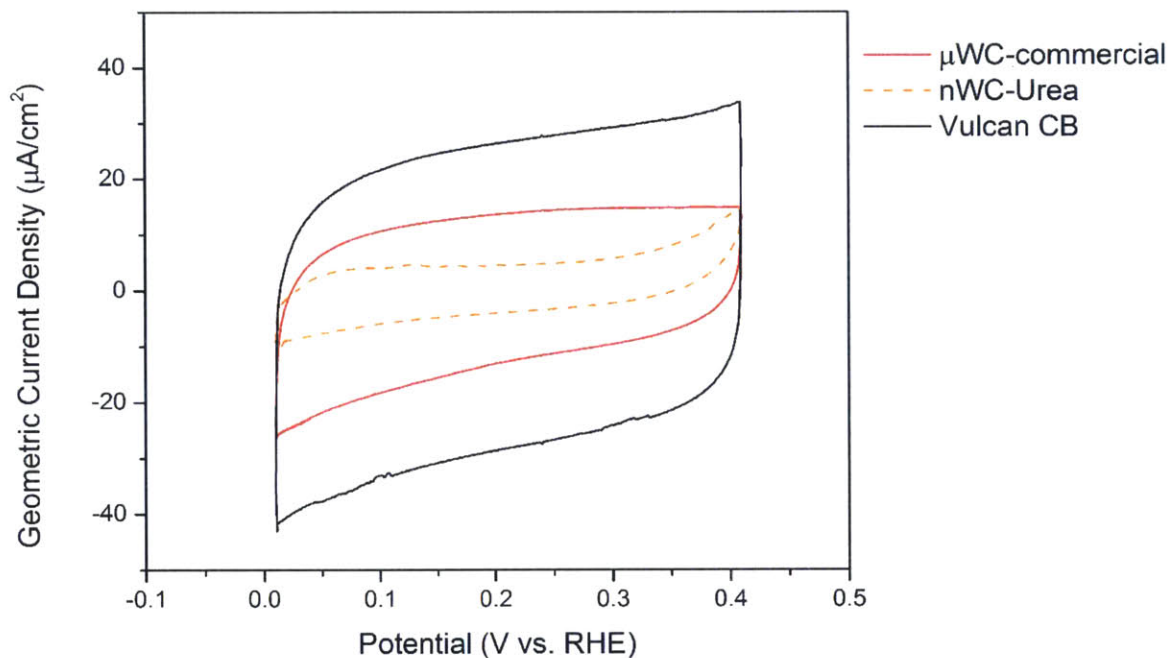


Figure S4.28. (Zoomed in) Capacitances of the various catalysts in room-temperature, argon-saturated 0.5 M H₂SO₄. The twentieth scan is shown. CV scan rate = 50 mV/s

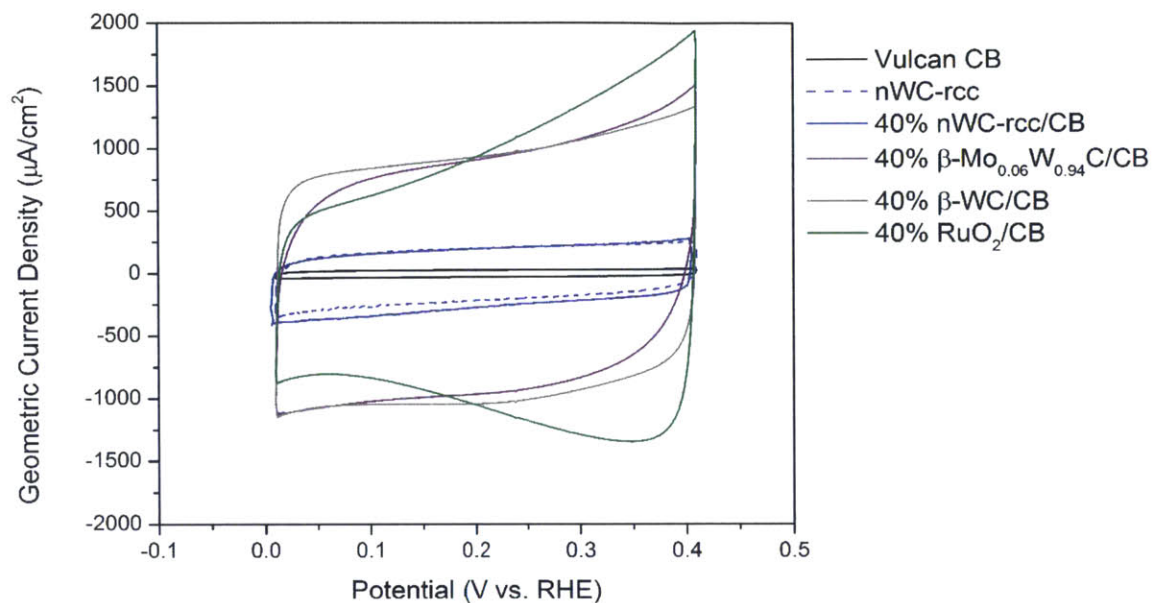


Figure S4.29. Capacitances of the various catalysts compared to 40wt% amorphous RuO₂/CB in room-temperature, argon-saturated 0.5 M H₂SO₄. The twentieth scan is shown. CV scan rate = 50 mV/s

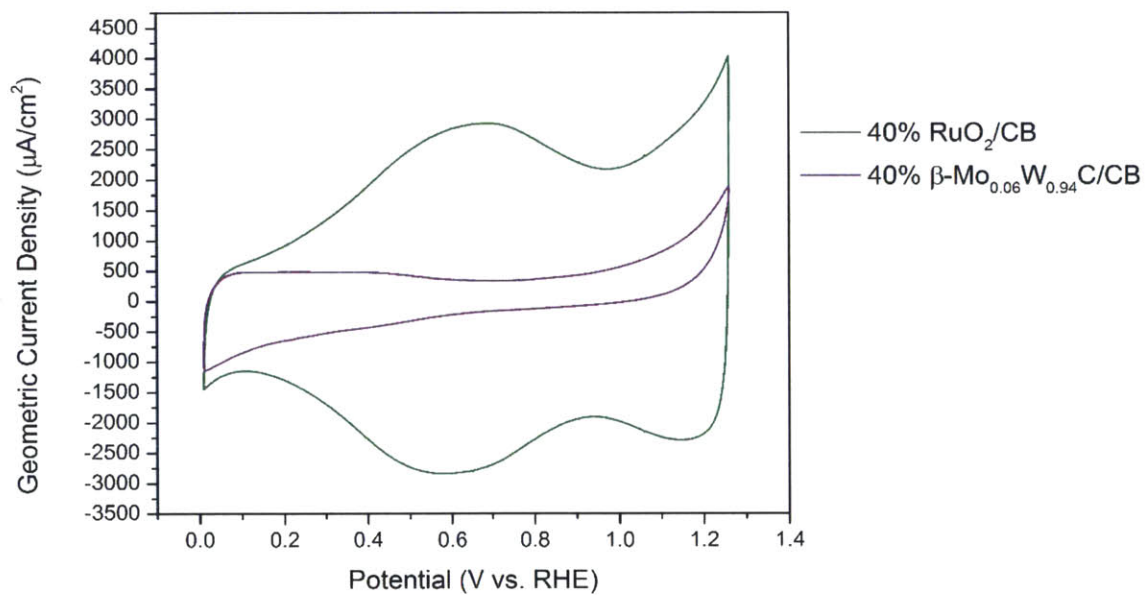


Figure S4.30. Capacitances over a wide potential window in room-temperature, Ar-saturated 0.5M H₂SO₄. The twentieth scan is shown. CV scan rate = 50 mV/s

HER Activity and Stability Comparison and Facile Regeneration of the Carbide Electrodes

The HER has been well-studied for bulk WC thin film catalysts, and in 0.5 M H₂SO₄, it occurs at potentials in which the carbides are non-passivated and are highly stable.^[33,41,48] Stability for these nanoscale carbide catalysts was studied by comparing LSV scans before and after various electrochemical and wet-chemical treatments as presented in **Figure 4.3**. **Figure S4.31** depicts LSV scans of 40wt% Pt/CB in various sulfuric acid concentrations. For 40 wt% α -WC/CB and 40 wt% β -Mo_{0.06}W_{0.94}C/CB prepared using the removable ceramic coating method, as well as a commercial α -WC material, the working electrode was first dipped for 1 min in 0.1 M NaOH and rinsed thoroughly with degassed, DI water. After conditioning the electrode for 20 cycles in room-temperature H₂-saturated 0.5M H₂SO₄ between 0 and +0.4 V vs. RHE, an initial HER LSV scan was recorded. The electrode was then subjected to 3000 cycles (~30 h on stream) between -0.3 and +0.6 V vs. RHE at 50 mV/s. Afterwards, a second HER LSV was recorded, in which it was seen that both the α and β carbides suffered minimal deactivation. The working electrode was then dipped in 0.1 M NaOH solution for 1 min, rinsed thoroughly with degassed DI water, and then cycled 20 times between 0 and +0.4 V in room-temperature H₂-saturated 0.5M H₂SO₄. A third and final LSV was then recorded, which showed that both the α and β carbides can be easily regenerated back to their initial activities even after previously undergoing 3000 cycles between -0.3 and +0.6 V vs. RHE. While W₂C and α -W are known to be less electrochemically stable than α -WC in acidic medium, β -WC is not a well-studied material. To verify the stability of both the α and β phases after both the 3000 cycles and the two dips in 0.1 M NaOH, the regenerated catalysts were analyzed by XRD. Although poor signal is obtained due to the small sample size (~50 μ g), the α and β phases remain intact post-stability and regeneration testing as shown in **Figure S4.32**.

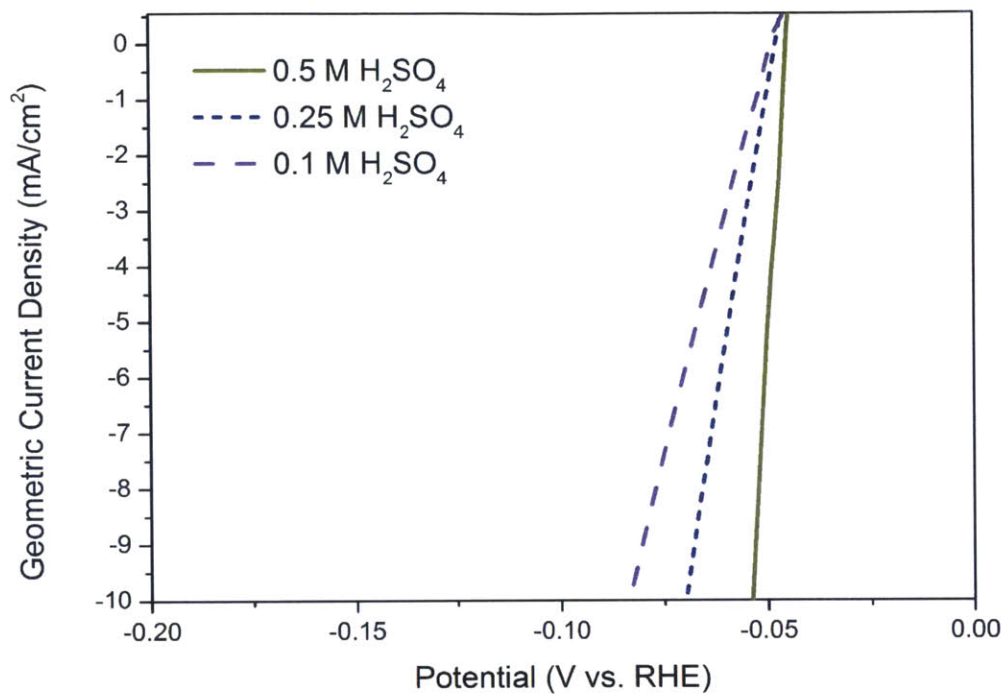


Figure S4.31. LSVs of 40wt% Pt/CB in H₂-saturated sulfuric acid solutions of various concentrations at room temperature. The scan rate used was 2mV/s.

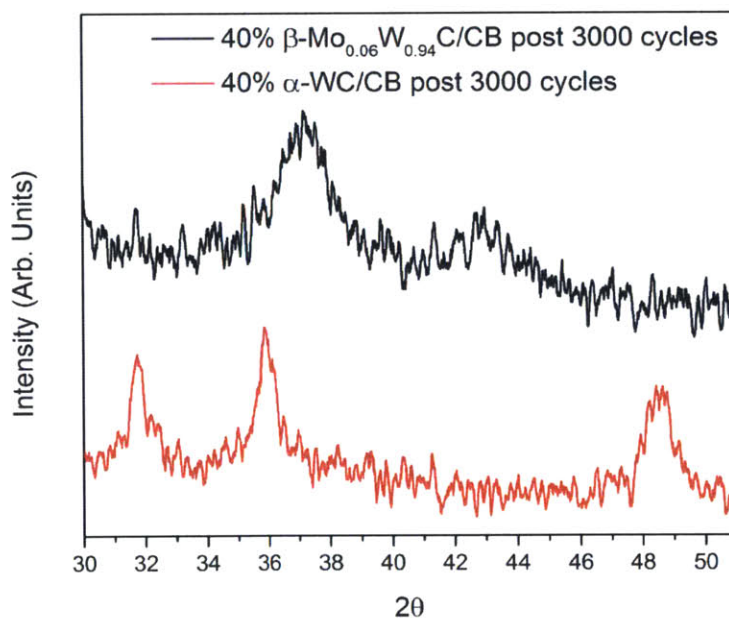
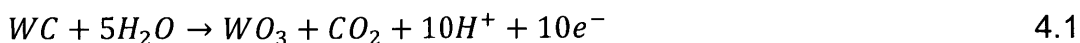


Figure S4.32. XRD of 50 µg of 40 wt% β -Mo_{0.06}W_{0.94}C/CB and 40 wt% α -WC/CB after 3000 HER cycles from -0.3 to +0.6 V vs. RHE and subsequent regeneration through dipping in 0.1 M NaOH (noise due to small size of powder material analyzed).

Methanol Electrooxidation

To mimic operating conditions in a direct methanol fuel cell, methanol electrooxidation was studied in a mixture of aqueous 2M methanol and 0.5M sulfuric acid at 40°C. The temperature reported is the temperature of the electrolyte measured using an analogue thermometer in the vicinity of the working electrode-electrolyte interface at steady state. **Figure S4.33** depicts initial CV scans of the various catalysts in 2M methanol and 0.5M H₂SO₄ at 40°C while **Figure S4.34** depicts the twentieth cycle. **Figure S4.35** and **Figure S4.36** depict initial CV scans for the lower-activity materials at appropriate scales. It can be seen that the commercial carbide material has a distinct hump whereas those prepared using the “urea route”^[47] do not. **Figure S4.37** shows the long-term activity of the commercial carbide held potentiostatically at +0.75 V vs. RHE. **Figure S4.38** shows the activity of 40wt% α-WC/CB made using the removable ceramic coating method in the presence of methanol and without methanol. Typically, MOR CA scans are only shown in the literature over the first 5 min. To clarify the initial activities, **Figure S4.39** and **Figure S4.40** depict the initial 5 min of the MOR reaction under potentiostatic conditions at +0.75 V vs. RHE in 2 M methanol and 0.5 M sulfuric acid at 40°C, which shows that each of the three WC controls are at least two orders of magnitude less active than the WC material prepared using the removable ceramic coating method. Those materials prepared using the “urea route” quickly decayed to zero in under 15 minutes, oscillating between anodic and cathodic currents for the remainder of the testing (results not shown). Remarkably, the WC material prepared using the “rcc” method is still more “active” than any of the WC controls even when methanol is not present, as shown in **Figure S4.40**. This result is further explored below.

For all WC materials examined, the measured current can arise from methanol electrooxidation, capacitive discharging, or oxidation of the WC surface to WO₃ via **Equation 4.1**.



This anodic reaction results in the passivation of the carbide NPs with an oxide layer that protects against further corrosion in acidic media. However, to confirm that the current

measured is indeed due to the oxidation of methanol rather than the corrosion of the carbide or capacitive discharging, we examined the total charge required to oxidize the entirety of WC loaded on the electrode to WO_3 based on the above ten electron transfer process. Based on 50 μg loadings of 40 wt% α -WC/CB on a 0.071cm^2 electrode, this corresponds to 1.48 C/cm^2 of charge required to fully oxidize all of the WC to WO_3 . Integrating the curve of **Figure S4.38** indicates that 1.50 C of charge was passed in the first 45 min of the study in the presence of methanol. Notably, 0.5 C of charge was passed in the first 5 min (**Figure S4.39**). Over the span of 4 h, in excess of 5 C/cm^2 of charge was passed by the electrode, three times more charge than can be attributed to the bulk oxidation of all WC present to WO_3 , indicating that the current observed is due to a faradaic and catalytic surface oxidation reaction rather than capacitive discharging or bulk oxidation/dissolution of the electrode.

As shown in **Figure S4.38** and **Figure S4.40**, the α -WC/CB material prepared using the “rcc” method was still able to pass a significant current even when methanol was not present. Even without methanol present, the current was always significantly higher than any of the WC controls, even higher than the commercial WC after 4 h. Integrating the curve of **Figure S4.38** indicates that without methanol present, 40 wt% α -WC/CB prepared using the “rcc” method passed 0.05 C/cm^2 of charge in the first 5 min (one order of magnitude less charge than when methanol is present), and 0.75 C/cm^2 of charge over the next 4 h. The total charge passed of 0.8 C/cm^2 is less than the 1.48 C/cm^2 required to fully oxidize the WC to WO_3 , and thus it cannot be concluded that this current is a catalytic, faradaic surface reaction.

Comparison of **Figure S4.37** and **Figure S4.38** also shows that after 4 h, 40 wt% α -WC/CB prepared using the “rcc” method is over two orders of magnitude more active than the commercial carbide material. The materials prepared using the “urea route” had activities that quickly decayed to zero current density within 15 min (with the electrode oscillating between anodic and cathodic currents), likely because carbide NPs prepared using this route are covered in deactivating surface carbon (N.B. the synthesis requires a 6 fold molar excess of carbon) whereas the commercial carbide prepared by “top-down” ball-milling has exposed surfaces that are carbide-terminated.

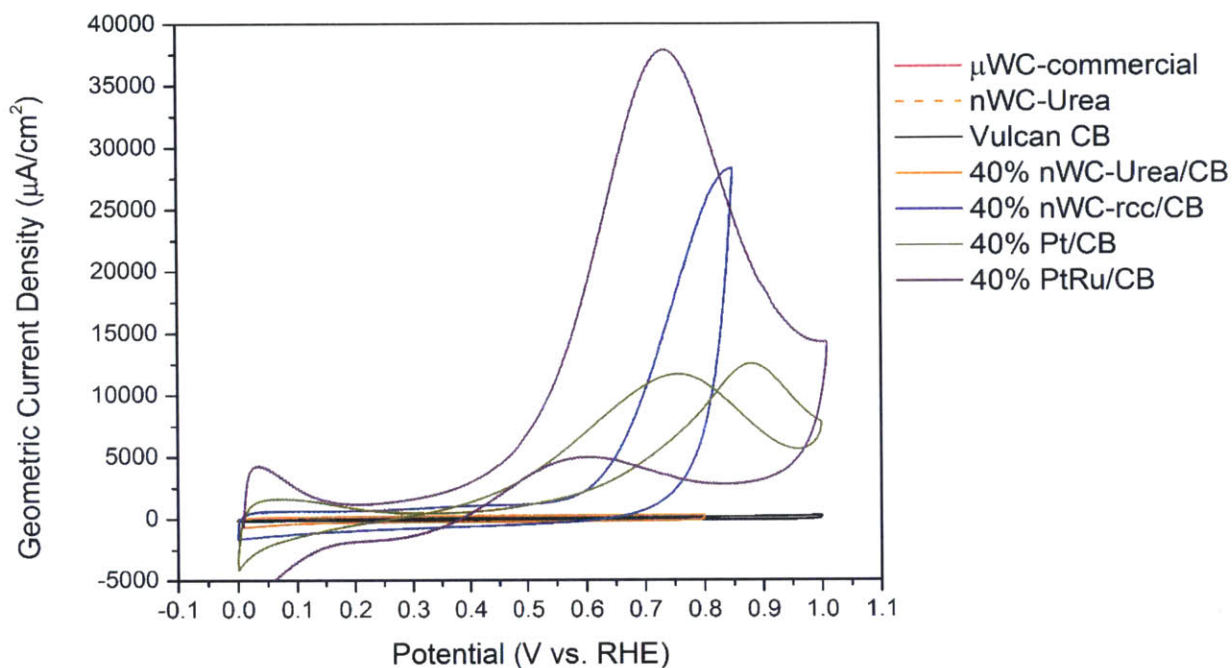


Figure S4.33. Initial CV scans at 50 mV/s in an aqueous electrolyte consisting of 2 M methanol and 0.5 M H₂SO₄ at 40°C.

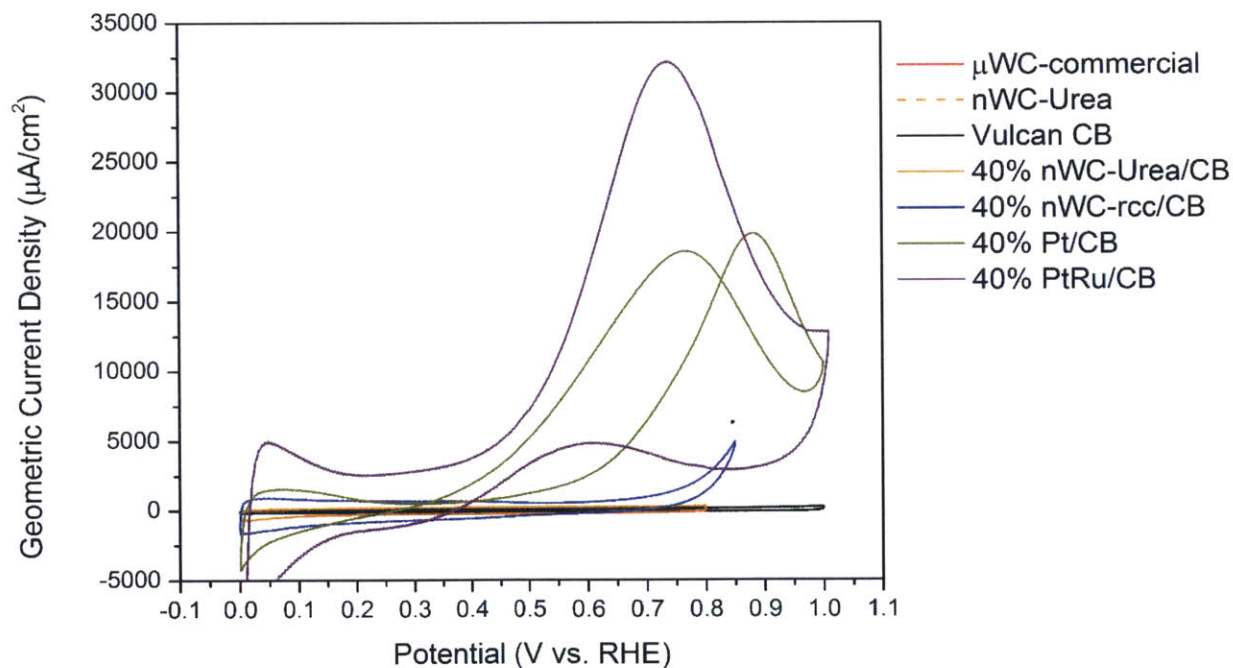


Figure S4.34. Twentieth CV scans at 50 mV/s in an aqueous electrolyte consisting of 2 M methanol and 0.5 M H₂SO₄ at 40°C.

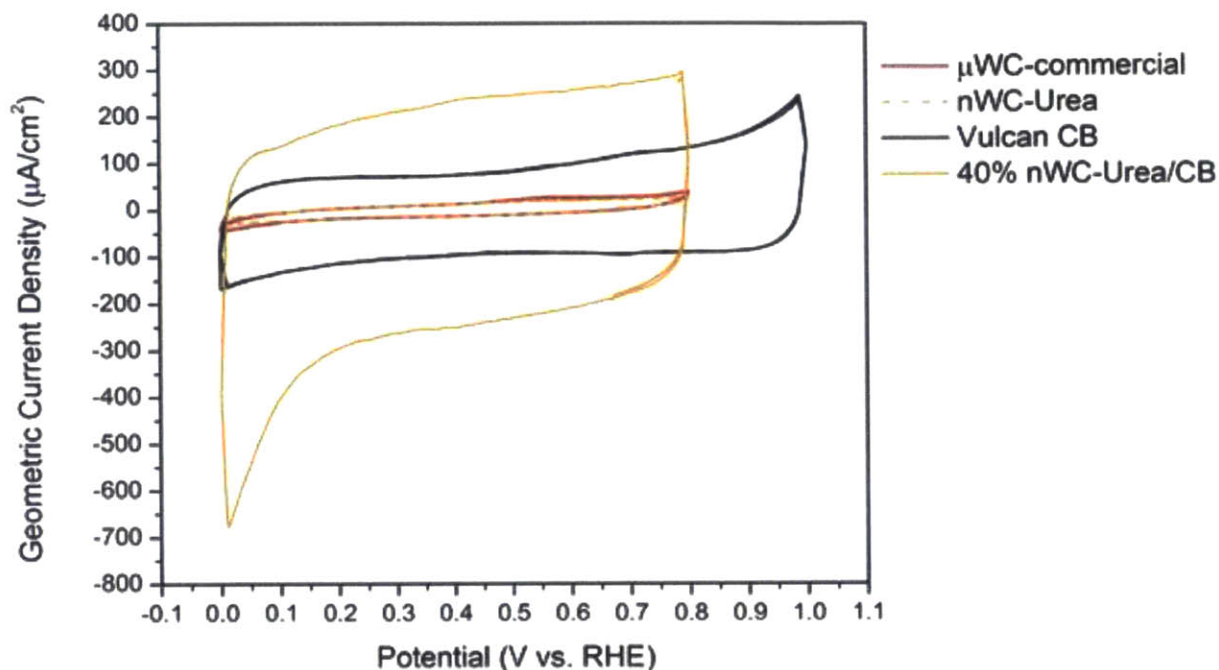


Figure S4.35. (Zoomed in) initial CV scans at 50 mV/s in an aqueous electrolyte consisting of 2 M methanol and 0.5 M H₂SO₄ at 40°C.

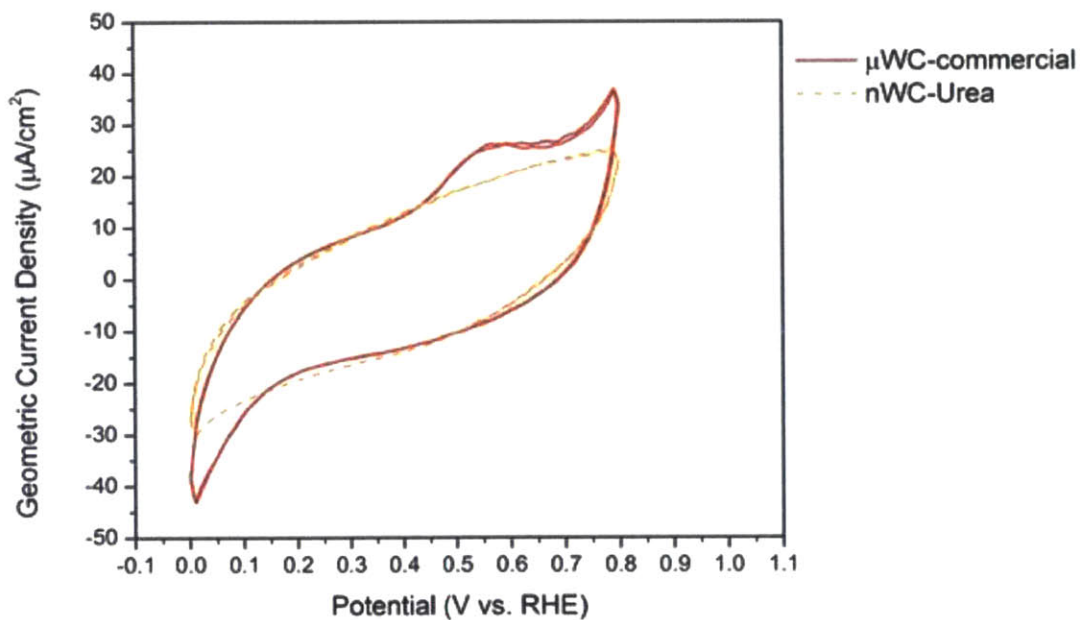


Figure S4.36. (Zoomed in) initial CV scans at 50 mV/s in an aqueous electrolyte consisting of 2 M methanol and 0.5 M H₂SO₄ at 40°C.

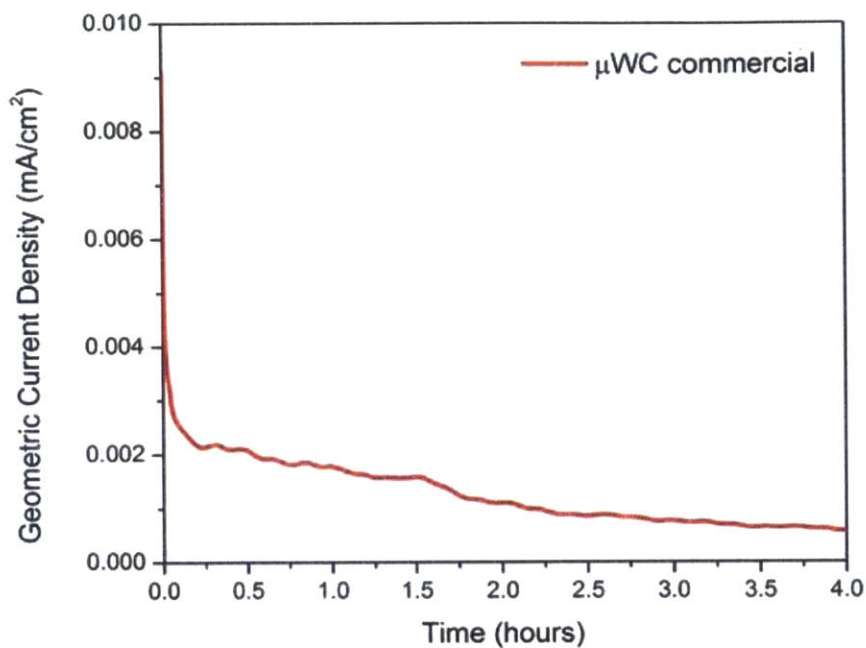


Figure S4.37. Extended CA scan for commercial 2–3 μ m WC in aqueous 2 M methanol and 0.5 M H₂SO₄ at 40°C held potentiostatically at +0.75 V vs. RHE for 4 h.

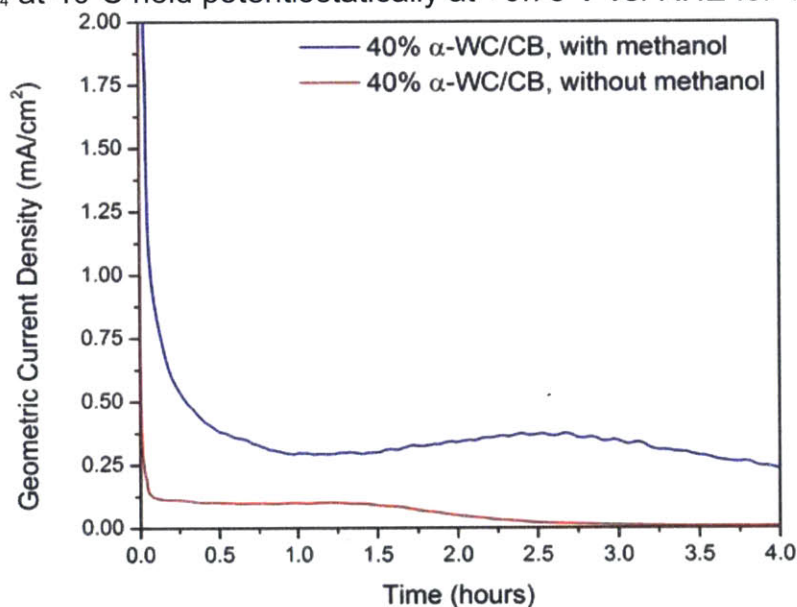


Figure S4.38. Extended CA scans for 40 wt% α -WC/CB made using the removable ceramic coating method in (blue) aqueous 2 M methanol and 0.5 M H₂SO₄ at 40°C held potentiostatically at +0.75 V vs. RHE for 4 h and (red) aqueous 0.5 M H₂SO₄ at 40°C held potentiostatically at +0.75 V vs. RHE for 4 h.

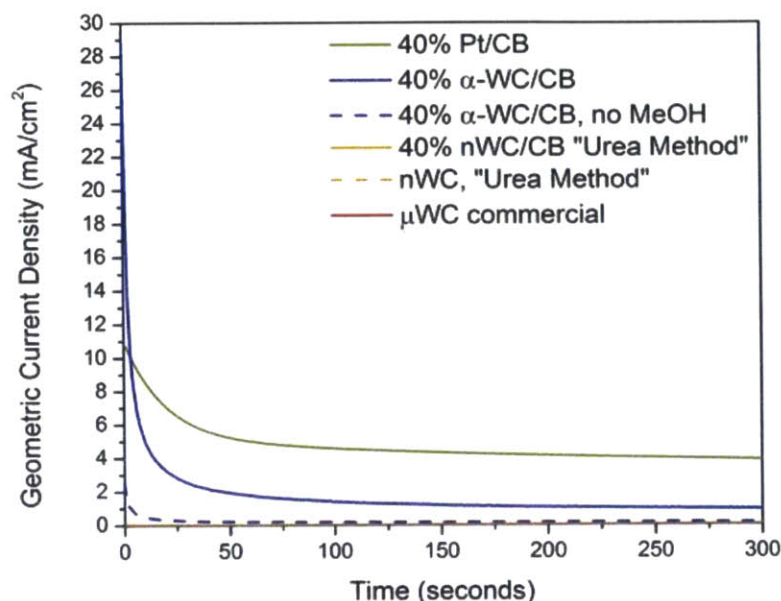


Figure S4.39. CA scans over the first 5 min performed in aqueous 2 M methanol and 0.5 M H_2SO_4 at 40°C held potentiostatically at +0.75 V vs. RHE, with the exception of “40% α -WC/CB, no MeOH,” which was held potentiostatically at +0.75 V vs. RHE in 0.5 M H_2SO_4 at 40°C without the presence of methanol.

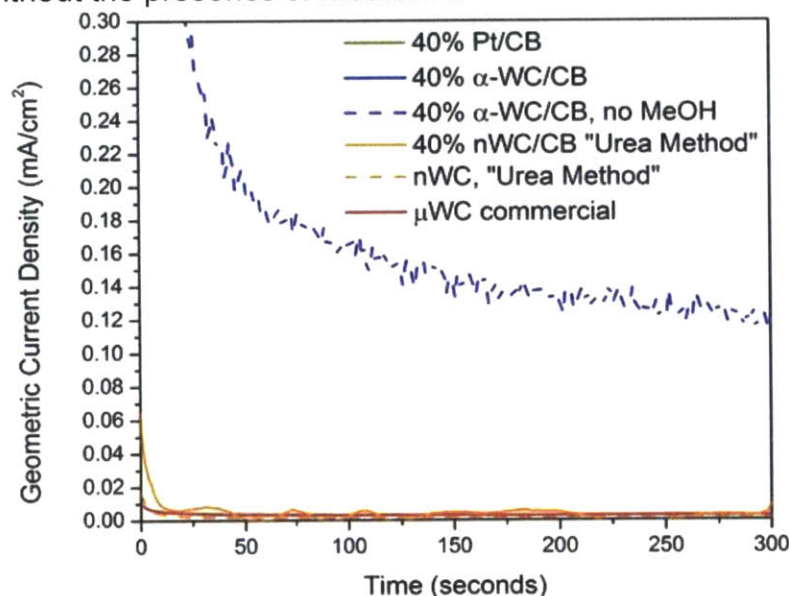


Figure S4.40. (zoomed in) CA scans over the first 5 min performed in aqueous 2 M methanol and 0.5 M H_2SO_4 at 40°C held potentiostatically at +0.75 V vs. RHE, with the exception of “40% α -WC/CB, no MeOH,” which was held potentiostatically at +0.75 V vs. RHE in 0.5 M H_2SO_4 at 40°C without the presence of methanol. The 40% nWC/CB material prepared using the “Urea Method” exhibited oscillatory behavior in each run, oscillating between acting as an anode and a cathode at +0.75 V, indicating it is not active for MOR. nWC nanopowder prepared using the “Urea method” began to oscillate between acting as an anode and cathode within the first 15 min (not shown).

Chapter 5

Characterization of Bimetallic Carbide

Nanoparticles and Electrocatalytic Study of Ta_{0.3}W_{0.7}C

1. Introduction

The development of bimetallic nanoparticles (NPs) has greatly advanced the continuing search for electrocatalysts with higher activity and stability, and lower cost. Catalytic activity can be enhanced through strain and ligand effects between the bimetallic alloys, often giving rise to enhanced or new catalytic activity at the surface.^[135] An example would be the excellent performance of PtRu bimetallic NPs for oxygenate electrooxidation.^[136] Similarly, catalytic stability has been enhanced by alloying active metal sites with more electrochemically stable metals such as gold and iridium.^[137,138] Bimetallic NPs have also been used to create less expensive catalysts with unique catalytic properties, such as in the development of PtSn,^[139] Pt₃Ni,^[67] PtMo,^[140] and PtW formulations.^[141] Unfortunately, the advancements provided by the study of bimetallic NPs have not been translated to the development of early transition metal carbide (TMC) catalysts.

Nanostructured early transition metal carbides (TMCs) are a long-sought-after class of earth-abundant materials with the potential to transform and enable sustainable energy technologies.^[14] TMCs are notable for their high thermal and electrochemical stabilities, chemical resistance, low cost, and unique catalytic activities.^[13] In particular, tungsten carbide (WC) and molybdenum carbide (Mo₂C) have attracted much attention due to their catalytic similarities to the platinum group metals (PGMs).^[18] As such, TMCs have been investigated in numerous thermal and electrocatalytic reactions as standalone catalysts,^[29,49] co-catalysts,^[35] substrates for active monolayers,^[32,33,48] and catalyst supports.^[70,118,142-146] Unfortunately, the high synthesis temperatures (c.a. > 700 °C) required to synthesize TMCs has made the study of catalytically active nanomaterials difficult due to sintering and excess surface carbon deposition.^[14,37,49,72] For these reasons, the study of TMCs, and in particular bimetallic formulations, has been relegated to low surface area materials such as bulk microparticles^[127] or sputtered thin films.^[147]

While early TMCs are substantially less expensive and more abundant than the PGMs, they are often considered to be less active and stable. To this end, we have recently demonstrated that successfully synthesizing ultrasmall TMC NPs can offset their lower reactivity with respect to PGMs.^[49] We showed that non-sintered, metal-terminated TMC NPs have high electrocatalytic activity for the hydrogen evolution reaction (HER) and the methanol electrooxidation reaction (MOR), with activities approaching that of commercial PGM-based NP catalysts.^[49] However, while such ultrasmall NPs are highly active, they become inherently less electrochemically stable due to their greater specific surface energy.^[10,148] The intrinsic instability of ultrasmall NPs is also true for PGM-based materials. For instance, Pt NPs in the range of 2 – 3 nm are highly active for ORR, but feature decreased long-term operating stability when compared to larger NPs.^[10]

The development of bimetallic carbide NPs offers the possibility of preserving the high activity of ultrasmall NPs while mitigating their intrinsically lower stability. While increased durability under oxidizing conditions is important for applications of TMCs as standalone catalysts, it is also critical for applications in which TMCs act as electrocatalyst supports or as substrates in core-shell formulations. In these applications, oxidation and/or dissolution of the TMC surface would be detrimental to the supported active phase. Extensive surface science studies on polycrystalline foils have identified highly stable carbide materials in acidic media. While Mo₂C and hexagonal WC foils begin to passivate below +0.4 V and +0.7 V vs. RHE, respectively,^[41,42] titanium carbide (TiC) and tantalum carbide (TaC) foils are stable up to +1.6 V and +1.2 V vs. RHE in acidic media, respectively.^[43] Unfortunately, bulk TaC has low reactivity, exhibiting an overpotential for the onset of HER around 250 mV greater than bulk WC.^[149] To date, detailed investigations of the impact of alloying stable but unreactive carbides with more reactive but less stable ones in nanoparticle formulations have not been performed.

In this chapter, we synthesize, characterize and electrochemically test the performance of bimetallic tantalum tungsten carbide (Ta_xW_{1-x}C) NPs with the ultimate goal of combining the favorable reactivity of WC and the exceptional stability of TaC into a single material. We show that Ta_{0.3}W_{0.7}C NPs in the 2 – 3 nm range exhibit the same HER activity as 2 – 3 nm WC NPs while the onset of passivation is increased from +0.2 V to +0.45 V vs. RHE. The maximum surface oxidation current is increased from +0.4 V vs.

RHE to +0.75 V vs. RHE, resulting in a substantially increased stability window. Extended X-ray Absorption Fine Structure (EXAFS) is used to probe the internal structure of the new bimetallic nanoparticles, offering insights into how bimetallics can be used to further enhance TMC stability without affecting catalytic activity by modulating strain effects. The chapter ends with the characterization of other bimetallic carbide and nitride nanoparticles.

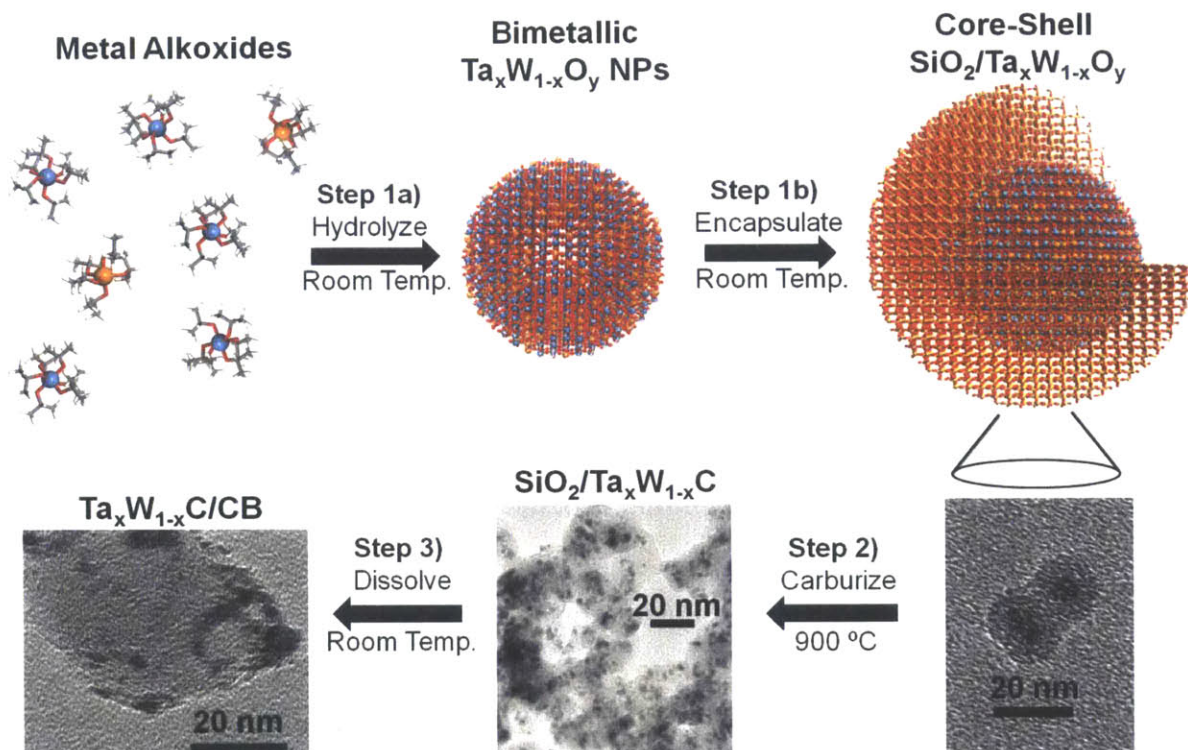


Figure 5.1. Synthesis of Non-Sintered, Metal-Terminated $Ta_xW_{1-x}C$ Nanoparticles Supported on Carbon Black

2. Experimental Methods

WC and $Ta_xW_{1-x}C$ NPs were synthesized using our recently developed reverse microemulsion (RME) method that allows for the design of non-sintered, metal-terminated TMC NPs with tunable sizes and crystal phases.^[49] This method, modified for the synthesis of bimetallic $Ta_xW_{1-x}C$ NPs, is depicted in **Figure 5.1**. Briefly, an optically transparent water-in-oil (w/o) RME consisting of discrete nano-sized water domains dispersed in a continuous nonpolar media was made by mixing 240 mL *n*-heptane, 7.8

mL deionized water, 0.7 mL reagent grade ammonium hydroxide, and 54 mL polyoxyethylene (4) lauryl ether (Brij® L4, a commercial nonionic surfactant).^[120] Metal alkoxide precursors were then diluted in 120 mL of *n*-heptane and slowly added to the RME under constant mechanical stirring. For the synthesis of WC, tungsten (VI) isopropoxide (WIPO, 5% w/v in isopropanol) was used as the metal precursor to make WO_x NPs. For the synthesis of Ta_xW_{1-x}C, WIPO was first mixed with tantalum (V) isopropoxide (TaIPO, 5% w/v in isopropanol) in the desired molar ratio (30:70) before addition to the RME to form Ta_{0.3}W_{0.7}O_x NPs as depicted in step 1a of **Figure 5.1**. The RME mixture containing the mono or heterometallic oxide NPs was then coated in silica by slowly injecting 2.6 mL of reagent-grade ammonium hydroxide followed by 1.2 mL of tetraethyl orthosilicate (TEOS) into the RME, forming SiO₂/WO_x or SiO₂/Ta_xW_{1-x}O_y core-shell NPs as depicted in step 1b of **Figure 5.1**. After 16.5 h, the core-shell NPs were precipitated by the addition of 300mL of methanol. After decanting, the NPs were rinsed with 30 mL of acetone to remove excess surfactant and recovered via centrifugation at 4000 rpm for 10 min. A TEM image of the SiO₂/Ta_{0.3}W_{0.7}O_x NPs is provided in step 1b of **Figure 5.1**, showing that the bimetallic metal oxide NPs are singly coated within silica shells.

In step 2 of **Figure 5.1**, the SiO₂/WO_x and SiO₂/Ta_xW_{1-x}O_y NPs were then calcined at 450 °C for 1 h under 100 sccm of air to burn off excess surfactant and increase the microporosity of the silica shells.^[49] The core-shell NPs were then heated to 900 °C (1173 K) in a tube furnace under 33 sccm of methane and 120 sccm of hydrogen for 4 h to form silica-encapsulated transition metal carbides: SiO₂/WC or SiO₂/Ta_xW_{1-x}C. The core-shell NPs were then held at 900 °C for 1 h under 120 sccm H₂ to remove excess surface carbon. The core-shell NPs were then allowed to naturally cool to room temperature under 120 sccm H₂ with the furnace lid closed. Once at room temperature, the material was passivated for 3 h at room temperature in a 1% O₂/Ar atmosphere. A heating ramp rate of 2°C/min was used throughout the entire synthesis procedure. The hold times are reported once the steady-state temperatures were achieved. A TEM image of the resulting SiO₂/Ta_{0.3}W_{0.7}C material shows that while the sacrificial silica shells have sintered, they have prevented the sintering of the Ta_{0.3}W_{0.7}C NPs.

In step 3 of **Figure 5.1**, the silica shells were removed from the SiO_2/WC or $\text{SiO}_2/\text{Ta}_x\text{W}_{1-x}\text{C}$ NPs using a room temperature solution consisting of 20wt% ammonium bifluoride (ABF) in water. An appropriate mass of Vulcan® XC-72r carbon black (CB) was added to 20 mL of a 20wt% ABF solution containing 200 mg of SiO_2/WC or $\text{SiO}_2/\text{Ta}_x\text{W}_{1-x}\text{C}$ to generate WC/CB or $\text{Ta}_x\text{W}_{1-x}\text{C}/\text{CB}$ supported catalysts with a loading of 40wt%. The ABF/water/TMC NP/CB suspension was mechanically mixed for 18 h and then neutralized dropwise with reagent-grade ammonium hydroxide to a pH of 6 – 7. The resulting WC/CB or $\text{Ta}_x\text{W}_{1-x}\text{C}/\text{CB}$ material was recovered by centrifugation and rinsed thoroughly with DI water.

The loadings of the material on carbon black were characterized using thermogravimetric analysis (TGA) and inductively coupled plasma atomic emission spectroscopy (ICP-AES). For the bimetallic carbide, the molar ratio of Ta:W was determined using ICP-AES and X-ray Photoelectron Spectroscopy (XPS). The phase-purity and average crystallite size of the materials were determined using Powder X-ray Diffraction (PXRD). The particle size distributions (PSDs) were determined using Transmission Electron Microscopy (TEM) and images of the material were also taken using High Angle Annular Dark Field Scanning Transmission Electron Microscopy (HAADF-STEM). PSDs were obtained from manual measurements on five images taken from different areas of the TEM grid.

X-ray Absorption Spectroscopy (XAS) was performed at the Brazilian Synchrotron Light Laboratory (LNLS) at CNPEM, Campinas, Brazil using the XDS beamline. The measurements were performed in transmission mode at room temperature at the W L_3 -edge (10207 eV) and the Ta L_3 -edge (9881 eV). WO_3 , WO_2 , W, WC, W_2C , Ta, and TaC bulk standards were purchased from a commercial vendor (Alfa Aesar) and consisted of micron-sized particles. All samples were pelletized and mounted on slides using Kapton® tape. The standards were mixed with boronitride powder while the silica-encapsulated carbide NPs were pelletized directly. For all XAS measurements, each scan took ca. 30 min and three complete scans were measured for each material and then merged.

Electrocatalytic testing was performed using a CH Instruments 627e potentiostat/galvanostat. The electrolyte consisted of room-temperature 0.5 M H_2SO_4 prepared using ultrahigh purity DI water. The electrolyte was saturated using a pure H_2

or Ar gas bubbler for at least 1 h before measurements were taken. An Ag/AgCl in 1 M KCl solution reference electrode (+0.239 V vs. SHE) was used in the characterization, but all potentials are reported versus RHE in 0.5 M H₂SO₄. A Pt wire was used as the counterelectrode. Working electrodes were prepared by sonicating 7.5 mg of β -WC/CB or β -Ta_xW_{1-x}C/CB catalyst in 1 mL of DI water with 100 μ L of a 5% Nafion® 112 solution to form a catalyst ink. 7 μ L of this ink was then dripped onto a 3 mm glassy carbon disk electrode polished to a mirror finish with 0.05 μ m alumina powder. The working electrode was then dried under vacuum for 1 h, dipped in 0.1 M NaOH solution to remove surface passivated oxides,^[41,49] and then rinsed with copious amounts of water before being placed in the electrolyte.

3. Characterization of Ta_xW_{1-x}C NPs using Standard Techniques

The composition of the SiO₂/Ta_xW_{1-x}C bimetallic carbide NPs was 30% Ta and 70% W, and the loading of the metal NPs in silica was 26 wt% and 20 wt% on a metals basis for Ta_{0.3}W_{0.7}C and WC, respectively (as determined by ICP-AES). **Figure 5.2a** shows that after carburization both SiO₂/WC and SiO₂/Ta_{0.3}W_{0.7}C were crystallized in phase- pure face-centered cubic (fcc) lattices. While bulk WC traditionally crystallizes in a hexagonal lattice (α -WC), it has recently been shown that the face-centered cubic (fcc) lattice (β -WC) is also stable in the synthesis of ultrasmall NPs.^[49] This is in agreement with density functional theory (DFT) calculations showing that the fcc and hexagonal lattices are both stable configurations of WC in ultrasmall NPs.^[119] Unlike WC, monometallic TaC natively crystallizes in an fcc lattice.

The two metals within a bimetallic NP can exist in four main configurations: a random alloy, perfect intermetallic mixing, a core-shell configuration, or as a janus particle.^[139,150] The RME method is driven by the diffusion-limited co-hydrolysis of WIPO and TaIPO metal alkoxide precursors, which ensures good mixing of Ta and W within a single bimetallic carbide NP. These alloyed oxides can then be reduced and carburized at high temperatures. While the starting bimetallic oxides are likely random hydrated mixtures, the extent of mixing in the final carbide NPs is controlled by lattice mismatch between the two metals and the kinetics of solid state interdiffusion between the two

metals at the high carburization temperatures. The PXRDs in **Figure 5.2a** suggest that the resulting bimetallic carbide contains Ta moieties distributed throughout the W lattice rather than in a separate phase. **Figure 5.2a** shows that the NPs are single-phase and that the lattice parameter for the bimetallic $\beta\text{-Ta}_{0.3}\text{W}_{0.7}\text{C}$ NPs is larger than the monometallic $\beta\text{-WC}$ NPs. Specifically, using the peak positions for the (111) crystallographic plane, the lattice parameter for the 2 – 3 nm $\beta\text{-WC}$ NPs is calculated to be 4.12 Å while the lattice parameter for the 2 – 3 nm $\beta\text{-Ta}_{0.3}\text{W}_{0.7}\text{C}$ NPs is calculated to be 4.19 Å. We note that the native lattice parameter for bulk $\beta\text{-WC}$ is 4.24 Å (PDF 00-020-1316) and for bulk fcc TaC is 4.45 Å (PDF 00-035-0801). These data suggest that the NPs exhibit lattice compression relative to the bulk carbides while the bimetallic $\beta\text{-Ta}_{0.3}\text{W}_{0.7}\text{C}$ NPs exhibit tensile strain relative to the unmodified $\beta\text{-WC}$ NPs.

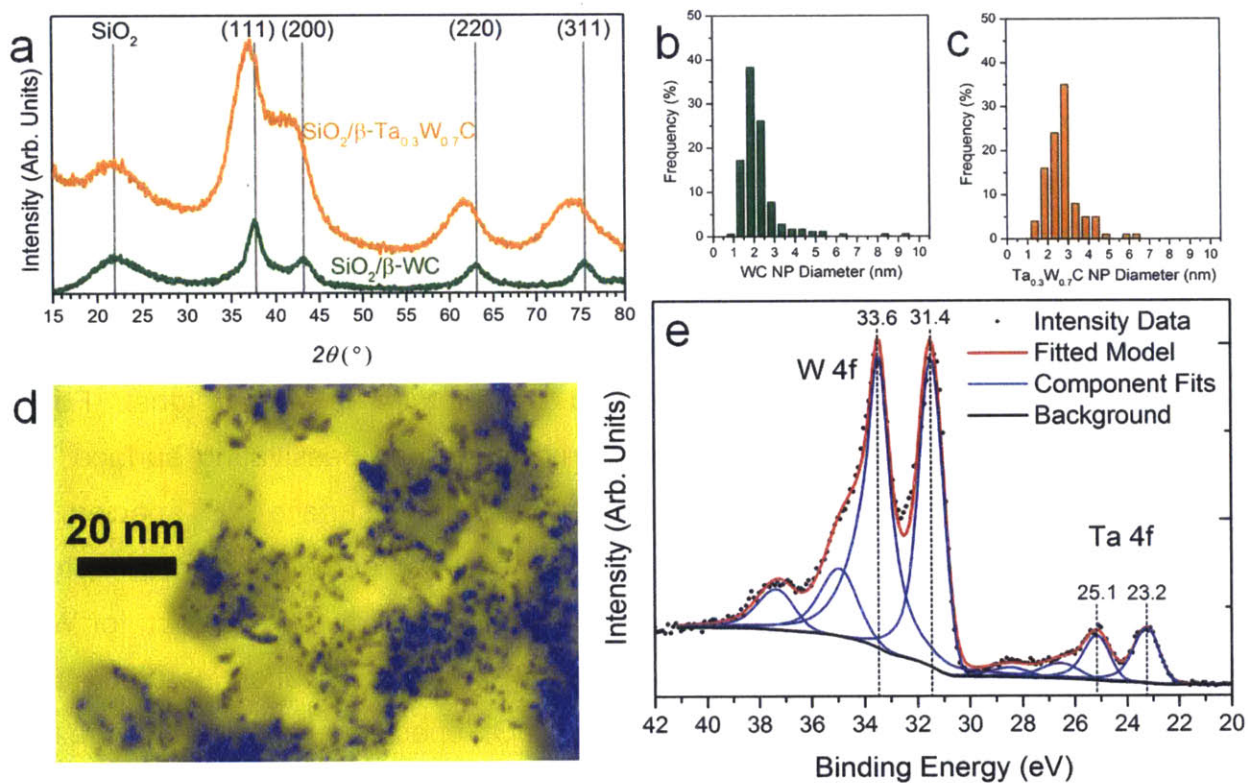


Figure 5.2. Materials Characterization of $\beta\text{-WC}$ and $\beta\text{-Ta}_{0.3}\text{W}_{0.7}\text{C}$ Nanoparticles. **(a)** shows the PXRD diffractograms of $\text{SiO}_2/\beta\text{-WC}$ and $\text{SiO}_2/\beta\text{-Ta}_{0.3}\text{W}_{0.7}\text{C}$. **(b)** shows the PSD for 2 – 3 nm $\beta\text{-WC}$ NPs supported on carbon black. **(c)** shows the PSD for 2 – 3 nm $\beta\text{-Ta}_{0.3}\text{W}_{0.7}\text{C}$ NPs supported on carbon black. **(d)** depicts a wide-view HAADF-STEM image of $\beta\text{-Ta}_{0.3}\text{W}_{0.7}\text{C}$ NPs supported on carbon black. **(e)** XPS of $\beta\text{-Ta}_{0.3}\text{W}_{0.7}\text{C}$ NPs supported on carbon black.

TEM images were used to obtain particle size distributions (PSDs) for the WC and Ta_{0.3}W_{0.7}C NPs by measuring the diameters of over 100 nanoparticles. The PSDs are shown in **Figure 5.2b** and c, respectively. Both PSDs are narrow with the majority of NPs in the 2 – 3 nm regime. The WC NPs had an average diameter of 2.2 ± 1.1 nm while the Ta_{0.3}W_{0.7}C NPs had an average diameter of 2.7 ± 0.8 nm. **Figure 5.2d** depicts a HAADF-STEM image of the Ta_{0.3}W_{0.7}C NPs dispersed on carbon black at ~40wt%.

XPS was used to examine the surface composition of the NPs as well as the extent of surface passivation with Ta_xW_{1-x}O_y species. **Figure 5.2e** shows the XPS spectrum of pre-reaction β-Ta_{0.3}W_{0.7}C/CB. Surface silica was undetectable (Si 2p signal not shown), indicating the dissolution procedure resulted in its complete removal. The W 4f_{7/2} and 4f_{5/2} peaks at 31.4 eV and 33.6 eV, respectively, correspond to reduced W while the higher binding energy peaks correspond to surface WO_x passivation species. The Ta 4f_{7/2} and 4f_{5/2} peaks at 23.2 eV and 25.1 eV, respectively, correspond to reduced carbidic Ta while the higher binding energy peaks correspond to surface TaO_x passivation species. Deconvolution and integration of the entire W 4f and Ta 4f signals (reduced and oxidized features) shows that the surface composition is 24% Ta and 76% W, in close agreement with the bulk composition determined by ICP-AES. XPS also allows the extent of surface passivation to be examined via peak deconvolutions. For this analysis, the area of the oxidation peaks for each signal was compared to the total area of that signal. For the Ta_{0.3}W_{0.7}C/CB catalyst, 34% of detectable Ta is present as passivating surface TaO_x species while 16% of detectable W is present as passivating surface WO_x species. The higher extent of oxidation of Ta in comparison to W is in agreement with recent studies on TaC foils where DFT shows a higher oxygen binding energy for TaC than for WC.^[43] Likewise, the synthesized TaC foils had substantial surface passivation features. It was suggested that the high stability of surface TaO_x species gives rise to the high electrochemical stability of TaC.

The total percentage of surface passivating oxide signal intensity, denoted as I_{ox}/I_{tot}, was determined by summing the intensities of the W 4f and Ta 4f oxidation signals (the unlabeled peaks in **Figure 5.2e** and dividing by the total intensities of the W 4f and Ta 4f signals. It was determined that 19% of the total detectable metal signal is present as surface passivating oxide moieties. While XPS is a surface-sensitive technique, in the

case of 2 – 3 nm NPs, the detectable signal results from both the surface and bulk of the NP. Assuming the NPs are 2.5 nm face center-cubic cubo-octahedrons, then approximately 33% of atoms reside in the top monolayer of the NP. Therefore, if both the surface and bulk metal atoms in the 2 – 3 nm NPs contributed equally to the detectable XPS signal, then a value of approximately 33% for $I_{\text{Ox}}/I_{\text{tot}}$ would correspond to a complete monolayer coverage of passivating metal oxides. In reality, the signal from the bulk metal atoms is screened by the surface atoms, thereby contributing less to the detectable XPS signal.^[151] In this case, a complete monolayer coverage of passivating surface metal oxides would correspond to an $I_{\text{Ox}}/I_{\text{tot}}$ value that is greater than 33%. Therefore, an $I_{\text{Ox}}/I_{\text{tot}}$ value of 19% for the 2 – 3 nm $\beta\text{-Ta}_{0.3}\text{W}_{0.7}\text{C}$ NPs corresponds to sub-monolayer coverage of surface passivating oxide moieties.

4. Characterization of $\text{Ta}_x\text{W}_{1-x}\text{C}$ NPs using X-ray Absorption Spectroscopy (XAS)

XAS was used to probe the local electronic structure and coordination environment within the NPs. This technique has been especially useful to determine the size and structure of ultrasmall bimetallic NPs, but has not been applied to the study of ultrasmall WC NPs.^[152] This study presents the first XAS analysis of monometallic and heterometallic W-based TMC NPs. **Figure 5.3** depicts the Ta L_3 -edge X-ray Absorption Near-Edge Structure (XANES) spectra for the bimetallic carbide NPs as well as for micron-sized powders of metallic Ta and TaC standards. Extended X-ray Absorption Fine Structure (EXAFS) was not collected for the Ta L_3 -edge due to the presence of the W L_3 -edge in the bimetallic NPs. **Figure 5.4a** and **b** show the XANES spectra for the W L_3 -edge while **Figure 5.4c** and **d** show the k^2 -weighted EXAFS analysis of the materials in R -space. Because WC NPs have not been studied using XAS techniques, a variety of bulk micron-sized powders were used as references, including metallic W, $\alpha\text{-WC}$, WO_2 , and WO_3 . We note that WO_3 is not stable under synchrotron radiation and undergoes partial reduction during analysis.^[153] Therefore, WO_3 is reported as WO_{3-x} in **Figure 5.4**. A commercial bulk W_2C powder was also analyzed, but analysis of its PXRD diffractogram indicates that this

material is actually a composite of α -WC and W_2C (diffractogram not shown). It is therefore labeled as W_2C -WC in **Figure 5.4** and is included only as a qualitative reference.

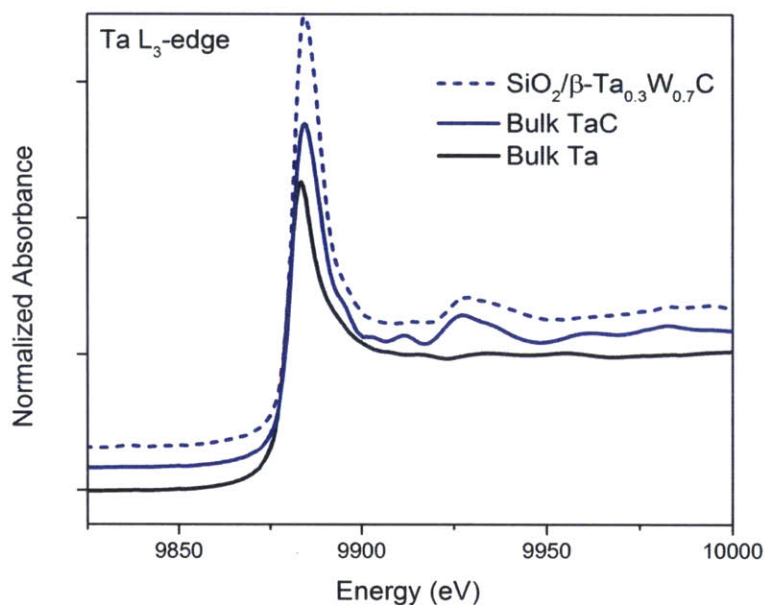


Figure 5.3. XANES spectra of the Ta L₃ edge for SiO₂/β-Ta_{0.3}W_{0.7}C NPs compared to the XANES spectra for bulk micron-sized TaC and Ta powder references.

Edge shifts were determined from the maximum in the first derivative of the XANES spectra. Analysis of the Ta L₃-edge in **Figure 5.3** and the W L₃-edge in **Figure 5.4a** shows the edge shifts to higher energy for increasing oxidation state. Relative to metallic Ta in **Figure 5.3**, both the bulk TaC standard and the SiO₂/β-Ta_{0.3}W_{0.7}C NPs had edge shifts of +1.5 eV, indicative of a +4 oxidation state. Relative to metallic W in **Figure 5.4a**, both α -WC and WO₂ exhibited an edge shift of +1.5 eV, indicative of a +4 oxidation state. WO_{3-x} has the highest oxidation state and therefore had the highest edge shift of +3 eV. The bulk W₂C-WC powder had an edge shift of only +0.5 eV. We observed that both SiO₂/β-WC and SiO₂/β-Ta_{0.3}W_{0.7}C had W L₃-edge shifts of +1.5 eV, indicating that their oxidation states are similar to α -WC.

The “white line” is the intense absorption peak at the top of the edge in the XAS spectra of **Figure 5.3** and **Figure 5.4a**. The intensity of the white line is indicative of the electronic density of unoccupied d states.^[154] As shown in **Figure 5.4a**, the white line intensity for the tungsten-based reference powders increases with increasing oxidation

state, indicative of charge transfer from tungsten to the nonmetal ligands. The following trends were observed in order of decreasing white line intensity: $\text{SiO}_2/\beta\text{-WC}$ NPs > $\text{SiO}_2/\beta\text{-Ta}_{0.3}\text{W}_{0.7}\text{C}$ NPs > WO_{3-x} > $\alpha\text{-WC}$ > WO_2 > $\text{W}_2\text{C-WC}$ > W . The data show that the β NPs are more electronically similar to hexagonal $\alpha\text{-WC}$ than $\text{W}_2\text{C-WC}$ while also showing an increased density of unoccupied d states for the ultrasmall NPs relative to bulk metal carbides or bulk metal oxides. An increased white line intensity is also observed for the Ta L_3 edge of $\beta\text{-Ta}_{0.3}\text{W}_{0.7}\text{C}$ NPs vs. bulk TaC in **Figure 5.3**.

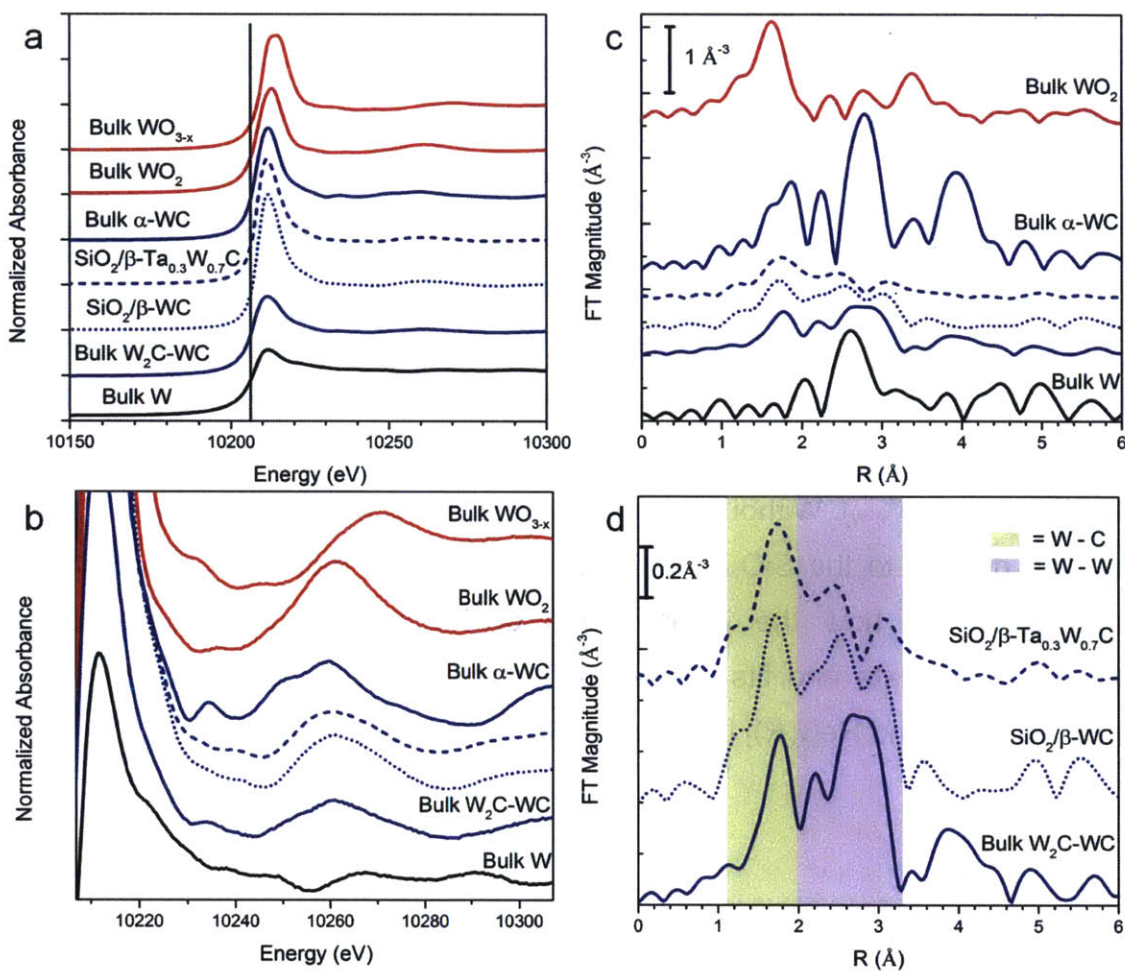


Figure 5.4. W L_3 edge XANES and k^2 -weighted Fourier transform magnitudes of the EXAFS spectra for $\text{SiO}_2/\beta\text{-WC}$ nanoparticles and $\text{SiO}_2/\text{Ta}_{0.3}\text{W}_{0.7}\text{C}$ nanoparticles in comparison with micron-sized powder references for bulk W , W_2C , $\alpha\text{-WC}$, WO_2 , and WO_{3-x} . (a) Normalized XANES spectra. (b) Magnified plot of the normalized XANES spectra. (c) k^2 -weighted Fourier transform magnitudes of the EXAFS spectra. (d) Magnified plot of the k^2 -weighted Fourier transform magnitudes of the EXAFS spectra.

Differences in the lattice environment were further investigated using the k^2 -weighted EXAFS analysis of the materials in R -space for the W L_3 -edge, shown in **Figure 5.4c** and **d**. We note the α -WC spectrum in **Figure 5.4c** agrees closely with that reported in literature.^[153] With the exception of the mixed-phase bulk W_2C -WC, the bulk reference powders had larger Fourier transform (FT) magnitudes arising from larger amplitude oscillations in k^2 space when compared to the two NP carbide materials. This is consistent with previous literature comparing bulk metallic W with W NPs.^[155]

To determine the local coordination environment within the carbide NPs, the EXAFS spectra in **Figure 5.4c** and **d** were curve-fit to theoretical standards using IFEFFIT.^[156,157] Details of the fitting methodology as well as all $k^2\chi(k)$ and $\text{Re}[\chi(R)]$ plots are provided below. Briefly, multishell fits were performed on the bulk WO_2 , bulk W, and bulk α -WC reference powders, with the tabulated results provided in **Table 5.2**. The data and fits are presented as $k^2\chi(k)$ and $\text{Re}[\chi(R)]$ in **Figure 5.5** to **Figure 5.7**. The fitting results from the α -WC standard were used to constrain the amplitude reduction factor (S_0^2) and the energy threshold correction (ΔE_0) in the NP fits. A multishell fit using the first 36 scattering paths of β -WC was performed on the SiO_2/β -WC NP EXAFS data to obtain first shell coordination numbers (N_W , N_C), bond lengths (r_{W-C} , r_{W-W}), and the variances in the bond lengths (σ_{W-C}^2 , σ_{W-W}^2). Without any alteration, the model for the SiO_2/β -WC NPs was then applied directly to the SiO_2/β - $Ta_{0.3}W_{0.7}C$ NPs EXAFS data over an appropriate k -range to determine how the incorporation of Ta affected the local coordination environment. The data and fits for the monometallic and bimetallic carbide NPs are presented as $k^2\chi(k)$ and $\text{Re}[\chi(R)]$ in **Figure 5.8** and **Figure 5.9**, respectively.

Table 5.1. Coordination numbers (N_C , N_W), bond lengths (r_{W-C} , r_{W-W}), and bond length variances (σ_{W-C}^2 , σ_{W-W}^2) of 20wt% SiO₂/ β -WC and 20wt% SiO₂/ β -Ta_{0.3}W_{0.7}C NPs determined from EXAFS experiments

	β -WC NPs	β -Ta _{0.3} W _{0.7} C NPs
k -range (\AA^{-1})	3.3 – 11.8	3.3 – 10.8
R -range (\AA)	1 – 4	1 – 4
Paths	36	36
Independent Pts.	15.8	14.1
Parameters	7	7
R-factor of Fit	0.005	0.013
S_0^2 (fixed)	0.83	0.83
ΔE_0 (eV, fixed)	7.7	7.7
N_C	4.2 ± 0.6	3.8 ± 0.6
N_W	8.8 ± 1.0	8.7 ± 2.2
r_{W-C} (\AA)	2.12 ± 0.00	2.13 ± 0.00
r_{W-W} (\AA)	2.95 ± 0.00	2.97 ± 0.01
σ_{W-C}^2 (first shell)	$0.0067 \pm .0020$	$0.0068 \pm .0025$
σ_{W-W}^2 (first shell)	$0.0080 \pm .0009$	$0.0148 \pm .0029$
σ^2 (other paths)	$0.0193 \pm .0041$	$0.0186 \pm .0049$

Table 5.1 summarizes the coordination numbers, bond lengths, and bond length variances obtained from the EXAFS experiments. In bulk β -WC, the first shell W-C and W-W coordination numbers are 6 and 12, respectively. In ultrasmall NPs, termination effects resulting from surface atoms cause the average bulk coordination numbers to decrease.^[158] Within the statistical uncertainty in the EXAFS fits, both the monometallic and bimetallic formulations were determined to have an average W-C coordination number of 4, and an average W-W coordination number of 9. These decreases in bulk average coordination numbers are consistent with NPs in the 2 – 3 nm regime.^[159] The equivalent reduction in coordination numbers between the two carbide NPs is consistent with the similar TEM PSDs in **Figure 5.2b** and c. In bulk β -WC, the first shell bond lengths are 2.12 \AA for r_{W-C} and 3.00 \AA for r_{W-W} . In agreement with the PXRD data in **Figure 5.2a**, both NP formulations are compressed relative to bulk β -WC while the incorporation of Ta

expands the NP lattice. This effect is evidenced by the decrease in r_{W-W} to 2.95 Å for the β -WC NPs and the increase to 2.97 Å for the β -Ta_{0.3}W_{0.7}C NPs in the EXAFS fits in **Table 5.1**. The lattice compression had little effect on the first shell W-C bond length, r_{W-C} , which is nearly identical to the bulk W-C bond length in both NP formulations. Similarly, the disorder parameter in the first shell W-C bond length, σ^2_{W-C} , was the same for both the monometallic and bimetallic carbide NPs. However, the addition of 30% Ta into the β -WC lattice greatly increased the disorder parameter in the first shell W-metal bond length, σ^2_{W-W} , which showed a statistically significant 85% increase. This large increase in lattice disorder signifies that the bimetallic β -Ta_{0.3}W_{0.7}C NPs are well-mixed random alloys.

Details on EXAFS Curve-Fitting to Theoretical Standards

All materials were modeled using their naturally occurring space groups (P 2₁/c for WO₂, Im-3m for W, P-6m2 for α -WC, and Fm-3m for β -WC). We report that P-6m2 is the correct space group for α -WC and not P6₃/m as has been reported in a previous EXAFS study of WC.^[153] All EXAFS spectra were fitted using multiple k -weights of 1, 2, and 3 and a Hanning k -window. The k -range used for fitting was chosen at nodes in the $k^2\chi(k)$ spectra for mathematical convenience. A k -range below 3 Å⁻¹ was not considered due to high sensitivity to the background subtraction, sensitivity to E_0 , and sensitivity to the assumption that S_0^2 is independent of k . The maximum in the k -range was chosen based on the quality of the $k^2\chi(k)$ spectra at high k .

Table 5.2. Bulk Reference Powder EXAFS Fits

	Bulk WO₂ powder	Bulk W powder	Bulk α-WC powder
k-range (Å⁻¹)	3.3 – 11.8	3.8 – 14.8	3.1 – 14.3
R-range (Å)	1 – 4	1 – 5.4	1 – 5
Paths	256	25	115
Independent Points	15.9	30.3	28.1
Parameters	5	5	5
S_0^2	0.65 ± 0.07	0.44 ± 0.03	0.83 ± 0.04
ΔE_0 (eV)	12.3 ± 1.0	8.5 ± 0.6	7.7 ± 0.4
Δr (Å)	0.005 ± 0.008	-0.007 ± 0.002	0.000 ± 0.002
σ^2 (first shell)	0.0006 ± 0.0010	0.0019 ± 0.0003	0.0040 ± 0.0009
σ^2 (other paths)	0.0065 ± 0.0050	0.0029 ± 0.0003	0.0020 ± 0.0001
R-factor of Fit	0.016	0.007	0.004

As shown in **Table 5.2**, bulk WO_2 , W, and α -WC were fit with 5 parameters. The addition of a separate σ for multiscattering paths improved the R-factor of the fits in all cases. However, using the Hamilton test, the improvement in the R-factors were too small to statistically justify inclusion of this sixth parameter in the final fits.^[157] All paths with an R_{eff} up to 6 Å were used in the fits for the standard reference powders. There are more than 256 paths with an R_{eff} below 6 Å for WO_2 , but for tractability, only the first 256 paths were included. Both metallic W and α -WC have exactly 25 and 115 scattering paths with an R_{eff} up to 6 Å, all of which were included in the models. In the fit of bulk WO_2 powder, σ^2 (first shell) corresponds to the first 6 nearest-neighbor O atoms as well as the first two nearest-neighbor W atoms. In the fit of bulk W powder, σ^2 (first shell) corresponds to the 8 nearest-neighbor W atoms. In the fit of bulk α -WC powder, σ^2 (first shell) corresponds to the 6 nearest-neighbor C atoms. The resulting fitted parameters for WO_2 , W, and α -WC agree with previous literature.^[153]

In the modeling of the NPs, N_w was used for the first shell W-metal coordination number, and N_c was used for the first shell W-C coordination number. All subsequent single and multishell paths were parameterized with linear combinations of these first shell coordination numbers. The addition of first shell oxide paths including a σ^2 , N_o , and Δr for these paths improved the fits at low R. However, the additional improvement in the R-factor was too small to justify the inclusion of these extra three parameters in the final fit based on the Hamilton test. Furthermore, the small useable k-ranges of the NPs resulted in large error bars in the fitted oxide parameters due to the small number of independent points. We note that the quality of each EXAFS fit reported, including those for the β -WC and β - $\text{Ta}_{0.3}\text{W}_{0.7}\text{C}$ NPs were insensitive to moderate changes in the k-window, R-window, and method of background subtraction.

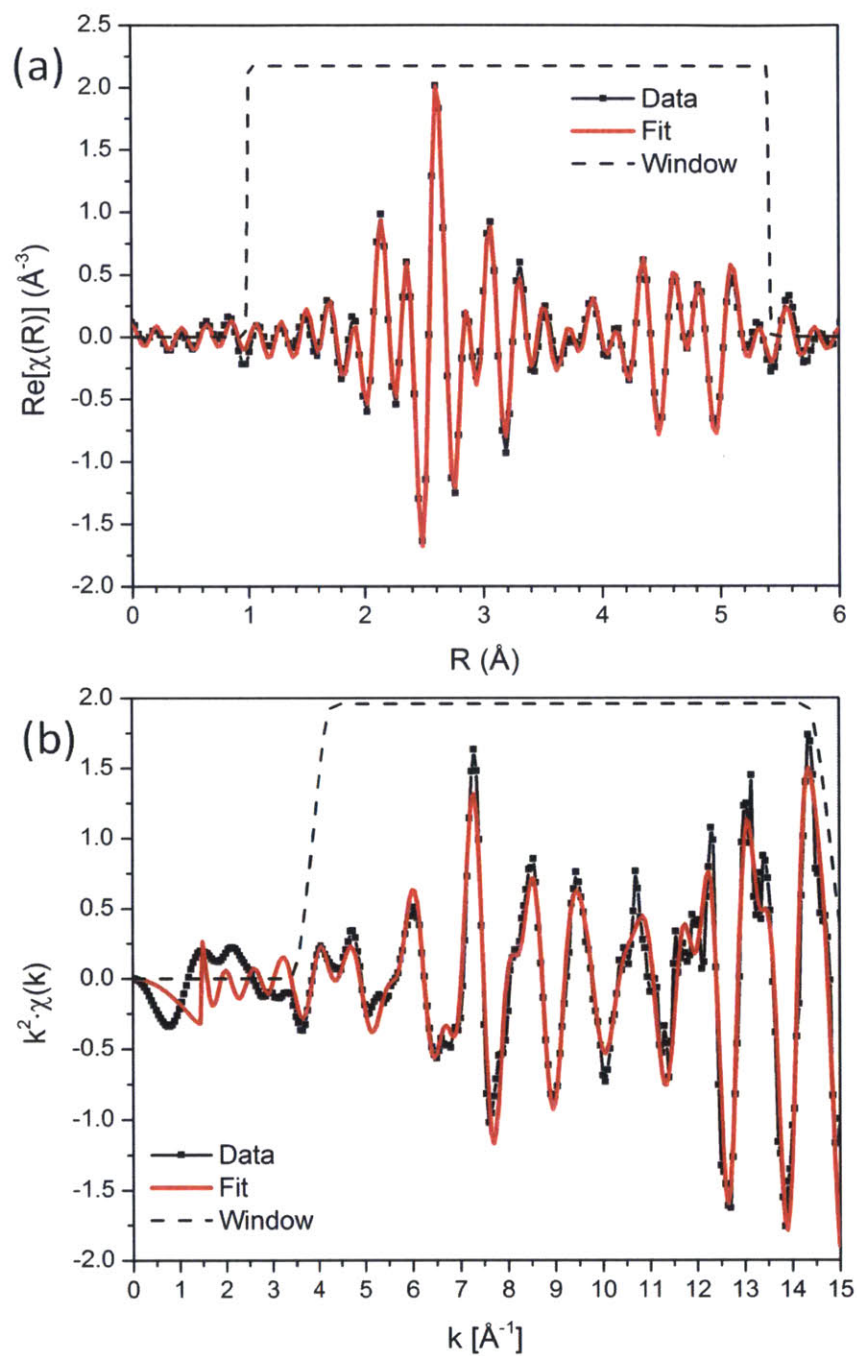


Figure 5.5. EXAFS data (black) and curve fits to theoretical standards (red) plotted in (a) $\text{Re}[\chi(R)]$ and (b) $k^2\chi(k)$ space for the bulk W powder reference material.

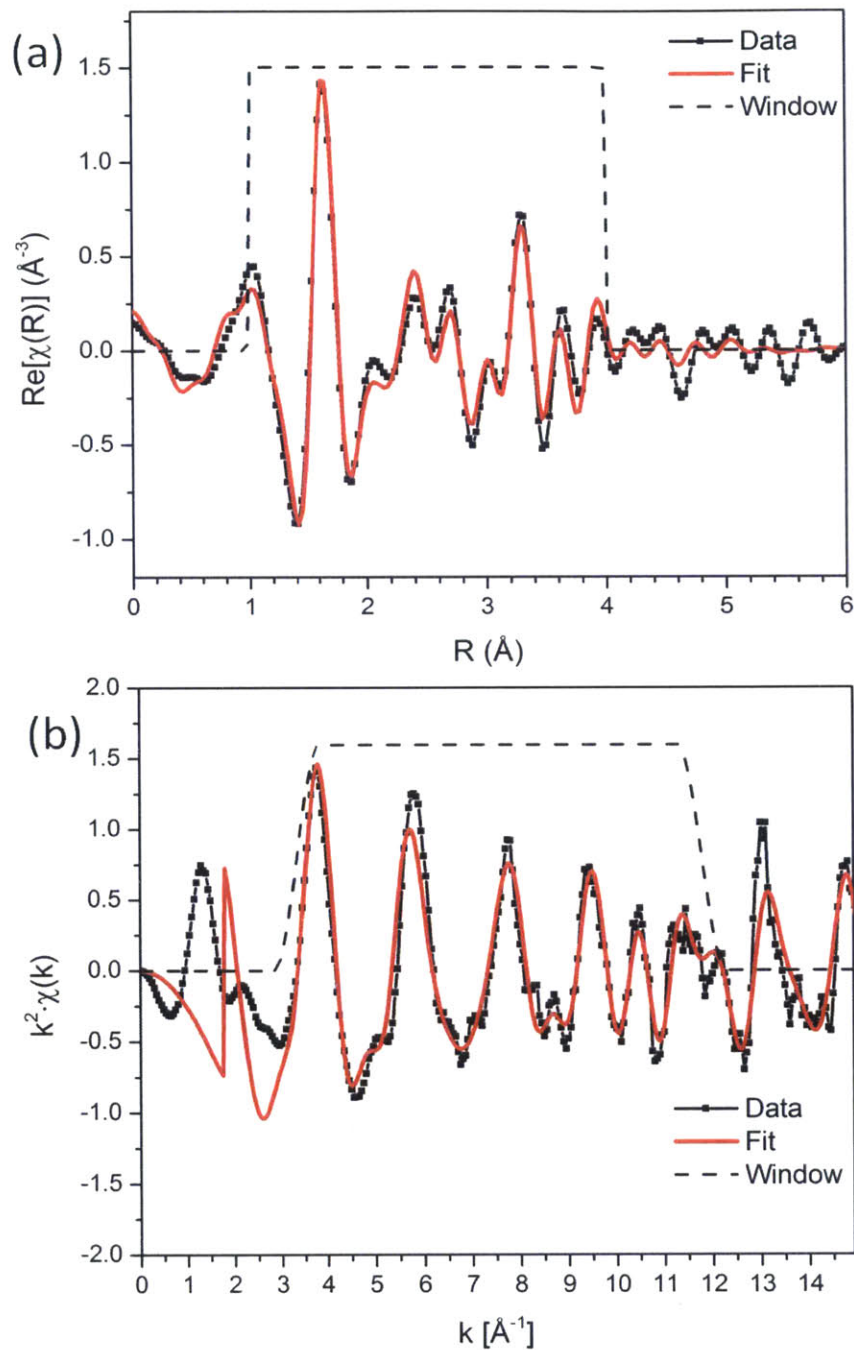


Figure 5.6. EXAFS data (black) and curve fits to theoretical standards (red) plotted in (a) $\text{Re}[\chi(R)]$ and (b) $k^2\chi(k)$ space for the bulk WO_2 powder reference material.

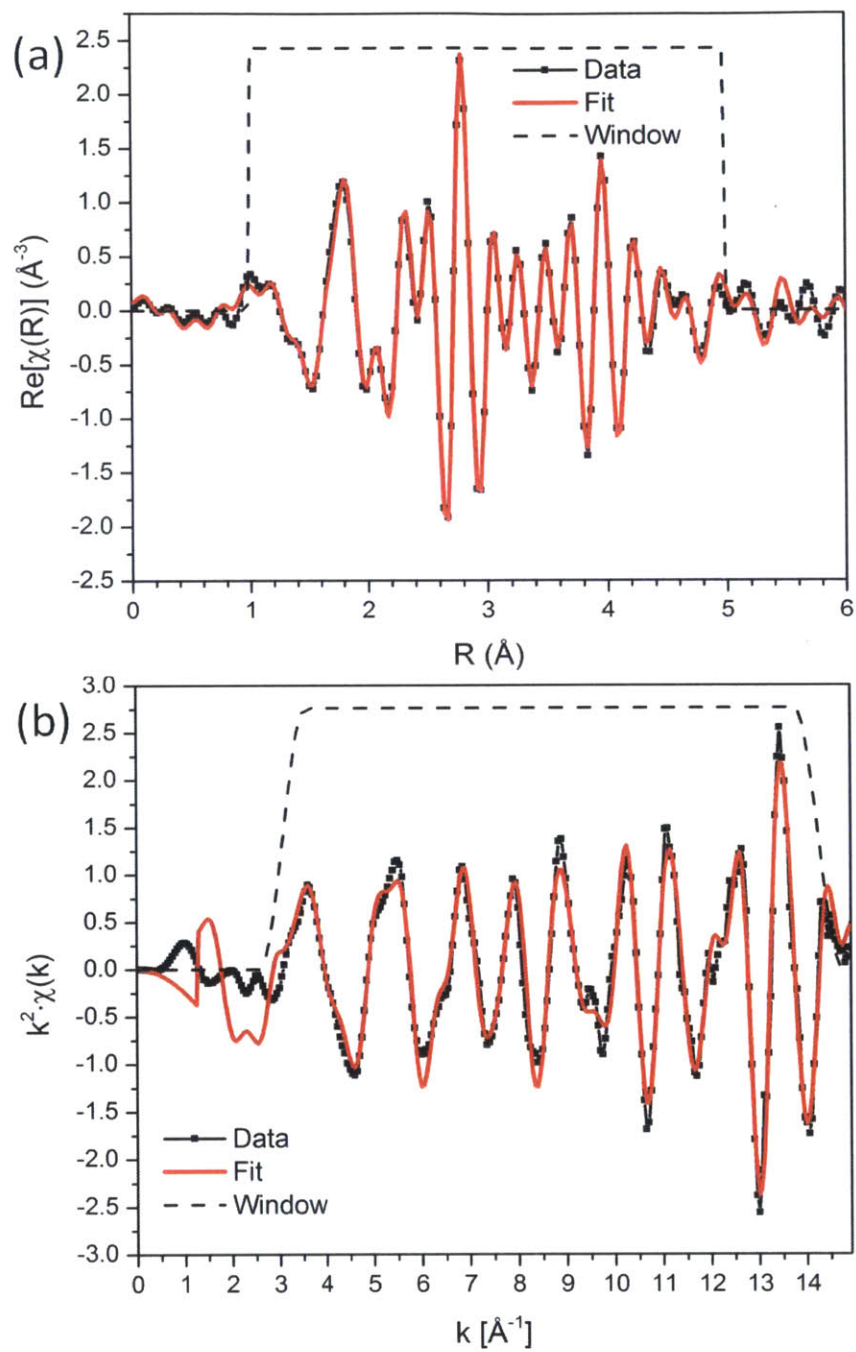


Figure 5.7. EXAFS data (black) and curve fits to theoretical standards (red) plotted in (a) $\text{Re}[\chi(R)]$ and (b) $k^2\chi(k)$ space for the bulk α -WC powder reference material.

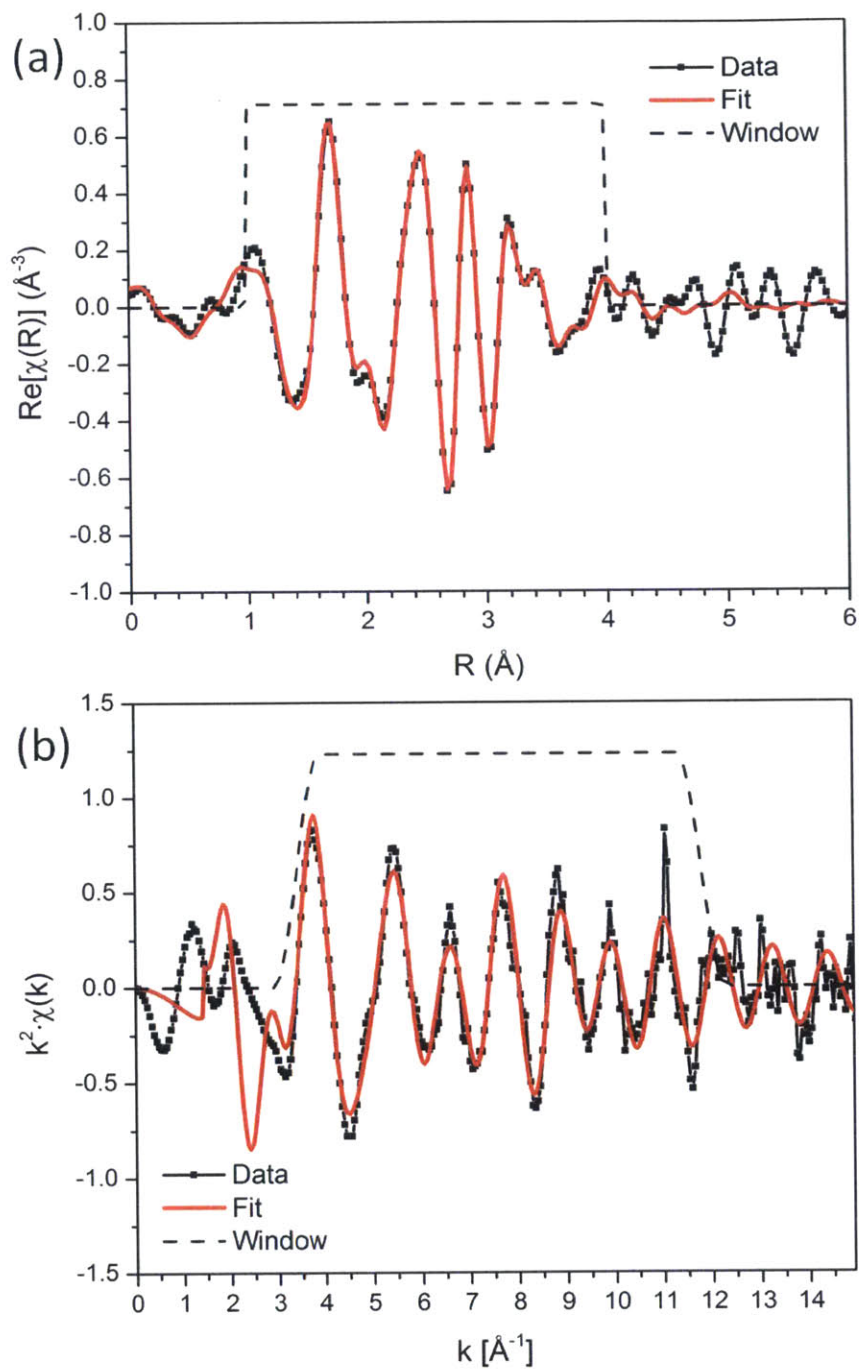


Figure 5.8. EXAFS data (black) and curve fits to theoretical standards (red) plotted in (a) $\text{Re}[\chi(R)]$ and (b) $k^2\chi(k)$ space for the 2 – 3 nm β -WC NPs.

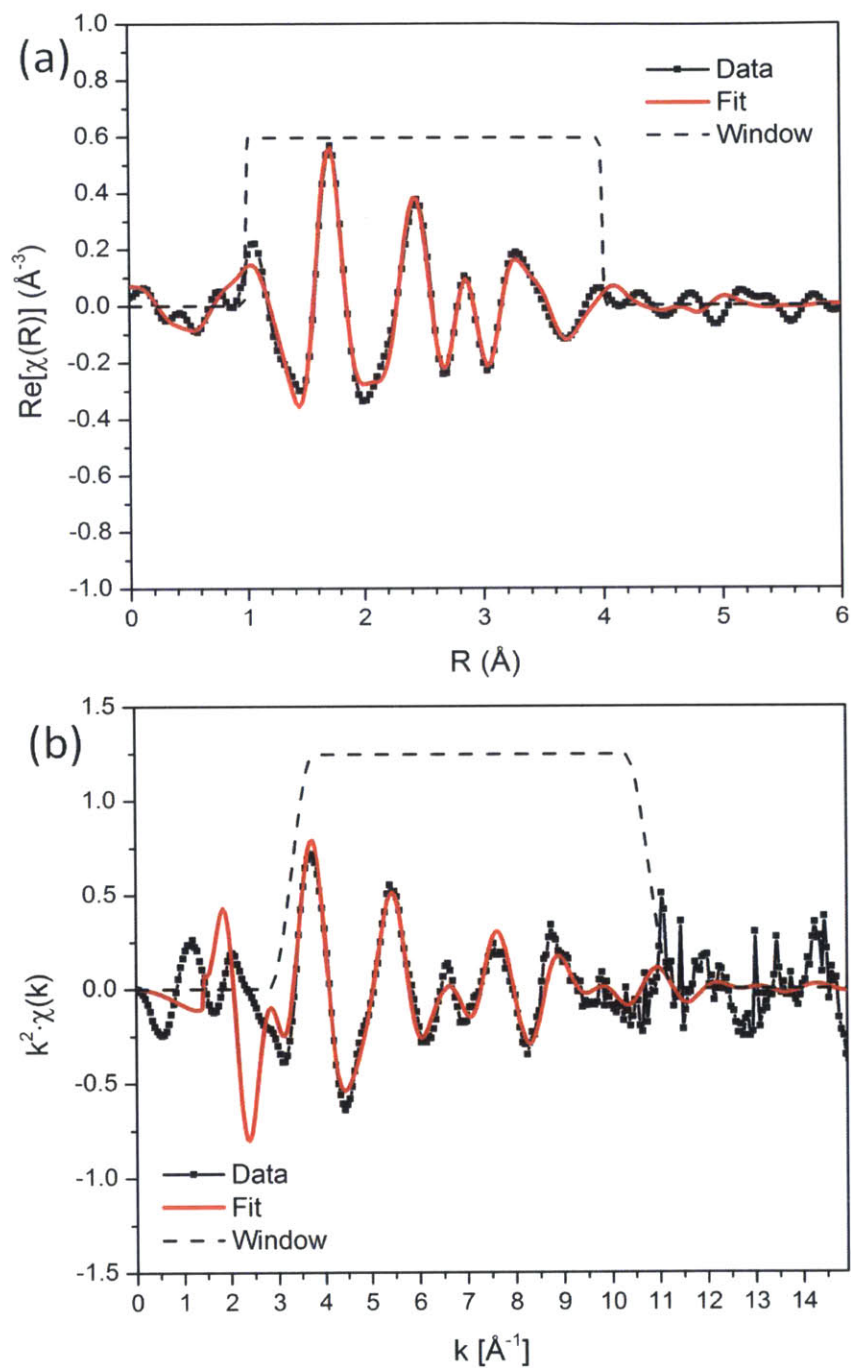


Figure 5.9. EXAFS data (black) and curve fits to theoretical standards (red) plotted in (a) $\text{Re}[\chi(R)]$ and (b) $k^2\chi(k)$ space for the 2 – 3 nm $\beta\text{-Ta}_{0.3}\text{W}_{0.7}\text{C}$ NPs.

5. HER Activity and Electrochemical Stability of Ta_{0.3}W_{0.7}C

The HER electrochemical activity of the β -Ta_{0.3}W_{0.7}C NPs was compared to that of the monometallic β -WC NPs in a H₂-saturated 0.5 M H₂SO₄ solution at room temperature using Linear Sweep Voltammetry (LSV). **Figure 5.10a** shows that the HER activity of β -Ta_{0.3}W_{0.7}C/CB is comparable to that of β -WC/CB with both materials exhibiting onset potentials of ca. 100 mV vs. RHE. Empty Vulcan® XC-72r is shown for comparison. **Figure 5.10b** shows a Tafel analysis of the LSV data in **Figure 5.10a**, yielding Tafel slopes of 60 mV dec⁻¹ and 72 mV dec⁻¹ for β -WC/CB and β -Ta_{0.3}W_{0.7}C/CB, respectively, which are lower than for other nanoscale WC-based materials reported in the literature.^[35,160] Using chronopotentiometry (CP), the overpotential required to drive 1 mA cm⁻² of hydrogen evolution was 166 mV for the carbon-supported β -Ta_{0.3}W_{0.7}C NPs, which is comparable to that of obtained for carbon-supported α -WC NPs.^[49] At an overpotential of 166 mV, the specific activity of the supported β -Ta_{0.3}W_{0.7}C NPs was 3.7 mA mg⁻¹. Based on the EXAFS and TEM analysis of the average NP size, we estimated the turnover frequency (TOF) as 1.4 mol H₂ (mol surface metal)⁻¹ min⁻¹. We note that this mass-activity is similar to that reported for the state-of-the-art carbon nanotube-supported Mo₂C NPs despite the significantly higher molecular weight of Ta_{0.3}W_{0.7}C.^[132]

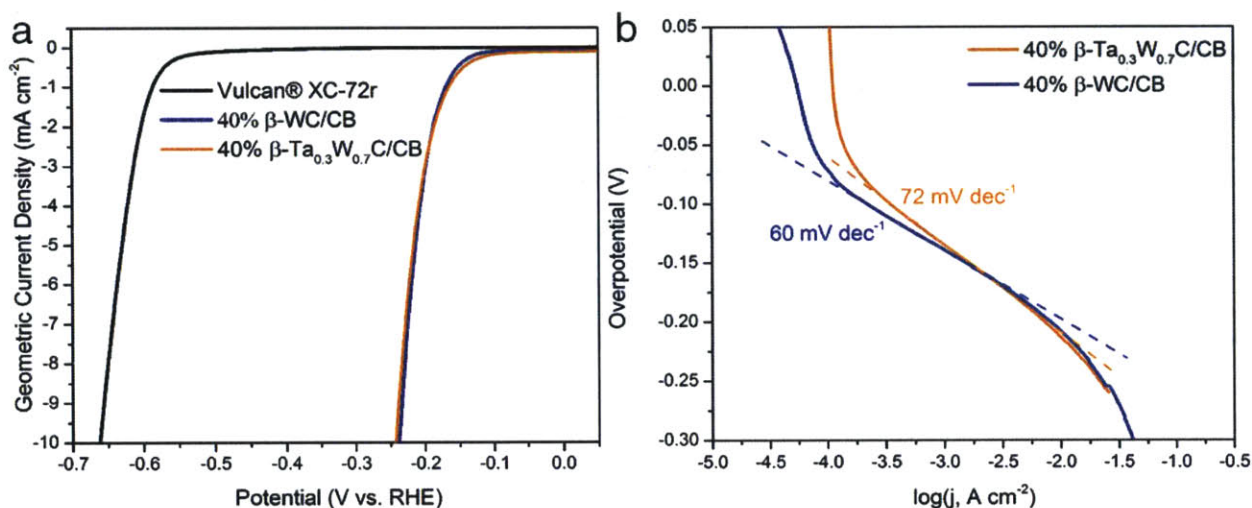


Figure 5.10. (a) LSVs of 40wt% β -WC/CB, 40wt% β -Ta_{0.3}W_{0.7}C/CB, and Vulcan® XC-72r at 2mV/s in 0.5 M H₂SO₄ at room temperature. (b) Tafel plot showing the Tafel slopes.

Monometallic TaC has been shown to be a poor HER electrocatalyst with an onset potential for HER measured to be 250 mV higher than the onset potential for HER on WC.^[149] We attribute the high HER activity of β -Ta_{0.3}W_{0.7}C/CB to strain effects arising from the highly compressed lattice in which the Ta atoms are situated. While bulk TaC has a Ta-Ta bond length of 3.15 Å, the Ta atoms in the β -Ta_{0.3}W_{0.7}C lattice are well mixed with the W atoms and have an average bond length of 2.97 Å as shown in **Table 5.1**. This lattice compression increases d-band orbital overlap, broadening the d-band and decreasing the d-band center, which leads to a decrease in the hydrogen binding energy.^[23]

Beyond HER, TMCs have been proposed as supports for active monolayers of PGMs in a core-shell configuration or as co-catalysts with dispersed PGM NPs.^[32,33,35,48] In these applications, it is critical to increase the passivation resistance of TMCs under oxidizing potentials. Traditionally, the electrochemical stability of TMCs has been examined using chronopotentiometry (CP) where an anodic geometric current density of 0.1 mA cm⁻² is defined as the current of bulk oxidation for measurement convenience.^[41-43] Anodic current densities below 0.1 mA cm⁻² are then defined as passivation currents where only the surface metal sites are being oxidized. While this method is convenient for screening TMC stability ranges over large potential and pH ranges, it is not useful for examining the onset of passivation. To better understand the onset of passivation for β -WC and β -Ta_{0.3}W_{0.7}C NPs, we instead used linear sweep voltammetry (LSV). While this is a transient technique, a low scan rate of 2mV/s minimizes the contribution of capacitive effects arising from the changing electrochemical double layer. This allows a more accurate potential for the onset of surface passivation to be identified since electrochemical passivation is a faradaic surface reaction.

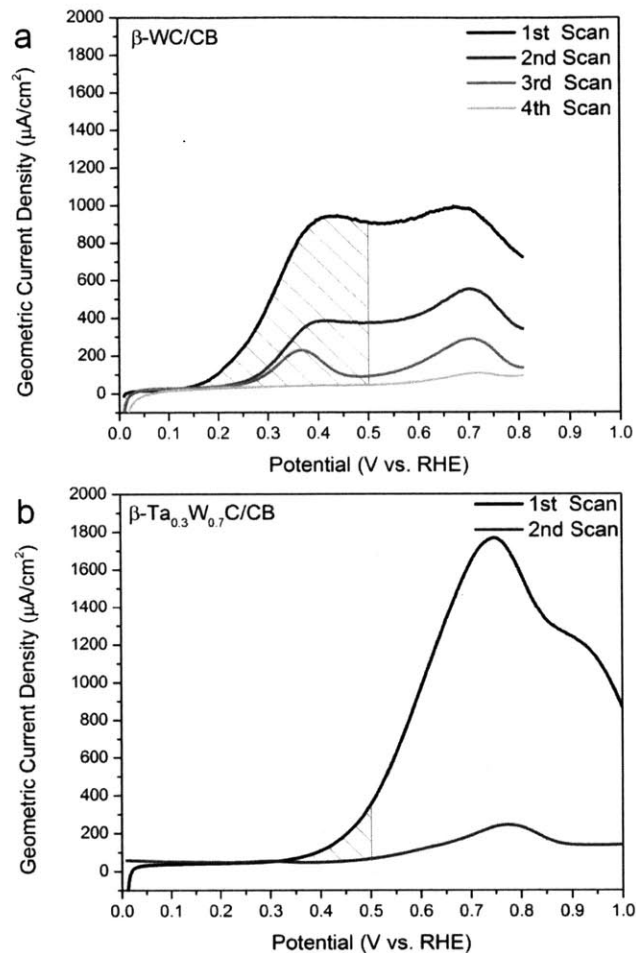


Figure 5.11. (a) LSV scans of 40wt% $\beta\text{-WC}/\text{CB}$ at 2mV/s in Ar-sat 0.5 M H_2SO_4 at room temperature (b) LSV scans of 40wt% $\beta\text{-Ta}_{0.3}\text{W}_{0.7}\text{C}/\text{CB}$ at 2mV/s in Ar-sat 0.5 M H_2SO_4 at room temperature. The hashed areas depict the integrations of the first scan from 0 to +0.5 V vs. RHE.

Figure 5.11 shows sequential LSV scans for $\beta\text{-WC}/\text{CB}$ and $\beta\text{-Ta}_{0.3}\text{W}_{0.7}\text{C}/\text{CB}$. The electrochemical stability of bulk WC crystallized in an fcc lattice has not been studied before, but interestingly, the NP formulation shown here (**Figure 5.11a**) exhibits two surface oxidation peaks at +0.4 V and +0.7 V vs. RHE with an onset of passivation beginning at ca. +0.2 V vs. RHE. We attribute these two passivation peaks to differing electrochemical stabilities between the two primary low index (111) and (200) crystal planes of $\beta\text{-WC}$. A similar phenomenon has been observed for Au where the onset of oxidation for Au (111) is +0.2 V more anodic than for Au (100) in 1 M HClO_4 .^[161] **Figure 5.11b** shows that the alloying of fcc WC with 30% Ta significantly alters the

electrochemical surface passivation behavior with an onset of passivation at ca. +0.45 V vs. RHE and a single peak at +0.75 V followed by a shoulder at +0.9 V vs. RHE. We hypothesize that this effect is due to the protecting surface TaO_x species identified from the XPS spectra in **Figure 5.2e** before electrochemical analysis.

The passivation LSV scans in **Figure 5.11a** and **b** were integrated to estimate the extent of electrochemical surface oxidation from the measured anodic current. The electrochemical oxidation processes for WC and TaC in acidic media are described by **Equation 5.1** and **Equation 5.2**, respectively.



Based on electrode loadings used, the complete electrochemical oxidation of WC to WO₃ requires a total of 1.48 C cm⁻², while the full conversion of Ta_{0.3}W_{0.7}C to its highest bulk oxide phase requires a total of 1.44 C cm⁻². Integrating the first LSV scans in **Figure 5.11a** and **b** up to 0.5 V shows that 0.1 C cm⁻² of passivation current is passed on the WC electrode, corresponding to 7% oxidation. However, only 0.01 C cm⁻² of passivation current is passed on the Ta_{0.3}W_{0.7}C electrode, corresponding to 0.7% oxidation. This is due to its significantly delayed onset potential for passivation. Detailed integration results are provided in **Table 5.3**.

By +0.8 V, 16% of the WC electrode is oxidized during the first scan while only 13% of the Ta_{0.3}W_{0.7}C is oxidized. Integrating all of the scans from 0 to +0.8 V for the WC electrode and from 0 to +1.0 V for the Ta_{0.3}W_{0.7}C electrode yields 26% oxidation for WC/CB and 23% for Ta_{0.3}W_{0.7}C /CB. This is consistent with complete surface passivation for 3 nm NPs, which theoretically requires ~25% of the total charge required for bulk oxidation to be passed for complete surface passivation to occur. These data, taken together with the drastically different onset potentials of passivation, show that β-Ta_{0.3}W_{0.7}C has an increased resistance towards oxidation when compared to β-WC.

Table 5.3. Integration Results for Electrochemical Stability Studies

0 to 0.8 V	Scan1	Scan 2	Scan 3	Scan 4	
WC/CB	0.23	0.10	0.04	0.01	C cm ⁻² of charge passed
	1.48	1.48	1.48	1.48	C cm ⁻² to fully oxidized
	15.7%	6.7%	2.8%	0.8%	% oxidized during scan
0 to 0.8 V	Scan1	Scan 2			
Ta _{0.3} W _{0.7} C/CB	0.19	0.03			C cm ⁻² of charge passed
	1.44	1.44			C cm ⁻² to fully oxidized
	13.3%	1.9%			% oxidized during scan
0 to 1.0 V	Scan 1	Scan 2			
Ta _{0.3} W _{0.7} C/CB	0.31	0.03			C cm ⁻² of charge passed
	1.44	1.44			C cm ⁻² to fully oxidized
	21.3%	1.9%			% oxidized during scan

6. Characterization of other Bimetallic Carbide and Nitride Nanoparticles

Figure 5.1 depicts the removable ceramic coating method for the synthesis of a single bimetallic carbide: Ta_xW_{1-x}C. However, one could just as easily co-hydrolyze any other combination of metal alkoxide species to arrive at a variety of bimetallic oxides. Furthermore, rather than simply carburize the silica-encapsulated oxides, they can be nitridized using a pure ammonia stream at 800 °C. A small survey of synthesis space is presented as **Figure 5.12** below

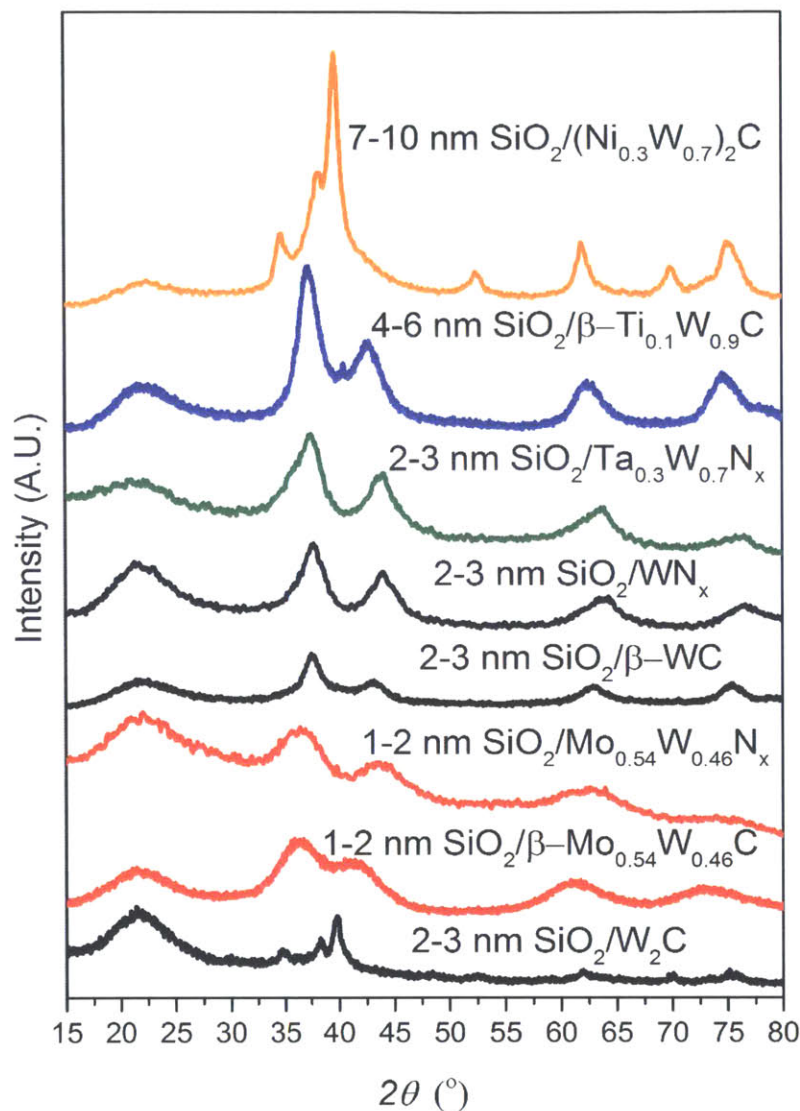


Figure 5.12. PXR D Study of Silica-Encapsulated Carbides and their Corresponding Nitrides

EXAFS can be used to examine local variations in lattice geometry as both particle size and heterometallic composition are varied. It was observed that long-range order decreases with increasing heterometal content and decreasing particle size. Both can be attributed to an increase in the bond length variance as captured by an increase in the Debye-Waller factor. The EXAFS studies versus particle size and heterometallic composition are shown in **Figure 5.13** to **Figure 5.15**.

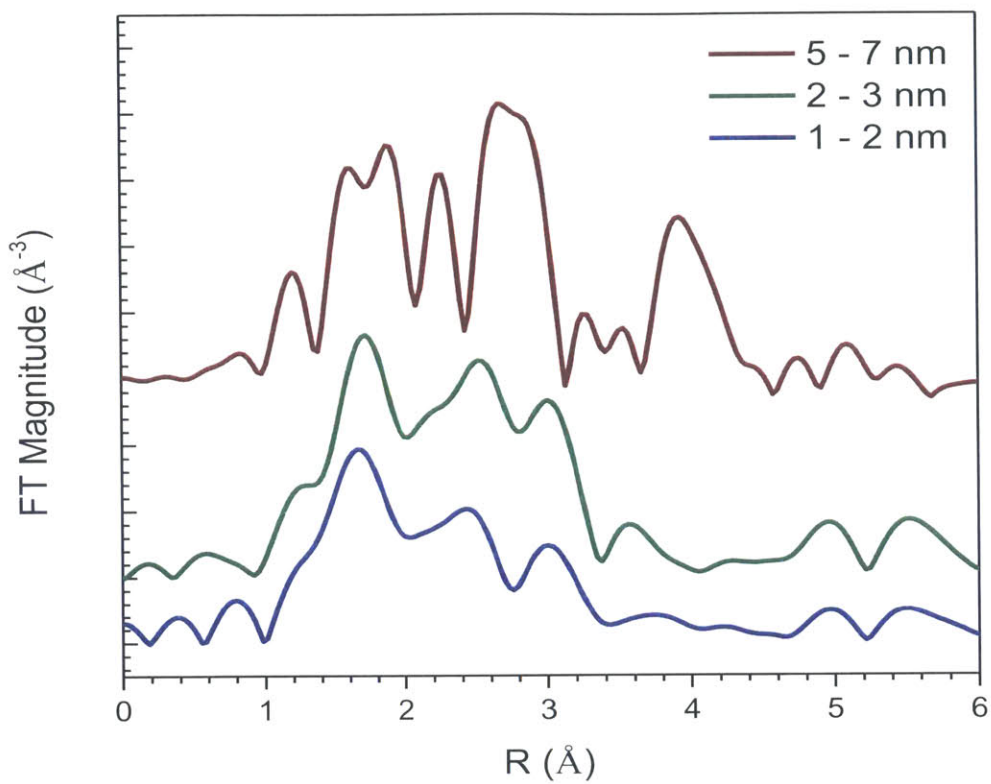


Figure 5.13. k^2 -weighted Fourier transform magnitudes of the EXAFS spectra as a function of WC particle size.

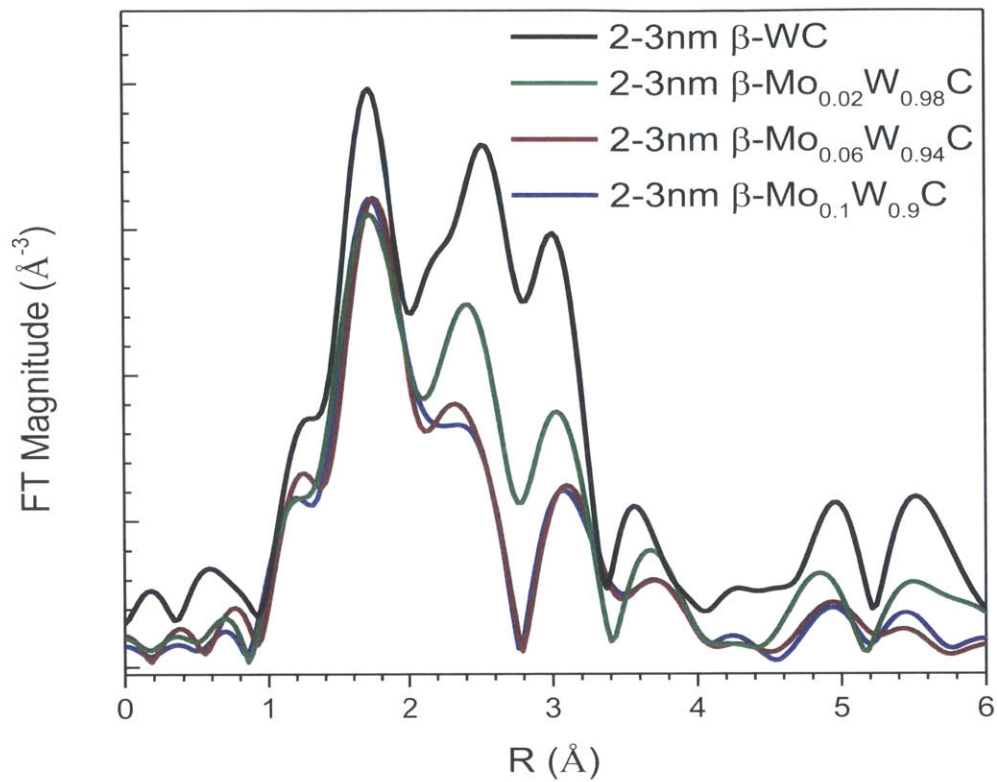


Figure 5.14. k^2 -weighted Fourier transform magnitudes of the EXAFS spectra as a function of increasing Mo content.

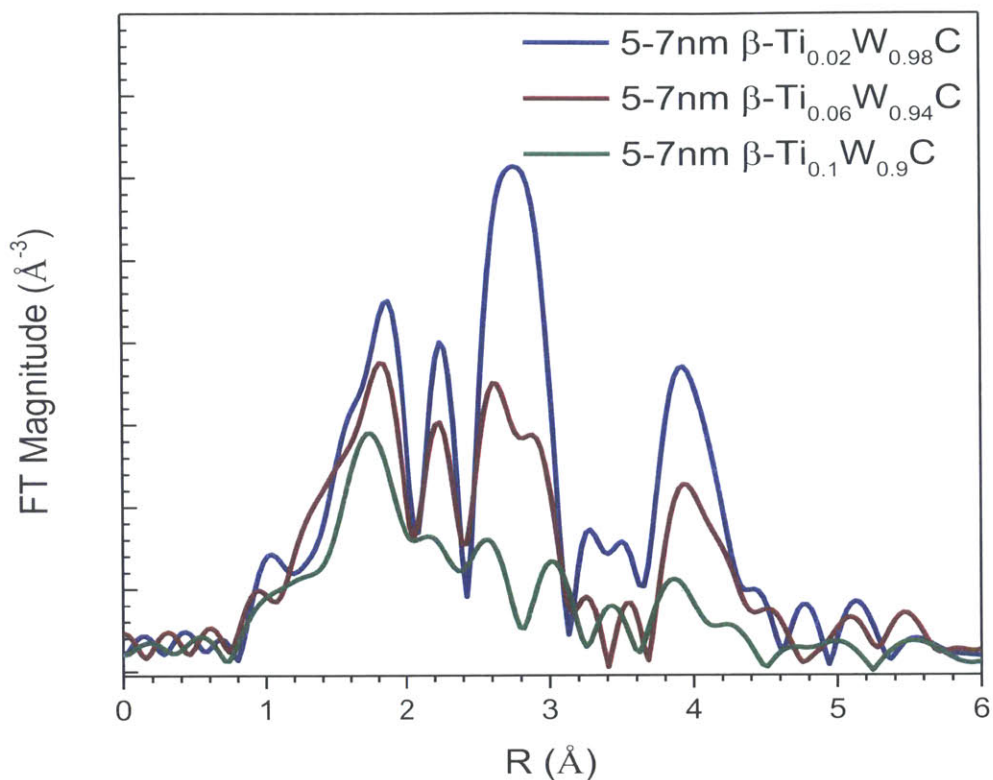


Figure 5.15. k^2 -weighted Fourier transform magnitudes of the EXAFS spectra as a function of increasing Ti content.

7. Conclusions

Just as bimetallic nanoparticles have opened new avenues for tuning the activity and stability of catalysts, bimetallic metal carbide nanoparticles are poised to make a similar impact in the development of better earth-abundant alternatives to noble metals. Unfortunately, the systematic investigation of these materials has been hindered by synthetic difficulties. In this chapter, it was shown that the removable ceramic coating method offers a viable method for exploring bimetallic metal carbide nanoparticle phase. The synthesis and advanced characterization of $Ta_xW_{1-x}C$ shows that the resulting bimetallic carbide nanoparticles will likely be random alloys as opposed to intermetallic ordered alloys. It was then shown that lattice compression in bimetallic $Ta_{0.3}W_{0.7}C$ nanoparticles enables high hydrogen evolution electrocatalytic activity to be achieved while simultaneously increasing oxidation resistance under anodic potentials. The relevance of this finding is made apparent in **Chapter 7** where bimetallic $Ti_{0.1}W_{0.9}C$ is

commonly used as a highly stable core for noble metal shells during hydrogen oxidation and methanol electrooxidation.

Acknowledgements

This work was sponsored by the Chemical Sciences, Geosciences and Biosciences Division, Office of Basic Energy Sciences, Office of Science, U.S. Department of Energy, grant no. DE-FG02-12ER16352. I thank the National Science Foundation for financial support through the National Science Foundation Graduate Research Fellowship under Grant No. 1122374. T.M.K. thanks CAPES for the PhD fellowship. The authors acknowledge LNLS, Campinas, Brazil and its staff for the access to the XDS beamline. C.B. Rodella, I.B. Aragão and E.M. Anderson assisted with the EXAFS measurements.

Chapter 6

Self-Assembly of Noble Metal Monolayers on Transition Metal Carbide Nanoparticle Catalysts

1. Introduction

Noble metal (NM) catalysts critically enable many existing and emerging technologies, such as catalytic converters,^[162] reforming,^[163] and fuel cells.^[164] However, their scarcity and high cost necessitate the development of catalytic systems with significantly reduced NM loadings, increased activity, and improved durability. In this respect, various nanostructured architectures have been investigated, including atomically-dispersed NM catalysts,^[165] hollow nanocages,^[67,68] alloyed nanoparticles,^[166,167] and core-shell structures.^[7,168,169] In particular, core-shell nanoparticles composed of an earth-abundant core coated with an atomically-thin NM shell are a promising platform that offers both design flexibility and reduced precious metal loadings.^[7,168,169] However, achieving independent control over the particle size, core composition, shell composition, and shell thickness poses a substantial challenge.^[7,168,169] For this reason, state-of-the-art synthetic methods are predominantly limited to a few earth-abundant metallic cores (e.g., Fe, Co, Ni, and Cu) that allow for more precise synthetic control; however, these metal cores form intrinsically metastable core-shell particles that restructure during heating^[11,170,171] or electrochemical cycling.^[172,173]

Early transition metal carbides (TMCs) are earth-abundant ceramics with ideal topochemical properties for supporting precious metal shells.^[31,174-176] First, TMCs exhibit metallic electrical conductivity, corrosion-resistance, and extremely high melting points.^[13] Second, precious metals tend to bind strongly to metal-terminated early TMC surfaces (**Figure 2.3**), but cannot readily form stable carbides.^[45] Thus, NMs should coat TMC surfaces, but should not alloy with the underlying core. In particular, tungsten carbide (WC) is inexpensive (**Figure 1.8**), exhibits a “platinum-like” density of electronic states,^[18,19] and its metal-terminated surface forms interfacial Pt-WC bonds that are ca. 90 kJ mol⁻¹ stronger than interfacial Pt-Pt bonds (**Figure 2.3**). While experimental studies on model

thin film systems have corroborated these attractive properties,^[31,48,177] synthetic efforts to date have not achieved TMC nanoparticles coated with NM monolayers.^[70,71] Until recently, TMC nanoparticles alone were difficult to engineer with controlled properties because their synthesis requires high temperatures (typically above 700 °C) followed by passivation with dilute oxygen.^[49] Without proper synthetic control, these conditions result in sintered TMC particles covered in both graphitic coke and an oxide surface layer. Such surface impurities preclude core-shell formation due to the unfavorable binding energies between precious metals and contaminated TMC surfaces (**Figure 2.3**).

Here, we present a high temperature self-assembly method to synthesize size-tunable TMC nanoparticles (<10 nm) coated with monometallic or heterometallic NM surface shells of controlled thicknesses ranging from sub-monolayer to multilayer coverages. In Chapter 7, we show that these core-shell materials achieve superior catalytic activity, improved stability, and reduced NM loadings compared to state-of-the-art commercial catalysts for electrochemical applications. Chapter 7 also shows these materials are sinter-resistant with the core-shell structure remaining stable at high temperatures under various atmospheres.

2. Results and Discussion

2.1 The High-Temperature Self-Assembly Process

Figure 6.1 shows aberration-corrected scanning transmission electron microscopy (STEM) images depicting the stages of the NM/TMC (shell/core) self-assembly process as a function of temperature using Pt/WC nanoparticle formation as a representative example. In the first step, WO_x nanoparticles are impregnated uniformly with a $(NH_4)_2PtCl_6$ salt and encapsulated in silica nanospheres using a room-temperature reverse microemulsion (RME) (**Figure 6.1A**). This method generated $SiO_2/(NH_4)_2PtCl_6/WO_x$ composites with precise control over the nanoparticle size and Pt loading. The Supporting Information provides comprehensive synthetic details.

The $SiO_2/(NH_4)_2PtCl_6/WO_x$ composites were then subjected to a temperature ramp under a 15% $CH_4/85\%$ H_2 gas flow (**Figure 6.1B to D**). At temperatures under 200 °C, H_2 permeates through the silica nanospheres,^[49] reducing the encapsulated Pt salt into Pt

nanoclusters over the WO_x domains (**Figure 6.1B** and **Figure S6.5**). By 600°C , the central WO_x nanoparticles undergo reduction, forming metallic mixtures of Pt and W that are trapped within the silica nanospheres (**Figure 6.1C**, **Figure S6.5**, and **Figure S6.6**). Near 900°C , these small metallic clusters sinter to form single central nanoparticles while carbon from methane decomposition intercalates into the W-rich domains, forming WC (**Figure 6.1D**). Since NMs are insoluble in TMC lattices, Pt phase-segregates from the WC domains and wets the central carbide core as an atomically-thin shell, resulting in the self-assembly of uniform core-shell nanoparticles—shown in **Figure 6.1E** by an energy-dispersive X-ray spectroscopy (EDX) map and linescan. The silica template is dissolved at room temperature, and the resulting nanoparticles can then be dispersed in solution with or without a capping agent (**Figure S6.7**) or dispersed onto a high surface area matrix (**Figure 6.1E** and **Figure S6.18**). The final Pt/WC particle size and Pt shell thickness is controlled by engineering the WO_x NP size and $(\text{NH}_4)_2\text{PtCl}_6$ loading in the RME prior to silica encapsulation and carburization.

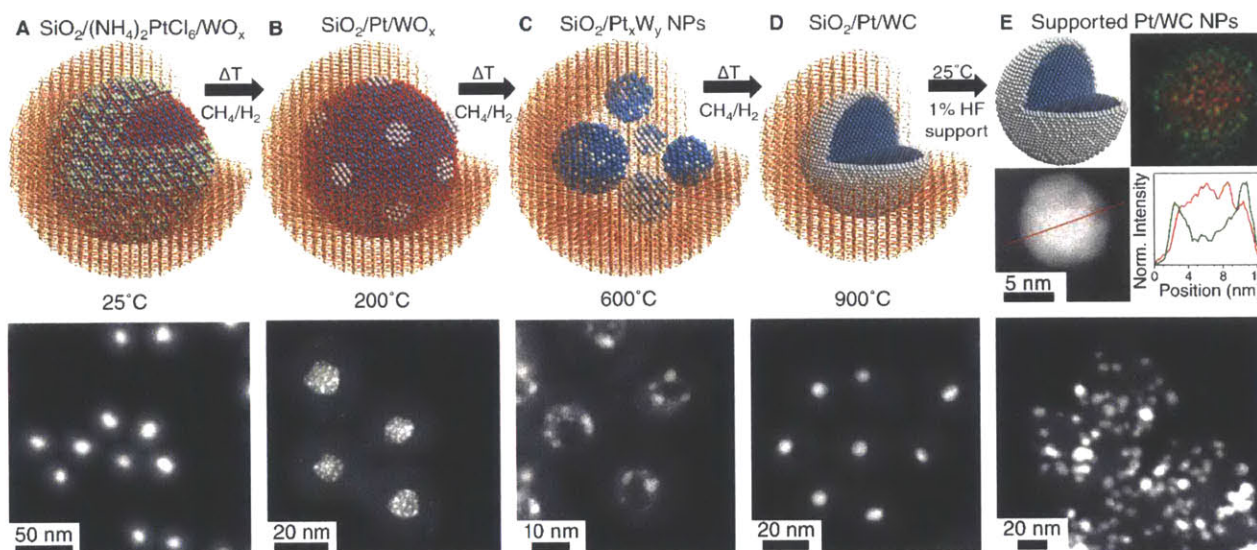


Figure 6.1. High Temperature Self-Assembly of Noble Metal Monolayers on Transition Metal Carbide Cores. (**A to D**) Schematic representations and corresponding STEM images of (A) silica-encapsulated $(\text{NH}_4)_2\text{PtCl}_6/\text{WO}_x$ nanoparticles synthesized in a one-pot reactor at room temperature and subsequently heated to (B) 200°C , (C) 600°C , and (D) 900°C in a CH_4/H_2 atmosphere. (**E**) STEM image, EDX map, and linescan (Pt signal in green, W signal in red) of a resulting core-shell Pt/WC nanoparticle and a STEM image of Pt/WC formulated on a carbon black support after silica removal.

2.2 Silica as a Core-Shell Structure Directing Agent

Silica encapsulation is critical for controlling core-shell nanoparticle formation. **Figure 6.2A-C** compares two carbon-supported NM/TMC materials, one with silica encapsulation (denoted as $\text{Pt}_{\text{C-S}}$, 28%Pt/72% $\text{Ti}_{0.1}\text{W}_{0.9}\text{C}$ supported at 28 wt%), and the other without silica encapsulation (denoted as $\text{Pt}_{\text{direct}}$, 20%Pt/80% $\text{Ti}_{0.1}\text{W}_{0.9}\text{C}$ supported at 20 wt%). Because TiC is the most electrochemically stable carbide,^[43] a bimetallic TiWC core was used to enhance stability without significantly affecting the WC lattice parameter. The powder X-ray diffraction (PXRD) pattern for $\text{Pt}_{\text{C-S}}$ shows reflections consistent with phase-pure fcc WC (PDF #00-020-1316) without additional fcc Pt reflections (PDF #00-004-0802), whereas the pattern for $\text{Pt}_{\text{direct}}$ exhibits distinct, sintered fcc Pt crystallites (**Figure 6.2A**). These data are consistent with core-shell formation for $\text{Pt}_{\text{C-S}}$ but Pt phase-segregation for $\text{Pt}_{\text{direct}}$. In addition, $\text{Pt}_{\text{C-S}}$ shows a difference between the bulk and surface Pt:TiW ratios (28% vs. 49% as determined by inductively coupled plasma mass spectrometry [ICP] and X-ray photoelectron spectroscopy [XPS], respectively). This surface ratio enhancement is indicative of Pt monolayers screening a TiW-rich core. In contrast, such surface screening was not observed for $\text{Pt}_{\text{direct}}$ where the bulk and surface Pt:TiW ratios were 20% and 18%, respectively (**Figure 6.2B**, **Table S6.1**, **Figure S6.9**).

Silica encapsulation prevents undesirable coking during carburization, as verified by a 6-fold lower carbon-to-metal surface ratio for $\text{Pt}_{\text{C-S}}$ compared to $\text{Pt}_{\text{direct}}$ (**Figure 6.2B**). Characteristic graphitic coke fibrils and sintered particles encapsulated in 4-5 nm of graphitic coke are visible in the transmission electron microscopy (TEM) images of $\text{Pt}_{\text{direct}}$ (**Figure 6.2C**). In contrast, $\text{Pt}_{\text{C-S}}$ shows well-dispersed crystalline nanoparticles with a uniform particle size distribution (PSD) of 6-8 nm and the absence of detectable graphitic coke layers. A heterometallic 27% $\text{Pt}_{0.67}\text{Ru}_{0.33}$ /73% $\text{Ti}_{0.1}\text{W}_{0.9}\text{C}$ material (denoted as $\text{PtRu}_{\text{C-S}}$) was synthesized analogously to $\text{Pt}_{\text{C-S}}$ and exhibits similar physico-chemical properties (**Figure 6.2C** and **Figure S6.8-Figure S6.10**). Its core-shell structure is clearly visible on the aberration-corrected STEM-EDX map shown in **Figure 6.2D**.

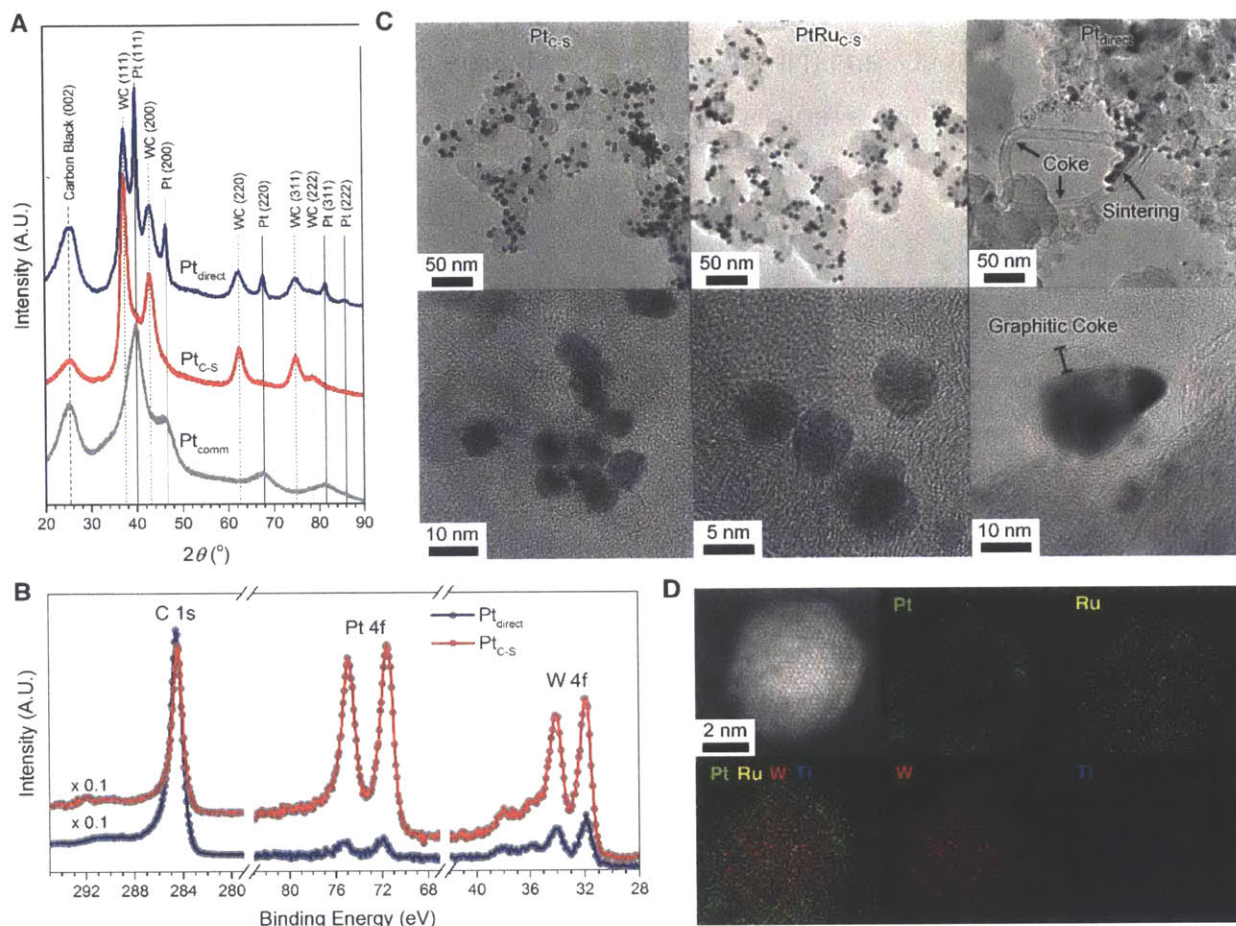


Figure 6.2. Experimental Corroboration of Core-Shell Structure. **(A)** PXRDs of Pt_{C-s} and Pt_{direct} compared to Pt_{comm}. **(B)** XPS comparison of the C 1s, Pt 4f, and W 4f signals of Pt_{C-s} and Pt_{direct}. **(C)** TEM images of Pt_{C-s}, PtRu_{C-s}, and Pt_{direct}. **(D)** STEM and EDX maps of PtRu_{C-s}.

2.3 Demonstration of Synthetic Control

Remarkably, the high temperature self-assembly process employed here permits comprehensive control of the entire core-shell architecture for a variety of early and late transition metals (**Figure 6.3**). Using TiWC cores, we successfully synthesized nanoparticles with varying sizes (3-10 nm), mono- and bimetallic shell compositions (Ru, Rh, Ir, Pt, and Au), and NM monolayer (ML) coverages (ca. 0.5-3 ML) (**Figure 6.3A**, **Figure S6.15**, and **Figure S6.16**). All materials crystallized into fcc WC lattices and displayed enhanced surface NM:TiW ratios, consistent with core-shell structures (**Figure S6.9-Figure S6.14** and **Table S6.1**). In addition, we show that NM shells will lattice-match

and self-assemble onto bimetallic semicarbide cores (PDF #00-020-1315) such as $(\text{Cu}_{0.2}\text{W}_{0.8})_2\text{C}$, $(\text{Co}_{0.2}\text{W}_{0.8})_2\text{C}$, and $(\text{Ni}_{0.3}\text{W}_{0.7})_2\text{C}$ (**Figure 6.3B** and **C**, **Figure S6.14**, and **Figure S6.17**), offering even more avenues for tuning reactivity.

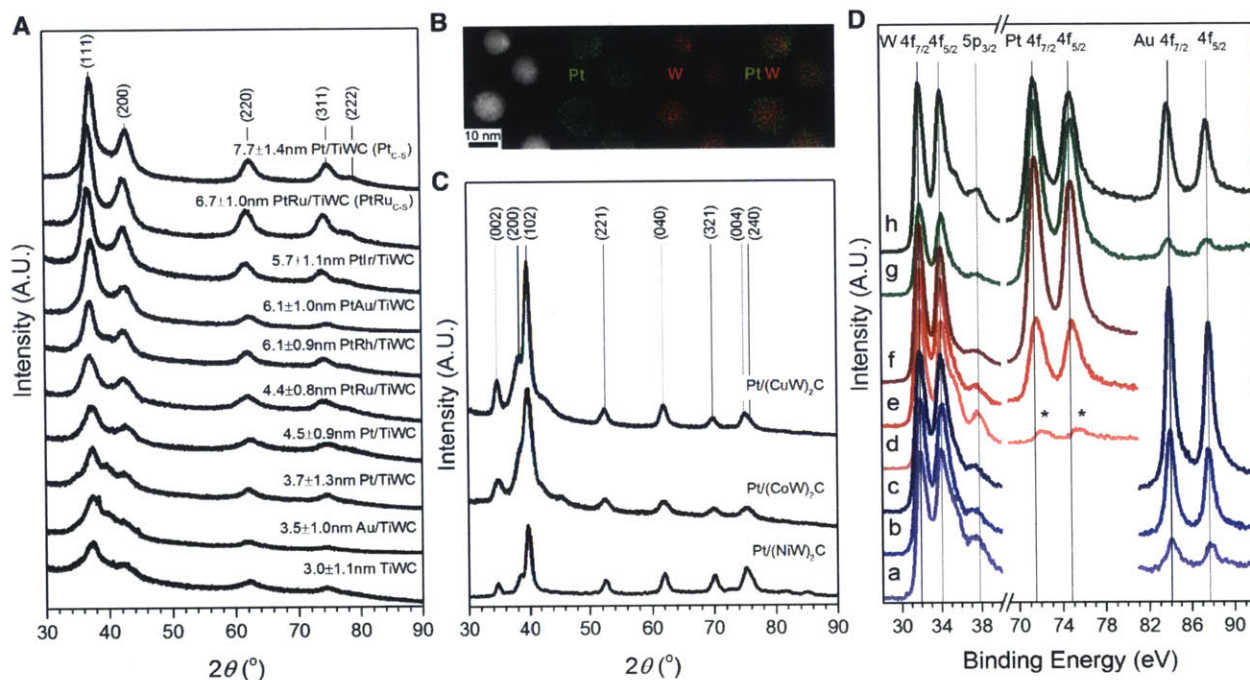


Figure 6.3. Experimental Exploration of Various Noble Metal/Transition Metal Carbide (Shell/Core) Architectures. **(A)** XRD diffractograms of NM/TiWC nanoparticles of various sizes, compositions, and NM coverages. **(B)** STEM image and EDX maps of carbon-supported Pt/(CuW)₂C nanoparticles. **(C)** XRD diffractograms of Pt monolayers on various bimetallic semicarbide core nanoparticles. **(D)** XPS spectra of (a-c) Au/TiWC nanoparticles, (d-f) Pt/TiWC nanoparticles, and (g,h) PtAu/TiWC nanoparticles with sub-monolayer, monolayer, and multilayer NM shell thicknesses. The * in panel D marks the Pt²⁺ signal.

For Au, Pt, and PtAu monolayers self-assembled on TiWC cores, we show that the RME method also allows control of the NM shell thickness from sub-monolayer (ca. 0.5 ML) to multilayer (ca. 3 ML) coverages (**Figure 6.3D**). For each material, the extent of the XPS-determined surface NM:TiW ratio enhancement over the ICP-determined bulk NM:TiW ratio correlates with the monolayer coverage, ranging from 1-3% at sub-monolayer coverages to 10-20% enhancement at multilayer coverages (**Table S6.1**). Unlike Au surfaces, the surface of Pt ambiently passivates with a PtO layer, which is detectable as Pt²⁺ with XPS. As the monolayer coverage decreased for the Pt/TiWC

system (**Figure 6.3D**, spectra f to d), the Pt 4f signals shifted to higher binding energies, reaching 72.3 and 75.7 eV for the sub-monolayer sample (denoted as Pt_{sub-ML}). The presence of only PtO is consistent with sub-monolayer coverage, and such materials could have important applications in thermal catalysis as well as electrocatalysis where both WC and Pt surface functionalities are accessible for catalytic transformations.

2.4 Sub-Monolayer and “Single Atom” Pt/TiWC Nanoparticles

While thicker shells of ca. 2-3 ML can be imaged directly using STEM-EDX mapping, sub-monolayer coverages are not amenable to direct observation. However, their structure can be interrogated using PXRD, a comparison of XPS-determined surface compositions to ICP-determined bulk compositions, and TEM imaging.

Figure 6.4A depicts wide angle x-ray diffractograms of the nanoparticles supported on carbon black. The commercial Pt/C consists of 1.4 ± 0.3 nm NPs dispersed at 20wt% on a Vulcan XC-72r support (**Figure S6.19**), manifested as broad reflections at 39.9°, 46.2°, 67.8°, and 81.2°. These reflections are consistent with the 111, 200, 220, and 311 planes, respectively, of phase-pure fcc Pt. In contrast, the core-shell nanoparticles as well as the TiWC control only exhibit reflections centered around 37.0°, 42.9°, 62.5°, 74.9°, and 79.0°, consistent with the 111, 200, 220, 311, and 222 planes, respectively, of phase-pure fcc β -WC. Even 2 ML Pt/TiWC/C, which contains 28 mol% Pt, does not show indications of a separate, discrete fcc Pt phase. These spectra are consistent with Pt shells lattice matched to the TiWC core.

In **Figure 6.4B**, XPS spectra are shown of the various nanoparticles formulated as nanodispersions, rather than supported on carbon black, which affords the maximum signal intensity of the metal peaks. The 2 ML catalyst has a clear and intense Pt 4f signal centered at 71.5 eV and 74.9 eV, consistent with Pt⁰. Deconvolution of this peak (**Figure S6.9**) shows a substantial signal contribution from signals centered around 72.6 eV and 76 eV, consistent with a Pt²⁺ passivation layer. The ratio of Pt²⁺:Pt⁰ is 0.3, consistent with a 2 – 3 ML shell. Importantly, the 0.25 ML catalyst (also referred to as Pt_{sub-ML}) shows only two Pt²⁺ peaks, centered around 72.3 eV and 75.7 eV. The lack of any Pt⁰ signal implies the near-complete Pt dispersion associated with sub-monolayer coverages. The

downshift in the Pt^{2+} peak locations from the 2 ML sample also implies immediate interaction with the TiWC substrate. The 0.05 ML and 0.004 ML catalysts could not be quantitated due to the incredibly low Pt coverages. While the 0.05 ML catalyst does have a detectable signal, the surface Pt concentration in the 0.004 ML catalyst exceeds the instrument detection limits. Despite the low signal intensity, the 0.05 ML catalyst appears comprised of Pt^{2+} as well as a second Pt^{x+} species in a chemical environment that is intermediate between Pt^{2+} and Pt^{4+} .

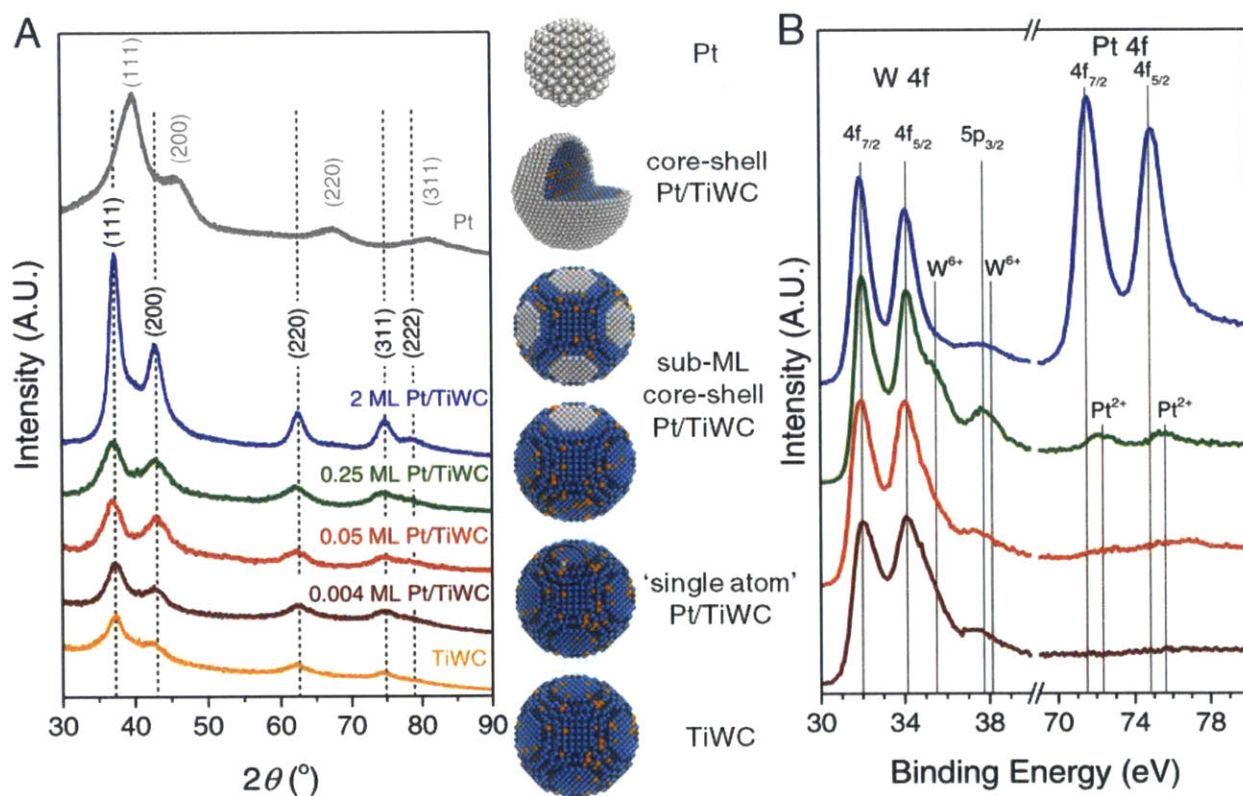


Figure 6.4. Characterization of Sub-Monolayer and 'Single Atom' Pt/TiWC. **(A)** PXRD diffractograms of Pt/TiWC nanoparticles of varying monolayer coverages in comparison to bare TiWC nanoparticles and Pt_{comm} . **(B)** XPS spectra of Pt/TiWC nanoparticles of varying monolayer coverages. For PXRD, the nanoparticles are supported on carbon black whereas the nanoparticles are unsupported nanodispersions for XPS analysis to maximize signal intensity. The graphics are for visual representation of the catalysts.

For the 2 ML and 0.25 ML catalysts where the Pt 4f signals are quantifiable, comparison of XPS-determined surface compositions in Figure 2 with ICP-determined bulk compositions in **Table S6.1** provides evidence for the core-shell structure of these materials. In a radially isotropic heterometallic nanoparticle, the XPS-determined surface composition will agree with the ICP-determined overall composition. However, in a core-shell nanoparticle, the species that is enriched at the surface screens the XPS signal of the sub-surface core. Therefore, if the nanoparticle is not radially isotropic, but a core-shell nanoparticle, then the XPS-determined surface composition will not agree with the ICP-determined bulk composition. Instead, the surface composition will be enriched relative to the bulk. The extent of this enrichment is directly related to the ML coverage, with thicker shells exhibiting a higher enrichment relative to submonolayer coverages. In the case of the 2 ML sample, the ICP-determined overall ratio of Pt:W was 28%. However, the XPS-determined ratio of Pt:W was 49%, indicative of extensive screening of the core by the Pt shell. Similarly, the ICP-determined ratio of Pt:W in the 0.25 ML sample was 4% while the XPS-determined ratio of Pt:W was 11%, again indicative of Pt screening the W signal. While the XPS signal was too low for the 0.05 ML and 0.004 ML samples to examine screening effects, the ML coverage was estimated from a combination of TEM-determined PSDs and ICP-determined overall compositions. **Figure S6.16** depicts representative TEM images of this class of materials. Once the average particle size was determined, the surface dispersion was calculated using standard methods assuming spherical particles. Assuming complete phase-separation of Pt from the TiWC core, the ML coverage was then estimated from the ICP-determined Pt:TiW molar ratio.

We note that the Pt concentration in the 0.004 ML sample is so low that the average 3 nm TiWC NP would have a surface coverage of 0.6 Pt atoms, meaning that this sample approaches the level of on average a single Pt atom decorating a TiWC nanoparticle. This loading level is consistent with the undetectable XPS signal shown for this sample in Figure 1b.

3. Detailed Synthetic Method

Preparation of the tungsten alkoxide precursor

The tungsten precursor stock solution was prepared from commercial WCl_4 by addition of anhydrous isopropanol (IPA). Under constant stirring, 10 mL of anhydrous IPA was injected into a round bottom flask containing 5.0 g of WCl_4 under a continuous N_2 purge at $60^\circ C$ in a well-ventilated fume hood. Within the first minute, the grey-green WCl_4 transitioned to a purple intermediate and then to a black-brown liquid. The residual liquid was allowed to slowly evaporate at $60^\circ C$ under a constant N_2 purge, leaving a black-brown solid. This procedure was repeated two additional times with 20 mL of anhydrous IPA to remove any residual HCl. The final product was diluted by addition of 100 mL of anhydrous IPA and stored under inert conditions.

Preparation of titanium, copper, and cobalt alkoxide precursors

Stock solutions of titanium (IV) isopropoxide (TiIPO), copper (II) isopropoxide (CuIPO), and cobalt (II) isopropoxide (CoIPO), were prepared by diluting the commercially available isopropoxides with anhydrous isopropanol to a final concentration of 5% w/v for TiIPO and 1% w/v for CuIPO and CoIPO. This step resulted in a slurry for CuIPO and CoIPO solutions.

Synthesis of $SiO_2/NMCl_x/TMO$ NPs

A reverse microemulsion (RME) was prepared under constant stirring in ambient conditions by mixing 240 mL of *n*-heptane, 54 mL of Brij-L4® surfactant, 7.8 mL of ultrapure deionized water, and 1.4 mL of NH_4OH solution, resulting in an optically transparent and colorless RME. In the synthesis involving Ir or Rh, NH_4Cl was dissolved in ultrapure deionized water before addition into the emulsion (molar ratio of NH_4Cl to Rh or Ir = 6:1).

A metal alkoxide mixture was prepared by mixing aliquots of the metal alkoxide stock solutions in the desired ratio. Typically, 1.1 mmoles of metal alkoxides were added at this scale. Under ambient conditions without the need for a Schlenk line, the metal alkoxide mixture was diluted with 120 mL of *n*-heptane. The diluted metal alkoxide mixture was then added to the RME under constant mixing over the span of a few minutes. The RME was allowed to mix under ambient conditions for 4 h to form bimetallic transition

metal oxide (TMO) NPs. During this time, the RME remained optically transparent for all syntheses, but the color varied depending on the metals used and the metal ratios. This solution will be referred to as the TMO RME. Further details on controlling the TMO NP particle size and composition is provided elsewhere^[49-51].

While the TMO RME was reacting, a separate RME containing noble metal salts, further referred to as the NM RME, was prepared. Commercially available hydrated noble metal chloride salts were weighed in the desired ratios and then fully dissolved in 1 mL of ultrapure deionized water. The noble metal chloride solution was then rapidly injected to a mixture of 46 mL of *n*-heptane with 7.2 mL of Brij-L4® surfactant to obtain an optically transparent RME of various colors depending on the noble metals employed.

The NM RME was gravity-fed dropwise over ~ 30 min into the TMO RME under constant mixing to form the NM/TMO RME. After 4 h of mixing the NM/TMO RME remained optically transparent. Next, 1.5 mL of tetraethyl orthosilicate (TEOS) was added rapidly to the NM/TMO RME and allowed to react for 16.5 h. During this time, the NM/TMO RME gradually became translucent.

After 16.5 h, 300 mL of methanol was added rapidly to the RME under constant mixing to precipitate the SiO₂/NMCl_x/TMO NPs. After 15 min, the mixing was stopped and the SiO₂/NMCl_x/TMO NPs were allowed to flocculate and sediment over 1 h to form a three-phase mixture: a heptane-rich upper phase, a methanol-rich middle phase, and the SiO₂/NM/TMO NP precipitant on the bottom. The NPs were obtained by decanting off the top two layers and centrifuging the remaining slurry at 2,000 rpm. The wet cake was then redispersed in acetone to remove residual surfactant and centrifuged at 6,000 rpm. The acetone was then removed and the SiO₂/NMCl_x/TMO wet cake was dried under a stream of N₂. The product cake was then stored under ambient conditions. The above standard synthesis produces ca. 600 mg of recovered SiO₂/NMCl_x/TMO product. For most syntheses explored in this work, all of the quantities reported above were doubled to obtain > 1 g of product.

Carburization of SiO₂/NM/TMO NPs

Approximately 500 mg of as-synthesized SiO₂/NMCl_x/TMO powder was spread into an alumina crucible and purged with N₂ for 30 min in a tubular furnace. The inlet gas was then switched to 130 cm³(STP) min⁻¹ of H₂ and 23 cm³(STP) min⁻¹ of CH₄. Using a 2 °C min⁻¹

ramp rate, the furnace was then heated to 900°C and held for 5 h. During the final 30 min, the flowrate of CH₄ was turned off. The furnace was then allowed to cool naturally with the lid closed under 130 cm³(STP) min⁻¹ of H₂ to room temperature. Once at room temperature, the furnace was purged with N₂ bubbled through an H₂O saturator for 2 h at 95 cm³(STP) min⁻¹ and then passivated using a 1%O₂/99%N₂ mixture for 2 h. After passivation, the samples were stored in a dry N₂ glovebox.

For samples containing Ru, Rh, or Ir, the tubular furnace was heated to 1000°C under 130 cm³(STP) min⁻¹ of H₂ and 23 cm³(STP) min⁻¹ of CH₄. Once 1000°C was reached, the methane flow was stopped and the samples were held at 1000°C for 30 min under 130 cm³(STP) min⁻¹ of H₂ before cooling to room temperature and passivating normally.

Removing SiO₂ to obtain NM/TMC nanodispersions or supported NM/TMC

To remove the encapsulating SiO₂ shells, ~ 60 mg of SiO₂/NM/TMC powder was added to a well-mixed solution of 10 mL of degassed ethanol and 200 µL of reagent-grade 48 wt% aqueous HF solution prepared such that the molar ratio of HF:SiO₂ was approximately 6:1. Next, 600 µL of 70% technical grade oleylamine or a high surface area support, such as carbon black, were added to obtain a nanodispersion or a supported catalyst, respectively. After 18 h at room temperature and constant mixing, the NM/TMC was recovered by centrifuging at 6,000 rpm and rinsed thoroughly with degassed ethanol and degassed water. The powder was dried under vacuum and stored in a dry N₂ glovebox.

4. Conclusions

The developed method is a direct consequence of the insolubility of noble metals in transition metal carbide lattices. Through exploitation of this basic thermodynamic property in combination with proper materials engineering to mitigate sintering and coking, we have synthesized the first NM/TMC core-shell nanoparticles. In addition to confirming the existence of this new class of materials through direct imaging and other complementary characterization techniques, the method itself betrays unique properties of this class of materials unknown to other core-shell architectures. These properties include exceptional thermal stability and sinter-resistance—a first for core-shell

nanoparticles—and the prevention of bulk alloying during thermal treatments or electrochemical cycling. These structural properties along with the unique catalytic activities of this new class of materials is explored further in Chapter 7. Finally, the method offers comprehensive synthetic control over a wide range of heterometallic transition metal combinations—a dichotomy in light of the extreme conditions required to make these materials. The ultimate goal in catalysis is to have complete control over the material properties that govern reactivity and stability. As such, this level of synthetic control is critical to the development of new and better catalysts with reduced noble metal loadings.

Acknowledgements

Dr. Maria Milina is gratefully acknowledged for her major contribution to this chapter. This work was supported by the Department of Energy, Office of Basic Energy Sciences (DE-FG02-12ER16352, DE-SC0014058). The authors acknowledge use of facilities and instrumentation supported by the University of Wisconsin Materials Research Science and Engineering Center (DMR-1121288). I thank the National Science Foundation for financial support through the National Science Foundation Graduate Research Fellowship under Grant No. 1122374. Dr. Maria Milina thanks the Swiss National Science Foundation (Project number P2EZIP2_159124) for financial support.

5. Supporting Information

5.1. Materials

Reverse microemulsions were prepared from anhydrous *n*-heptane (Sigma-Aldrich, 99%, stored under ambient conditions), polyoxyethylene (4) lauryl ether (Sigma-Aldrich, Brij® L4, average $M_n \sim 362$), ammonium hydroxide solution (Sigma-Aldrich, 28-30%), and deionized (DI) water (18.2 M Ω ·cm). For syntheses involving the precipitation of Ir and Rh chloride salts, ammonium chloride (Sigma-Aldrich, 99.5%) was also added. Monometallic and heterometallic transition metal oxide (TMO) nanoparticles (NPs) were obtained by co-hydrolysis of commercially available metal alkoxides and metal alkoxides prepared from commercially available metal chloride salts. These consisted of tungsten (IV)

chloride (Strem Chemicals, 97%) prepared with anhydrous isopropanol (IPA, Sigma-Aldrich, 99.5%), titanium (IV) isopropoxide (Sigma-Aldrich, 97%), cobalt (II) isopropoxide (Alfa Aesar), nickel (II) methoxyethoxide (Alfa Aesar, 5% w/v), and copper (II) isopropoxide (Alfa Aesar, 98%). The metal oxide NPs were coated with noble metals (NM) using as-received commercially available hydrated noble metal chloride (NMCl_x) salts. These consisted of ruthenium (III) chloride hydrate (Strem Chemicals, 99.9% Ru), rhodium (III) chloride hydrate (Strem Chemicals, 38-41% Rh), iridium (III) chloride hydrate (Strem Chemicals, 99.9% Ir), chloroplatinic acid (Strem Chemicals, 99.9%), and chloroauric acid (Strem Chemicals, 99.8%). The NMCl_x/TMO NPs were coated with silica nanospheres upon hydrolysis of tetraethyl orthosilicate (Sigma-Aldrich, 99%).

The materials were carburized in a methane/hydrogen atmosphere (Airgas, uhp grade 5). The silica shells were removed using 1% HF diluted in ethanol (200 proof) prepared from 48 wt% HF in H_2O solution (Sigma-Aldrich, 99.99% trace metals basis). The NM/TMC NPs were supported on carbon black (Cabot, Vulcan® XC-72r) or dispersed using oleylamine (Sigma-Aldrich, 70%).

5.2 Methods

Transmission Electron Microscopy (TEM) and Scanning Transmission Electron Microscopy (STEM)

was performed on a JEOL 2010F equipped with a field emission gun (FEG) operating at 200 kV. Magnifications of obtained images ranged from 25,000x to 600,000x. STEM was performed using high-angle annular dark field (HAADF) mode.

Aberration-Corrected STEM with EDX Mapping/Linescans

was performed on an FEI equipped with a CEOS probe-side aberration corrector operated at 200 kV, with a probe convergence angle of 24.5 mrad. HAADF mode was used for imaging, with a probe current of ~ 25 pA, and spatial resolution < 0.1 nm. EDS spectrum images were taken (EDAX EDS detector, 128 eV resol.) with a probe current ~ 200-780 pA, and spatial resolution ~ 0.16-0.29 nm. Sample preparation for STEM included dispersion in ethanol or acetone, ultra-sonication for 30 min, and then deposition onto carbon copper TEM grids. STEM samples were plasma cleaned for 15 min before loading into the microscope.

X-ray Photoelectron Spectroscopy (XPS)

was performed on a PHI Versaprobe II equipped with a multichannel hemispherical analyzer and a monochromatic aluminum anode X-ray source operating at 100 W with a 100 μm beam scanned over a 1.4 mm line across the sample surface. A dual-beam charge neutralization system was used with an electron neutralized bias of 1.2 eV and an argon ion beam energy of 10 eV. All spectra were charge corrected by referencing the adventitious C 1s signal to 284.7 eV. Samples were prepared by mounting powders onto electrically conductive copper tape. For unsupported nanodispersions, the nanodispersions were dispersed in DI water without the use of any ligands or capping agents. The nanodispersion was then dripped onto the copper tape and the water was evaporated under vacuum to obtain a nanoparticle thin film.

Signal-to-noise (S/N) ranged from over 300 for W 4f spectra to 70 for Ti 2p spectra. During peak deconvolution, the $\Sigma(X^2)$ was kept below 1. Peaks with S/N values below 70 could not meet this criteria, and the results from peak deconvolutions are listed as N.R. (not reported) on Table S5. We note that an S/N value greater than 3 is commonly considered a detectable peak^[178]. As such, all XPS spectra obtained were well above the detection limits of the PHI Versaprobe II.

Inductively Coupled Plasma Mass Spectrometry (ICP-MS)

was performed on an Agilent 7900 ICP-MS. Caution: Sample digestion in acidic media is extremely dangerous and should only be performed in small quantities in a well-ventilated fume hood approved for HF use. Proper PPE includes all of the following: safety glasses, full face shield, butyl rubber gloves with secondary gloves, a lab coat, and a full-body HF-resistant apron. Calcium gluconate must be readily available within an arm's reach. Aqua regia mixtures generate toxic fumes and if sealed will become pressurized.

Sample masses were averaged from triplicate measurements, with errors in the measurements of ca. ± 0.02 mg. 2-3 mg samples were dissolved in a sealed polypropylene tube by adding 6 drops of reagent-grade HCl and 2 drops of reagent-grade HNO₃. After a few minutes, 6 drops of reagent-grade aqueous HF was added and the tube contents were well-mixed for 40 hours. The tubes were vented after the first 15 minutes, after 1 hour, and after 2 hours. For nanoparticles supported on carbon black, the dissolved sample was diluted with 2% HNO₃ and filtered. 1 mL of fresh aqua regia was

used to rinse the filter followed by several more mL rinses with 2% HNO₃. In all cases, the final solution was diluted with 2% HNO₃ to 100-500 ppb. The detection limits for each element studied was below 100 ppt, and the R² value for each calibration curve always exceeded 0.999. The method for carbon-supported materials was benchmarked against total wt% loading determination using TGA. ICP and TGA agreed to less than 1% error. Mass loading errors during run-to-run replicates never exceeded 3% error.

Powder X-ray Diffraction (PXRD)

was performed on a Bruker D8 diffractometer using Cu K α radiation. Data were recorded in the range of 15-90° 2 θ with an angular step size of 0.01° and a counting time of 0.1 s per step.

Thermogravimetric Analysis (TGA)

was performed on a Q500 thermal analysis system (TA Instruments) between 25 and 800°C (with 15 min isothermal hold at 150°C) using a heating ramp of 5°C min⁻¹ under 25 sccm of air and 5 sccm of N₂ flow.

5.3 Detailed Self-Assembly Investigation

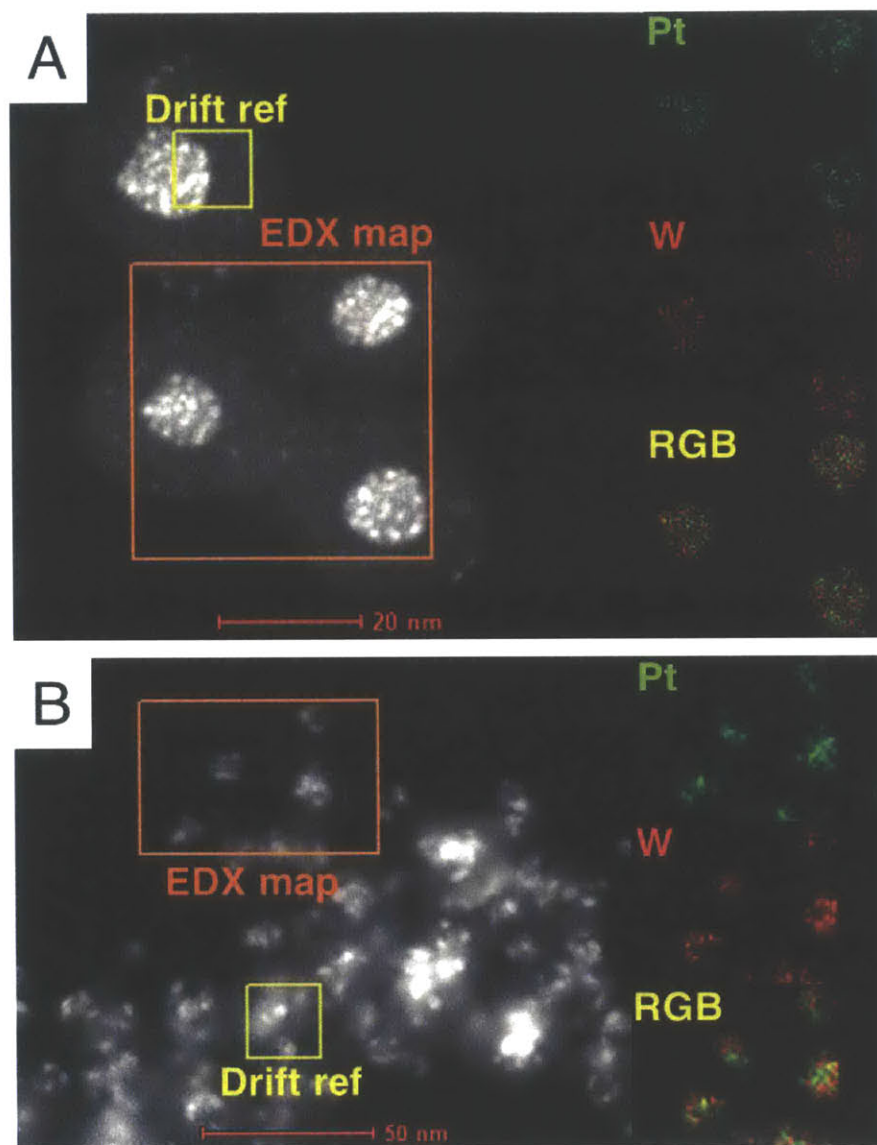


Figure S6.5. Structural Changes in SiO₂/(NH₄)₂PtCl₆/WO_x System During Carburization. **(A)** STEM image and EDX map of SiO₂/Pt/WO_x after heating to 200°C in a 15% CH₄/85% H₂ atmosphere corresponding to Fig. 1B. **(B)** STEM and EDX map of SiO₂/Pt_xW_y after heating to 600°C in a 15% CH₄/85% H₂ atmosphere corresponding to Fig. 1C.

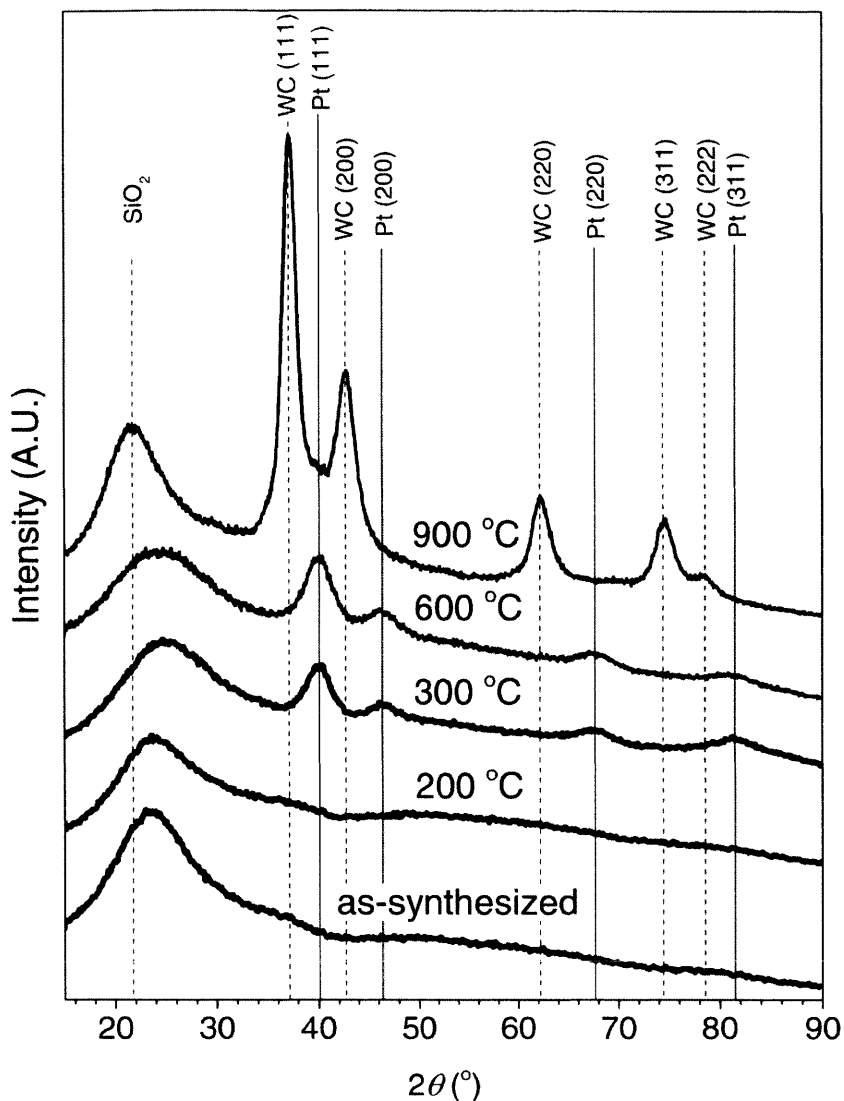


Figure S6.6. PXR D Study of the Core-Shell Nanoparticle Self-Assembly Process During Carburization. PXR D diffractograms of as-synthesized $\text{SiO}_2/(\text{NH}_4)_2\text{PtCl}_6/\text{WO}_x$ after heating to 200 °C, 300 °C, 600 °C, and 900 °C in a 15% $\text{CH}_4/85\%$ H_2 atmosphere with a heating ramp of 2°C min^{-1} . The sample heated to 900 °C was kept at this temperature for 5 h. The PXR D diffractograms for the materials as-synthesized (i.e. 25 °C), 200 °C, 600 °C, and 900 °C correspond to the materials presented in Fig. 1A-D.

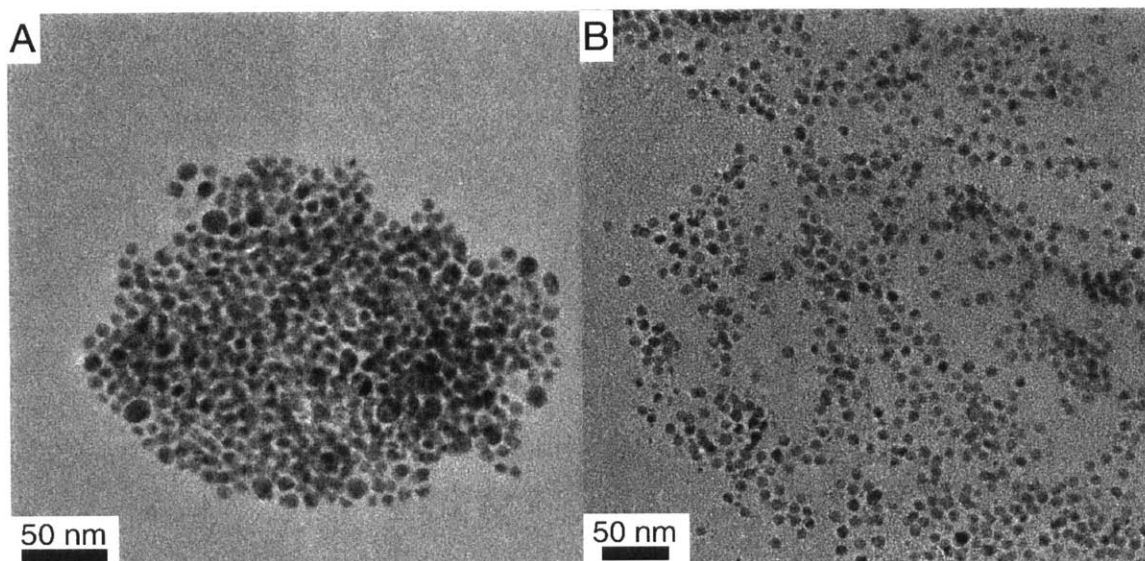


Figure S6.7. Microscopic Analysis of the Core-Shell NM/TMC Nanodispersions **(A)** A representative TEM image of an NM/TMC nanoaggregate dispersed in ethanol obtained by dissolving the silica shells without adding either a catalyst support or a surfactant capping agent. The material is Pt/Ti_{0.1}W_{0.9}C core-shell NPs corresponding to Pt_{C-S} and is typical of the material formulation used for XPS analysis of NM/TMC NPs. **(B)** A representative TEM image of NM/TMC NPs dispersed in ethanol using oleylamine as a capping agent after removal of the silica template. The above material consists of PtRu(1:1)/Ti_{0.1}W_{0.9}C core-shell NPs.

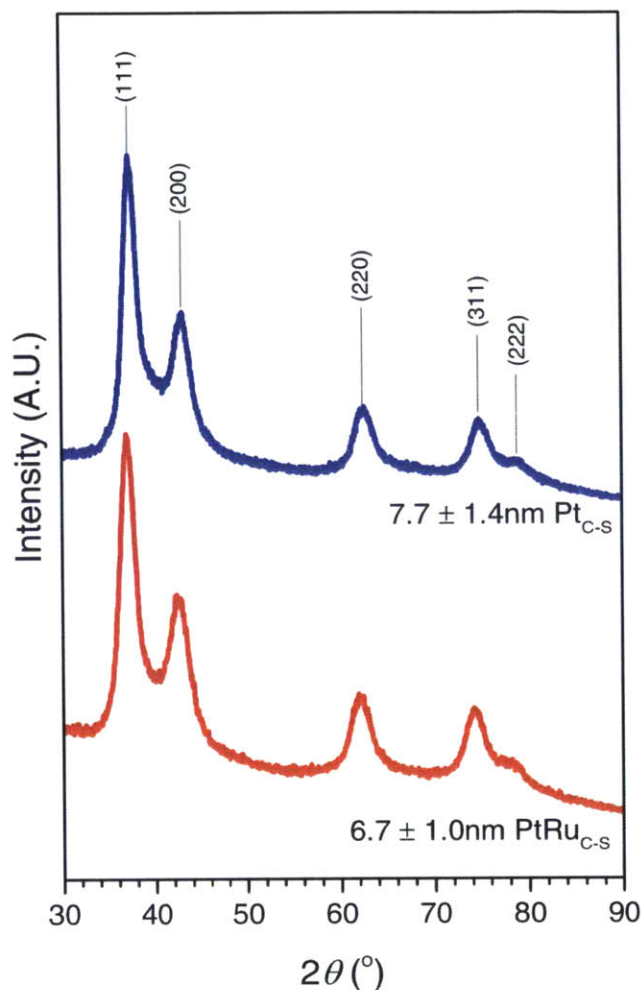


Figure S6.8. PXRD Comparison Between $\text{Pt}_{\text{c-s}}$ and $\text{PtRu}_{\text{c-s}}$. PXRD patterns of $\text{Pt}_{\text{c-s}}$ and $\text{PtRu}_{\text{c-s}}$ showing phase-pure fcc WC lattices without additional reflections associated with metallic Pt or Ru.

5.4 XPS Analysis of Core-Shell Nanodispersions

In this section, a detailed XPS analysis of all synthesized materials formulated as bare nanodispersions (i.e. unsupported) was performed. Using constrained peak deconvolutions, **Table S6.1** was constructed to compare ICP-determined bulk compositions to XPS-determined surface compositions. The estimated monolayer coverages were determined from TEM PSD dispersion estimates combined with bulk ICP-determined compositions assuming perfect partitioning of NMs from the TMC core. A selection of deconvoluted XPS spectra is included as **Figure S6.9-Figure S6.14**

Table S6.1. Chemical Composition of Core-Shell Materials

Material	ICP-determined bulk composition			XPS-determined surface composition			Estimated number of ML
	NM ratio	TMC ratio	NM:TMC ratio	NM ratio	TMC ratio ¹	NM:TMC ratio	
Au/TiWC	Au	Ti _{0.10} W _{0.90}	6%	Au	N.R.	7%	~ 0.5
Au/TiWC	Au	Ti _{0.18} W _{0.82}	13%	Au	Ti _{0.12} W _{0.88}	22%	~ 1
Au/TiWC	Au	Ti _{0.14} W _{0.86}	29%	Au	N.R.	37%	~ 2-3
Pt/TiWC	Pt	Ti _{0.08} W _{0.92}	3%	Pt	N.R.	6%	< 0.5
Pt/TiWC	Pt	Ti _{0.10} W _{0.90}	9%	Pt	N.R.	26%	~ 1
Pt _{C-S}	Pt	Ti _{0.10} W _{0.90}	28%	Pt	Ti _{0.10} W _{0.90}	49%	~ 2-3
Pt/(CuW) ₂ C	Pt	Cu _{0.23} W _{0.77}	26%	Pt	Cu _{0.22} W _{0.78}	52%	~ 2-3
PtRu _{C-S}	Pt _{0.67} Ru _{0.33}	Ti _{0.11} W _{0.89}	27%	Pt _{0.76} Ru _{0.24}	Ti _{0.10} W _{0.90}	43%	~ 2-3
PtRh/TiWC	Pt _{0.57} Rh _{0.43}	Ti _{0.13} W _{0.87}	26%	Pt _{0.59} Rh _{0.41}	Ti _{0.13} W _{0.87}	52%	~ 2-3
PtIr/TiWC	Pt _{0.81} Ir _{0.19}	Ti _{0.21} W _{0.79}	25%	Pt _{0.81} Ir _{0.19}	Ti _{0.18} W _{0.82}	45%	~ 2-3
PtAu/TiWC	Pt _{0.93} Au _{0.07}	Ti _{0.11} W _{0.89}	26%	Pt _{0.94} Au _{0.06}	N.R.	55%	~ 2-3
PtAu/TiWC	Pt _{0.69} Au _{0.31}	Ti _{0.18} W _{0.82}	27%	Pt _{0.73} Au _{0.27}	Ti _{0.16} W _{0.84}	45%	~ 2-3

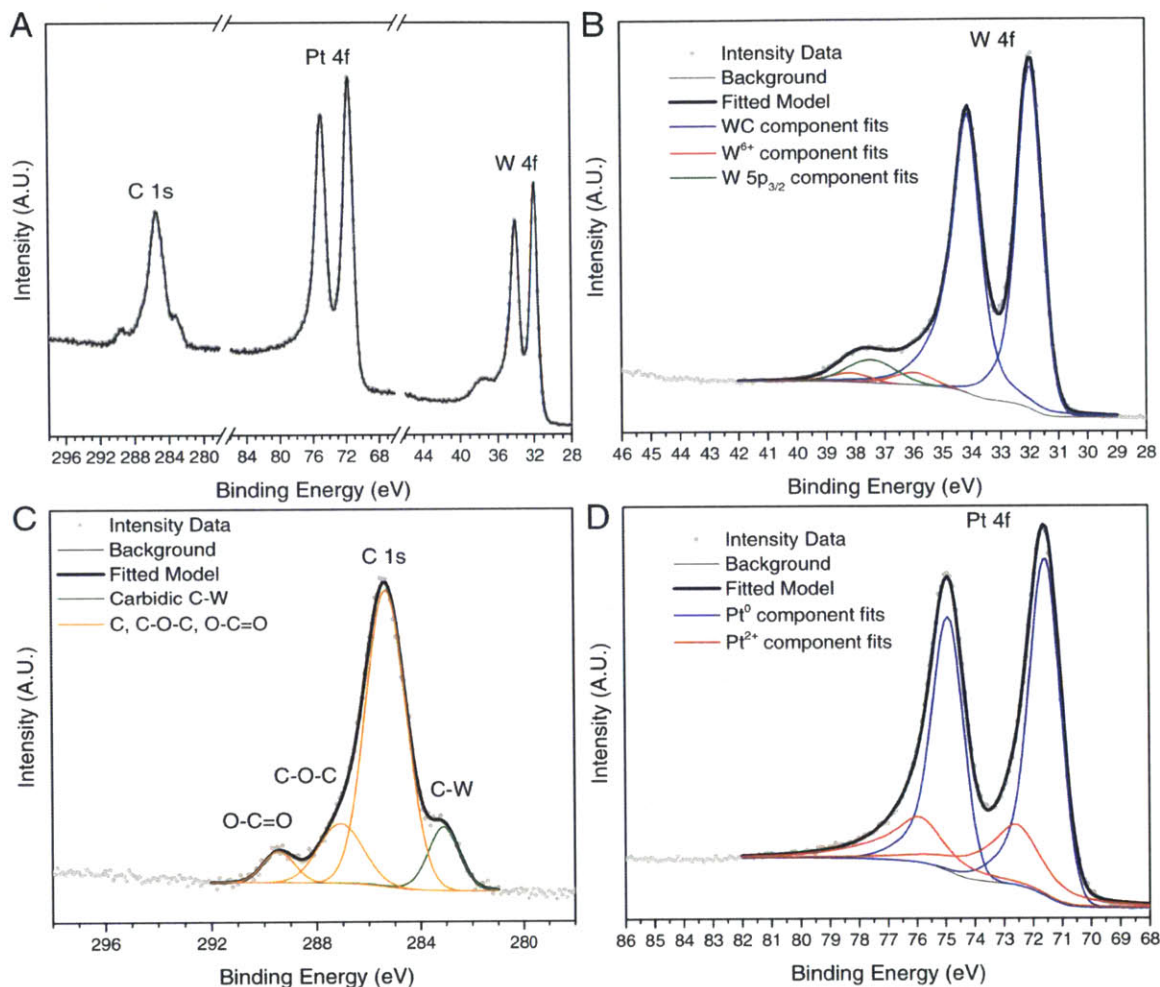


Figure S6.9. XPS Analysis of Pt_{c.s.}

(A) Raw XPS intensity data obtained for 28%Pt/72%Ti_{0.1}W_{0.9}C core-shell NP nanoaggregates (Pt_{c.s.} formulated as a nanoaggregate in ethanol without carbon black support added during silica removal to obtain a clearer C 1s spectrum).

(B) XPS peak deconvolution of the W 4f spectrum.

(C) XPS peak deconvolution of the C 1s spectrum. The C:TiW ratio was 0.73

(D) XPS peak deconvolution of the Pt 4f spectrum.

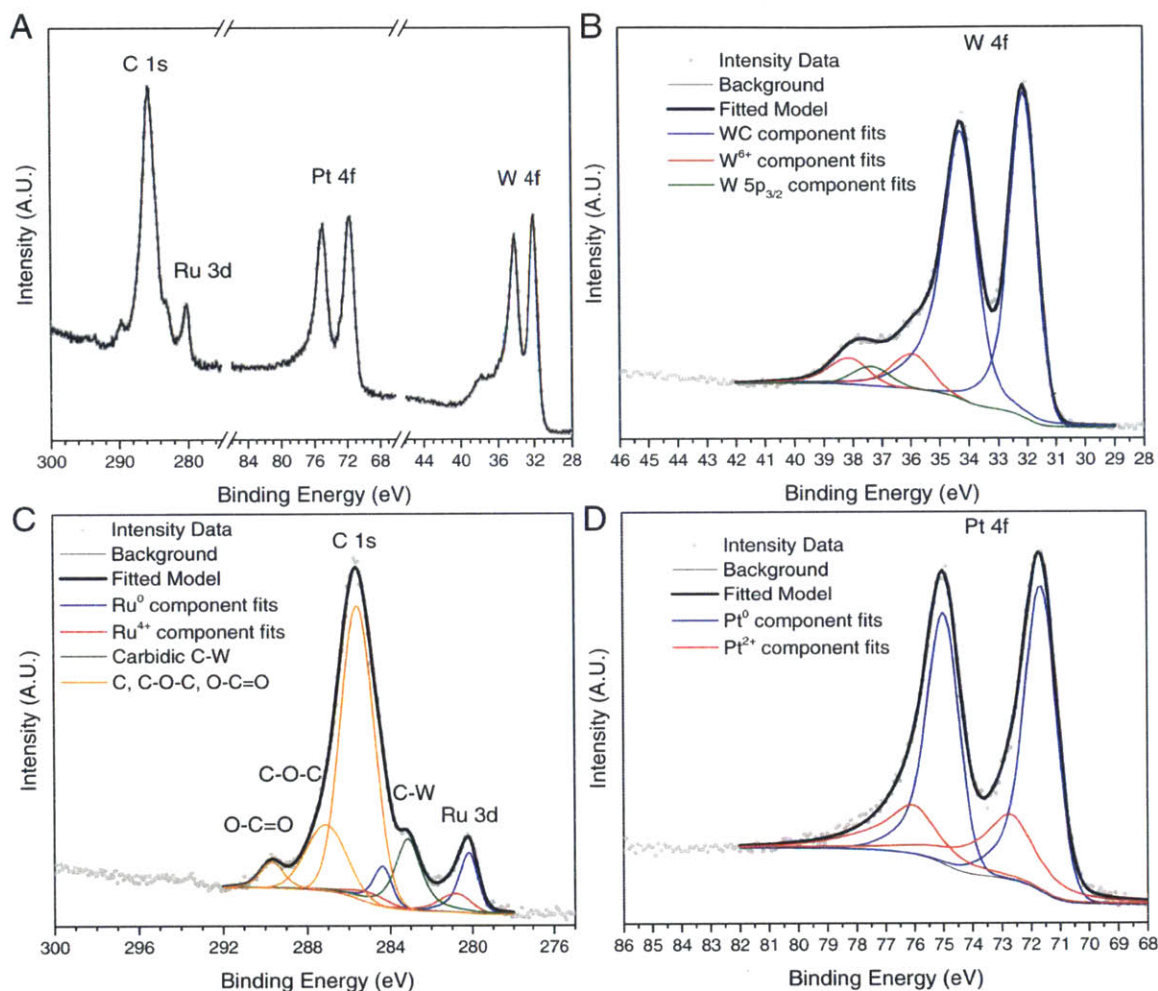


Figure S6.10. XPS Analysis of PtRu_{C-s}.

(A) Raw XPS intensity data obtained for 27% Pt_{0.67}Ru_{0.33} / 73% Ti_{0.1}W_{0.9}C core-shell NP nanoaggregates (PtRu_{C-s} formulated as a nanoaggregate in ethanol without carbon black support added during silica removal to obtain clear C 1s spectrum).

(B) XPS peak deconvolution of the W 4f spectrum.

(C) XPS peak deconvolution of the C 1s and Ru 3d spectra. The carbidic C:TiW ratio was 0.78

(D) XPS peak deconvolution of the Pt 4f spectrum.

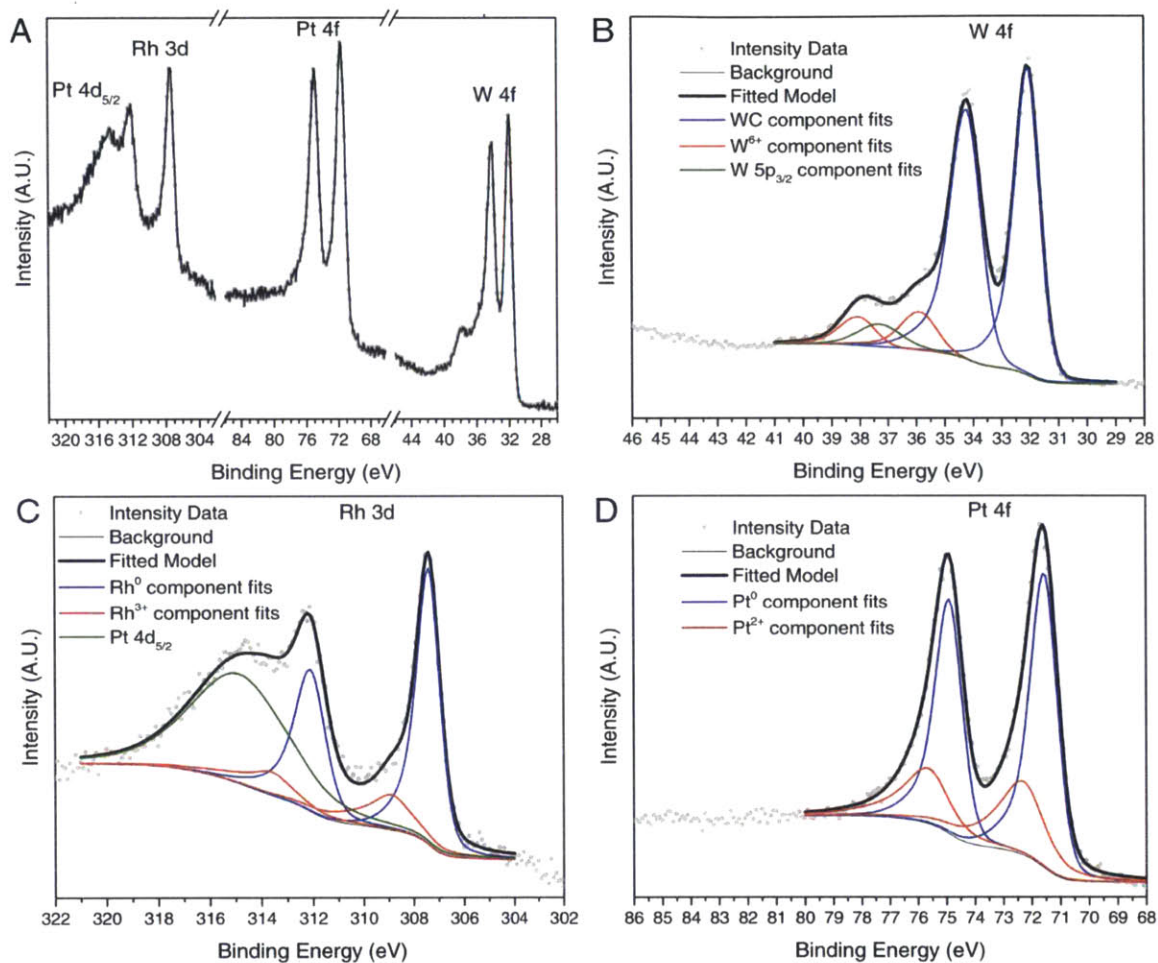


Figure S6.11. XPS Analysis of PtRh/TiWC NPs.

(A) Raw XPS intensity data obtained for 26%Pt_{0.6}Rh_{0.4}/74% Ti_{0.1}W_{0.9}C core-shell NP nanoaggregates.

(B) XPS peak deconvolution of the W 4f spectrum.

(C) XPS peak deconvolution of the Rh 3d spectrum.

(D) XPS peak deconvolution of the Pt 4f spectrum.

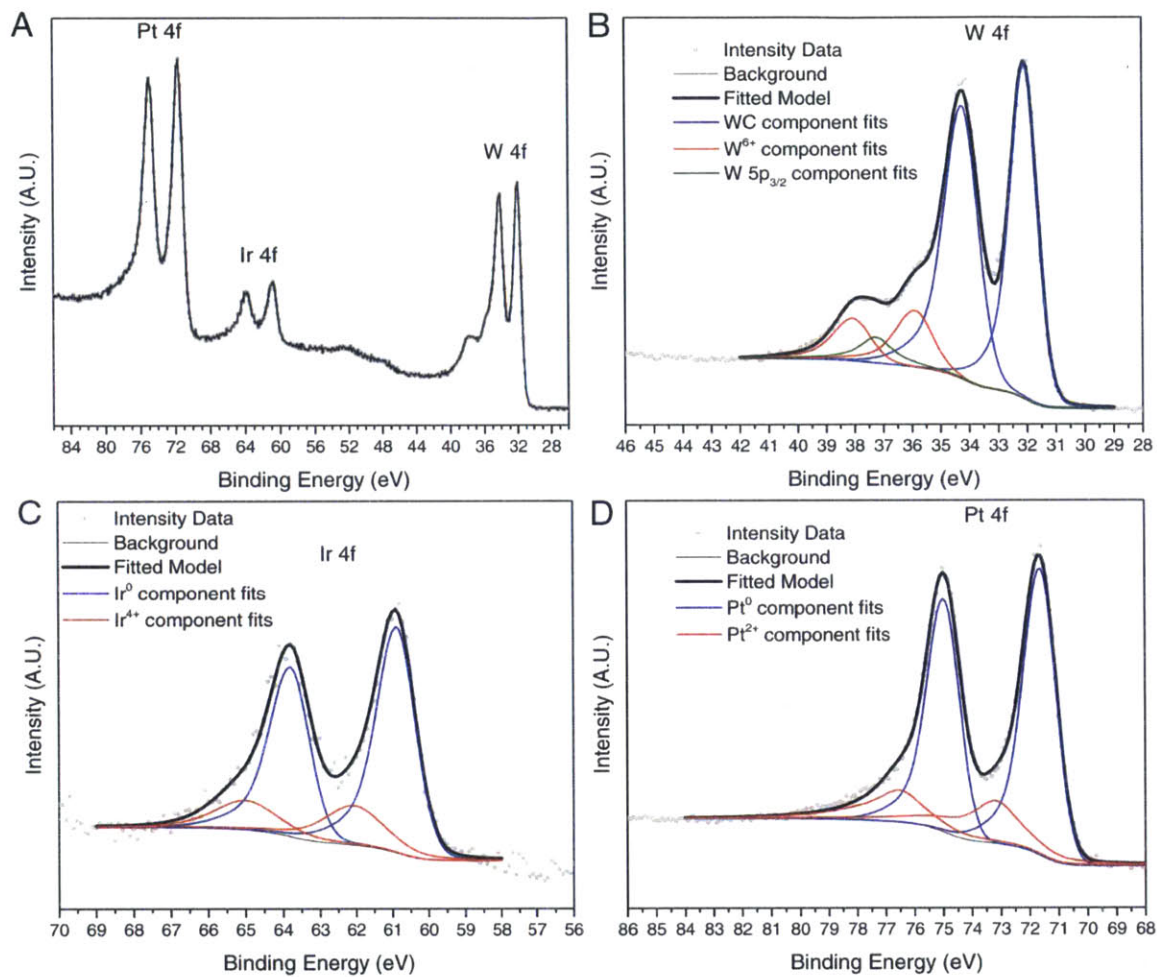


Figure S6.12. XPS Analysis of PtIr/TiWC NPs.

(A) Raw XPS intensity data obtained for 25%Pt_{0.8}Ir_{0.2}/75%Ti_{0.2}W_{0.8}C core-shell NP nanoaggregates.

(B) XPS peak deconvolution of the W 4f spectrum.

(C) XPS peak deconvolution of the Ir 4f spectrum.

(D) XPS peak deconvolution of the Pt 4f spectrum.

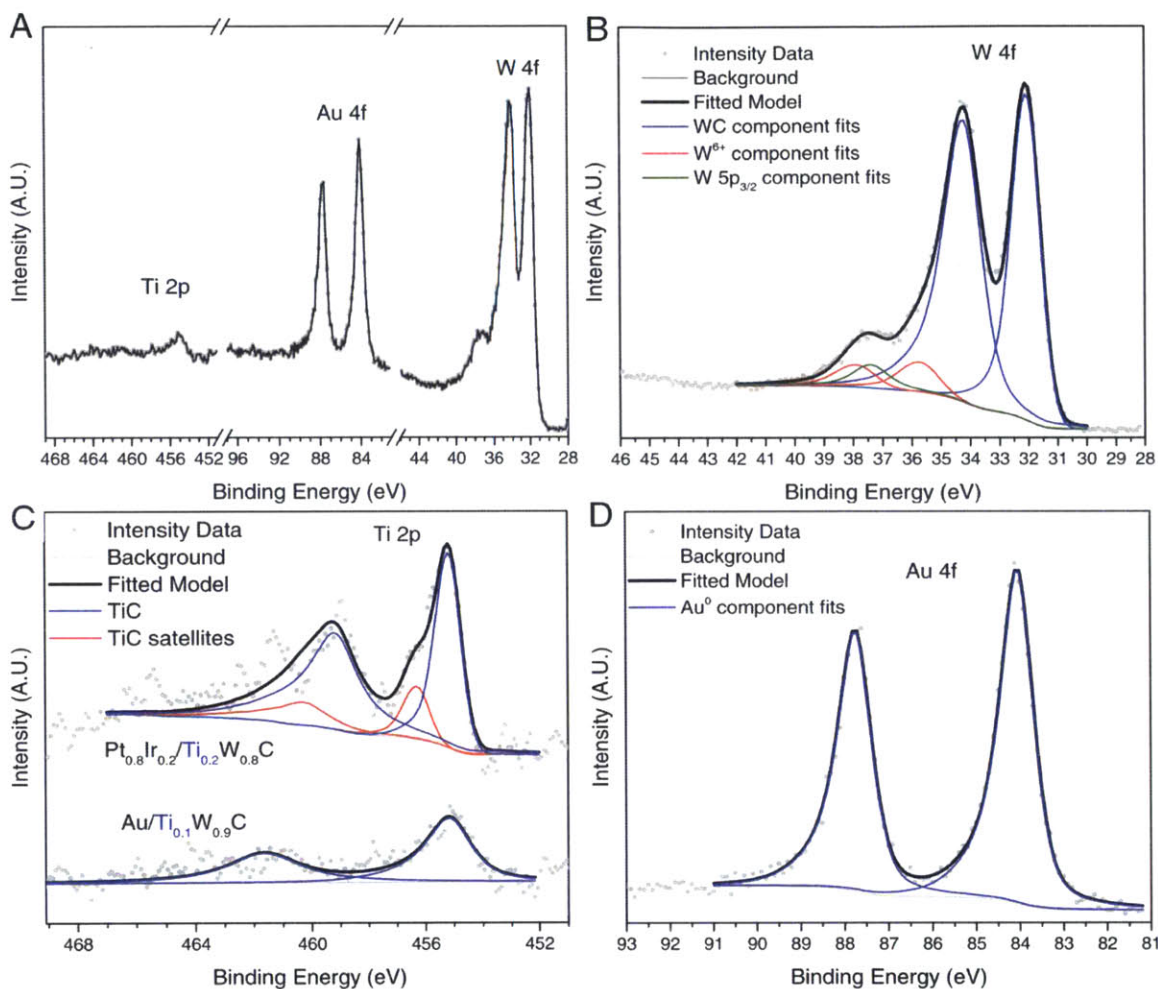


Figure S6.13. XPS Analysis of Au/TiWC NPs.

- (A) Raw XPS intensity data obtained for 13%Au/Ti_{0.1}W_{0.9}C core-shell NP nanoaggregates.
- (B) XPS peak deconvolution of the W 4f spectrum.
- (C) XPS peak deconvolution of the Ti 2p spectrum. The Ti 2p spectrum is difficult to deconvolute for three reasons: the atomic sensitivity factor is low for ejected Ti 2p photoelectrons, the Ti concentration is low in the carbide cores, and the Ti signal is screened by the overlayer of noble metals. For these reasons, the Ti 2p spectrum for Pt_{0.8}Ir_{0.2}/Ti_{0.2}W_{0.8}C is shown. This is a representative core-shell material with a higher core percentage of Ti. In cases where the core percentage is 10%, a deconvolution is difficult to perform and instead an estimate of the Ti composition is obtained from simple integration as shown for the Ti 2p spectrum for Au/Ti_{0.1}W_{0.9}C.
- (D) XPS peak deconvolution of the Au 4f spectrum.

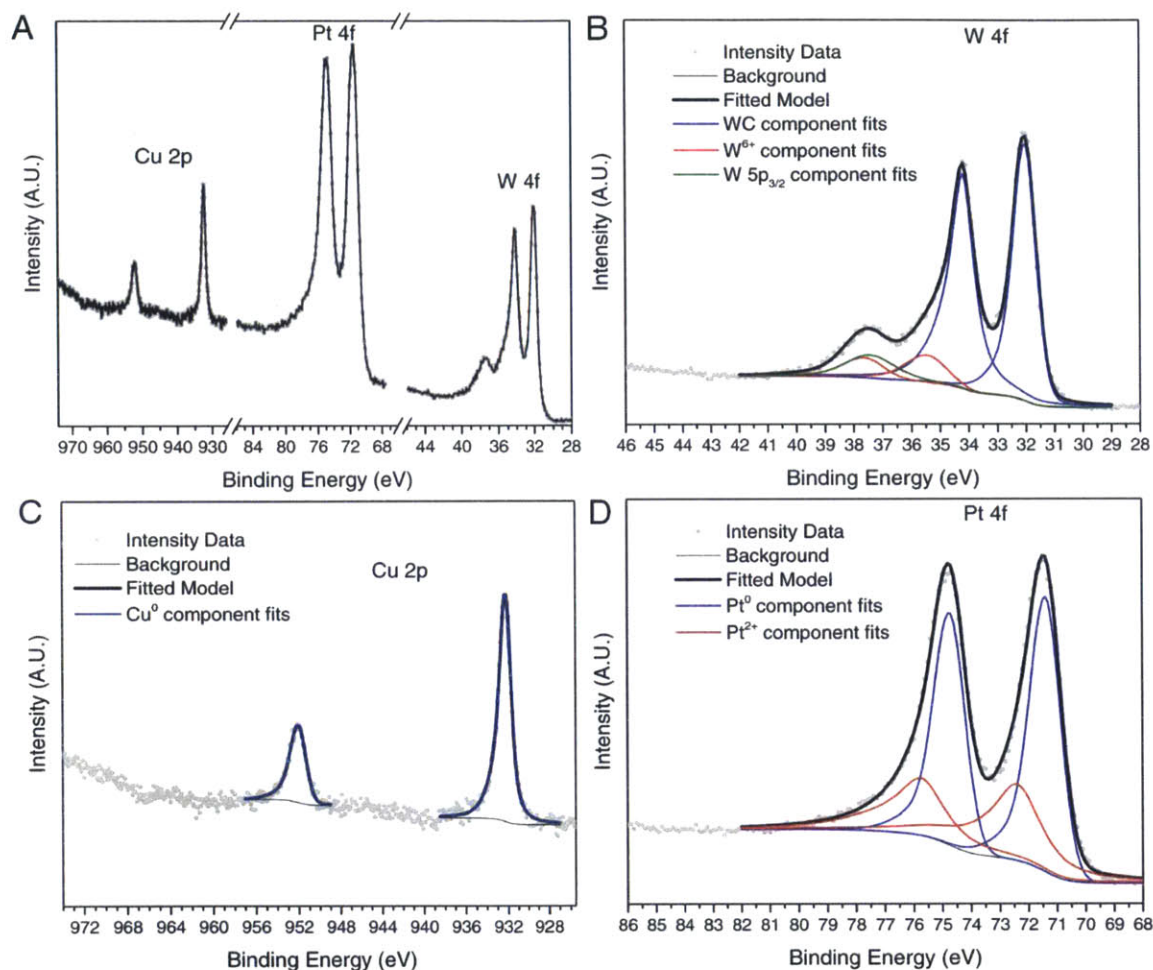


Figure S6.14. XPS Analysis of Pt/CuWC NPs.

(A) Raw XPS intensity data obtained for 26%Pt/(Cu_{0.2}W_{0.8})₂C core-shell NP nanoaggregates. Quantitative results are shown in **Table S6.1**.

(B) XPS peak deconvolution of the W 4f spectrum.

(C) XPS peak deconvolution of the Cu 2p spectrum.

(D) XPS peak deconvolution of the Pt 4f spectrum.

5.5 Microscopy Imaging of Encapsulated and Dispersed NM/TMC NPs

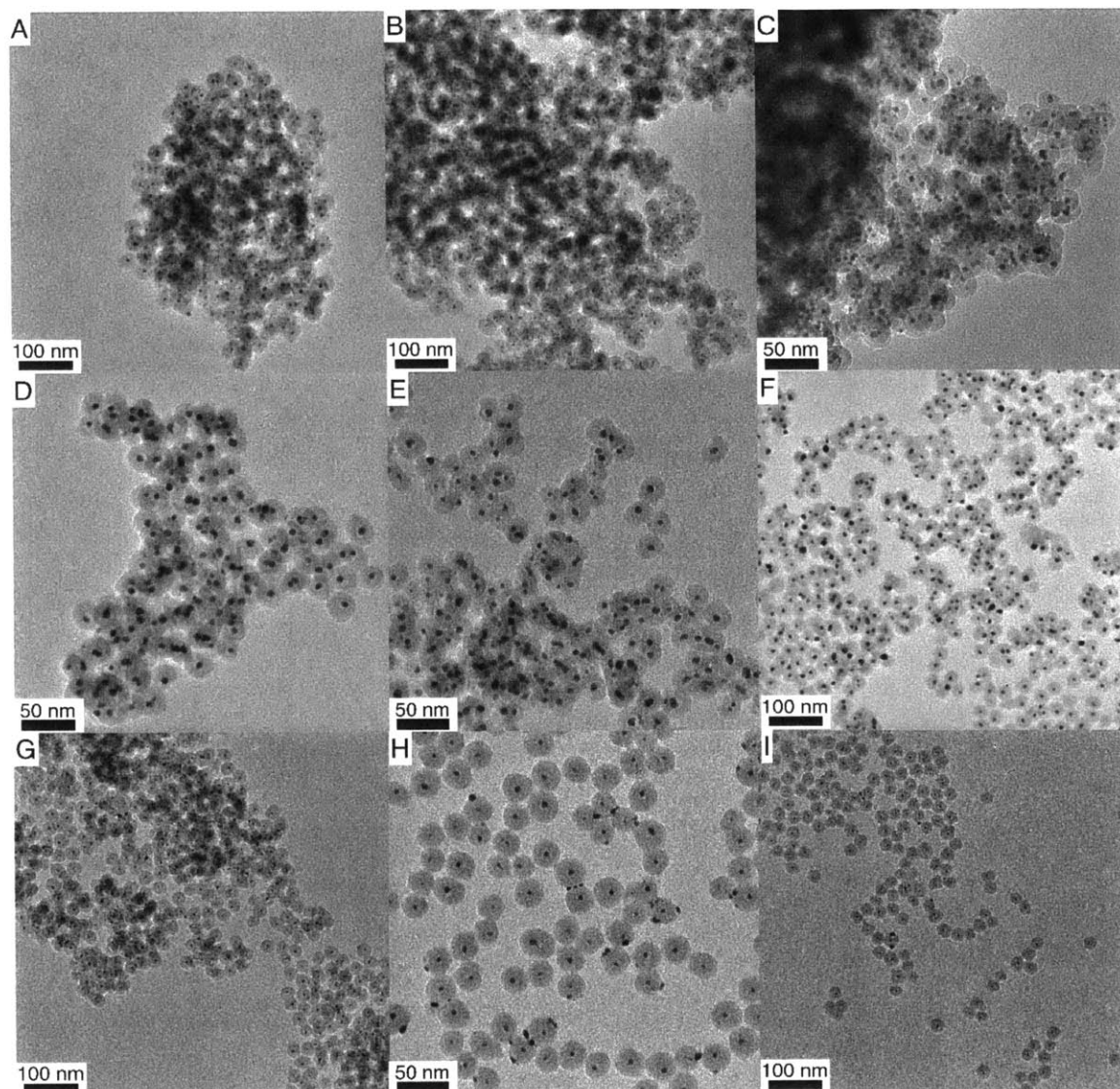


Figure S6.15. TEM Analysis of NPs with Varying Shell Composition Encapsulated in Silica TEM images for a representative selection of different NM/TMC core-shell NPs encapsulated in silica after carburization at 900°C-1000°C in a 15% CH₄/85% H₂ atmosphere. All percentages are based on total metals basis as determined by ICP.

- (A) 6.1 ± 0.9 nm 26% Pt_{0.6}Rh_{0.4} / 74% Ti_{0.1}W_{0.9}C
- (B) 6.4 ± 1.0 nm 27% Pt_{0.5}Ru_{0.5} / 73% Ti_{0.1}W_{0.9}C
- (C) 5.7 ± 1.1 nm 25% Pt_{0.8}Ir_{0.2} / 75% Ti_{0.2}W_{0.8}C
- (D) 6.1 ± 1.0 nm 17% Pt_{0.93}Au_{0.07} / 83% Ti_{0.1}W_{0.9}C
- (E) 9.7 ± 2.0 nm 27% Pt_{0.7}Au_{0.3} / 73% Ti_{0.2}W_{0.8}C
- (F) 7.7 ± 1.4 nm 28% Pt / 72% Ti_{0.1}W_{0.9}C (Pt_{C-S})
- (G) 2.9 ± 0.6 nm 13% Au / 87% Ti_{0.3}W_{0.7}C
- (H) 3.5 ± 1.0 nm 6% Au / 94% Ti_{0.2}W_{0.8}C
- (I) 3.7 ± 1.3 nm 4% Pt / 96% Ti_{0.1}W_{0.9}C

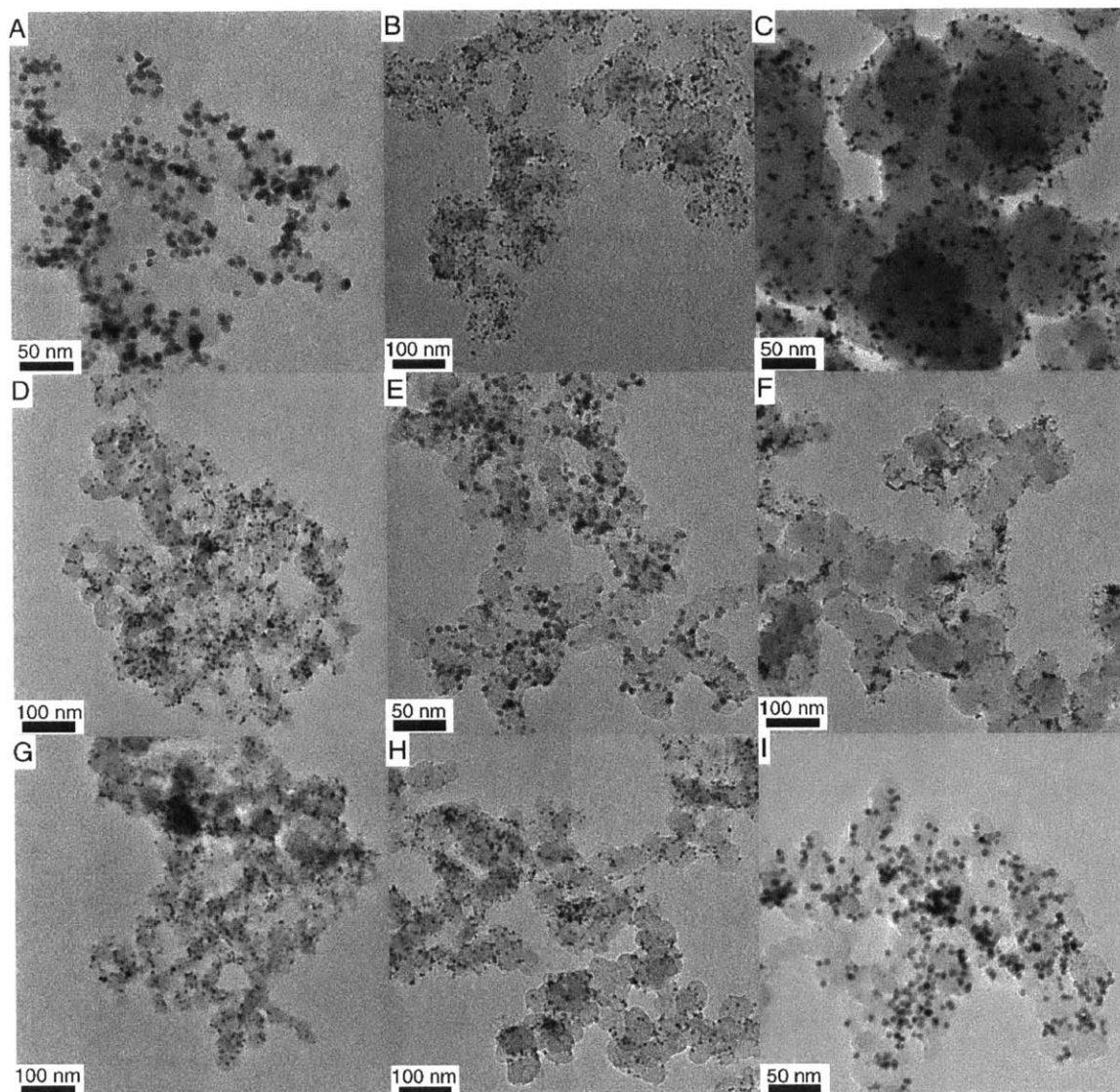


Figure S6.16. TEM Analysis of NPs with Varying Shell Composition Supported on Carbon
 TEM images for a representative selection of different NM/TMC core-shell NPs supported on Vulcan® XC-72r carbon black after removal of the silica template.

- (A) 7.7 ± 1.4 nm 28% Pt / 72% $\text{Ti}_{0.1}\text{W}_{0.9}\text{C}$ NPs supported on carbon ($\text{Pt}_{\text{C-S}}$)
- (B) 7.1 ± 1.4 nm 21% Pt / 79% $\text{Ti}_{0.1}\text{W}_{0.9}\text{C}$ NPs supported on carbon
- (C) 2.9 ± 0.6 nm 13% Au / 87% $\text{Ti}_{0.1}\text{W}_{0.9}\text{C}$ NPs supported on carbon
- (D) 6.1 ± 0.9 nm 26% $\text{Pt}_{0.6}\text{Rh}_{0.4}$ / 74% $\text{Ti}_{0.1}\text{W}_{0.9}\text{C}$ NPs supported on carbon
- (E) 5.7 ± 1.1 nm 25% $\text{Pt}_{0.8}\text{Ir}_{0.2}$ / 75% $\text{Ti}_{0.2}\text{W}_{0.8}\text{C}$ NPs supported on carbon
- (F) 6.1 ± 1.0 nm 17% $\text{Pt}_{0.93}\text{Au}_{0.07}$ / 83% $\text{Ti}_{0.1}\text{W}_{0.9}\text{C}$ NPs supported on carbon
- (G) 4.4 ± 0.8 nm 14% $\text{Pt}_{0.6}\text{Ru}_{0.4}$ / 86% $\text{Ti}_{0.2}\text{W}_{0.8}\text{C}$ NPs supported on carbon
- (H) 6.4 ± 1.0 nm 27% $\text{Pt}_{0.5}\text{Ru}_{0.5}$ / 73% $\text{Ti}_{0.1}\text{W}_{0.9}\text{C}$ NPs supported on carbon
- (I) 6.7 ± 1.0 nm 27% $\text{Pt}_{0.67}\text{Ru}_{0.33}$ / 83% $\text{Ti}_{0.1}\text{W}_{0.9}\text{C}$ NPs supported on carbon ($\text{PtRu}_{\text{C-S}}$)

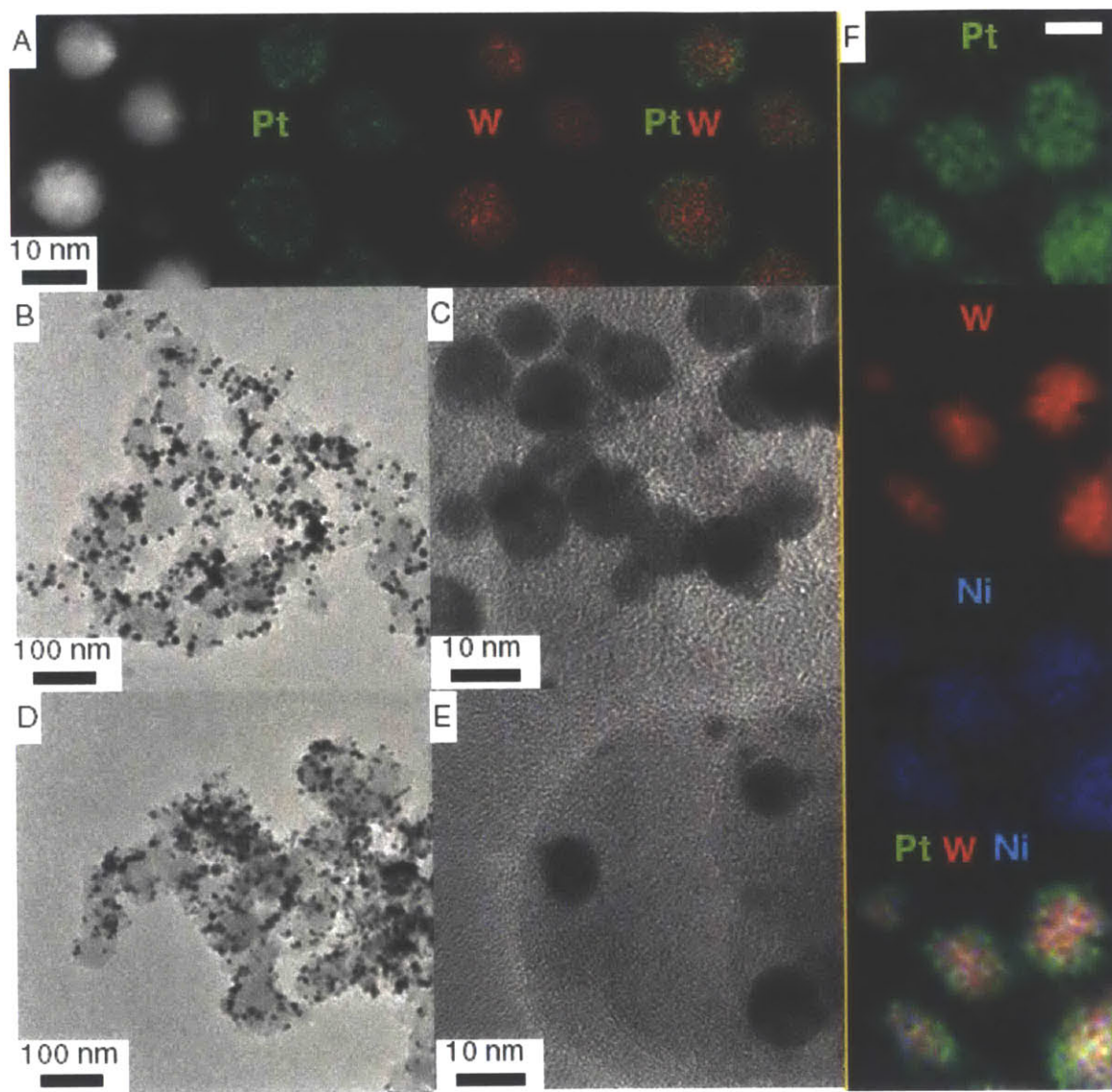


Figure S6.17. Microscopy Analysis of Semicarbide NPs with Varying Core Compositions
(A) STEM-EDX maps and **(B,C)** TEM images of 26%Pt/(Cu_{0.2}W_{0.8})₂C supported on carbon black.
(D, E) TEM images of 23%Pt/(Co_{0.2}W_{0.8})₂C supported on carbon black.
(F) STEM-EDX maps of 16%Pt/(Ni_{0.3}W_{0.7})₂C supported on carbon black. The scale bar shown for Pt is 10 nm and applies to all micrographs.
 The PXRD patterns of these material are shown in **Figure 6.3C**.

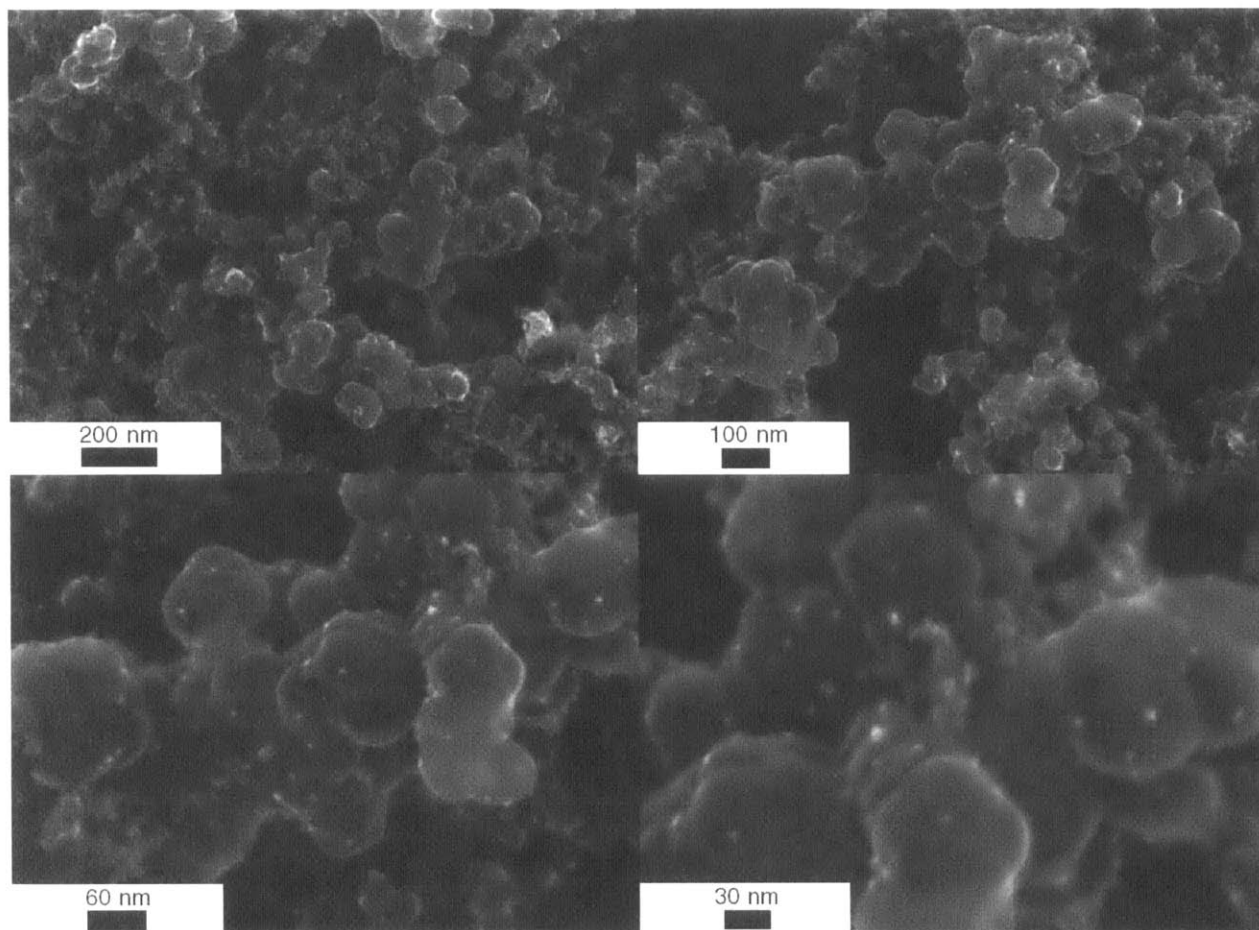


Figure S6.18. Scanning Electron Microscopy (SEM) Analysis of Pt_{c-s} at four different magnifications. While SEM cannot achieve the resolution of TEM, its large depth of field provides for a more three-dimensional representation of how the Pt_{c-s} catalyst is dispersed across the surface of the carbon black support. Special thanks to Mark Weidman for imaging this sample. The sample was prepared by placing a drop of IPA:EtOH:H₂O ink on a silicon wafer. The material was then imaged directly without the need for additional treatments due to the already high electrical conductivity of carbon black.

5.6 Characterization of Commercial Catalysts

Pt_{comm} and PtRu_{comm} are supported on Vulcan® XC-72r carbon black at 20wt%. PtRu_{comm} is formulated in a 1:1 Pt:Ru ratio. The loadings were confirmed using both ICP-MS and TGA, and the errors between the measurements were less than 1%. These commercial catalysts are highly optimized systems exhibiting excellent dispersion. In addition, they are monodisperse and feature ultrasmall nanoparticles in the 1 – 2 nm regime. While larger nanoparticles would be more stable,^[10] ultrasmall nanoparticles are required to

improve the dispersion and by proxy the overall activity. This constraint limits the tunability of this simple architecture for activity and stability improvements as well as cost reductions.

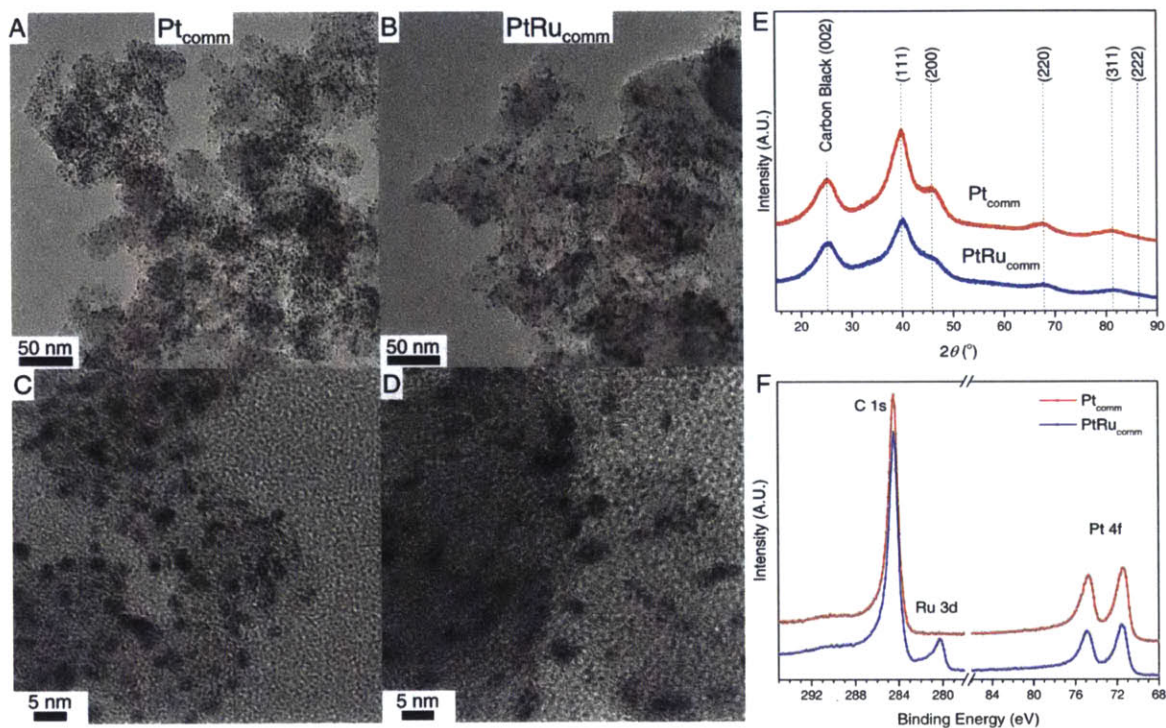


Figure S6.19. Characterization of Commercial Pt_{comm} and $\text{PtRu}_{\text{comm}}$ catalysts. Wide-view TEM and HR-TEM images of (A,C) Pt_{comm} and (B,D) $\text{PtRu}_{\text{comm}}$. (E) PXRD patterns of Pt_{comm} and $\text{PtRu}_{\text{comm}}$. (F) XPS spectra of Pt_{comm} and $\text{PtRu}_{\text{comm}}$. These catalysts are sometimes referred to as Pt/C and PtRu/C.

While Pt_{comm} and $\text{PtRu}_{\text{comm}}$ are highly optimized, the synthesis of even these simple catalysts is non-trivial. For example, the excellent particle sizes and dispersion have not been translated to other commercial catalysts, such as 20wt% Ir/C and 20wt% Au/C imaged below. These catalysts were also purchased from Premetek.

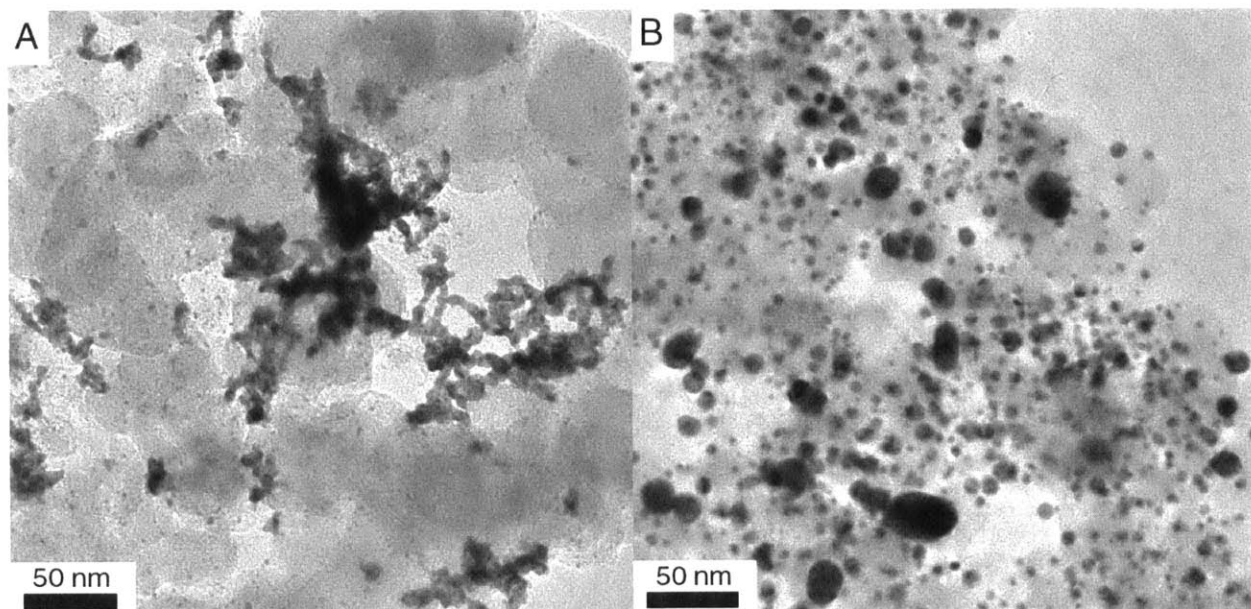


Figure S6.20. Microscopy Analysis of Ir/C and Au/C Commercial Catalysts. (A) shows a TEM image of 20wt% Ir/C which features a bimodal PSD, exhibiting ultrasmall 1 – 3 nm nanoparticles as well as large aggregates of ca. 10 nm crystallites. (B) shows a TEM image of 20wt% Au/C which features on average 4 – 5 nm nanoparticles in a very polydisperse PSD. Some particles shown reach more than 20 nm, which have dispersions under 1%.

Chapter 7

Applications of NM/TMC Core-Shell Nanoparticles in Thermal and Electrocatalysis

1. Introduction

In this chapter, the core-shell materials synthesized and characterized in **Chapter 6** are extensively investigated for applications and electro- and thermo- catalysis. For electrocatalysis, the focus is on cathodic and anodic reactions in acidic media. Currently, acidic media is preferred to alkaline media due to the faster kinetics and the proliferation of Nafion® proton exchange membranes. However, stability is exceptionally challenging in acidic media, and noble metals remain the only viable catalysts for hydrogen oxidation (HOR), methanol electrooxidation (MOR), oxygen reduction (ORR), and oxygen evolution (OER). Impressive earth-abundant catalysts have been developed for hydrogen evolution (HER), where stability is less challenging and the simple reaction is amenable to many surfaces.

This chapter begins with a detailed analysis of how to count surface sites for the 2ML Pt_{C-S} and PtRu_{C-S} catalysts. In doing so, the exceptional CO-tolerance of these catalysts, predicted by DFT calculations in **Chapter 2**, was verified. The materials are then shown to be highly active HER, HOR, and MOR electrocatalysts, remaining stable over 10,000 cycles. CO-tolerance was further examined by performing HOR under 1000 ppm of CO impurities. Currently, H₂ fuel streams for proton exchange membrane fuel cells (PEMFCs) must be rigorously purified to less than 10 ppm of CO via the dangerous expensive preferential oxidation (PRO_x) process. These core-shell electrocatalysts are shown to offer new avenues for improving NM activity, stability, and tolerance to common impurities. As such, they offer the possibility of reducing noble metal loadings while also reducing the purification costs associated with fuel production.

It was shown in **Chapter 4** and **Chapter 5** that WC-based nanoparticles are active and stable HER electrocatalysts. Recently, electrocatalysts based on phosphides and sulfides have been shown to have higher HER activity.^[133,179-183] While all of these earth-

abundant electrocatalysts are asymmetric and therefore poor at HOR, only WC-based electrocatalysts have been demonstrated to have suitable anodic stability up to 600 mV. We show that ultralow sub-monolayer Pt shells offer a viable method for activating WC for both HER and HOR at low overpotentials. A techno-economic analysis was then performed, which shows that sub-monolayer core-shell nanoparticles offer the least expensive water splitting cathode costs over a 50,000 h lifecycle.

Finally, the chapter concludes with an analysis of the thermal stability of sub-monolayer Pt/TiWC nanoparticles under various atmospheres. Both WC and Pt have unique catalytic reactivity for a variety of high temperature reactions, such as isomerization, hydrogenation, dehydrogenation, and hydrodeoxygenation. The mechanisms often proceed through different reactive intermediates. While Pt generally has higher reactivity, it is readily sintered and coked. We show that sub-monolayer Pt/TiWC is thermally stable and offers a new avenue for stabilizing Pt and activating WC for thermal catalytic reactions.

For characterization of the materials analyzed in this chapter, it is recommended that **Chapter 6** is read first. Briefly, Pt_{C-S} consists of 7.1 ± 1.4 nm nanoparticles with a composition of 28%Pt/72%Ti_{0.1}W_{0.9}C dispersed on carbon black at 28wt% (8wt% on carbon, Pt basis). PtRu_{C-S} consists of 6.7 ± 1.0 nm nanoparticles with a composition of 27%Pt_{0.67}Ru_{0.33}/73%Ti_{0.1}W_{0.9}C dispersed on carbon black at 28wt% (7.6wt% on carbon, Pt_{0.67}Ru_{0.33} basis). The electrocatalytic properties of Pt_{C-S} and PtRu_{C-S} were compared to 20wt% carbon-supported commercial electrocatalysts, denoted as Pt_{comm} and PtRu_{comm} using gas diffusion electrodes (GDEs)^[184] and rotating disk electrodes (RDEs).^[185] The commercial catalysts were characterized in **Figure S6.19**. The catalysts are also compared to a control synthesis performed without using silica encapsulation called Pt_{direct}. This highly sintered and coked control was characterized in **Figure 6.2**. The sub-monolayer Pt/TiWC catalysts are characterized in **Figure 6.4** and range from 2 ML of Pt to 0.004 ML of Pt supported on TiWC cores. The thermal study is performed on Pt_{sub-ML}, which is ca. 0.25 ML of Pt/TiWC crystallized as 3 nm nanoparticles.

2. Results and Discussion

2.1 Measurement of Electrochemical Active Surface Area

There are three primary normalization schemes to compare electrocatalytic reactivity: geometric activity, mass activity, and specific activity. Geometric activity normalizes by the exposed surface area of the working electrode and is the simplest but least informative. Mass activity is the most commercially relevant, indicating how efficiently different catalyst architectures utilize scarce materials. Specific activity is the most relevant to materials design and understanding the intrinsic activity of different catalysts. To normalize by specific activity, the catalytically active sites have to be titrated with a probe molecule. In thermal catalysis, this is typically done using *ex-situ* chemisorption experiments. Site titrations are considerably easier in electrocatalysis where they can be performed *in-situ* on an as-prepared working electrode using the underpotential deposition of hydrogen (H_{upd}), the oxidation of pre-adsorbed CO (“CO-stripping”), or the stripping of probe metals from solution such as Cu and Pb.

Once all of the active sites have been counted, the specific surface area can be divided by the mass loading to obtain the electrochemical active surface area (ECSA) or divided by the geometric surface area of the working electrode to obtain the roughness factor (r_f). Many assumptions are involved for the different specific surface area measurement methods, which are satisfied to varying degrees for different materials.^[186] For Pt nanoparticles supported on carbon black, both CO-stripping (to obtain the CO-ECSA) and H_{upd} (to obtain the H_{upd} -ECSA) are well-defined. For PtRu nanoparticles, H_{upd} is not well-defined because the pseudocapactive contribution of surface RuO_x species during scanning obfuscates the onset of underpotentially deposited hydrogen.^[187] For bimetallic Pt-based nanoparticles and Pt loaded on ceramic supports, the agreement in ECSA values obtained from H_{upd} and CO-stripping can deviate substantially.^[188,189] Therefore, careful analysis of specific activity measurements must be performed on novel materials before those measurements can be reliably utilized to normalize by specific surface area.

Table 7.1. Electrochemical Active Surface Areas of Core-Shell and Commercial Catalysts

Catalysts	CO- r_f ($\text{cm}^2_{\text{NM}} \text{cm}^{-2}_{\text{geo}}$)	CO-ECSA ($\text{m}^2 \text{g}^{-1}_{\text{NM}}$)	H_{upd} -ECSA ($\text{m}^2 \text{g}^{-1}_{\text{NM}}$)	CO-ECSA / H_{upd} -ECSA
Pt _{comm}	34.6 ± 3.0	67.9 ± 5.8	68.0 ± 7.0	1.00 ± 0.02
PtRu _{comm}	50.3 ± 3.6	98.9 ± 7.1	N.R.	N.R.
Pt _{C-S}	10.2 ± 0.4	49.9 ± 2.2	54.9 ± 6.6	0.92 ± 0.07
PtRu _{C-S}	14.1 ± 0.3	72.8 ± 1.5	46.4 ± 2.0	1.53 ± 0.05

N.R. - not reported

Table 7.1 depicts the H_{upd} and CO-stripping results for triplicate electrode mountings of the electrocatalysts. In agreement with the literature for bimetallic electrocatalysts,^[188] there was a deviation in the ratios between CO-ECSA and H_{upd} -ECSA for the core-shell catalysts. For PtRu_{C-S}, this could be attributed to the pseudocapacitive effect of RuO_x species while for Pt_{C-S}, this could be attributed to the overlap in transition between complete H_{upd} and the onset of HER. As such, CO-stripping was used as the more reliable normalization scheme. Rather than using the CO-ECSAs directly, all normalizations are reported using the roughness factors (CO- r_f). The CO stripping scans, the post CO stripping scans, and the pre CO-stripping scans for the carbide materials are shown in **Figure 7.1**.

These measurements were collected by holding the working electrode potentiostatically at +0.025 V vs. RHE in CO-saturated 0.1 M HClO₄ at 30°C under a rotation rate of 1600 rpm followed by an Ar-purge and scanning at 50 mV s⁻¹ with iR compensation. The reported “post CO-strip” CVs are the second scan obtained immediately after the first CO-stripping scan. In some cases, a “pre CO-strip” CV was obtained immediately prior to the actual CO stripping measurement in accordance with a recently developed method to obtain a more accurate background.^[189] However, due to the complex pre-peak of the core-shell samples, an optimized Tougaard background was used when integrating the charge under the CO-stripping voltammograms instead of standard linear backgrounds, which were found to bisect the data. The Tougaard background was found to be more suitable and more conservative than using either the pre or post CO-stripping scans as backgrounds. If the carbide cores were not subsurface,

Figure 7.1E shows that the contribution from the carbide core to the CO-stripping voltammograms in **Figure 7.1C** and **D** would be less than 10%. CO-stripping was performed as the last step in all experimental sequences, after conditioning scans, HER, HOR, CO/HOR, and MOR studies.^[188]

Both Pt_{comm} and $\text{PtRu}_{\text{comm}}$ have high CO-ECSAs of $68 \pm 6 \text{ m}^2 \text{ g}^{-1}_{\text{NM}}$ and $99 \pm 7 \text{ m}^2 \text{ g}^{-1}_{\text{NM}}$, respectively. Despite having larger PSDs (6-8 nm) than the commercial samples, both $\text{Pt}_{\text{C-S}}$ and $\text{PtRu}_{\text{C-S}}$ achieve comparable CO-ECSAs of $50 \pm 2 \text{ m}^2 \text{ g}^{-1}_{\text{NM}}$ and $73 \pm 2 \text{ m}^2 \text{ g}^{-1}_{\text{NM}}$, respectively. $\text{Pt}_{\text{direct}}$ did not exhibit a measureable CO-ECSA because the surface Pt sites are blocked by extensive coking (**Figure 6.2**). Reliable CO-ECSA and H_{upd} -ECSA was also unobtainable for 0.25 ML Pt/TiWC, 0.05 ML Pt/TiWC, and 0.004 ML Pt/TiWC catalysts, which had poorly defined regions for hydrogen underpotential deposition and appeared inert to CO adsorption. As such, specific activities could not be compared for the sub-monolayer catalysts and instead geometric and mass activities were used.

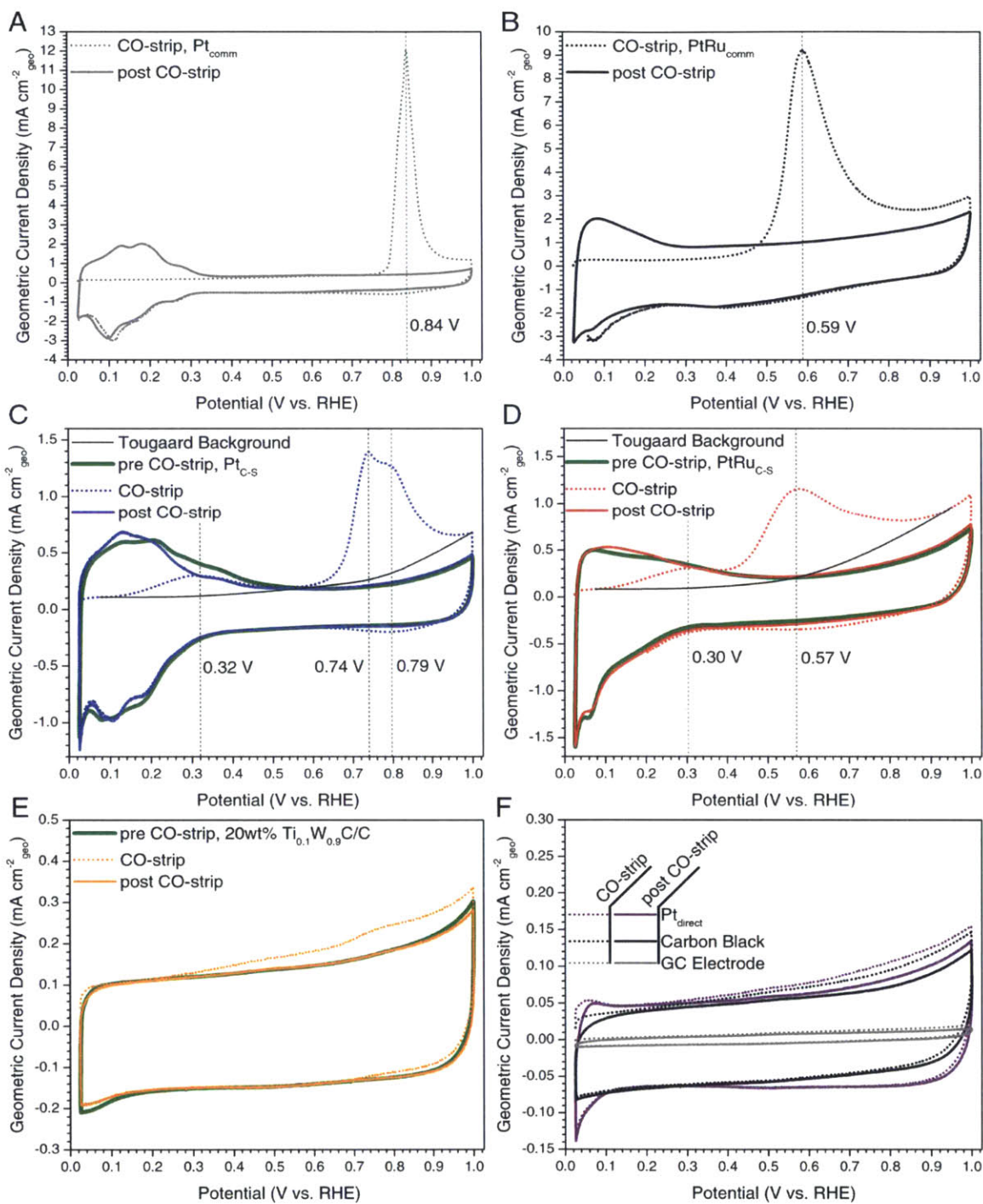


Figure 7.1. CO-Stripping Voltammograms of (A) Pt_{comm}, (B) PtRu_{comm}, (C) Pt_{C-S}, (D) PtRu_{C-S}, (E) 20 wt% Ti_{0.1}W_{0.9}C, and (F) Pt_{direct}, carbon black, and empty GC electrode

2.2 Core-Shell Pt/TiWC and PtRu/TiWC for Hydrogen Evolution and Oxidation, CO-tolerant Electrocatalysis, and Methanol Electrooxidation

In this section, we show that TiWC cores favorably modulate the electrocatalytic properties of 2-3 ML Pt and PtRu shells. The implications of these modulations are observed even in simple cyclic voltammetry scans shown in **Figure 7.2**.

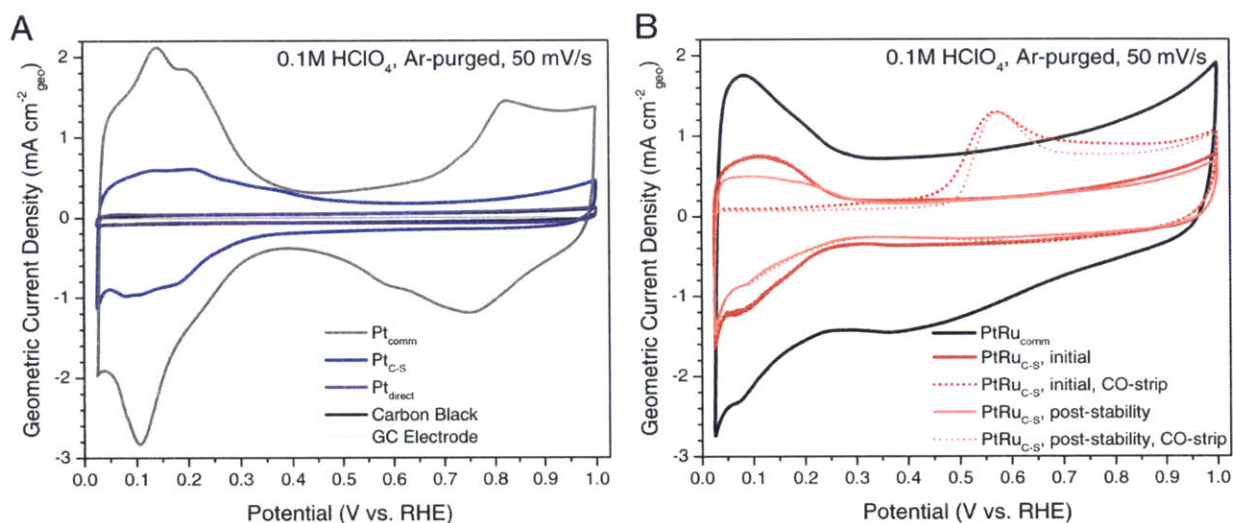


Figure 7.2. Cyclic Voltammograms. **(A)** and **(B)** Post-conditioning CVs collected from +0.025 V to 1.0 V at 50 mV s⁻¹ in Ar-saturated 0.1 M HClO₄ at 30 °C under a rotation rate of 1000 rpm.

Pt_{direct} exhibits similar electrochemical behavior as the Vulcan® XC-72r carbon black control, in agreement with the TEM and XPS analysis (**Figure 6.2**) illustrating particle sintering and blockage of active sites by graphitic coke. In contrast, the cyclic voltammograms (CVs) for Pt_{C-S} and PtRu_{C-S} exhibit high capacitance and characteristic peaks for hydrogen adsorption/desorption (H_{upd}) below 0.4 V, but with notable differences from Pt_{comm} and PtRu_{comm}, such as suppressed OH adsorption/desorption (OH_{ad}) features above 0.6 V. These differences suggest that the TiWC cores modulate the electrochemical behavior of the Pt and PtRu shells.

Figure 7.3 depicts an overall reactivity and stability study of Pt_{C-S} and PtRu_{C-S} for HER, HOR, HOR under CO contamination, and MOR. Both Pt_{C-S} and PtRu_{C-S} exhibited improved specific activity for HER and HOR, indicating that TiWC cores are excellent

supports for NM monolayers and can favorably alter catalytic activity. Despite a 60% reduction in NM loading, Pt_{c-s} and PtRu_{c-s} exhibited a near-symmetric activity profile during HER and HOR linear sweep voltammetry (LSV) measurements performed using GDEs in the absence of mass transfer limitations that is similar to that observed for the commercial catalysts (**Figure 7.3A**). Both core-shell materials exhibited HER and HOR Tafel slopes of ca. 30 mV dec⁻¹ even after 10,000 cycles between -50 and 600 mV (**Table 7.2**, **Figure 7.4**, and **Figure 7.5**). At an HER overpotential of 50 mV, both core-shell materials show a 4-fold improvement in specific activity and a 3-fold improvement in mass activity over the commercial catalysts (**Table 7.3**) and maintain this enhancement after cycling.

Enhanced catalytic activity is corroborated by DFT calculations for thermally equilibrated Pt/TiWC slabs as outlined in **Chapter 2**. Specifically, our calculations show Fermi level matching with Pt, which translates to minimal alterations to the workfunction of surface Pt by subsurface TiWC (**Figure 2.4** and **Figure 2.5**),^[190] but show that the d-band center for a 2 monolayer Pt shell downshifts from -2.7 eV to -2.8 eV (**Figure 2.5**). This downshift provides access to potentially favorable surface properties, such as a significant weakening of the CO binding energy by ca. 40 kJ/mol.^[2] In turn, this effect can increase the tolerance of Pt_{c-s} and PtRu_{c-s} towards CO poisoning, thereby overcoming one of the major challenges afflicting the performance of industrial Pt-based catalysts in many electrochemical applications.^[139,171]

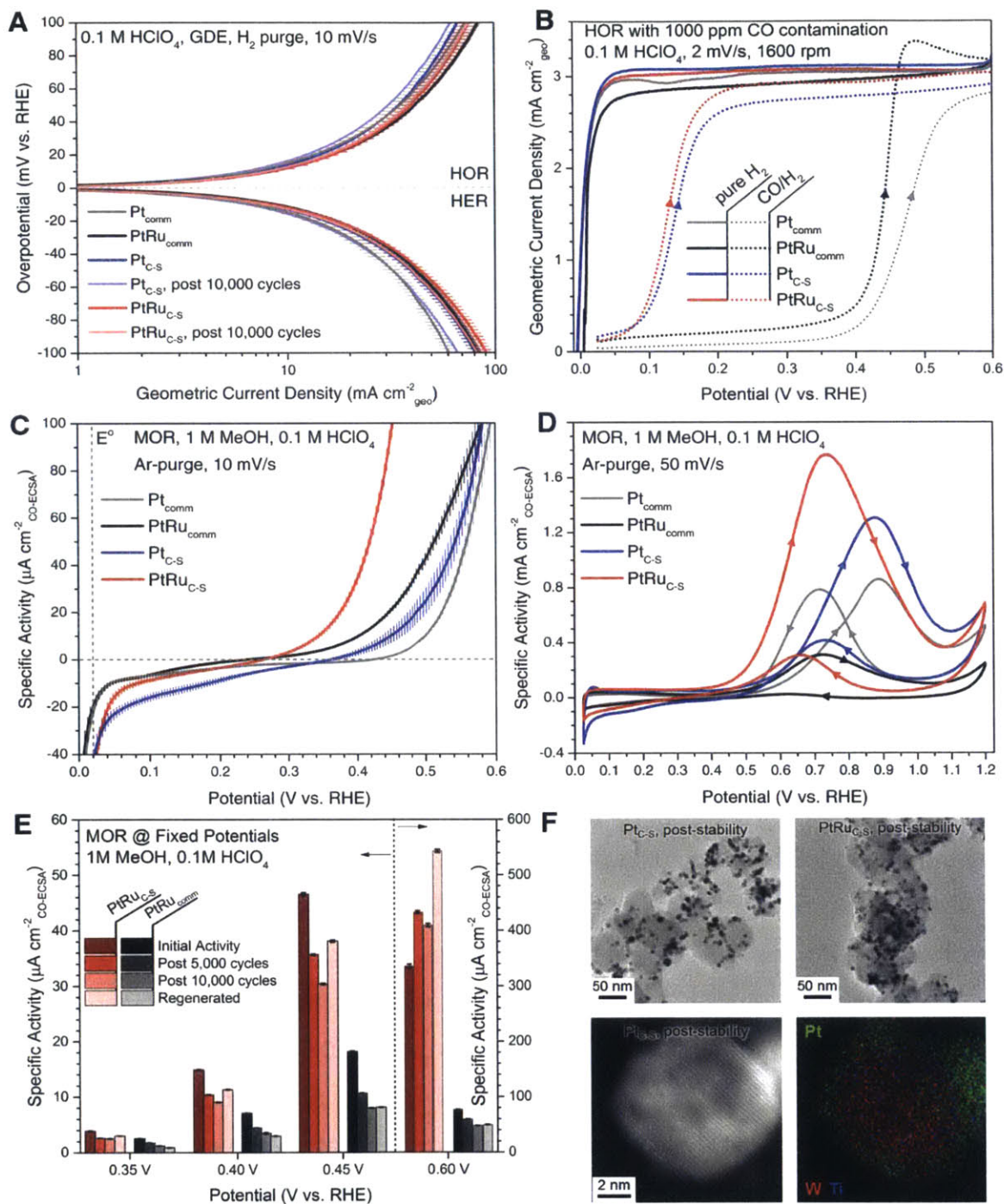


Figure 7.3. Electrochemical Activity and Stability of Pt_{c-s} and PtRu_{c-s} compared to commercial catalysts. (A) HOR/HER Tafel plots (B) HOR LSVs with and without CO contamination. (C) LSVs and (D) CVs for MOR normalized by CO-ECSA roughness factors. (E) Steady-state specific activity at fixed potentials after stability cycling and regeneration in alkaline media. (F) TEM images of Pt_{c-s} and PtRu_{c-s} and a STEM image with EDX map of a Pt_{c-s} nanoparticle after stability cycling. All electrochemistry measurements were performed at 30 °C.

Indeed, HOR experiments performed in the presence of high CO concentrations confirm that the TiWC cores mitigate poisoning on Pt and PtRu monolayers. Specifically, while 1000 ppm of CO contamination markedly increases the HOR onset potential by ca. 400 mV for PtRu_{comm} (**Figure 7.3B**) and by ca. 200 mV for a state-of-the-art Pt/PtSn catalyst,^[139] both Pt_{C-S} and PtRu_{C-S} catalyze HOR with an overpotential as low as 50 mV. Under pure CO, both Pt_{C-S} and PtRu_{C-S} achieved an approximately 200 mV lower onset potential and a 30-fold enhancement in specific activity for CO electrooxidation at 400 mV when compared to the commercial catalysts (**Figure 7.6**).

By decreasing the CO binding strength, the TiWC core is responsible for enhancing the MOR kinetics observed for Pt_{C-S} compared to Pt_{comm}. The former features a higher specific activity over a wide potential window and a ca. 100 mV lower onset potential than Pt_{comm} (**Figure 7.3C, D** and **Figure 7.7**). Ru is known to improve the performance of Pt catalysts at low MOR overpotentials via a bifunctional mechanism,^[191] and despite extensive efforts, little improvement in the activity and durability of MOR catalysts have been achieved over commercial PtRu/C in acidic media.^[192] Indeed, both PtRu_{C-S} and PtRu_{comm} achieve a low onset potential of ca. 250 mV. However, PtRu_{C-S} displays a significantly higher steady-state turnover frequency (TOF) of 15.9 min⁻¹ at 0.6 V compared to 3.6 min⁻¹ using PtRu_{comm} (**Table 7.4**), further evidencing the favorable activity modulation achievable using a TiWC core.

PtRu_{C-S} also demonstrates enhanced stability compared to PtRu_{comm} (**Figure 7.3E**, **Figure 7.8**, and **Figure 7.9**). After 10,000 cycles, PtRu_{comm} loses more than 50% of its steady-state activity at 0.35 V, 0.4 V, and 0.45 V, whereas the PtRu_{C-S} activity decreases by only 35% at these potentials and actually improves at 0.6 V. Notably, a simple 2 min alkaline dip partially regenerated the activity of PtRu_{C-S} at all potentials, but had no appreciable benefit for PtRu_{comm}. Specifically, after regeneration, the overall loss in activity at 0.45 V was 18% and 55% for PtRu_{C-S} and PtRu_{comm}, respectively. The final TOF at 0.6 V after 10,000 cycles and regeneration was 25.7 min⁻¹ for PtRu_{C-S}, 2.4 min⁻¹ for PtRu_{comm}, 1.8 min⁻¹ for Pt_{C-S}, and 1.1 min⁻¹ for Pt_{comm} (**Table 7.4**), which represents an order of magnitude improvement of our core-shell material over the commercial catalysts.

No appreciable deactivation via particle sintering was observed for the core-shell materials after 10,000 cycles (**Figure 7.3F**). HR-STEM and EDX mapping of Pt_{C-S} after

stability cycling show a highly crystalline composite nanoparticle with an intact Pt shell and a well-alloyed TiWC core (**Figure 7.3F** and **Figure 7.10**). We attribute the improved stability of the core-shell materials to the strong NM-TMC interfacial bonds and to the lower surface free energies of large nanoparticles relative to the surface free energies of ultrasmall nanoparticles.^[10] These results clearly demonstrate the ability of our method to reformulate a classic bimetallic NM catalyst, such as PtRu, into a new architecture that preserves the complexity of the original bimetallic surface chemistry while favorably modulating catalytic performance through subsurface strain and ligand effects. As a unique class of materials that breaks the traditional metal-adsorbate scaling relations for transition metals,^[24] TMCs not only serve as ideal core candidates to reduce NM loadings, but could favorably impact catalytic activity for several industrially-relevant reactions, such as HOR, MOR, water-gas shift, or methanol synthesis wherein CO coverage effects deeply influence catalyst performance.

Hydrogen Evolution and Hydrogen Oxidation Measurements

Exchange current densities (j_0) and Tafel slopes (b) were determined from both the HOR and HER LSVs (shown in **Figure 7.3A** and **Figure 7.5**) using a GDE in 1 M HClO₄ and 0.1 M HClO₄. Also shown are j_0 and b values determined from both HOR and HER LSVs (**Figure 7.4A**) obtained using an RDE in 0.1 M HClO₄. Linear fits for all materials were performed at overpotentials from 15 to 30 mV. The reported errors are propagated from the standard errors in the regression. For the RDE measurements, the kinetic HOR current was obtained from the Koutecky-Levich equation. We note that HOR/HER kinetics of platinum group metals are exceptionally fast,^[193] making the kinetic analysis from the RDE underestimated and the GDE data more reliable.^[184,194] While the RDE data is only included for comparison, it is likely still relevant to the operating activity of an integrated device.^[195]

Table 7.2. HOR and HER kinetics**GDE in 1.0 M HClO₄, H₂ purge, 30 °C, 10 mV s⁻¹**

Catalyst	HOR j_0 (mA cm ⁻²)	HER j_0 (mA cm ⁻²)	HOR b (mV dec ⁻¹)	HER b (mV dec ⁻¹)
Pt _{comm}	24.4 ± 4.0	25.8 ± 4.5	31.9 ± 1.0	33.3 ± 1.1
PtRu _{comm}	26.7 ± 4.7	29.1 ± 4.9	33.3 ± 1.1	32.3 ± 1.0
Pt _{C-S}	32.8 ± 6.3	35.4 ± 6.1	34.1 ± 1.2	30.8 ± 0.9
PtRu _{C-S}	34.2 ± 6.0	34.4 ± 6.4	33.1 ± 1.0	32.4 ± 1.0

GDE in 0.1 M HClO₄, H₂ purge, 30 °C, 10 mV s⁻¹

Catalyst	HOR j_0 (mA cm ⁻²)	HER j_0 (mA cm ⁻²)	HOR b (mV dec ⁻¹)	HER b (mV dec ⁻¹)
Pt _{comm}	3.45 ± .25	3.72 ± .31	32.6 ± .9	35.1 ± 1.1
PtRu _{comm}	4.30 ± .39	4.52 ± .41	33.1 ± 1.0	33.6 ± 1.0
Pt _{C-S}	3.77 ± .29	4.05 ± .34	33.5 ± 1.0	33.8 ± 1.0
Pt _{C-S} post 10,000	3.21 ± .23	3.42 ± .26	33.3 ± 1.0	34.1 ± 1.0
PtRu _{C-S}	4.60 ± .41	4.64 ± .43	35.1 ± 1.1	34.1 ± 1.1
PtRu _{C-S}	4.20 ± .35	4.18 ± .37	33.8 ± 1.0	31.5 ± 1.0

RDE in 0.1 M HClO₄, H₂-saturated, 30 °C, 10 mV s⁻¹, 1600 rpm

Catalyst	HOR j_0 (mA cm ⁻²)	HER j_0 (mA cm ⁻²)	HOR b (mV dec ⁻¹)	HER b (mV dec ⁻¹)
Pt _{comm}	1.14 ± .04	1.13 ± .04	30.6 ± .6	32.4 ± .9
PtRu _{comm}	1.14 ± .04	1.14 ± .03	33.8 ± .7	33.5 ± .7
Pt _{C-S}	1.06 ± .03	1.03 ± .05	28.3 ± .4	32.4 ± 1.0
Pt _{C-S} post 10,000	1.09 ± .02	1.29 ± .04	28.3 ± .3	31.8 ± .9
PtRu _{C-S}	1.11 ± .03	1.16 ± .04	29.6 ± .5	31.3 ± .8
PtRu _{C-S}	1.03 ± .03	1.25 ± .04	28.5 ± .4	29.6 ± .7

Note that the theoretical Tafel slope is 30 mV dec⁻¹ for a 2-electron reaction where the rate-limiting step is Tafel recombination. Furthermore, the equivalent j_0 and b for HER and HOR imply a symmetric charge transfer coefficient (β) of 0.5. All materials tested above exhibit Tafel slopes close to the theoretical value. The similarity between the HOR and HER j_0 and b values implies near-symmetric charge transfer for all materials.

Chronoamperometry (CA) and chronopotentiometry (CP) measurements were performed in H₂-saturated 0.1 M HClO₄ at 30°C under a rotation rate of 2500 rpm. Initial activities were averaged from triplicate electrode mountings. $\eta@j_{geo=10}$ is the overpotential required to drive a geometric current density of 10 mA cm⁻² as determined by CP measurements. Conversely, $j_{geo}@\eta=50\text{mV}$ is the geometric current density achieved at a fixed overpotential of 50 mV as determined by CA measurements. The achieved current

densities were also normalized by surface sites (determined from CO-stripping measurements) to obtain $j_{\text{specific}}@_{\eta=50\text{mV}}$ and by mass of NM loaded to obtain $j_{\text{mass}}@_{\eta=50\text{mV}}$. The specific activity was used to determine the turnover frequency (TOF@ $\eta=50\text{mV}$), where the TOF is given as mol H₂ per mol of surface sites per second.

Table 7.3. HER Activity from CP and CA measurements

Catalyst	$\eta@j_{\text{geo}=10}$ (mV)	$j_{\text{geo}}@_{\eta=50\text{mV}}$ (mA cm ⁻² _{geo})	$j_{\text{specific}}@_{\eta=50\text{mV}}$ ($\mu\text{A cm}^{-2}$ _{CO-ECSA})	$j_{\text{mass}}@_{\eta=50\text{mV}}$ (mA mg ⁻¹ _{NM})	TOF@ $\eta=50\text{mV}$ (s ⁻¹)
Pt _{comm}	39.4 ± .7	13.1 ± .2	379 ± 33	258 ± 4	0.80 ± 0.08
PtRu _{comm}	42.4 ± .8	13.7 ± .3	272 ± 20	269 ± 6	0.65 ± 0.05
Pt _{C-S}	37.5 ± .9	15.1 ± .4	1482 ± 76	740 ± 20	3.53 ± 0.18
Pt _{C-S} post 10,000	43.8 ± .7	12.4 ± .1	1221 ± 5	610 ± 3	2.91 ± 0.01
PtRu _{C-S}	38.1 ± 1.2	13.9 ± .7	987 ± 58	719 ± 40	2.35 ± 0.14
PtRu _{C-S} post 10,000	38.2 ± .3	14.4 ± .1	1226 ± 8	742 ± 4	3.01 ± 0.02
Pt _{direct}	148 ± 4	0.45 ± .03	N.R.	N.R.	N.R.
Vulcan Carbon	594 ± 6	0.03 ± .00	N.R.	N.R.	N.R.

N.R. - not reported

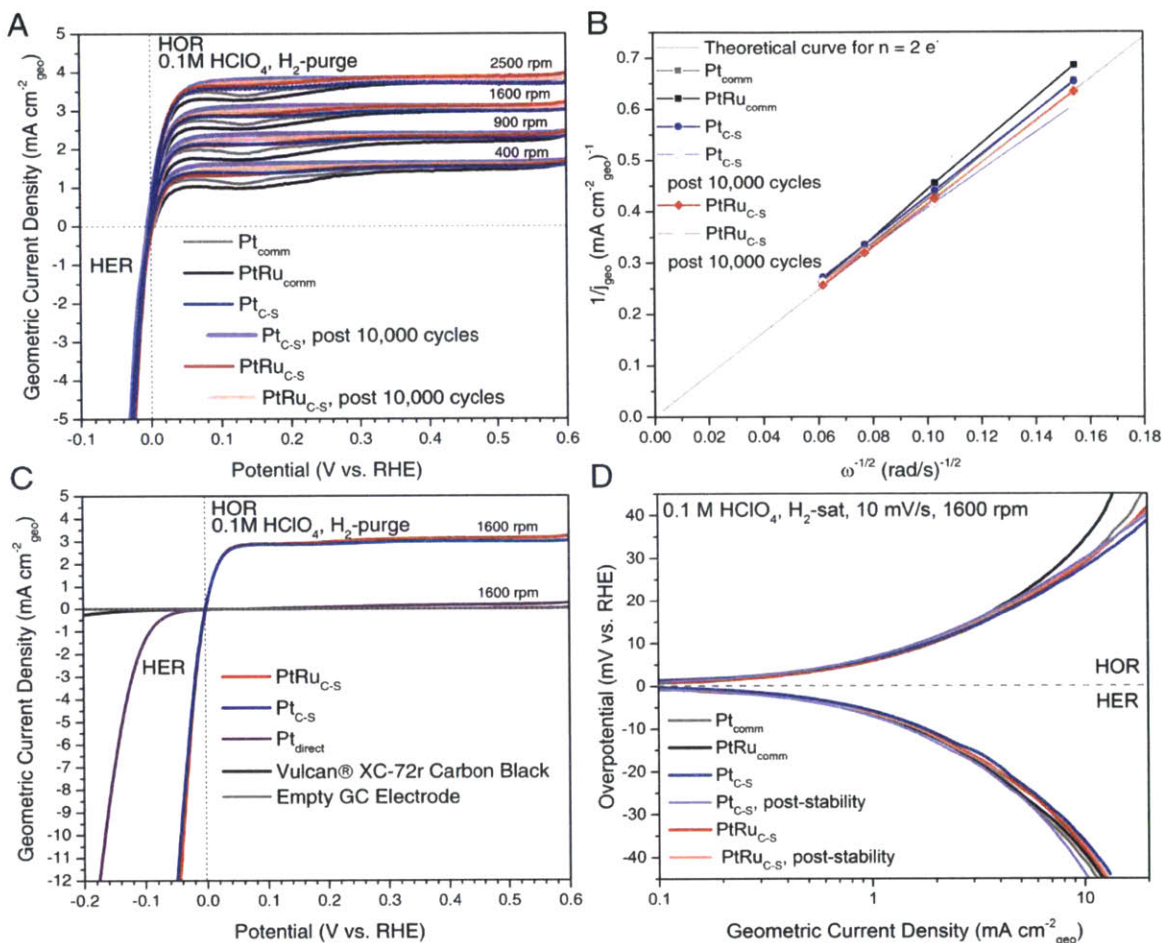


Figure 7.4. HOR and HER Activity Analysis using RDEs

All measurements were performed in H_2 -saturated 0.1 M HClO_4 at 30°C and 10 mV s^{-1} using various rotation rates listed on each panel.

(A) Raw LSV data collected for various catalysts before and after 10,000 potential cycles. These data were used to obtain the Tafel plots in panel D

(B) A Koutecky-Levich plot obtained from the LSVs shown in (A) using the current densities at 0.5 V and various rotation rates. The theoretical line was constructed for a 2-electron transfer process using a diffusion coefficient of $4.5 \cdot 10^{-5} \text{ cm}^2 \text{ s}^{-1}$, a solution viscosity of $0.008 \text{ cm}^2 \text{ s}^{-1}$ at 30°C , and a concentration of $7.2 \cdot 10^{-7} \text{ mol H}_2 \text{ cm}^{-3}$ electrolyte.

(C) Raw LSV data obtained at 1600 rpm for $\text{Pt}_{\text{C-S}}$ and $\text{PtRu}_{\text{C-S}}$ compared to empty Vulcan® XC-72r carbon black, an empty GC electrode, and $\text{Pt}_{\text{direct}}$. The extensive coking and sintering suppresses both the HER and HOR activity of $\text{Pt}_{\text{direct}}$ in comparison with the core-shell materials prepared using silica encapsulation/removal.

(D) Tafel plot constructed from the 1600 rpm RDE data in panel A. This plot was used to extract the RDE kinetic parameters in **Table 7.2**.

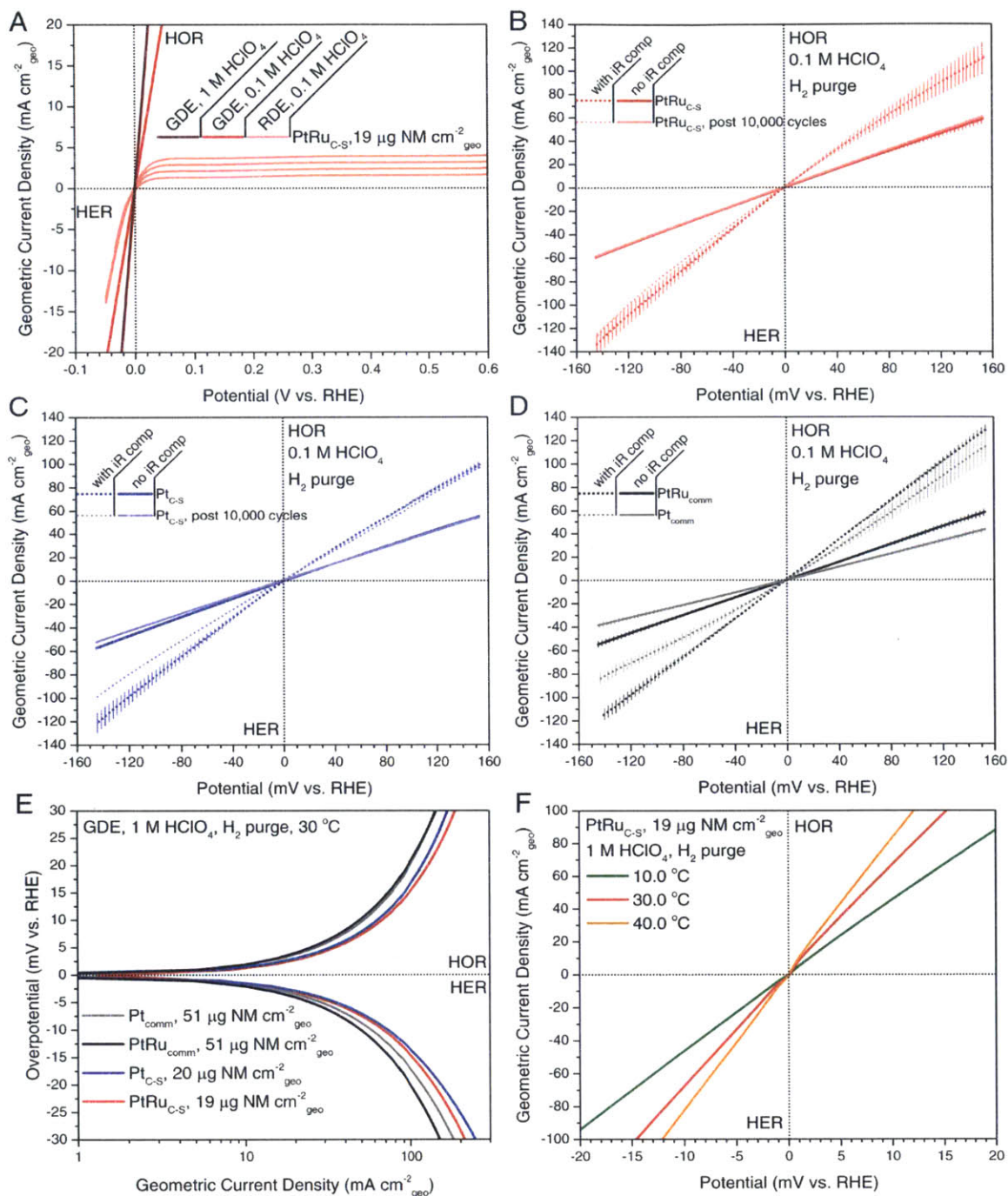


Figure 7.5. HOR and HER Activity Analysis using GDEs

All measurements were performed under an H₂ purge at 10 mV s⁻¹.

(A) PtRu_{C-S} HOR/HER LSVs using a GDE in 1 M HClO₄, a GDE in 0.1 M HClO₄, and an RDE in 0.1 M HClO₄ at various rotation rates. No iR compensation was applied.

(B) PtRu_{C-S} LSVs obtained with and without instrument-applied iR compensation before and after 10,000 cycles. Error bars are shown for the initial activity measurements and

were obtained from triplicate electrode mountings. The iR-compensated data was used to construct **Figure 7.3A**.

(C) Pt_{C-S} LSVs obtained with and without instrument-applied iR compensation before and after 10,000 cycles. Error bars are shown for the initial activity measurements and were obtained from triplicate electrode mountings. The iR-compensated data was used to construct **Figure 7.3A**.

(D) Pt_{comm} and PtRu_{comm} LSVs obtained with and without instrument-applied iR compensation. Error bars are shown for the initial activity measurements and were obtained from triplicate electrode mountings. The iR-compensated data was used to construct **Figure 7.3A**.

(E) Tafel plot of iR-compensated LSVs obtained in 1 M HClO₄ for Pt_{comm}, PtRu_{comm}, Pt_{C-S}, and PtRu_{C-S}.

(F) PtRu_{C-S} iR-compensated LSVs obtain in 1 M HClO₄ at different temperatures.

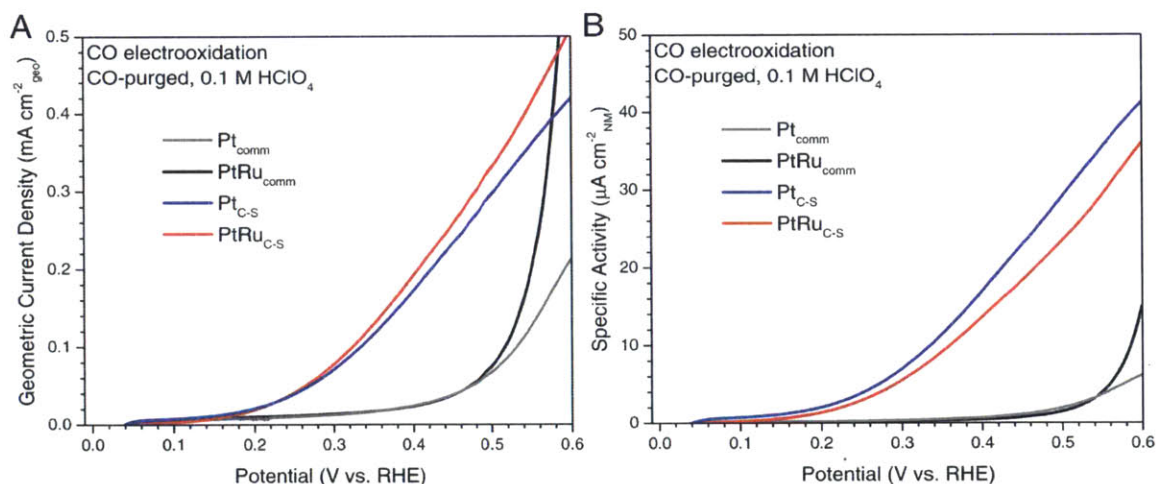
CO Electrooxidation and Methanol Electrooxidation Measurements

Below are shown the activity of the materials for electrooxidation of CO in CO-purged 0.1 M HClO₄ at 30°C and for the electrooxidation of methanol (MOR) in Ar-purged 1 M MeOH and 0.1 M HClO₄ at 30°C. The measurements were performed using RDEs at a rotation rate of 1000 rpm unless specified otherwise.

Kinetic estimates were obtained from steady-state CA measurements performed over 15 min intervals at fixed potentials. The data is shown in **Figure 7.3E** and **Figure 7.7**. Turnover frequencies (TOFs) were estimated from the steady-state activity measurements at 0.45 V and 0.6 V assuming complete 6-electron transfer oxidations normalized by CO-ECSA roughness factors. This assumption is reasonable for PtRu_{comm} and PtRu_{C-S} at both 0.45 and 0.6 V.^[187] As such, TOF estimates are given as mol CO₂ per mol of surface sites per minute.

Table 7.4. MOR Initial and Post-Stability Steady-State Kinetic Estimates

Catalyst	TOF@0.45 V Initial (min ⁻¹)	TOF@0.45 V Post 10,000 and Regeneration (min ⁻¹)	TOF@0.6 V Initial (min ⁻¹)	TOF@0.6 V Post 10,000 and Regeneration (min ⁻¹)
Pt _{comm}	0.00 ± .00	0.00 ± .00	0.96 ± .08	1.11 ± .10
Pt _{C-S}	0.03 ± .00	0.02 ± .00	1.55 ± .07	1.83 ± .08
PtRu _{comm}	0.86 ± .06	0.38 ± .03	3.65 ± .26	2.35 ± .17
PtRu _{C-S}	2.20 ± .05	1.80 ± .04	15.87 ± .37	25.69 ± .53

**Figure 7.6.** CO Electrooxidation Activity.

LSVs with iR compensation showing **(A)** geometric current densities and **(B)** specific activities for various catalysts performing CO electrooxidation in CO-saturated 0.1 M HClO₄ at 30 °C and 2 mV s⁻¹ under a rotation rate of 1600 rpm. For comparison, the current density at +0.4 V is improved by a factor of 8 for the NM/TMC core-shell materials relative to PtRu_{comm} on a geometric basis and by a factor of 30 on a specific activity basis.

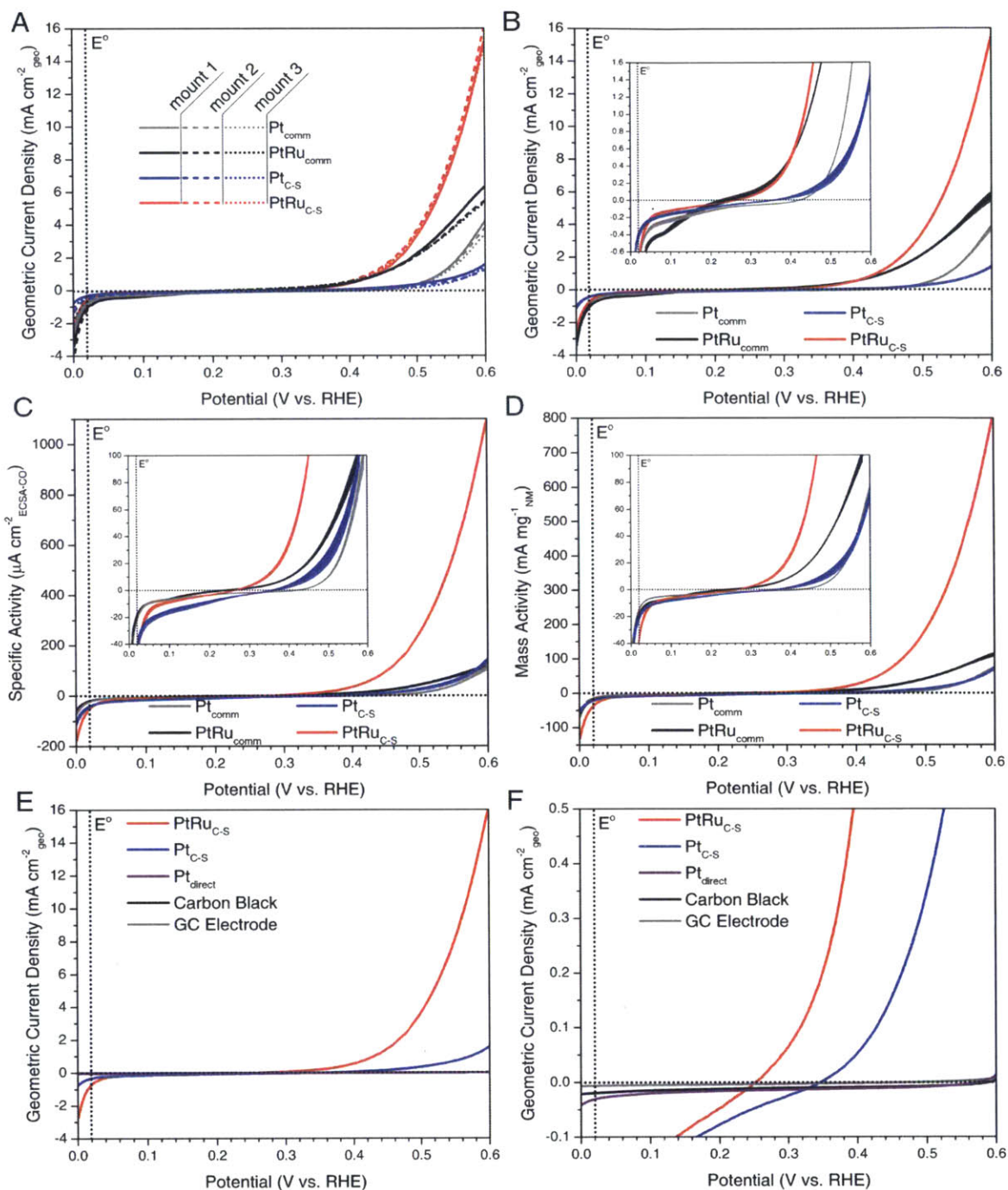


Figure 7.7. MOR Initial Activity Comparison and Reproducibility Study.

(A) LSVs with iR compensation normalized by geometric current density for the NM/TMC core-shell catalysts and commercial controls at 10 mV s^{-1} in 1 M MeOH and 0.1 M HClO_4 at 30°C and 1000 rpm. Each catalyst ink was mounted on three separate electrodes to examine measurement reproducibility. The vertical line represents E° , the thermodynamic reversible potential for MOR, which is 0.02 V vs. RHE.

(B) The LSVs from (A) with the triplicate runs averaged at each 1 mV interval. The line thickness includes standard deviation error bars. The inset panel is magnified to show differences in the onset potential for MOR.

(C) The LSVs from (B) normalized by specific surface area determined from CO stripping. The errors in the specific surface area measurements are propagated with the errors from the triplicate runs. The inset panel is magnified to show differences in the onset potential for MOR.

(D) The LSVs from (B) normalized by loaded NM mass with errors propagated. The inset panel is magnified to show differences in the onset potential for MOR.

(E) and **(F)** PtRu_{Uc-S} and Pt_{C-S} LSVs compared to Pt_{direct} and the bare controls under identical conditions where (F) is a magnified view of (E).

Chronoamperometry studies were held at fixed potentials for 15 min intervals in 1 M MeOH and 0.1 M HClO₄ at 30 °C and 1000 rpm (0.35, 0.4, and 0.45 V) or 2500 rpm (0.6 V). The final current density was averaged over the last 1 min of the measurement. Initial activity measurements were performed after conditioning cycles. The CA measurements were repeated after performing 5,000 cycles from -50 to 600 mV at 100 mV s⁻¹, after 10,000 cycles from -50 to 600 mV at 100 mV s⁻¹, and after regeneration (dipping the electrode for 2 min in 0.1 M NaOH solution).

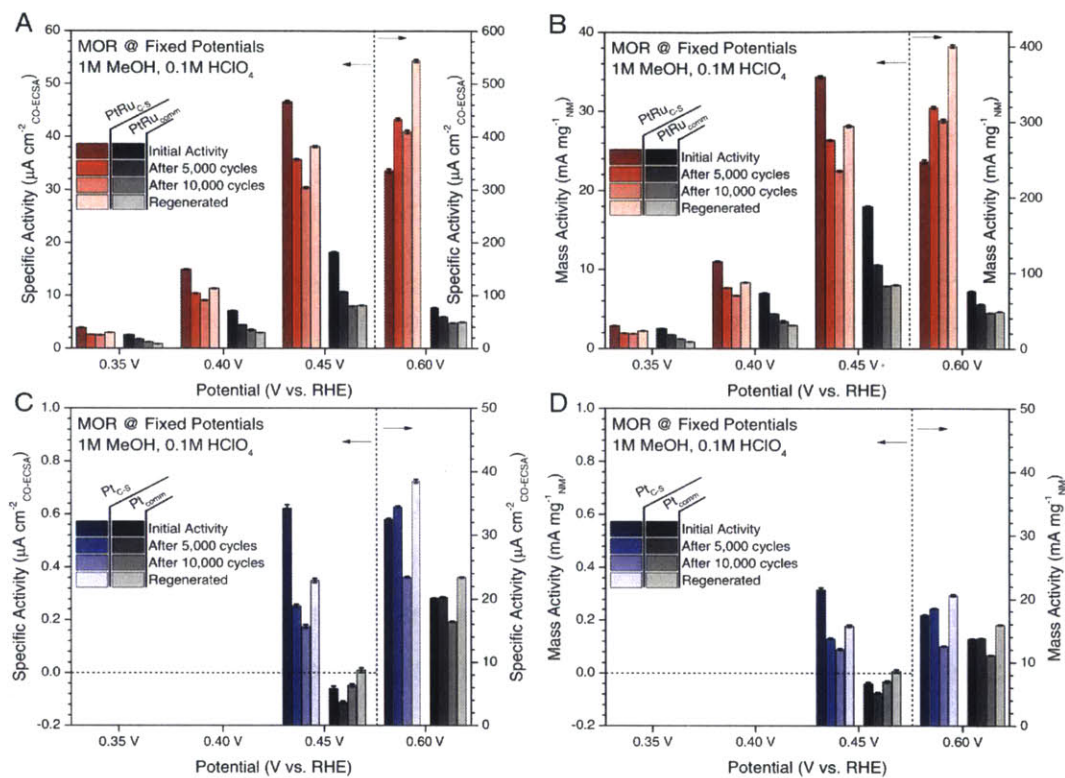


Figure 7.8. MOR Stability Study.

(A) PtRu_{C-S} compared to PtRu_{comm} on a specific activity basis (Figure 7.3E).

(B) PtRu_{C-S} compared to PtRu_{comm} on a mass activity basis.

(C) Pt_{C-S} compared to Pt_{comm} on a specific activity basis.

(D) Pt_{C-S} compared to Pt_{comm} on a mass activity basis.

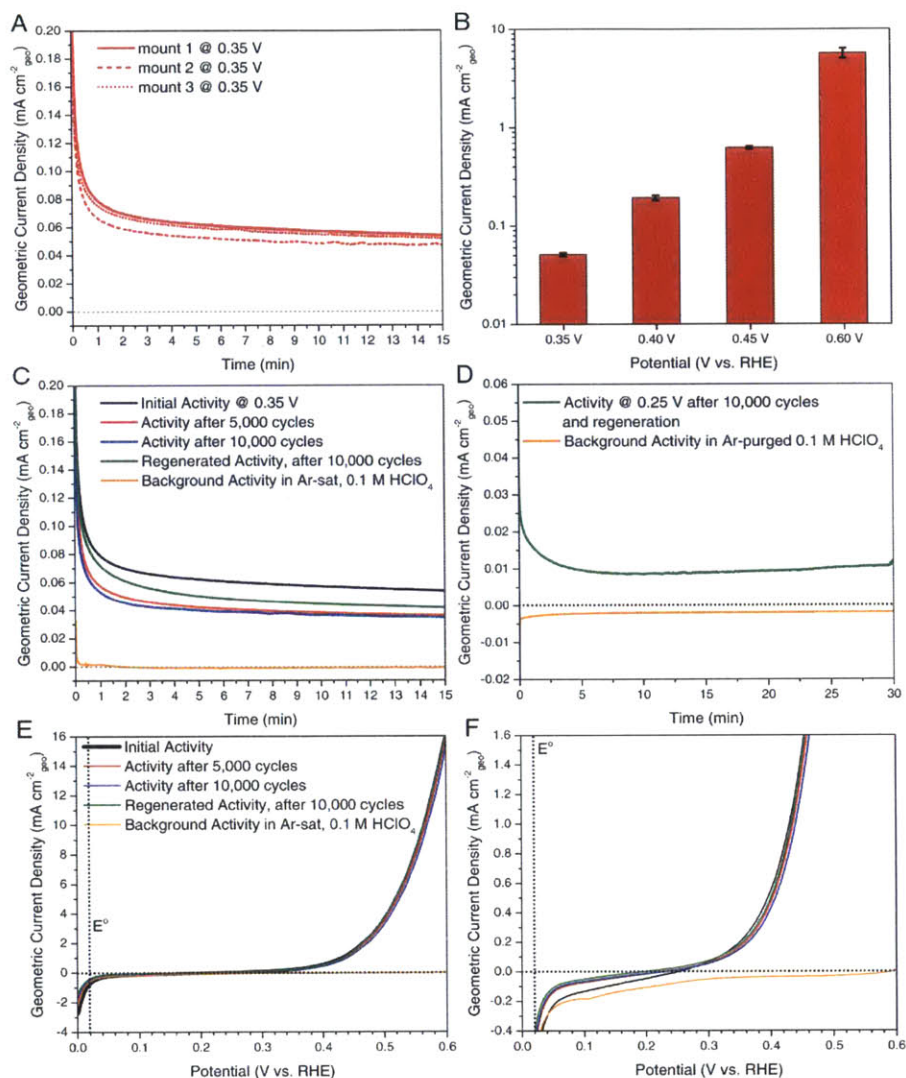


Figure 7.9. Detailed Analysis of PtRu_{c-s} Performance for MOR.

All measurements were performed in 1 M MeOH and 0.1 M HClO₄ at 30 °C under a rotation rate of 1000 rpm (2500 rpm for CA measurements at 0.6 V) with iR compensation applied.

(A) Initial activity CA curves at 0.35 V for triplicate mountings.

(B) Initial activity reproducibility study obtained from averaging the current response over the last minute of CA data collected for 15 min for triplicate electrode mountings. Representative raw CA data is shown in (A).

(C) Representative CA data collected at 0.35 V over 15 min before, during, and after stability cycling as well as regeneration. The background current is obtained in the absence of MeOH. Data averaged over the last minute at various potentials are presented in **Figure 7.3E, F**.

(D) After 10,000 cycles and regeneration in alkaline media, PtRu_{c-s} maintains a positive current density even at the low potential of 0.25 V over 30 min.

(E) LSVs at 10 mV s⁻¹ before, during, and after stability cycling as well as regeneration.

(F) A magnified version of panel (E) showing the onset potential for MOR.

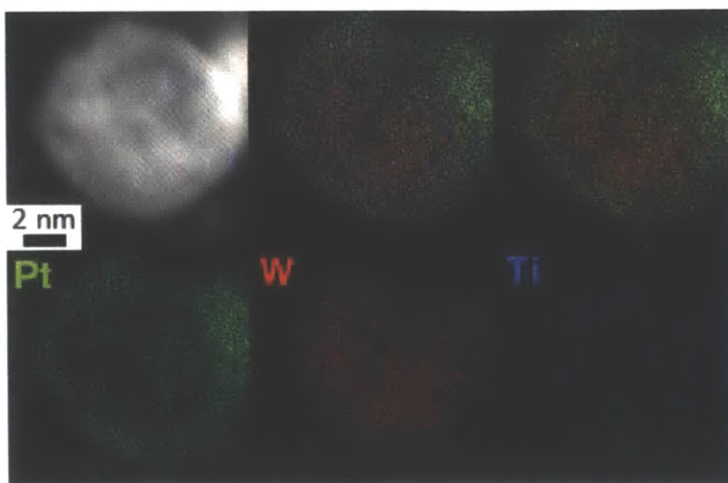


Figure 7.10. Microscopic Evidence of Pt_{c-s} Stability after Cycling

Above shows an HR-STEM and EDX map of Pt_{c-s} after stability cycling from -50 mV to 600 mV. The individual Pt, W, and Ti maps are shown as well as an overlay of all three elements and an overlay of just Pt and W.

2.3 Activating Earth-Abundant Electrocatalysts for Inexpensive and Efficient HER/HOR: Sub-Monolayer Core-Shell Nanoparticles

HER and HOR Electrochemical Activity Measurements

As previously noted, the efficiency of the developed method for nanoparticle assembly in a core-shell structure hinges on the insolubility of Pt in carbide lattices. While the previous characterization results suggest high dispersion of Pt at the surface of the nanoparticles, electrochemical activity measurements provide further evidence for both the suitability of this method at synthesizing core-shell nanoparticles of varying Pt surface coverages as well as the ability of this method to allow for the design of versatile, active, inexpensive, and stable electrocatalysts.

Using gas diffusion electrodes (GDEs) in 1.0 M HClO₄ under an H₂ partial pressure of 101.3 kPa, the materials were examined for both HER and HOR using linear sweep voltammetry (LSV) at 10 mV s⁻¹ at 30.0°C. The exact Pt loading on each electrode was determined by digestion of the GDEs in aqua regia, performed in triplicates. The error in the Pt loadings using this method ranged from 2-5%. This method could not be used for the 0.004ML sample as dissolution of this electrode resulted in ppt quantities of Pt. Instead, its loading was calculated based on the volume of ink added to the electrode and the catalyst concentration of the ink. Comparison of these methods were found to be in close agreement. For instance, the 0.25 ML Pt/TiWC sample was loaded onto the electrode at 2.05±0.06 μg_{Pt} cm⁻²_{geo} determined by ICP, while the loading was calculated to be 2.13 μg_{Pt} cm⁻²_{geo} when calculated from the volume loaded and the ink concentration. The Pt loadings used to normalize each electrode were determined to be as follows: 51 μg_{Pt} cm⁻²_{geo} for the commercial Pt, 20 μg_{Pt} cm⁻²_{geo} for 2 ML Pt/TiWC, 2.1 μg_{Pt} cm⁻²_{geo} for 0.25 ML Pt/TiWC, 0.4 μg_{Pt} cm⁻²_{geo} for 0.05 ML Pt/TiWC, and 0.03 μg_{Pt} cm⁻²_{geo} for 0.004 ML Pt/TiWC.

Figure 7.11A depicts the LSVs obtained for each material a broad potential range to include the activity of unmodified TiWC catalyst. While at first, the activity of TiWC may appear to be low compared to state-of-the-art earth-abundant electrocatalysts, we note that it is loaded at 50 μg_{TiWC} cm⁻²_{geo}, which is a factor of 10-100 lower than that typically loaded in recent earth-abundant studies. The modification of TiWC with as little as 0.4 μg_{Pt} cm⁻²_{geo} (0.05 ML Pt/TiWC sample) drastically improves the activity not only for HER,

but also for HOR. The activity of 0.25 ML Pt/TiWC and 2 ML Pt/TiWC is not discernible from the Pt commercial control at the scale used.

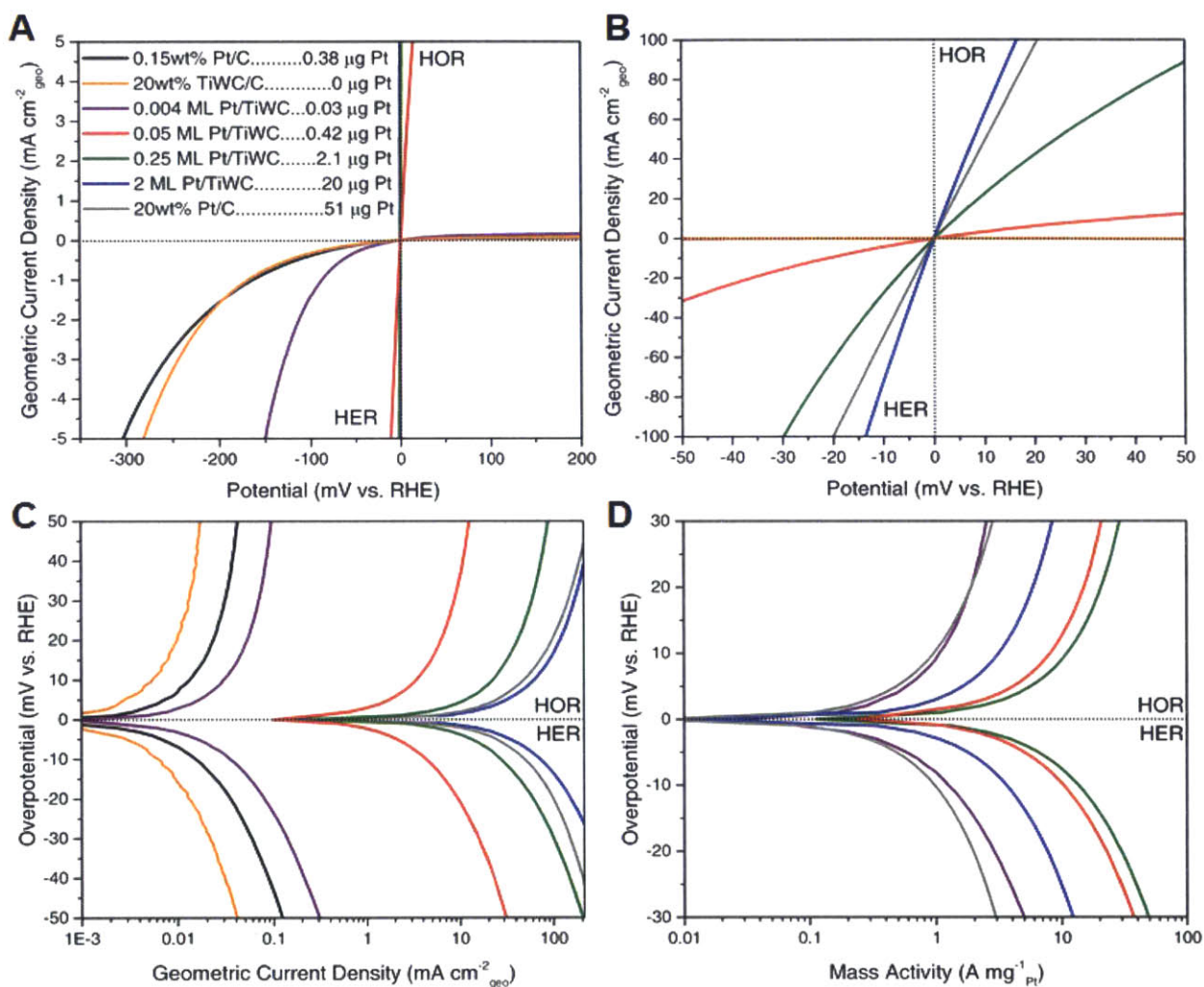


Figure 7.11. HER and HOR Activity of Sub-Monolayer Pt/TiWC.

All measurements were performed using GDEs under an H_2 purge at 10 mV s^{-1} in 1.0 M HClO_4 at 30°C with iR compensation applied.

(A) HOR/HER LSVs

(B) The same figure from (A) zoomed in to show the differences in Pt-based catalysts

(C) The same data from (A) and (B) plotted as a Tafel plot

(D) The data from (C) normalized by mass of Pt

When the LSVs presented in **Figure 7.11A** are plotted in a narrower potential range (**Figure 7.11B**), it can be seen that 2 ML Pt/TiWC is actually more active than the Pt control, despite a factor of 2.5 reduction in Pt loading, suggesting that the TiWC core

favorably modifies the electrochemical activity of Pt towards HER. DFT calculations have revealed a more favorable hydrogen binding energy (HBE) on Pt/WC in comparison to native Pt. However, in contrast, the significant gain in activity for Pt/TiWC in nanoparticle formulations presented here, this did not translate into an activity improvement in thin film studies.

Re-expressing the data as a semilog plot typical for Tafel analyses in **Figure 7.11C** shows that the 0.05 ML Pt/TiWC sample achieves a nearly 3 order of magnitude improvement in current densities compared to the unmodified TiWC control. While comparing the reactivity normalized by the number of surface sites using the electrochemical active surface area (ECSA) measurements is the most accepted method, we found that extremely low concentrations of Pt in 0.25 ML Pt/TiWC and 0.05 ML Pt/TiWC samples made them unsusceptible to CO stripping. Thus, we could not reliably normalize the activity by the concentration of surface sites and used the Pt loadings instead. This is also the most informative normalization scheme for examining intrinsic improvements in Pt utilization efficiency. **Figure 7.11D** shows substantial improvements in mass activity for 0.05 ML, 0.25 ML, and 2 ML samples, with 0.25 ML exhibiting the biggest improvement in mass activity.

Kinetic Fits using the Butler-Volmer Equation

To quantitate the kinetics of this new class of core-shell catalysts, the fits were performed over the kinetically limited portions of each data set using the Butler-Volmer equation shown below as **Equation 7.1**:

$$j = j_0 \times \left(e^{\frac{\beta_{\text{HOR}} F \eta}{RT}} - e^{-\frac{\beta_{\text{HER}} F \eta}{RT}} \right) \quad 7.1$$

where j_0 is the exchange current density in $\text{A cm}^{-2}_{\text{geo}}$, β_{HOR} and β_{HER} are the symmetry of charge transfer for HOR and HER, respectively, and η is the overpotential in V. The fits were performed using a standard nonlinear least squares curve fitting solver package and are shown in **Figure 7.12A**, normalized on a mass basis. The results of the fitting analysis are summarized both in **Table 7.5** and **Figure 7.12B**.

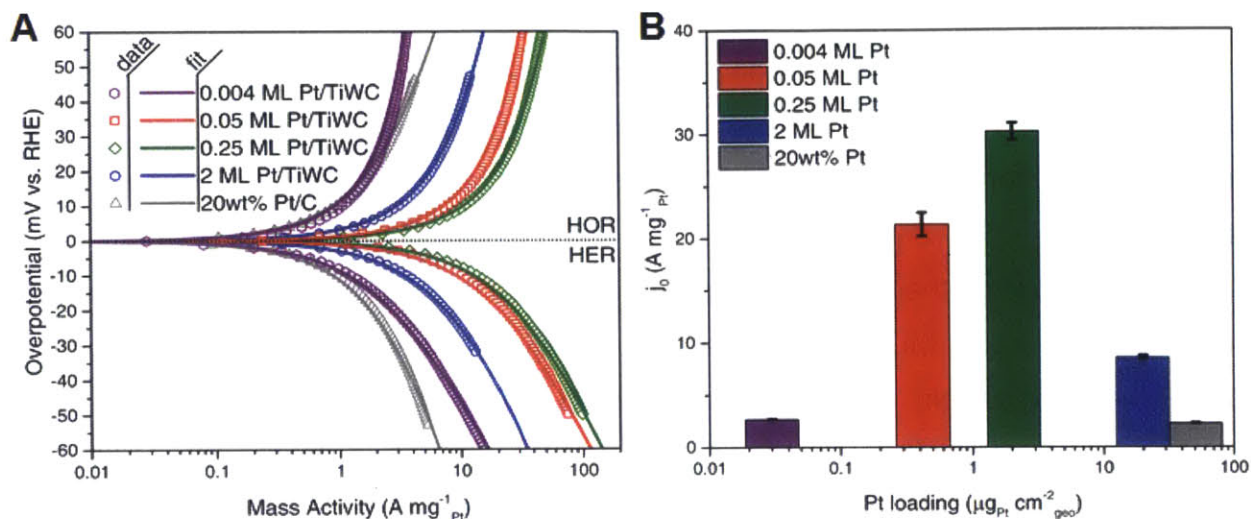


Figure 7.12. Butler-Volmer Fits and Exchange Current Densities

(A) shows the data from **Figure 7.11D** fitted to **Equation 7.1** using nonlinear least squares curve fitting. (B) shows the resulting exchange current densities on a mass platinum basis plotted against the mass of Pt loaded. Error bars are standard deviations propagated from errors in the mass loadings and errors in the nonlinear least squares regression.

Table 7.5. Butler-Volmer Fitting Parameters

Catalyst	j_0 ($mA\ cm^{-2}\ geo$)	j_0 ($A\ mg^{-1}\ Pt$)	β_{HOR}	β_{HER}
20wt% TiWC/C	0.05 ± 0.00	--	0.05 ± 0.00	0.95 ± 0.00
0.004 ML Pt/TiWC	0.07 ± 0.00	2.7 ± 0.0	0.17 ± 0.00	0.83 ± 0.00
0.05 ML Pt/TiWC	9.0 ± 0.1	21.3 ± 1.1	0.22 ± 0.00	0.78 ± 0.00
0.25 ML Pt/TiWC	62.0 ± 0.3	30.2 ± 0.8	0.28 ± 0.00	0.72 ± 0.00
2 ML Pt/TiWC	172.0 ± 1.0	8.6 ± 0.2	0.36 ± 0.01	0.64 ± 0.01
20wt% Pt/C	117.2 ± 1.0	2.3 ± 0.1	0.49 ± 0.01	0.51 ± 0.01

The commercial Pt control exhibits an exceptionally high exchange current density of $117.2 \pm 1.0 \text{ mA cm}^{-2}_{\text{geo}}$ and near-perfect symmetric charge transfer coefficients of 0.49 and 0.51 for HOR and HER, respectively (**Table 7.5**). In contrast, unmodified TiWC displayed an exchange current density of $0.05 \text{ mA cm}^{-2}_{\text{geo}}$ and almost totally asymmetric charge transfer coefficients of 0.05 and 0.95 for HOR and HER, respectively. However, as the ML coverage increases, the charge transfer symmetry progressively becomes more symmetric, reaching charge transfer coefficients of 0.36 and 0.64 for the 2 ML Pt/TiWC catalyst. For comparison, we note that Pd and Rh natively have charge transfer coefficients of 0.7 and 0.3 for HER and HOR, respectively.^[193]

When normalized on a mass basis, the 2 ML Pt/TiWC shows a factor of 3.7 improvement over the Pt catalyst as shown in **Figure 7.12B**. Since the Pt commercial control already consists of ultrasmall nanoparticles with high dispersion, this level of improvement cannot be explained by an increase in the metal dispersion alone, but rather by modification of the electronic structure of Pt by the subsurface TiWC core, as discussed extensively in **Chapter 2**.

Interestingly, as the ML coverage decreases to 0.25 ML and 0.05 ML, exposing surface TiWC sites, the mass activity shows factor of 13 and factor of 9 improvements over the Pt catalyst, respectively (**Figure 7.12B**). Because of these reactivity enhancements coupled with the increased asymmetry of the reactions (**Table 7.5**), we posit that adjacent TiWC surface sites are being activated for both HER and HOR at low overpotentials via the spillover of metallic H^0 from highly dispersed surface Pt sites. Under this hypothesis where TiWC serves as a co-catalyst, one would anticipate an overall increase in the observed activation energy for both HER and HOR considering that unmodified TiWC is orders of magnitude less active than native Pt.

$$\frac{\partial \log(j_0)}{\partial (1/T)} = - \frac{E_a}{2.303 \cdot R} \quad 7.2$$

The activation energy of 0.25 ML Pt/TiWC was investigated by varying the temperature from 10°C to 40°C and obtaining LSVs shown in **Figure 7.13A**. These data were then fit to **Equation 7.1** and then **Equation 7.2** was used to obtain the activation

energy, E_a . Pt is noteworthy for its exceptionally low activation energy of 16 kJ mol^{-1} in acidic media. For comparison, Pd has an activation energy of 31 kJ mol^{-1} . We obtained an activation energy of 26.6 kJ mol^{-1} for the optimal 0.25 ML Pt/TiWC catalyst (**Figure 7.13** and **Figure S7.21**). This further points toward a dual-pathway catalyst where TiWC actively participates in both HER and HOR. While this has the observed effect of reducing the HOR efficiency of Pt and slightly increasing the overall activation energy, the order of magnitude improvement in Pt mass activity towards both reactions indicates that sub-monolayer core-shell nanoparticles offer a new route for substantial reductions in Pt loadings in both water electrolyzers and fuel cells.

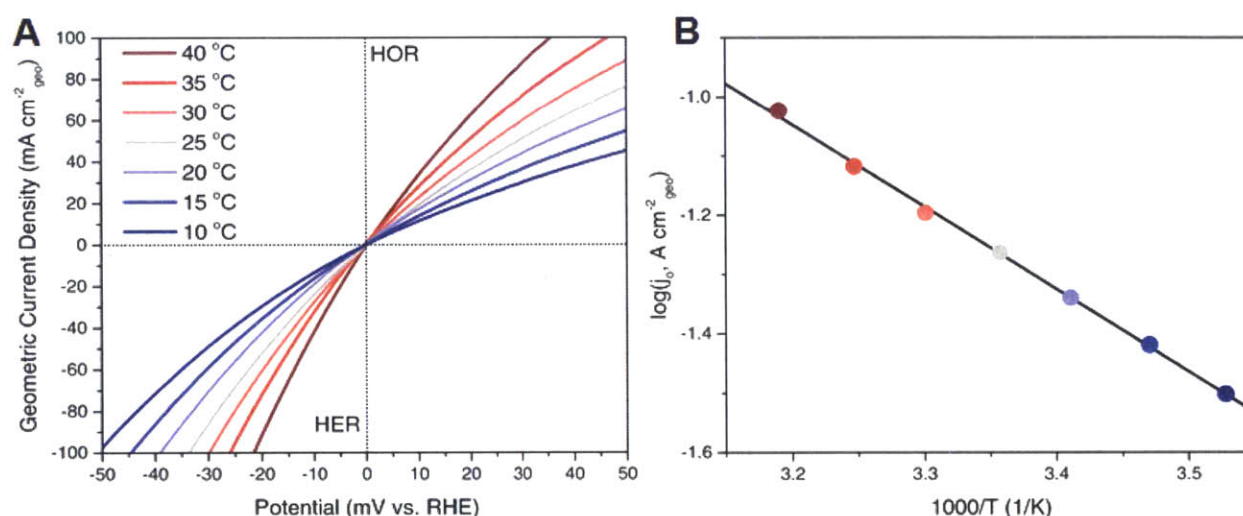


Figure 7.13. Temperature Study and Arrhenius Plot

(A) iR-compensated LSVs for 0.25 ML Pt/TiWC at various temperatures in 1.0 M HClO_4 under continuous H_2 purge. **(B)** Arrhenius plot constructed using **Equation 7.2**.

Comparison with Thin Film Studies

Chapter 3 shows studies have been performed on both WC and Mo_2C thin films in acidic media coated with varying monolayer coverages of Pt and Pd via physical vapor deposition. In the context of HER, these studies showed that TMC activity rapidly improves with monolayer coverage, and levels off near the activity of the native Pt and Pd thin films with just a single ML. Increasing the ML coverage beyond a single ML did not improve activity, even up to 30 ML.

With the translation of these findings to a nanoscale core-shell architecture, we can now examine structure-sensitivity differences between model catalysts and their commercially-relevant nanoscale counterparts. Using the kinetic modeling data from **Table 7.5** and the findings from D.V. Esposito et al, *Angew. Chem. Int. Ed.* 2010, 49 (51), 9859-9862,^[33] **Figure 7.14** was constructed to examine how varying ML coverages of Pt improves the reactivity of TiWC nanoparticles and WC thin films.

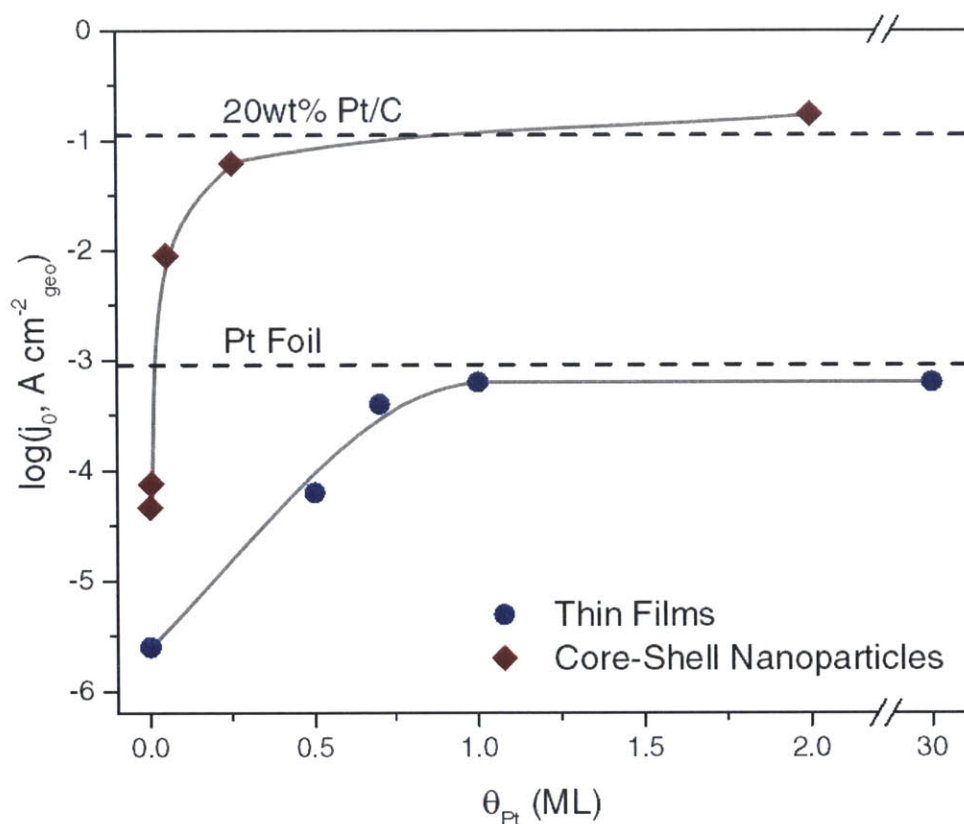


Figure 7.14. HER Activity vs. ML Coverage for Core-Shell Nanoparticles and Thin Film Model Catalysts

Despite low loadings of ca. $50 \mu\text{g}_{\text{metal}} \text{ cm}^{-2}_{\text{geo}}$, the supported TiWC and Pt nanoparticles outcompete their bulk counterparts by 1 and 2 orders of magnitude, respectively. For the model thin films, it requires greater than ca. 0.7 ML Pt/WC to achieve a comparable activity to the Pt foil thin film. By contrast, a 0.25 ML Pt coverage in the sub-monolayer core-shell nanoparticle formulation is sufficient to achieving a comparable

activity to the Pt/C nanoparticle catalyst. While this could be due to easier activation of high index TiWC edge sites, it could also be due to the differing surface concentrations of adjacent Pt-WC sites. For instance, a 0.25 ML Pt/WC thin film will have large contiguous sections of both bare WC sites and Pt sites surrounded only by Pt. By contrast, the nanoparticle formulation by its very nature would have the highest surface density of Pt sites with adjacent WC sites, allowing for more efficient spillover to be achieved at lower ML coverages than model thin films.

Stability Studies

Two stability studies were performed on the optimal 0.25 ML Pt/TiWC/C. The first study was an accelerated degradation test where the catalyst was subjected to 10,000 cycles at 100 mV s^{-1} between -50 mV and 600 mV in Ar-saturated 1.0 M HClO_4 using an Ag/AgCl reference electrode and a graphite rod counterelectrode. Uncompensated LSVs at 10 mV s^{-1} were collected before and afterwards in fresh electrolyte at $30 \text{ }^\circ\text{C}$. In the second study, chronopotentiometry (CP) was used to examine stability under sustained, aggressive turnover. Over 16 h, the potential was allowed to vary freely to sustain HOR currents of $5 \text{ mA cm}^{-2}_{\text{geo}}$ for 15 minute intervals followed by HER currents of $-5 \text{ mA cm}^{-2}_{\text{geo}}$ for 15 minute intervals. The open circuit voltage (OCV) was determined before and after measurement to correct for any reference electrode drift. Based on the electrode mass loadings, this study involved over 140,000 turnovers on a $\text{mol H}_2 \text{ mol}^{-1}$ Pt basis and 5,000 turnovers on a $\text{mol H}_2 \text{ mol}^{-1}$ metals basis. The results are shown below in **Figure 7.15**.

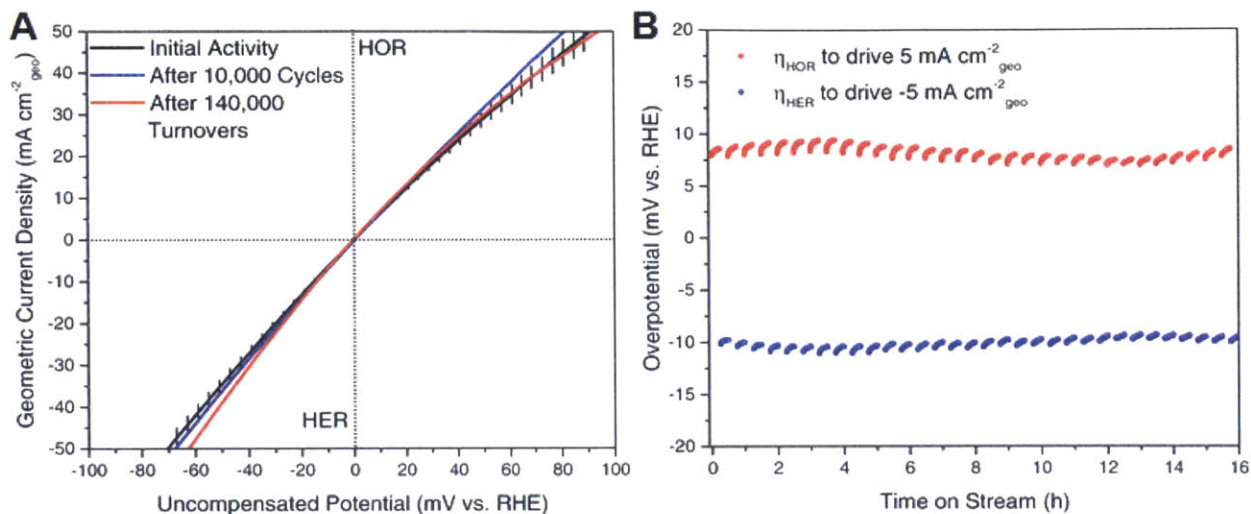


Figure 7.15. Stability studies of 0.25 ML Pt/TiWC/C

(A) Uncompensated LSVs of quintuplicate mountings of 0.25 ML Pt/TiWC/C GDEs showing initial activity. LSV scans are also shown after 10,000 cycles from -50 mV to 600 mV at 100 mV s⁻¹ and after 140,000 HER/HOR turnovers (shown in B)

(B) Uncompensated chronopotentiometry (CP) turnover study cycling between 5 mA cm⁻²_{geo} of HOR current for 15 minutes and -5 mA cm⁻²_{geo} of HER current for 15 minutes over 16 h in 1.0 M HClO₄ under 1 atm of H₂ at 30 °C.

From **Figure 7.15**, it is clear that the optimal 0.25 ML Pt/TiWC/C catalyst is highly stable, able to withstand anodic potential excursions to 600 mV and not degrading during sustained turnover. As a result of its high Pt mass activity for both HER and HOR as well as its high stability, sub-monolayer core-shell nanoparticles represent an exciting new direction for designing highly active and stable catalysts. Although Pt is used, a techno-economic analysis was performed, which shows that the cost of Pt is offset by the efficiency gains from the new catalyst via the reduction in operating overpotentials.

Technoeconomic Analysis

For water electrolysis in acidic media, OER remains the critical barrier to commercialization, requiring expensive IrO₂-based electrocatalysts with large overpotentials.^[195] While significant challenges persist to overcoming these barriers, it also prompts the development of ultralow-cost HER cathodes to help offset overall device cost. Likewise, for PEMFC fuel cells, ORR remains the critical barrier to commercialization, requiring expensive Pt-based electrocatalysts with large overpotentials. Unlike OER in

acidic media, impressive results have been obtained at reducing Pt loadings while simultaneously improving activity and stability for ORR.^[67,68,196] These encouraging achievements should push PEMFCs even closer to widespread commercial adoption, motivating the development of HOR electrocatalysts with lower Pt loadings and improved CO tolerance to further offset both the device cost and hydrogen fuel purification costs.

Here we present a technoeconomic analysis aimed at providing prediction intervals at 95% confidence for the cost reductions achievable with sub-monolayer core-shell nanoparticle formulations for both HER cathodes and HOR anodes using two economic descriptors. The first descriptor is the cost of Pt loaded. Using publicly available data that was subsequently inflation-adjusted using the consumer price index, the average 5-year cost of Pt over 2010-2015 was $50 \pm 6 \text{ \$ g}^{-1}_{\text{Pt}}$.

The second descriptor is the average U.S. cost of electricity. Again, using publicly available data that was inflation-adjusted using the consumer price index, the average 5-year cost of electricity over 2010-2015 was $12.5 \pm 0.4 \text{ ¢ kWh}^{-1}$. This descriptor is used to capture the cost associated with the overpotentials associated with HER and HOR for the various catalysts. For both HER and HOR, the overpotentials used in the analysis were the overpotentials required to drive $20 \text{ mA cm}^{-2}_{\text{geo}}$. While the cost of Pt is an upfront cost based on the size of the device, the energy cost is incurred over the useful hypothetical lifecycle of the device. Therefore, the technoeconomic analysis was conducted over a 1 m^2 device with a useful lifespan of 50000 h, and the results are shown in **Figure 7.16** for a cathode HER device (bottom) and for an anode HOR device (top). Prediction intervals were constructed assuming unknown means and unknown variances at a 95% confidence level.

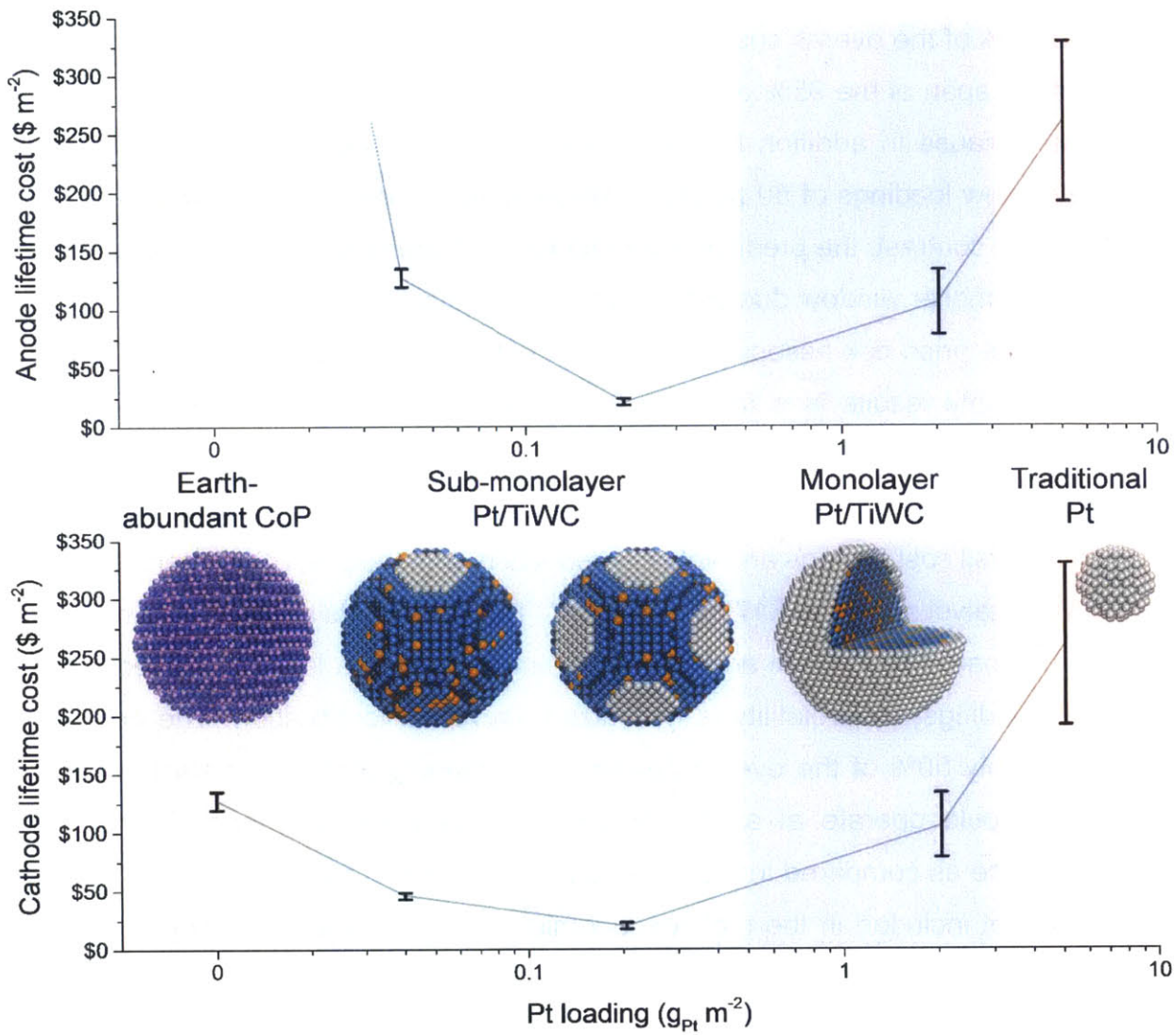


Figure 7.16. Technoeconomic Analysis of the Lifetime Cost of HER Cathode and HOR Anode Devices

Assumptions: 1 m² device operating over 50,000 h at a current density of 20 mA cm⁻²_{geo}. The cost of Pt is 50 ± 6 \$ g⁻¹_{Pt}, and the cost of electricity is 12.5 ± 0.4 ¢ kWh⁻¹. The error bars are the 95% prediction intervals assuming unknown means and unknown standard deviations.

It is clear from **Figure 7.16** (bottom panel) that already, earth-abundant catalysts such as CoP outperform Pt/C even with its low 50 µg cm⁻²_{geo}, resulting in total cathode lifetime costs of \$127 m⁻² for CoP as compared to \$260 m⁻² for Pt/C. Here, the cost of CoP is entirely associated with extra electricity required to power the cathode over the lifetime

of the device, whereas for Pt/C, the cost of extra electricity to power the cathode accounts for less than 2% of the overall cost. While Pt is expensive, perhaps more important than the price is the span of the 95% prediction interval, which ranges from \$191 m⁻² to \$329 m⁻². This is because in addition to being expensive, the price of Pt is also extremely volatile. Even low loadings of 50 µg cm⁻²_{geo} result in substantial risk exposure to Pt price fluctuations. By contrast, the prediction interval for CoP spans from \$119 m⁻² to \$135 m⁻², a significantly smaller window due to the much lower volatility in electricity costs.

While the price risk associated with Pt is eliminated, an earth-abundant cathode such as CoP only results in a factor of 2 decrease in the cost of an HER cathode, assuming that it could maintain its 100 mV overpotential at 20 mA cm⁻²_{geo}, an as of yet unproven assumption. Alternatively, sub-monolayer core-shell nanoparticles offer substantial overall cost savings and volatility reduction, with the prediction interval for 0.25 ML Pt/TiWC catalyst spanning \$17 m⁻² to \$23 m⁻². This represents a factor of 10 reduction in cost as compared to Pt/C. In addition, by maintaining both a low 8 mV overpotential and low Pt loadings, the volatility is minimized via risk diversification. The cost of Pt accounts for only 50% of the overall device cost, meaning that a fully earth-abundant catalyst that could operate at an 8 mV overpotential would only see another 50% reduction in price as compared to the sub-monolayer Pt/TiWC catalyst.

While not included in the techno-economic analysis, it is worth noting that earth-abundant catalysts currently require high loadings above ca. 1 mg cm⁻²_{geo}. While the cost of cobalt is small, an additional \$1-2 m⁻² should be anticipated. Moving loadings beyond 10 mg cm⁻²_{geo} would make the cost of the earth-abundant catalysts no longer negligible, especially compared to the sub-monolayer core-shell NPs. Above 10 mg cm⁻²_{geo}, the cost of an earth-abundant cathode becomes comparable to the sub-monolayer cathode with 2.1 µg_{Pt} cm⁻², making cost savings proposals specious.

For HOR, earth-abundant alternatives are so poor that the PEMFC would be inoperable without unreasonably large catalyst loadings. In **Figure 7.16** (top), it is seen that the price reductions associated with Pt/TiWC core-shell nanoparticles mirror closely that of the HER analysis. While these materials are asymmetric catalysts, the asymmetry of the reaction dominates at current densities above 20 mA cm⁻²_{geo} with the exception of the 0.05 ML Pt/TiWC catalyst, which requires more than 100 mV to achieve 20 mA cm⁻²_{geo}.

2.4 Thermal Stability Study of Sub-Monolayer Pt/TiWC Nanoparticles

Core-shell nanoparticles typically have limited applications in thermal catalysis due to the shell alloying with the core at high temperatures. As shown in **Chapter 6**, NM/TMC core-shell nanoparticles self-assemble at exceptionally high temperatures above 900°C. While this implies impressive thermal stability, the syntheses are performed under silica encapsulation, which was specifically engineered to mitigate sintering.

In this section, we investigate the thermal stability of unprotected NM/TMC core-shell nanoparticles focusing on 0.25 ML Pt/TiWC, denoted as Pt_{sub-ML} supported on carbon black at 20wt%. Carbon black was chosen as a support due to the weak interactions of nanoparticles with carbon supports as compared to other supports such as zeolites and metal oxides. This allows the intrinsic sinter-resistance of sub-monolayer core-shell nanoparticles to be examined in comparison to a traditional Pt/C catalyst. Sub-monolayer Pt/TiWC was chosen because it can easily be characterized by XPS where only Pt²⁺ is observed (**Figure 6.3** and **Figure 6.4**). In addition, the sub-monolayer configuration is the most relevant to thermal catalysis. This is because extremely low loadings are already employed and because the interplay between Pt and exposed TiWC sites could offer new avenues for optimizing reactivity. Because thermal stability is a prerequisite to investigating activity, we focus this section only on stability under various atmospheres. The activity of sub-monolayer core-shell NM/TMC nanoparticles remains an ongoing area of investigation in the Román Lab. **Figure 7.17** depicts TEM images of Pt_{sub-ML} as synthesized (panel A) and after heat treatments in various atmospheres for various lengths of time.

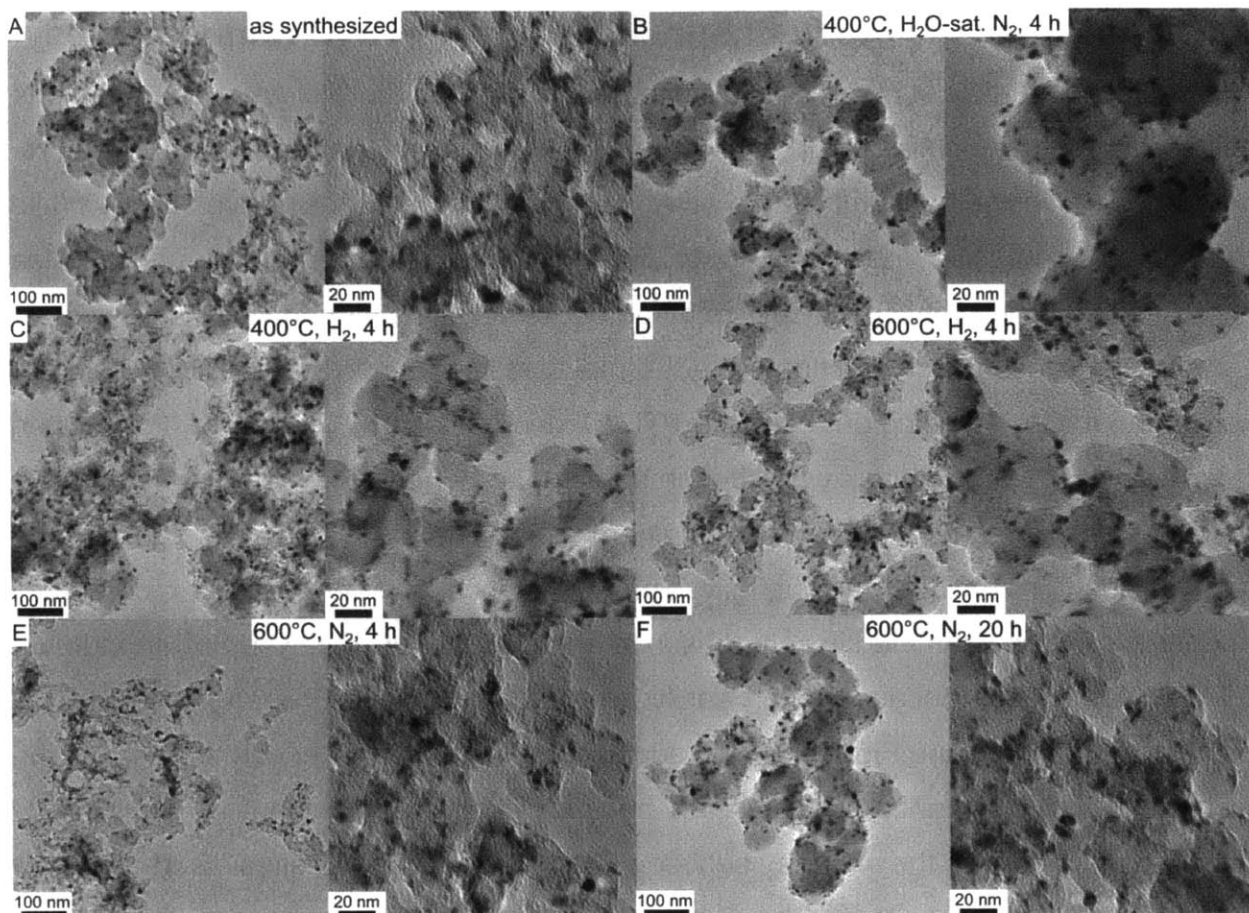


Figure 7.17. Microscopic Analysis of $\text{Pt}_{\text{sub-ML}}$ after Various Heat Treatments.

TEM images of 20 wt% carbon-supported 4%Pt/96% $\text{Ti}_{0.1}\text{W}_{0.9}\text{C}$ NPs (denoted as $\text{Pt}_{\text{sub-ML}}$) after various heat treatments in different atmospheres.

- (A) As synthesized
- (B) After the treatment at 400°C in wet N_2 for 4 h
- (C) After the treatment at 400°C in H_2 for 4 h
- (D) After the treatment at 600°C in H_2 for 4 h
- (E) After the treatment at 600°C in N_2 for 4 h
- (F) After the treatment at 600°C in N_2 for 20 h

While the TEM images in **Figure 7.17** suggest that sintering was mitigated, TEM is a local technique. PXRD was used to examine sintering as well as changes in the crystal structure after the various heat treatments. Identical heat treatments were also applied to Pt_{comm} , and its PXRD spectra are also shown.

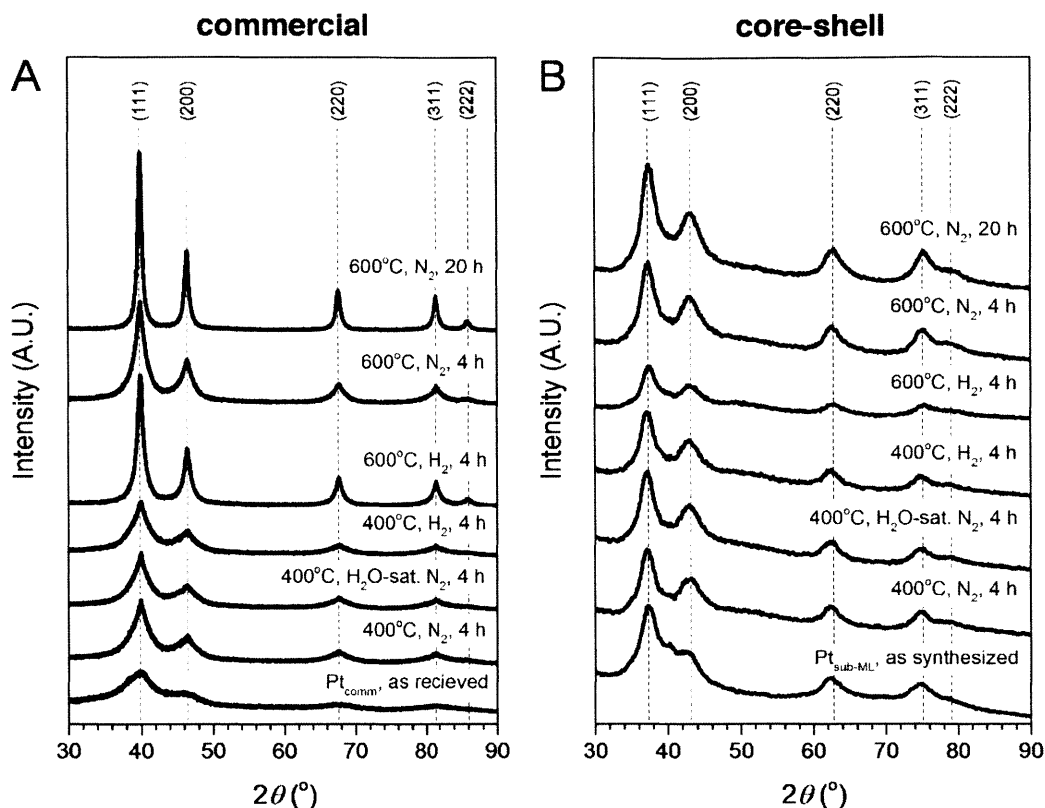


Figure 7.18. PXRD Analysis of Pt_{comm} and $\text{Pt}_{\text{sub-ML}}$ after Various Heat Treatments.

PXRD diffractograms of (A) Pt_{comm} and (B) $\text{Pt}_{\text{sub-ML}}$ heated to 400 or 600 °C in different atmospheres (H_2 , dry and wet N_2 flow) for 4 or 20 h.

As shown in **Figure 7.18**, the $\text{Pt}_{\text{sub-ML}}$ samples remains in an fcc β -WC lattice after all heat-treatments. The breadth of the peaks do not change even after 20 h at 600 °C and instead become slightly more crystalline after the heat treatments. By contrast, Pt_{comm} sinters rapidly as observed by the steady decrease in peak breadth with time and temperature. This shows the extreme thermal stability of carbide core supports, which can be attributed to their exceptionally high melting points and therefore higher Tammann temperatures. The TEM images were quantitated by determining the volume-weighted particle size distributions (PSDs) after each heat treatment, shown in **Figure 7.19**. In agreement with **Figure 7.18**, $\text{Pt}_{\text{sub-ML}}$ exhibits exceptional thermal stability in comparison to the Pt_{comm} control catalyst.

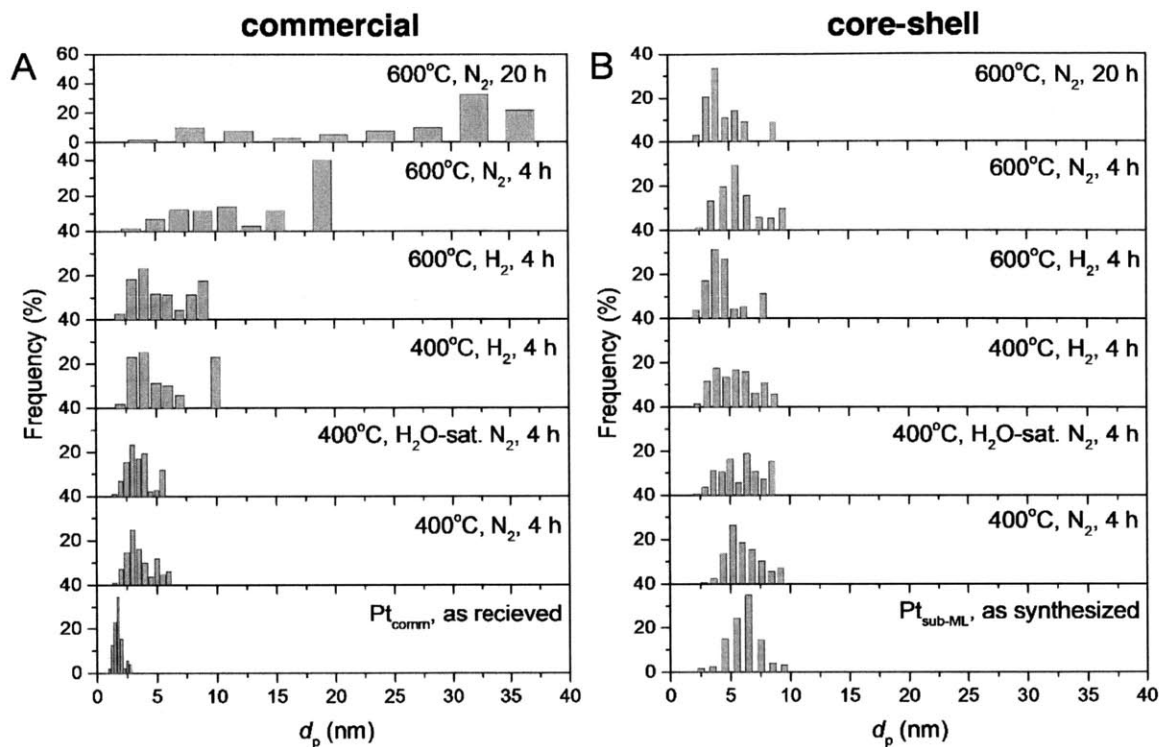


Figure 7.19. Impact of Various Heat Treatments on the PSDs of Pt_{comm} and $\text{Pt}_{\text{sub-ML}}$.

Volume-weighted particle size distribution (PSD) plots for **(A)** Pt_{comm} and **(B)** $\text{Pt}_{\text{sub-ML}}$ after various heat treatments in different atmospheres. The PSDs were determined from at least 200 nanoparticles from several images taken across the TEM grids.

While the previous techniques demonstrate that sintering is mitigated in the sub-monolayer catalyst, the state of the surface after each heat treatment is arguably more important than mitigating sintering. For instance, if the Pt were to solubilize in the core and alloy, then the catalytic activity attributable to Pt would greatly diminish. To examine the stability of the core-shell structures before and after each heat-treatment, XPS was used. The results are shown in **Figure 7.20**. Remarkably, the core-shell structure remains intact after each heat treatment. While the ICP-determined Pt:W ratio for this catalyst was 5%, the XPS-determined Pt:W ratios varied from 10-12%, indicating that after each heat treatment, the Pt still screens the sub-surface TiWC core. Furthermore, the Pt was always detected as Pt^{2+} . The lack of Pt^0 and the detectable screening of the TiWC core indicate that the shell structure did not aggregate to produce a Janus-type particle but instead remained dispersed over the surface of the TiWC core.

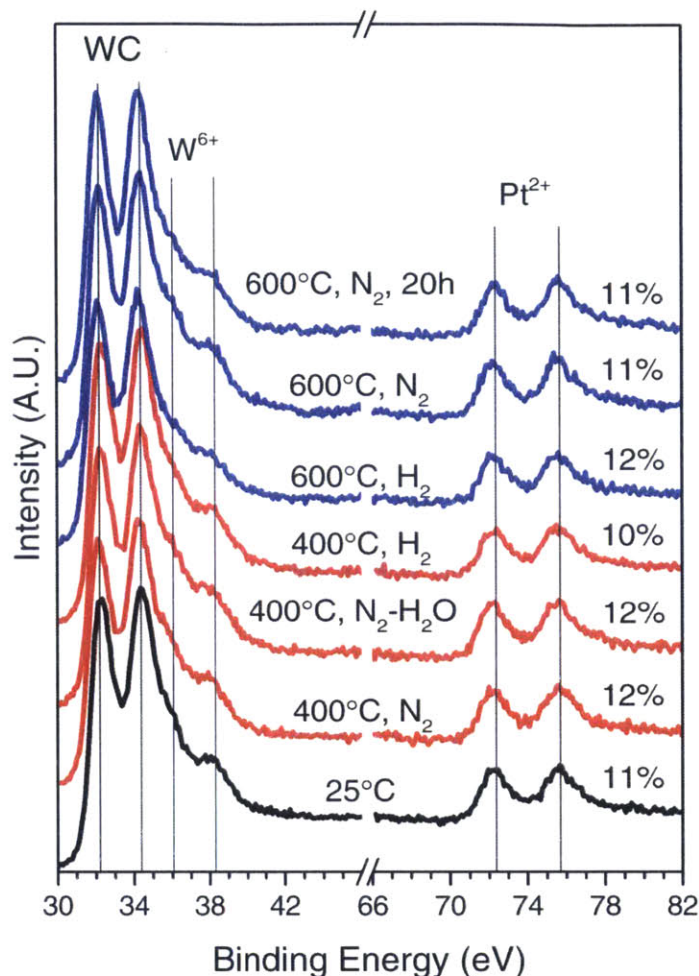


Figure 7.20. XPS Analysis of $\text{Pt}_{\text{sub-ML}}$ after Various Heat Treatments.

XPS study of the thermal stability of $\text{Pt}_{\text{sub-ML}}$ held in various atmospheres for 4 or 20 h and then passivated at room temperature. The percentages shown correspond to the XPS-determined Pt:W ratios and range from 10-12%. The ICP-determined bulk Pt:W ratio was 5%.

3. Methods

3.1 Electrochemical Methods for Sections 2.1 and 2.2

Electrochemical measurements were performed on a CH Instruments 627e potentiostat/galvanostat using a BASi RDE-2 rotating disk electrode equipped with a jacketed glass cell and PTFE cap.^[131,197,198] The cell was maintained at a constant temperature of 30.0°C. Viton® o-rings were used to seal the electrodes and bubbler into the ports of the PTFE cap. In all experiments, a platinized platinum coil was used as the

counter electrode. An eDAQ Hydroflex™ Hydrogen Reference Electrode was used as the reference electrode, except for experiments involving the presence of CO in the electrolyte, in which a leak-proof 3 M NaCl Ag/AgCl reference electrode calibrated to the eDAQ hydrogen reference electrode was employed. All potentials are reported versus RHE. iR compensation was used where reported, while the uncompensated solution resistance was typically $\sim 30 \Omega$.

Gases were delivered to the electrochemical cell using a high surface area fritted glass bubbler and controlled using a calibrated Sierra SmartTrak® mass flow controller. For measurements involving CO/H₂ mixtures, the CO was delivered using a calibrated Sierra MicroTrak® ultra low flow controller.

3 mm glassy carbon (GC) disk electrodes were used as the substrate for the catalyst inks. The GC working electrodes were freshly polished using a 0.05 μm alumina suspension on a Texmet pad for 2 min in a figure eight pattern, rotating 90° every 30 sec. The electrodes were then rinsed with methanol, sonicated for 5 s in acetone, rinsed thoroughly with DI water and dried in N₂ flow.

Catalyst inks were prepared from a common stock solution consisting of 50 mL of DI water, 4 mL of isopropanol, and 1 mL of 5% Nafion® 117 solution. For all experiments, the inks consisted of 3 mg of catalyst by total mass per 1 gram of solution. These inks were sonicated for 1 h in an ice bath. Immediately after sonicating, 6 μL droplets were loaded onto the surface of the freshly cleaned GC working electrodes. The electrodes were then dried by pulling a slow vacuum to -380 Torr, holding for 5 min, and then pulling a slow vacuum to -710 Torr and holding for 15 min to obtain an optically uniform black thin film. For the control catalysts, the NM loading was $\sim 51 \mu\text{g cm}^{-2}_{\text{geo}}$ while for the core-shell catalysts, the NM loading was $\sim 20 \mu\text{g cm}^{-2}_{\text{geo}}$. Exact loadings were determined using ICP-MS.

The working electrodes were then pre-treated by rinsing with DI water, swirling in 0.1 M NaOH solution for 2 min, and then rinsing again with copious amounts of DI water. The working electrode was always lowered into fresh electrolyte solutions under potential control at 0.1 V. The final pretreatment step consisted of 100 conditioning cyclic voltammetry (CV) scans performed from -0.05 V to 0.6 V at 200 mV s^{-1} and a rotation rate of 2500 rpm in Ar-purged 0.1 M HClO₄. Pt/C was conditioned by cycling from -0.05 V to

1.2 V. The electrolyte was then switched to fresh H₂-purged 0.1 M HClO₄ for HER/HOR studies at 0, 400, 900, 1000, 1600, and 2500 rpm. These measurements were performed at 10 mV s⁻¹ followed by chronoamperometry and chronopotentiometry HER studies at 2500 rpm.

Afterwards, a fresh H₂-purged 0.1 M HClO₄ electrolyte was used for CO/HOR studies. After an initial HOR scan at 2 mV s⁻¹ and 1600rpm, the working electrode was held at 0.025 V and 1600 rpm for an arbitrarily long time (e.g. 180 min) while the gas flow was switched to 99.9 ± 0.1 mL min⁻¹ H₂ and 100 ± 1 μL min⁻¹ of CO. Once the geometric current dropped below 0.1 mA cm⁻² (typically requiring approximately 2 h), an iR-compensated LSV was performed from 0.025 V to 0.6 V at 2 mV s⁻¹. A low potential of 0.025 V was used because the NM/TMC core shell materials would not saturate with CO at 0.05 V or above due to their high CO tolerance.

Next, the electrolyte was changed to Ar-saturated 0.1 M HClO₄ and the working electrode was conditioned from -0.05 V to 1.0 V at 1600 rpm and 50 mV s⁻¹ for 20 cycles. 3 cycles from 0.025 V to 1 V at 0 rpm and 20 mV s⁻¹ were performed to obtain an estimate for the H_{upd}-ECSA. The working electrode was then held at 0.025 V and 1600 rpm for 10 min under a pure CO purge and then for another 10 min under a pure Ar purge to remove excess CO. Immediately, 3 iR-compensated cyclic voltammograms (CVs) were performed from 0.025 V to 1.0 V at 50 mV s⁻¹. Prior to CO-stripping, a “simulation” scan was performed under identical conditions as the CO-stripping experiment but under an Ar-purge. This new method developed for ceramic-supported Pt catalysts was done to identify and correct for any potentially confounding signals from the TMC cores (such as surface oxidation) on the actual CO-stripping experiment.^[189]

Methanol electrooxidation (MOR) was performed in Ar-purged 1 M MeOH and 0.1 M HClO₄ solution at 30°C and a rotation rate of 1000 rpm. Under these conditions, the limiting current is approximately 4.5 A cm⁻²_{geo}. However, the measured currents in this study were at least 1.8 orders of magnitude below this limiting current. To remove excess bubbles, a rotation rate of 2500 rpm was used during high potential CV measurements and CA measurements when holding at a fixed potential of 0.6 V. After a working electrode was lowered into the MOR electrolyte, 100 conditioning scans were performed between -0.05 V and 0.6 V at 200 mV s⁻¹. Afterwards, iR-compensated CA measurements

were conducted by holding the electrode at fixed potentials for 15 min intervals at 0.35 V, 0.4 V, 0.45 V, and 0.6 V. The activity was computed by averaging the current over the last minute. Then, iR-compensated CV measurements were performed by cycling between 0.025 V and 1.2 V at 50 mV s⁻¹.

Stability studies were conducted in Ar-saturated 1 M MeOH and 0.1 M HClO₄ solution at 30°C and 1000 rpm from -0.05 V to 0.6 V at 100 mV s⁻¹. During this time, the working electrode oscillated rapidly between performing HER, HOR, and MOR. After 10,000 cycles, a regeneration was attempted by thoroughly rinsing each working electrode with DI water, swirling in 0.1 M NaOH solution for 2 min at room temperature, and then rinsing again with copious amounts of DI water.

Gas Diffusion Electrode (GDE) HOR/HER activity and stability studies were performed to supplement the RDE studies and obtain more accurate kinetic estimates using a recently developed method.^[184,194] Catalyst inks were prepared at 3 mg per gram of solution by adding water followed by a solution of IPA:EtOH:5% Nafion® 117 solution. The final ratios used were 25:50:25 H₂O:IPA:EtOH as the solvent with 18 µL of 5% Nafion® 117 solution per 3 mg of catalyst. Sigracet GDL 25 BC from fuelcellstore.com were used to prepare the GDEs, which were cut into 1 cm×2 cm strips. 17 µL of ink was applied to a 0.2 cm×1 cm line at one end of the GDE and dried vertically in ambient conditions for 2 minutes before being dried further using our standard vacuum protocol described above. For the control catalysts, the NM loading was ~ 51 µg cm⁻²_{geo} while for the core-shell catalysts, the NM loading was ~ 20 µg cm⁻²_{geo}. Exact loadings were determined using ICP-MS. In this way, the geometric activities can be compared between the RDE and GDE methods.

The GDE was then suspended vertically in the electrolyte solution from a freshly-polished Ti wire. The solution level was maintained such that the bottom 0.3 cm of the GDE was submerged in solution. In this configuration, the uncompensated solution resistance was ~ 8-10 Ω. The bubbler was not positioned in the electrolyte solution but rather directly above the solution and maintained with 300 cm³(STP) min⁻¹ of either UHP Ar or UHP H₂. Once submerged, the GDE was cycled from 0 V to 0.6 V at 200 mV s⁻¹ in Ar-purged 0.1 M HClO₄ at 30.0 °C. The electrolyte was refreshed, and the flow was then switched to H₂ and two uncompensated LSV scans were obtained at 10 mV s⁻¹. The first

was from 150 mV to -150 mV, and the second from -150 mV to 150 mV. The average of these two scans was taken^[184] for each electrode mounting. The LSV scans were then repeated with standard iR correction applied. Triplicate electrode mountings were performed for each catalyst and averaged. A 10,000 cycle stability study was then conducted for each of the two studied core-shell catalysts as described above. Representative electrodes were then studied in 1.0 M HClO₄ at 30.0 °C. In this electrolyte, the uncompensated solution resistance was ~ 4 Ω.

3.2 Electrochemical Methods for Section 2.3

Electrochemical measurements were performed on a CH Instruments 627e potentiostat/galvanostat using a jacketed glass cell with PTFE cap and gas diffusion electrodes (GDEs).^[184,194] In all experiments, a graphite rod (Alfa Aesar, 99.9995%) was used as the counter electrode. A leak-proof 3 M NaCl Ag/AgCl reference electrode calibrated to the eDAQ hydrogen reference electrode was employed as the reference electrode. All potentials are reported versus RHE. Catalyst inks were prepared at the concentration of 3 mg of catalyst per gram of solution by dispersing the carbon-supported materials in a mixture of water, isopropanol, ethanol, (H₂O:IPA:EtOH=25:50:25) and 5% Nafion® 117 (18 μL per 3 mg of catalysts). The inks were sonicated for 1 h in an ice bath. Sigracet GDL 25 BC from fuelcellstore.com was used to prepare the GDEs. The carbon paper was cut into 1 cm×2 cm strips and 17 μL of ink was applied to a 0.2 cm×1 cm line at one end of the GDE. The ink was left to dry vertically in ambient conditions for 2 min and under vacuum for 15 min.

For the control catalysts, the NM loading was ~ 51 μg cm⁻²_{geo} while for the core-shell catalysts, the NM loading was ~ 20 μg cm⁻²_{geo}. Exact loadings were determined using two methods that agreed to within 2% error. The first method involved digestion of the catalyst powder and analysis using ICP-MS to obtain the Pt wt% loading. Based on the ink concentration (3 mg_{cat} mL⁻¹_{ink}) and the volume added to the GDE (17 μL), the NM loadings on each electrode was calculated. The second method involved direct digestion of each electrode in aqua regia to obtain the exact Pt loading. This method was performed

for triplicate electrode mountings to determine the various in the electrode mounting procedure.

The GDE was then suspended vertically in the electrolyte solution using a freshly-polished Ti wire. The solution level was maintained such that the bottom 0.3 cm of the GDE was submerged in solution. In this configuration, the uncompensated solution resistance was $\sim 8\text{-}10\ \Omega$. The bubbler was not positioned in the electrolyte solution but rather directly above the solution and maintained with $300\ \text{cm}^3\ \text{min}^{-1}$ of either UHP Ar or UHP H_2 . Once submerged, the GDE was cycled from 0 V to 0.6 V at $200\ \text{mV}\ \text{s}^{-1}$ in Ar-purged 1.0 M HClO_4 at 30.0°C . The electrolyte was refreshed, and the flow was then switched to H_2 and two uncompensated LSV scans were obtained at $10\ \text{mV}\ \text{s}^{-1}$. The first was from 150 mV to -150 mV, and the second from -150 mV to 150 mV. The average of these two scans was taken^[184] for each electrode mounting. The LSV scans were then repeated with standard iR correction applied. The uncompensated solution resistance was ca. $4\ \Omega$. Triplicate electrode mountings were performed for each catalyst and averaged. A 10,000 cycle stability study was then conducted for the optimal 0.25 ML catalyst as described above.

3.3 Thermal Study Details for Section 2.4

4%Pt/96% $\text{Ti}_{0.1}\text{W}_{0.9}\text{C}$ supported on carbon black at 20wt% (denoted as Pt_{subML}) and Pt_{comm} were loaded into alumina crucibles and subjected to various heat treatments to examine the propensity towards sintering and the stability of sub-monolayer Pt loadings on the surface of TiWC NPs. Heating was always performed at $2\ ^\circ\text{C}\ \text{min}^{-1}$ in a 5% H_2 / 95% N_2 atmosphere using a quartz tubular furnace under $100\ \text{cm}^3(\text{STP})\ \text{min}^{-1}$ of total gas flow. Once the final temperature was reached, the atmosphere was changed to either 100% H_2 , 100% N_2 , or H_2O -saturated N_2 (saturated using a room-temperature saturator). The final temperature was maintained for 4 h, except for one heat study at 600°C in 100% N_2 where the final temperature was held for 20 h. After the specified time had elapsed, the furnace was allowed to cool naturally with the lid closed under $100\ \text{cm}^3(\text{STP})\ \text{min}^{-1}$ of whichever atmosphere was under study. Once at room temperature, the furnace was purged with N_2 bubbled through an H_2O saturator for 2 h at $95\ \text{cm}^3(\text{STP})\ \text{min}^{-1}$ and then

passivated using a 1%O₂/99%N₂ mixture for 2 h. After passivation, the samples were stored in a dry N₂ glovebox.

4. Conclusions

Collectively, TMC nanoparticles coated with NM monolayers offer new, highly tunable pathways for decreasing NM loading requirements while increasing activity and stability in thermo- and electrocatalysis. First, it was shown that 2 ML Pt/TiWC and 2 ML PtRu/TiWC core-shell nanoparticles were ca. 3 times as active as commercial Pt/C and PtRu/C for HER and HOR while remaining stable over 10,000 cycles. Then, it was shown that these catalysts could perform HOR under 1000 ppm of CO impurities with only a 50 mV overpotential as compared to 400 mV for PtRu/C. Finally, it was shown that PtRu/TiWC was an order of magnitude more active for MOR than PtRu/C and remained stable over 10,000 cycles.

Next, it was shown that sub-monolayer 0.25 ML Pt/TiWC achieves a factor of 13 improvement in mass activity of Pt towards both HER and HOR. A kinetic analysis revealed that Pt activates adjacent TiWC sites at low overpotentials via spillover of metallic H⁰. A techno-economic analysis showed that this electrocatalyst offers a factor of 12 reduction in overall device cost for both HER cathodes and HOR anodes as compared to commercial Pt/C as well as a factor of 6 reduction in HER cathode device cost as compared to earth-abundant CoP. In addition, 0.25 ML Pt/TiWC has the smallest prediction interval in cost volatility. The chapter concluded with the preliminary analysis of the thermal stability of 0.25 ML Pt/TiWC for thermal catalysis applications.

Acknowledgements

Dr. Maria Milina is gratefully acknowledged for her major contribution to this chapter. This work was supported by the Department of Energy, Office of Basic Energy Sciences (DE-FG02-12ER16352, DE-SC0014058). I thank the National Science Foundation for financial support through the National Science Foundation Graduate Research Fellowship under Grant No. 1122374. Dr. Maria Milina thanks the Swiss National Science Foundation (Project number P2EZR2_159124) for financial support.

5. Supporting Information

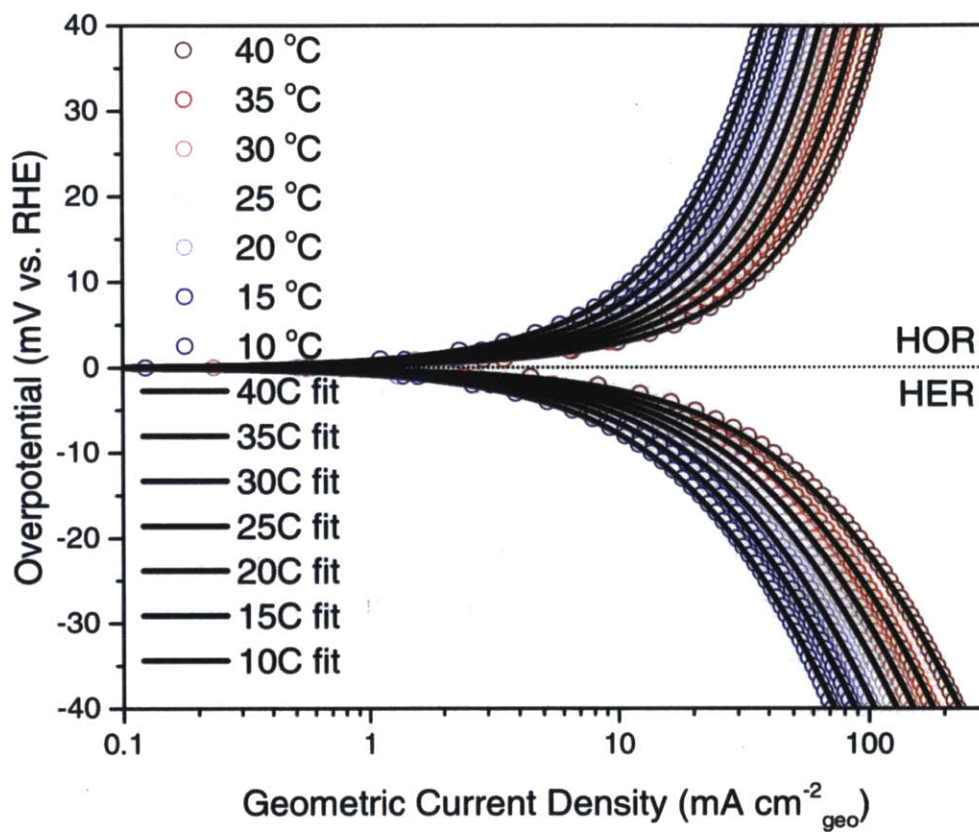


Figure S7.21. Butler-Volmer Fits to the Thermal Study of 0.25 ML Pt/TiWC

Chapter 8

Conclusions and Outlook

This thesis targeted an improved understanding of the design of early transition metal carbide nanoparticle catalysts. Particular emphasis was placed on designing synthetic methods that strive towards the ultimate goal of absolute synthetic control over the material properties that govern reactivity. While undoubtedly this goal was not fully achieved, substantial progress was made on several fronts. First, early transition metal carbide nanoparticles with finely controlled sizes and surfaces are now synthetically viable. Second, the developed method enables the synthesis of the first bimetallic carbide and nitride nanoparticles with controlled properties. Taken together, this opens avenues for the further synthetic exploration of carbide and nitride nanoparticles for the outright replacing noble metal catalysts in certain applications.

Third, expansion of the method enables the first syntheses of transition metal carbide nanoparticles coated with noble metal monolayers. In addition, demonstrated control was achieved over the shell thickness, the shell composition, the core size, and the core composition. This level of control exceeds many other methods, is obtained via a scalable, solution-processable route, and is achieved under extreme conditions beyond 900 °C. The resulting core-shell nanoparticles were demonstrated to have a host of unique properties unknown to other core-shell nanoparticle architectures. These properties include improved reactivity, high tolerance to impurities, and high electrochemical and thermal stability. Sub-monolayer configurations showed that this core-shell architecture enables the activation of the core material for bifunctional catalysis via the spillover of intermediates from the adjacent noble metal sites.

While the method offers exceptional controllability at the gram scale, several improvements could be made. First, silica encapsulation and removal is doable, but cumbersome. It is undoubtedly required for “high temperature” carbides and nitrides, such as those of W, Ti, Ta, and Zr. However, molybdenum carbide is highly active, particularly for thermal catalysis, and can be synthesized at temperatures below 600 °C. It is conceivable that a corollary method without silica encapsulation could be developed

whereby non-encapsulated ML NM/Mo₂C nanoparticles self-assemble at low temperatures on metal oxide supports. Such a method would be synthetically more accessible, particularly for large scale manufacturing of core-shell catalysts for reforming reactions.

Lastly, this method unlocks a vast array of synthetically achievable core-shell nanoparticles. A paltry fraction of synthetic phase space could be explored in this thesis alone. However, the power and accuracy of computational quantum chemistry improves exponentially each year. Even today, **Chapter 2** demonstrates the importance of computation in directing the search for new and better catalysts. In the future, rapid progress can be achieved through the seamless union of theory and experiment. I have no doubt that the materials developed here will be rendered obsolete in the coming future by newer and far more superior developments in catalyst design. However, I hope that the body of work presented in this thesis served as a small stepping stone for engineering the new and better catalysts of the future.

8.1 Limitations of this work

There are substantial limitations both to this work and to core-shell nanoparticles in general. With respect to this work, the developed method is by no means exhaustive, fully optimized, or for that matter, fully understood. The synthetic control derives from control over the room-temperature reverse microemulsion method and the carburization conditions. While a small study was performed in **Chapter 4** using various colloidal systems, there could be much more optimal and cost-effective systems that are yet to be explored. Furthermore, there could be sol-gel methods that abandon the use of a surfactant altogether, which would be very attractive. At present, the method is limited to amorphous metal oxide precursors that are stable at elevated pH due to the ammonium hydroxide present in solution needed to catalyze TEOS hydrolysis. Second, the silica must be removed after high temperature carburizations/nitridations due to its exceptionally low porosity. This requires the resulting carbide, nitride, or core-shell nanoparticle to be stable either in a mild HF solution or in strongly alkaline conditions. For

some materials, such as niobium nitride, these constraints would make synthesis via this method infeasible.

There are also limitations to core-shell materials that are not unique to the class developed in this work. The most apparent limitation is the limited ability to regenerate the catalyst. Supported metal nanoparticles must ideally have useful lifecycles extending for at least several years. Even over this lifespan, the catalysts must be routinely regenerated, usually via a high temperature calcination or annealing step. While the core-shell materials developed here could be amenable to such high temperature treatments (aside from calcination, which would oxidize the core), facile regeneration remains a critical impediment to the use of core-shell architectures commercially. An in situ chemical method for re-dispersing spent catalysts would help not only core-shell nanoparticles in gaining commercial traction, but catalysis in general if such a general method could be developed. Lastly, core-shell nanoparticles are exotic catalyst architectures. At present, they are extremely difficult to synthesize at scale. While the method presented here is solution-processable and could be scaled, it is cumbersome. Undoubtedly, the method could be significantly optimized. However, new, efficient, and general methods for the continuous manufacturing of novel nanoscale catalyst architectures would translate to cost savings for consumers, higher margins for producers, and an overall higher adoption rate of laboratory-scale research being translated into commercial systems.

8.2 Future Directions for Further Study

At the time of writing, the presented method for core-shell nanoparticle synthesis is under a year old. While I am leaving, the project should hopefully outlive my tenure. As described in the previous section, the method has many inefficiencies that should be addressed. While optimizing the system to achieve the same result is not particularly interesting from the standpoint of fundamental investigations into this new class of core-shell architectures, it is exceptionally utilitarian. This is especially true for new students who join the project. Any improvements in efficiencies to the synthetic framework at the beginning of their thesis would translate into an overall higher productivity rate by the end of their thesis. As such, I will list some ideas that come to mind for optimizing the system

first, followed by the many subsequent applications that this class of materials is poised to address.

Synthetic Optimization

The most expensive portion of the process is the cost of the surfactant. While the surfactant could be recovered at scale via foaming-out procedures, its use should still be minimized in the case of reverse microemulsions or eliminated if a sol-gel route can be devised. The method as presented uses polyoxyethylene (4) lauryl ether as a surfactant. Although this is a mass-produced surfactant currently manufactured by Croda Inc., it is highly soluble in the heptane media. As such, its utilization efficiency at the interface between the water droplets and the heptane is very low. Instead, Igepal® CO-520 is significantly less soluble in heptane, meaning only a small volume is needed to prepare a suitable microemulsion.

Synthesis space should also be explored systematically. Each metal oxide precursor behaves slightly differently, and these differences should be compiled for other researchers to more quickly adopt this method. While the relevant levers for controlling the synthesis have all been described, they must be tuned for each metal. In addition, it would be excellent if the system could be translated into a microfluidic system for continuous production. The development of a continuous carburization protocol is less straight-forward.

It is also important to consider ways to completely overhaul the method, for instance via a sol-gel route. However, as noted previously, it could be possible for certain NM/TMC combinations to forgo silica encapsulation all-together. This would significantly reduce processing times and improve yields.

Highly Stable Electrocatalysts for ORR and OER in Acidic Media

This is an exceptionally difficult problem but one that this architecture could address. Of all the earth-abundant cores currently amenable to core-shell syntheses, only TiC, ZrC, and TaC appear to be stable enough for long-term use in ORR and especially for OER. Undoubtedly, these surfaces will passivate into oxycarbides or oxide layers. The core-shell structure will likely change over time. Nevertheless, using such cores should stabilize surface NMs from dissolution and leaching. This is because the interaction of

NMs with carbon supports is very weak whereas the interaction is much stronger with carbides and oxides. It is envisioned that Pt or PtAu monolayers supported on these carbide cores would be highly stable ORR catalysts. DFT should be used to guide the synthesis towards designing the most active system. However, long-term durability is arguably more important than raw activity when it comes to ORR.

While much research and progress has been made in the design of earth-abundant HER electrocatalysts in acidic media, there has been almost no progress made in the improvement of OER electrocatalysts. OER is substantially more challenging than HER, and IrO₂ is the only known material active and durable enough for use as an OER electrocatalyst in acidic conditions. Potentially, Ir/TaC, Ir/ZrC, and Ir/TiC could allow for enhanced dispersion and reduced loadings of Ir needed to perform OER. While the catalysts would be prepared as listed above, they would revert in situ during OER testing into the active forms: IrO₂/TaC_xO_y, IrO₂/ZrC_xO_y, and IrO₂/TiC_xO_y. The resulting structures of the materials after durability studies could be very interesting.

Reducing Au Loadings for Electrochemical Reduction of CO₂ to CO

I have already performed promising preliminary studies of Au/TiWC core-shell nanoparticles supported on carbon black and compared them to a 20wt% Au/C commercial catalyst. The results were not included in this thesis, but it appears possible to greatly improve the mass activity of Au towards electrochemical CO₂ reduction (CDR). This is because commercial Au catalysts are polydisperse and consist of very large nanoparticles with low dispersions. As such, there is substantial room to improve Au utilization. The vast majority of carbides and nitrides are stable under CDR conditions due to the strongly cathodic potentials used. As such, this presents an ideal area for DFT to guide the synthesis of active and selective core-shell nanoparticles since the phase space of viable candidates is very large.

Bifunctional Surfaces for Thermal Catalysis

Electrocatalysis is an emerging area of research, but thermal catalysis reigns supreme commercially. However, supported metal catalysts are often simple systems, consisting of a monometallic nanoparticle supported on a high surface area oxide. There is strong interplay between the oxide supports and the NM nanoparticles. In addition to modulating

the NM d-band structure, the oxide supports are often active participants in the reactions, providing sites for adding or removing reactive intermediates from the NM surface. These systems are also highly optimized. Often, less than 1wt% NM loadings can already be used. As such, sub-monolayer NM/TMC architectures offer an interesting avenue for reducing NM loadings even lower, to below 0.1wt%, while offering new reactivities. As discussed extensively in **Chapter 1**, TMCs are noteworthy catalysts in their own right, often superior to NM catalysts in many thermal reactions. However, reactions progress through very different mechanisms due to the differences in oxophilicity and carbophilicity between NMs and TMCs. By putting NMs and TMCs in close proximity, new reaction pathways could be unlocked for performing highly efficient thermal catalytic reactions. Unlike other core-shell architectures, the insolubility of NMs in the TMC core, and the extremely high melting points of TMCs should enable a system that is not only uniquely reactive, but highly stable and sinter-resistant over long times on stream.

References

- [1] B. Hammer, and J.K. Norskov. "Why gold is the noblest of all the metals." *Nature*, **1995**, 376, 238-240.
- [2] B. Hammer, Y. Morikawa, and J. Norskov. "CO chemisorption at metal surfaces and overlayers." *Physical Review Letters*, **1996**, 76, 2141-2144.
- [3] P. Sabatier. "Catalysis in Organic Chemistry." D. Van Nostrand Company: New York, **1922**.
- [4] C.J. Yang. "An impending platinum crisis and its implications for the future of the automobile." *Energy Policy*, **2009**, 37, 1805-1808. 10.1016/j.enpol.2009.01.019
- [5] E. Berger, W. Fong, and R. Chornock. "An r-process Kilonova Associated with the Short-hard GRB 130603B." *The Astrophysical Journal Letters*, **2013**, 774, L23.
- [6] L.S. Collaboration, C. Virgo, B.P. Abbott, R. Abbott, T.D. Abbott, M.R. Abernathy, F. Acernese, K. Ackley, C. Adams, T. Adams, P. Addesso, R.X. Adhikari, V.B. Adya, C. Affeldt, M. Agathos, K. Agatsuma, N. Aggarwal, O.D. Aguiar, L. Aiello, A. Ain, P. Ajith, B. Allen, A. Allocca, P.A. Altin, S.B. Anderson, W.G. Anderson, K. Arai, M.A. Arain, M.C. Araya, C.C. Arceneaux, J.S. Areeda, N. Arnaud, K.G. Arun, S. Ascenzi, G. Ashton, M. Ast, S.M. Aston, P. Astone, P. Aufmuth, C. Aulbert, S. Babak, P. Bacon, M.K.M. Bader, P.T. Baker, F. Baldaccini, G. Ballardin, S.W. Ballmer, J.C. Barayoga, S.E. Barclay, B.C. Barish, D. Barker, F. Barone, B. Barr, L. Barsotti, M. Barsuglia, D. Barta, J. Bartlett, M.A. Barton, I. Bartos, R. Bassiri, A. Basti, J.C. Batch, C. Baune, V. Bavigadda, M. Bazzan, B. Behnke, M. Bejger, C. Belczynski, A.S. Bell, C.J. Bell, B.K. Berger, J. Bergman, G. Bergmann, C.P.L. Berry, D. Bersanetti, A. Bertolini, J. Betzwieser, S. Bhagwat, R. Bhandare, I.A. Bilenko, G. Billingsley, J. Birch, R. Birney, O. Birnholtz, S. Biscans, A. Bisht, M. Bitossi, C. Biwer, M.A. Bizouard, J.K. Blackburn, C.D. Blair, D.G. Blair, R.M. Blair, S. Bloemen, O. Bock, T.P. Bodiya, M. Boer, G. Bogaert, C. Bogan, A. Bohe *et al.* "Observation of Gravitational Waves from a Binary Black Hole Merger." *Physical Review Letters*, **2016**, 116, 061102.
- [7] P. Strasser, S. Koh, T. Anniyev, J. Greeley, K. More, C. Yu, Z. Liu, S. Kaya, D. Nordlund, H. Ogasawara, M.F. Toney, and A. Nilsson. "Lattice-strain control of the activity in dealloyed core-shell fuel cell catalysts." *Nat Chem*, **2010**, 2, 454-460. 10.1038/nchem.623
- [8] *Handbook of Heterogeneous Catalysis*; 2nd ed.; G. Ertl, H. Knozinger, F. Schuth, and J. Weitkamp, Eds.; John Wiley & Sons: Hoboken, NJ, 2008.
- [9] G.A. Somorjai, and Y. Li *Introduction to Surface Chemistry and Catalysis*; 2nd ed.; John Wiley & Sons: Hoboken, NJ, 2010.

- [10] E.F. Holby, W. Sheng, Y. Shao-Horn, and D. Morgan. "Pt nanoparticle stability in PEM fuel cells: influence of particle size distribution and crossover hydrogen." *Energy & Environmental Science*, **2009**, 2, 865-871. 10.1039/b821622n
- [11] C.S. Bonifacio, S. Carenco, C.H. Wu, S.D. House, H. Bluhm, and J.C. Yang. "Thermal Stability of Core–Shell Nanoparticles: A Combined in Situ Study by XPS and TEM." *Chemistry of Materials*, **2015**, 27, 6960-6968. 10.1021/acs.chemmater.5b01862
- [12] S. Zhang, Y. Hao, D. Su, V.V.T. Doan-Nguyen, Y. Wu, J. Li, S. Sun, and C.B. Murray. "Monodisperse Core/Shell Ni/FePt Nanoparticles and Their Conversion to Ni/Pt to Catalyze Oxygen Reduction." *Journal of the American Chemical Society*, **2014**, 136, 15921-15924. 10.1021/ja5099066
- [13] S.T. Oyama *The Chemistry of Transition Metal Carbides and Nitrides*; Blackie: Glasgow, 1996.
- [14] A.L. Stottlemeyer, T.G. Kelly, Q. Meng, and J.G. Chen. "Reactions of oxygen-containing molecules on transition metal carbides: Surface science insight into potential applications in catalysis and electrocatalysis." *Surface Science Reports*, **2012**, 67, 201-232. 10.1016/j.surfrep.2012.07.001
- [15] J.G. Chen. "Carbide and Nitride Overlayers on Early Transition Metal Surfaces: Preparation, Characterization, and Reactivities." *Chemical Reviews*, **1996**, 96, 1477-1498.
- [16] H. Böhm. "New non-noble metal anode catalysts for acid fuel cells." *Nature*, **1970**, 227, 483-484. 10.1038/227483a0
- [17] H. Bohm. "Adsorption and Anodic Oxidation of Hydrogen on Tungsten Carbide." *Electrochimica Acta*, **1970**, 15, 1273.
- [18] R.B. Levy, and M. Boudart. "Platinum-like behavior of tungsten carbide in surface catalysis." *Science*, **1973**, 181, 547-549. 10.1126/science.181.4099.547
- [19] L.H. Bennett, J.R. Cuthill, A.J. McAlister, N.E. Erickson, and R.E. Watson. "Electronic structure and catalytic behavior of tungsten carbide." *Science*, **1974**, 184, 563-565. 10.1126/science.184.4136.563
- [20] S.J. Peppernick, K.D.D. Gunaratne, and A.W. Castleman Jr. "Superatom spectroscopy and the electronic state correlation between elements and isoelectronic molecular counterparts." *Proceedings of the National Academy of Sciences of the United States of America*, **2010**, 107, 975-980. 10.1073/pnas.0911240107

- [21] J.E. Houston, G.E. Laramore, and R.L. Park. "Surface electronic properties of tungsten, tungsten carbide, and platinum." *Science*, **1974**, 185, 258-260. 10.1126/science.185.4147.258
- [22] J.G. Chen. "NEXAFS investigations of transition metal oxides, nitrides, carbides, sulfides and other interstitial compounds." *Surface Science Reports*, **1997**, 30, 1-152. [http://dx.doi.org/10.1016/S0167-5729\(97\)00011-3](http://dx.doi.org/10.1016/S0167-5729(97)00011-3)
- [23] J.G. Chen, C.a. Menning, and M.B. Zellner. "Monolayer bimetallic surfaces: Experimental and theoretical studies of trends in electronic and chemical properties." *Surface Science Reports*, **2008**, 63, 201-254. 10.1016/j.surfrep.2008.02.001
- [24] R. Michalsky, Y.J. Zhang, A.J. Medford, and A.A. Peterson. "Departures from the adsorption energy scaling relations for metal carbide catalysts." *The Journal of Physical Chemistry C*, **2014**, 118, 13026-13034
- [25] F. Abild-Pedersen, J. Greeley, F. Studt, J. Rossmeisl, T. Munter, P.G. Moses, E. Skulason, T. Bligaard, and J.K. Nørskov. "Scaling properties of adsorption energies for hydrogen-containing molecules on transition-metal surfaces." *Physical Review Letters*, **2007**, 99, 016105
- [26] A.J. Medford, A. Vojvodic, F. Studt, F. Abild-Pedersen, and J.K. Nørskov. "Elementary steps of syngas reactions on Mo 2 C (001): adsorption thermochemistry and bond dissociation." *Journal of Catalysis*, **2012**, 290, 108-117
- [27] S. Wang, V. Petzold, V. Tripkovic, J. Kleis, J.G. Howalt, E. Skulason, E. Fernandez, B. Hvolbæk, G. Jones, and A. Toftelund. "Universal transition state scaling relations for (de) hydrogenation over transition metals." *Physical Chemistry Chemical Physics*, **2011**, 13, 20760-20765
- [28] N. Ji, T. Zhang, M. Zheng, A. Wang, H. Wang, X. Wang, and J.G. Chen. "Direct catalytic conversion of cellulose into ethylene glycol using nickel-promoted tungsten carbide catalysts." *Angewandte Chemie International Edition*, **2008**, 47, 8510-8513. 10.1002/anie.200803233
- [29] R.W. Gosselink, D.R. Stellwagen, and J.H. Bitter. "Tungsten-based catalysts for selective deoxygenation." *Angewandte Chemie International Edition*, **2013**, 52, 5089-5092. 10.1002/anie.201209809
- [30] M.D. Porosoff, X. Yang, J.A. Boscoboinik, and J.G. Chen. "Molybdenum carbide as alternative catalysts to precious metals for highly selective reduction of CO₂ to CO." *Angewandte Chemie International Edition*, **2014**, 126, 6823-6827.

- [31] D.V. Esposito, and J.G. Chen. "Monolayer platinum supported on tungsten carbides as low-cost electrocatalysts: opportunities and limitations." *Energy & Environmental Science*, **2011**, 4, 3900-3912. 10.1039/c1ee01851e
- [32] T.G. Kelly, S.T. Hunt, D.V. Esposito, and J.G. Chen. "Monolayer palladium supported on molybdenum and tungsten carbide substrates as low-cost hydrogen evolution reaction (HER) electrocatalysts." *International Journal of Hydrogen Energy*, **2013**, 38, 5638-5644. 10.1016/j.ijhydene.2013.02.116
- [33] D.V. Esposito, S.T. Hunt, A.L. Stottlemeyer, K.D. Dobson, B.E. McCandless, R.W. Birkmire, and J.G. Chen. "Low-cost hydrogen-evolution catalysts based on monolayer platinum on tungsten monocarbide substrates." *Angewandte Chemie International Edition*, **2010**, 49, 9859-9862. 10.1002/anie.201004718
- [34] X. Zhou, Y. Qiu, J. Yu, J. Yin, and S. Gao. "Tungsten carbide nanofibers prepared by electrospinning with high electrocatalytic activity for oxygen reduction." *International Journal of Hydrogen Energy*, **2011**, 36, 7398-7404. 10.1016/j.ijhydene.2011.03.081
- [35] A.T. Garcia-Esparza, D. Cha, Y. Ou, J. Kubota, K. Domen, and K. Takanebe. "Tungsten carbide nanoparticles as efficient cocatalysts for photocatalytic overall water splitting." *ChemSusChem*, **2013**, 6, 168-181. 10.1002/cssc.201200780
- [36] E.C. Weigert, a.L. Stottlemeyer, M.B. Zellner, and J.G. Chen. "Tungsten Monocarbide as Potential Replacement of Platinum for Methanol Electrooxidation." *Journal of Physical Chemistry C*, **2007**, 111, 14617-14620. 10.1021/jp075504z
- [37] X. Yang, Y.C. Kimmel, J. Fu, B.E. Koel, and J.G. Chen. "Activation of Tungsten Carbide Catalysts by Use of an Oxygen Plasma Pretreatment." *ACS Catalysis*, **2012**, 2, 765-769. 10.1021/cs300081t
- [38] "Free Market Commodity Prices, Monthly, January 1960 – June 2015," United Nations Conference on Trade and Development (2015), <http://unctadstat.unctad.org/wds/TableView/tableView.aspx?ReportId=28768>.
- [39] "Gold Price in a Range of Currencies since December 1978," The World Gold Council (2015), <https://www.gold.org/research/download-the-gold-price-since-1978>.
- [40] "Platinum, Palladium, Rhodium, Iridium, Ruthenium Monthly Average Prices between 01 Jun 1992 and 31 Jul 2015," Johnson Matthey (2015), <http://www.platinum.matthey.com/prices/price-charts>.

- [41] M.C. Weidman, D.V. Esposito, I.J. Hsu, and J.G. Chen. "Electrochemical Stability of Tungsten and Tungsten Monocarbide (WC) Over Wide pH and Potential Ranges." *Journal of the Electrochemical Society*, **2010**, 157, F179. 10.1149/1.3491341
- [42] M.C. Weidman, D.V. Esposito, Y.-C. Hsu, and J.G. Chen. "Comparison of electrochemical stability of transition metal carbides (WC, W₂C, Mo₂C) over a wide pH range." *Journal of Power Sources*, **2012**, 202, 11-17. 10.1016/j.jpowsour.2011.10.093
- [43] Y.C. Kimmel, X. Xu, W. Yu, X. Yang, and J.G. Chen. "Trends in Electrochemical Stability of Transition Metal Carbides and Their Potential Use As Supports for Low-Cost Electrocatalysts." *ACS Catalysis*, **2014**, 4, 1558-1562. 10.1021/cs500182h
- [44] A.L. Ivanovskii. "Platinum group metal nitrides and carbides: synthesis, properties and simulation." *Russian Chemical Reviews*, **2009**, 78, 303-318. 10.1070/RC2009v078n04ABEH004036
- [45] S. Ono, T. Kikegawa, and Y. Ohishi. "A high-pressure and high-temperature synthesis of platinum carbide." *Solid State Communications*, **2005**, 133, 55-59. 10.1016/j.ssc.2004.09.048
- [46] A. Jain, S.P. Ong, G. Hautier, W. Chen, W.D. Richards, S. Dacek, S. Cholia, D. Gunter, D. Skinner, G. Ceder, and K.A. Persson. "Commentary: The Materials Project: A materials genome approach to accelerating materials innovation." *APL Materials*, **2013**, 1, 011002. 10.1063/1.4812323
- [47] C. Giordano, C. Erpen, W. Yao, and M. Antonietti. "Synthesis of Mo and W carbide and nitride nanoparticles via a simple "urea glass" route." *Nano Letters*, **2008**, 8, 4659-4663. 10.1021/nl8018593
- [48] D.V. Esposito, S.T. Hunt, Y.C. Kimmel, and J.G. Chen. "A new class of electrocatalysts for hydrogen production from water electrolysis: metal monolayers supported on low-cost transition metal carbides." *Journal of the American Chemical Society*, **2012**, 134, 3025-3033. 10.1021/ja208656v
- [49] S.T. Hunt, T. Nimmanwudipong, and Y. Roman-Leshkov. "Engineering non-sintered, metal-terminated tungsten carbide nanoparticles for catalysis." *Angewandte Chemie International Edition*, **2014**, 53, 5131-5136. 10.1002/anie.201400294
- [50] S.T. Hunt, T.M. Kokumai, D. Zanchet, and Y. Roman-Leshkov. "Alloying Tungsten Carbide Nanoparticles with Tantalum: Impact on Electrochemical Oxidation Resistance and Hydrogen Evolution Activity." *The Journal of Physical Chemistry C*, **2015**, 119, 13691-13699. 10.1021/acs.jpcc.5b02922

- [51] S.T. Hunt, and Y. Roman-Leshkov. "Reverse Microemulsion-Mediated Synthesis of Monometallic and Bimetallic Early Transition Metal Carbide and Nitride Nanoparticles." *J. Vis. Exp.*, **2015**, e53147. 10.3791/53147
- [52] S.T. Hunt, M. Milina, A.C. Alba-Rubio, C.H. Hendon, J.A. Dumesic, and Y. Roman-Leshkov. "Self-Assembly of Noble Metal Monolayers on Transition Metal Carbide Nanoparticle Catalysts." *Science*, **2016**. 10.1126/science.aad8471
- [53] S.T. Hunt, M. Milina, Z. Wang, and Y. Roman-Leshkov. "Activating Earth-Abundant Electrocatalysts for Inexpensive and Efficient Hydrogen Evolution and Oxidation: Atomically Dispersed Platinum on Carbide Nanoparticles." *Submitted*, **2016**.
- [54] C.H. Hendon, S.T. Hunt, M. Milina, A. Walsh, and Y. Roman-Leshkov. "Atomistic Origins of High-Performance Catalysis in Noble Metal-Coated Titanium Tungsten Carbide Nanoparticles." *Submitted*, **2016**.
- [55] P.A.M. Dirac *The Principles of Quantum Mechanics*; Clarendon Press: Oxford, 1930.
- [56] D. Seley, K. Ayers, and B.a. Parkinson. "Combinatorial search for improved metal oxide oxygen evolution electrocatalysts in acidic electrolytes." *ACS combinatorial science*, **2013**, 15, 82-89. 10.1021/co300086h
- [57] K. Honkala, A. Hellman, I.N. Remediakis, A. Logadottir, A. Carlsson, S. Dahl, C.H. Christensen, and J.K. Nørskov. "Ammonia synthesis from first-principles calculations." *Science*, **2005**, 307, 555-558. 10.1126/science.1106435
- [58] D.S. Sholl, and J.A. Steckel *Density Functional Theory: A Practical Introduction*; John Wiley & Sons, Inc.: Hoboken, NJ, 2009.
- [59] W. Kohn, and L.J. Sham. "Self-Consistent Equations Including Exchange and Correlation Effects." *Physical Review*, **1965**, 140, A1133-A1138.
- [60] G. Kresse, and J. Furthmüller. "Efficient iterative schemes for ab initio total-energy calculations using a plane-wave basis set." *Physical Review B*, **1996**, 54, 11169-11186.
- [61] J.P. Perdew, K. Burke, and M. Ernzerhof. "Generalized Gradient Approximation Made Simple." *Physical Review Letters*, **1996**, 77, 3865-3868.
- [62] F. Finocchi, A. Barbier, J. Jupille, and C. Noguera. "Stability of Rocksalt (111) Polar Surfaces: Beyond the Octopole." *Physical Review Letters*, **2004**, 92, 136101.

- [63] D.O. Scanlon, A. Walsh, B.J. Morgan, M. Nolan, J. Fearon, and G.W. Watson. "Surface Sensitivity in Lithium-Doping of MgO: A Density Functional Theory Study with Correction for on-Site Coulomb Interactions." *The Journal of Physical Chemistry C*, **2007**, *111*, 7971-7979. 10.1021/jp070200y
- [64] J.K. Nørskov, T. Bligaard, A. Logadottir, J. Kitchin, J. Chen, S. Pandelov, and U. Stimming. "Trends in the exchange current for hydrogen evolution." *Journal of the Electrochemical Society*, **2005**, *152*, J23-J26.
- [65] K.T. Butler, C.H. Hendon, and A. Walsh. "Electronic Chemical Potentials of Porous Metal–Organic Frameworks." *Journal of the American Chemical Society*, **2014**, *136*, 2703-2706. 10.1021/ja4110073
- [66] B. Hammer, and J.K. Nørskov. "Electronic factors determining the reactivity of metal surfaces." *Surface Science*, **1995**, *343*, 211-220. 10.1016/0039-6028(96)80007-0
- [67] C. Chen, Y. Kang, Z. Huo, Z. Zhu, W. Huang, H.L. Xin, J.D. Snyder, D. Li, J.A. Herron, M. Mavrikakis, M. Chi, K.L. More, Y. Li, N.M. Markovic, G.A. Somorjai, P. Yang, and V.R. Stamenkovic. "Highly Crystalline Multimetallic Nanoframes with Three-Dimensional Electrocatalytic Surfaces." *Science*, **2014**, *343*, 1339-1343. 10.1126/science.1249061
- [68] L. Zhang, L.T. Roling, X. Wang, M. Vara, M. Chi, J. Liu, S.-I. Choi, J. Park, J.A. Herron, Z. Xie, M. Mavrikakis, and Y. Xia. "Platinum-based nanocages with subnanometer-thick walls and well-defined, controllable facets." *Science*, **2015**, *349*, 412-416.
- [69] X. Liang, and C. Jiang. "Atomic layer deposited highly dispersed platinum nanoparticles supported on non-functionalized multiwalled carbon nanotubes for the hydrogenation of xylose to xylitol." *Journal of Nanoparticle Research*, **2013**, *15*, 1890. 10.1007/s11051-013-1890-0
- [70] Z. Yan, M. Cai, and P.K. Shen. "Nanosized tungsten carbide synthesized by a novel route at low temperature for high performance electrocatalysis." *Scientific Reports*, **2013**, *3*, 1646. 10.1038/srep01646
- [71] I.J. Hsu, Y.C. Kimmel, X. Jiang, B.G. Willis, and J.G. Chen. "Atomic layer deposition synthesis of platinum-tungsten carbide core-shell catalysts for the hydrogen evolution reaction." *Chemical Communications*, **2012**, *48*, 1063-1065. 10.1039/c1cc15812k
- [72] Y.C. Kimmel, D.V. Esposito, R.W. Birkmire, and J.G. Chen. "Effect of surface carbon on the hydrogen evolution reactivity of tungsten carbide (WC) and Pt-modified WC electrocatalysts." *International Journal of Hydrogen Energy*, **2012**, *37*, 3019-3024. 10.1016/j.ijhydene.2011.11.079

- [73] J.K. Nørskov, F. Studt, F. Abild-Pedersen, and T. Bligaard *Fundamental concepts in heterogeneous catalysis*; John Wiley & Sons, 2014.
- [74] J.G. Chen, C.A. Menning, and M.B. Zellner. "Monolayer bimetallic surfaces: Experimental and theoretical studies of trends in electronic and chemical properties." *Surface Science Reports*, **2008**, 63, 201-254
- [75] J.F. Moulder, W.F. Stickle, P.E. Sobol, and K.D. Bomben *Handbook of X-ray Photoelectron Spectroscopy*; Physical Electronics, Inc.: Eden Prairie, 1995.
- [76] D.V. Esposito, S.T. Hunt, A.L. Stottlemeyer, K.D. Dobson, B.E. McCandless, R.W. Birkmire, and J.G. Chen. "Low-Cost Hydrogen Evolution Catalysts Based on Monolayer Platinum on Tungsten Monocarbide Substrates." *Angewandte Chemie International Edition*, **2010**, 49, 9859-9862. 10.1002/anie.201004718
- [77] J.K. Nørskov, T. Bligaard, A. Logadottir, J.R. Kitchin, J.G. Chen, S. Pandelov, and J.K. Nørskov. "Trends in the exchange current for hydrogen evolution." *Journal of the Electrochemical Society*, **2005**, 152, J23-J26
- [78] P. Sabatier *Catalysis in Organic Chemistry*; D. Van Nostrand Company: New York, 1922.
- [79] J. Greeley, T.F. Jaramillo, J. Bonde, I.B. Chorkendorff, and J.K. Nørskov. "Computational high-throughput screening of electrocatalytic materials for hydrogen evolution." *Nature Materials*, **2006**, 5, 909-913. 10.1038/Nmat1752
- [80] C.A. Menning, and J.G. Chen. "General trend for adsorbate-induced segregation of subsurface metal atoms in bimetallic surfaces." *Journal of Chemical Physics*, **2009**, 130, 1-7. 10.1063/1.3125926
- [81] C.T. Campbell. "Bimetallic Surface-Chemistry." *Annual Review of Physical Chemistry*, **1990**, 41, 775-837.
- [82] B.D. Cullity In *Elements of X-ray diffraction*; Cohen, M., Ed.; Addison-Wesley: Reading, Mass., 1956, p 272-275.
- [83] D.V. Esposito, K.D. Dobson, B.E. McCandless, R.W. Birkmire, and J.G. Chen. "Comparative Study of Tungsten Monocarbide and Platinum as Counter Electrodes in Polysulfide-Based Photoelectrochemical Solar Cells." *Journal of the Electrochemical Society*, **2009**, 156, B962-B969.
- [84] P.N. Ross, and P. Stonehart. "Relation of Surface-Structure to Electrocatalytic Activity of Tungsten Carbide." *Journal of Catalysis*, **1977**, 48, 42-59.

- [85] L.I. Johansson. "Electronic and Structural-Properties of Transition-Metal Carbide and Nitride Surfaces." *Surface Science Reports*, **1995**, 21, 179-250.
- [86] L. Leclercq, A. Almazouari, M. Dufour, and G. Leclercq In *The Chemistry of Transition Metal Carbides and Nitrides*; Oyama, S. T., Ed.; Blackie: Glasgow, 1996, 345-361.
- [87] G. Leclercq, M. Kamal, J.M. Giraudon, P. Devassine, L. Feigenbaum, L. Leclercq, A. Frennet, J.M. Bastin, A. Lofberg, S. Decker, and M. Dufour. "Study of the preparation of bulk powder tungsten carbides by temperature programmed reaction with CH₄+H₂ mixtures." *Journal of Catalysis*, **1996**, 158, 142-169.
- [88] G.E. Rhead, M.G. Barthes, and C. Argile. "Determination of Growth Modes of Ultrathin Films from Auger-Electron Spectroscopy - an Assessment and Commentary." *Thin Solid Films*, **1981**, 82, 201-211.
- [89] M.P. Humbert, C.A. Menning, and J.G. Chen. "Replacing bulk Pt in Pt-Ni-Pt bimetallic structures with tungsten monocarbide (WC): Hydrogen adsorption and cyclohexene hydrogenation on Pt-Ni-WC." *Journal of Catalysis*, **2010**, 271, 132-139.
- [90] M. Weinert, and R.E. Watson. "Core-Level Shifts in Bulk Alloys and Surface Adlayers." *Physical Review B*, **1995**, 51, 17168-17180.
- [91] D.M. Riffe, N.D. Shinn, B. Kim, K.J. Kim, and T.H. Kang. "Core-level shifts at the Pt/W(110) monolayer bimetallic interface." *Surface Science*, **2009**, 603, 3431-3438.
- [92] G.A. Tsirlina, and O.A. Petrii. "Mechanism of Hydrogen Evolution on Smooth, Stoichiometric Tungsten Carbide." *Soviet Electrochemistry*, **1985**, 21, 653-660.
- [93] J.O.M. Bockris, A.K.N. Reddy, and M. Gamboa-Aldeco In *Modern electrochemistry*; 2nd ed.; Plenum Press: New York, 1998, p 211-405.
- [94] J. Barber, S. Morin, and B.E. Conway. "Specificity of the kinetics of H₂, evolution to the structure of single-crystal Pt surfaces, and the relation between opd and upd H." *Journal of Electroanalytical Chemistry*, **1998**, 446, 125-138.
- [95] D.J. Ham, R. Ganesan, and J.S. Lee. "Tungsten carbide microsphere as an electrode for cathodic hydrogen evolution from water." *International Journal of Hydrogen Energy*, **2008**, 33, 6865-6872.
- [96] Y. Shao-Horn, W.C. Sheng, S. Chen, P.J. Ferreira, E.F. Holby, and D. Morgan. "Instability of supported platinum nanoparticles in low-temperature fuel cells." *Topics in Catalysis*, **2007**, 46, 285-305.

- [97] Y.Y. Shao, J. Wang, R. Kou, M. Engelhard, J. Liu, Y. Wang, and Y.H. Lin. "The corrosion of PEM fuel cell catalyst supports and its implications for developing durable catalysts." *Electrochimica Acta*, **2009**, 54, 3109-3114.
- [98] P. Dabo, J. Fournier, L. Brossard, H. Menard, P. Magny, and B. Mahdavi. "Hydrogen deactivation of sputter-deposited platinum thin films on highly oriented pyrolytic graphite." *International Journal of Hydrogen Energy*, **1998**, 23, 167-175.
- [99] Y.Y. Shao, J. Liu, Y. Wang, and Y.H. Lin. "Novel catalyst support materials for PEM fuel cells: current status and future prospects." *Journal of Materials Chemistry*, **2009**, 19, 46-59.
- [100] H. Chhina, S. Campbell, and O. Kesler. "Thermal and electrochemical stability of tungsten carbide catalyst supports." *Journal of Power Sources*, **2007**, 164, 431-440.
- [101] J.P. Bosco, K. Sasaki, M. Sadakane, W. Ueda, and J.G. Chen. "Synthesis and Characterization of Three-Dimensionally Ordered Macroporous (3DOM) Tungsten Carbide: Application to Direct Methanol Fuel Cells." *Chemistry of Materials*, **2010**, 22, 966-973.
- [102] E.C. Weigert, A.L. Stottlemyer, M.B. Zellner, and J.G. Chen. "Tungsten monocarbide as potential replacement of platinum for methanol electrooxidation." *Journal of Physical Chemistry C*, **2007**, 111, 14617-14620.
- [103] E.C. Weigert, M.B. Zellner, A.L. Stottlemyer, and J.G. Chen. "A combined surface science and electrochemical study of tungsten carbides as anode electrocatalysts." *Topics in Catalysis*, **2007**, 46, 349-357.
- [104] P.J. Ferreira, G.J. Ia O', Y. Shao-Horn, D. Morgan, R. Makharia, S. Kocha, and H.A. Gasteiger. "Instability of Pt/C electrocatalysts in proton exchange membrane fuel cells - A mechanistic investigation." *Journal of the Electrochemical Society*, **2005**, 152, A2256-A2271. 10.1149/1.2050347
- [105] M.B. Zellner, and J.G. Chen. "Surface science and electrochemical studies of WC and W₂CPVD films as potential electrocatalysts." *Catalysis Today*, **2005**, 99, 299-307.
- [106] E.C. Weigert, D.V. Esposito, and J.G. Chen. "Cyclic voltammetry and X-ray photoelectron spectroscopy studies of electrochemical stability of clean and Pt-modified tungsten and molybdenum carbide (WC and Mo₂C) electrocatalysts." *Journal of Power Sources*, **2009**, 193, 501-506.
- [107] J. Greeley, J.K. Norskov, L.A. Kibler, A.M. El-Aziz, and D.M. Kolb. "Hydrogen evolution over bimetallic systems: Understanding the trends." *ChemPhysChem*, **2006**, 7, 1032-1035. 10.1002/cphc.200500663

- [108] H. Wolfschmidt, D. Weingarth, and U. Stimming. "Enhanced Reactivity for Hydrogen Reactions at Pt Nanoislands on Au(111)." *ChemPhysChem*, **2010**, *11*, 1533-1541. 10.1002/cphc.201000148
- [109] Platinum Today. London: Johnson Matthey; **2011**.
- [110] M. Wu, X. Lin, A. Hagfeldt, and T. Ma. "Low-cost molybdenum carbide and tungsten carbide counter electrodes for dye-sensitized solar cells." *Angewandte Chemie International Edition*, **2011**, *50*, 3520-3524. 10.1002/anie.201006635
- [111] S.R. Vallance, H.J. Kitchen, C. Ritter, S. Kingman, G. Dimitrakis, and D.H. Gregory. "Probing the microwave interaction mechanisms and reaction pathways in the energy-efficient, ultra-rapid synthesis of tungsten carbide." *Green Chemistry*, **2012**, *14*, 2184. 10.1039/c2gc35272a
- [112] P.K. Shen, S. Yin, Z. Li, and C. Chen. "Preparation and performance of nanosized tungsten carbides for electrocatalysis." *Electrochimica Acta*, **2010**, *55*, 7969-7974. 10.1016/j.electacta.2010.03.025
- [113] A.V. Nikiforov, I.M. Petrushina, E. Christensen, N.V. Alexeev, a.V. Samokhin, and N.J. Bjerrum. "WC as a non-platinum hydrogen evolution electrocatalyst for high temperature PEM water electrolyzers." *International Journal of Hydrogen Energy*, **2012**, *37*, 18591-18597. 10.1016/j.ijhydene.2012.09.112
- [114] Z.Z. Fang, X. Wang, T. Ryu, K.S. Hwang, and H.Y. Sohn. "Synthesis, sintering, and mechanical properties of nanocrystalline cemented tungsten carbide – A review." *International Journal of Refractory Metals and Hard Materials*, **2009**, *27*, 288-299. 10.1016/j.ijrmhm.2008.07.011
- [115] Z. Abdullaeva, E. Omurzak, C. Iwamoto, H. Okudera, M. Koinuma, S. Takebe, S. Sulaimankulova, and T. Mashimo. "High temperature stable WC_{1-x}@C and TiC@C core-shell nanoparticles by pulsed plasma in liquid." *R. Soc. Chem. Adv.*, **2013**, *3*, 513. 10.1039/c2ra22028h
- [116] J.A. Nelson, and M.J. Wagner. "High Surface Area Mo₂C and WC Prepared by Alkalide Reduction." **2002**, *1*, 1639-1642.
- [117] R. Ganesan, and J.S. Lee. "Tungsten carbide microspheres as a noble-metal-economic electrocatalyst for methanol oxidation." *Angewandte Chemie International Edition*, **2005**, *44*, 6557-6560. 10.1002/anie.200501272
- [118] Y. Yan, L. Zhang, X. Qi, H. Song, J.-Y. Wang, H. Zhang, and X. Wang. "Template-free pseudomorphic synthesis of tungsten carbide nanorods." *Small*, **2012**, *8*, 3350-3356. 10.1002/smll.201200877

- [119] V.G. Zavodinsky. "Small tungsten carbide nanoparticles: Simulation of structure, energetics, and tensile strength." *International Journal of Refractory Metals and Hard Materials*, **2010**, 28, 446-450. 10.1016/j.ijrmhm.2010.02.003
- [120] L. Xiong, and T. He. "Synthesis and Characterization of Ultrafine Tungsten and Tungsten Oxide Nanoparticles by a Reverse Microemulsion-Mediated Method." *Chemistry of Materials*, **2006**, 18, 2211-2218. 10.1021/cm052320t
- [121] A.K. Panda, S.P. Moulik, B.B. Bhowmik, and a.R. Das. "Dispersed Molecular Aggregates." *Journal of Colloid and Interface Science*, **2001**, 235, 218-226. 10.1006/jcis.2000.7323
- [122] A. Zarur, and J. Ying. "Reverse microemulsion synthesis of nanostructured complex oxides for catalytic combustion." *Nature*, **2000**, 403, 65-67. 10.1038/47450
- [123] J. Lu, B. Fu, M.C. Kung, G. Xiao, J.W. Elam, H.H. Kung, and P.C. Stair. "Coking- and Sintering-Resistant Palladium Catalysts Achieved Through Atomic Layer Deposition." *Science*, **2012**, 335, 1205-1208. 10.1126/science.1212906
- [124] Y. Dai, B. Lim, Y. Yang, C.M. Cobley, W. Li, E.C. Cho, B. Grayson, P.T. Fanson, C.T. Campbell, Y. Sun, and Y. Xia. "A sinter-resistant catalytic system based on platinum nanoparticles supported on TiO₂ nanofibers and covered by porous silica." *Angewandte Chemie International Edition*, **2010**, 49, 8165-8168. 10.1002/anie.201001839
- [125] S.H. Joo, J.Y. Park, C.-K. Tsung, Y. Yamada, P. Yang, and G.a. Somorjai. "Thermally stable Pt/mesoporous silica core-shell nanocatalysts for high-temperature reactions." *Nature Materials*, **2009**, 8, 126-131. 10.1038/nmat2329
- [126] H. Tulhoff, H.C.S. Berlin, and W. Goslar In *Ullman's Encyclopedia of Industrial Chemistry* **2012**, p 565-582.
- [127] G. Kawamura. "Tungsten Molybdenum Carbide for Electrocatalytic Oxidation of Methanol." *Journal of the Electrochemical Society*, **1987**, 134, 1653. 10.1149/1.2100730
- [128] L. Hu, S. Ji, T. Xiao, C. Guo, P. Wu, and P. Nie. "Preparation and characterization of tungsten carbide confined in the channels of SBA-15 mesoporous silica." *The journal of physical chemistry. B*, **2007**, 111, 3599-3608. 10.1021/jp066349b
- [129] C. Giordano, W. Yang, A. Lindemann, R. Crombez, and J. Texter. "Waterborne WC nanodispersions." *Colloids and Surfaces A*, **2011**, 374, 84-87. 10.1016/j.colsurfa.2010.11.014

- [130] H. Kim, and B.N. Popov. "Characterization of hydrous ruthenium oxide/carbon nanocomposite supercapacitors prepared by a colloidal method." *Journal of Power Sources*, **2002**, *104*, 52-61. 10.1016/S0378-7753(01)00903-X
- [131] T. Schmidt, H. Gasteiger, G. Stäb, P. Urban, D. Kolb, and R. Behm. "Characterization of High-Surface-Area Electrocatalysts Using a Rotating Disk Electrode Configuration." *Journal of the Electrochemical Society*, **1998**, *145*, 2354-2358.
- [132] W.-F. Chen, C.-H. Wang, K. Sasaki, N. Marinkovic, W. Xu, J.T. Muckerman, Y. Zhu, and R.R. Adzic. "Highly active and durable nanostructured molybdenum carbide electrocatalysts for hydrogen production." *Energy & Environmental Science*, **2013**, *6*, 943. 10.1039/c2ee23891h
- [133] J. Kibsgaard, Z. Chen, B.N. Reinecke, and T.F. Jaramillo. "Engineering the surface structure of MoS₂ to preferentially expose active edge sites for electrocatalysis." *Nature Materials*, **2012**, *11*, 963-969. 10.1038/nmat3439
- [134] R.B. Gordon, M. Bertram, and T.E. Graedel. "Metal stocks and sustainability." *Proceedings of the National Academy of Sciences of the United States of America*, **2006**, *103*, 1209-1214. 10.1073/pnas.0509498103
- [135] J.R. Kitchin, J.K. Nørskov, M.A. Barteau, and J.G. Chen. "Role of Strain and Ligand Effects in the Modification of the Electronic and Chemical Properties of Bimetallic Surfaces." *Physical Review Letters*, **2004**, *93*, 156801.
- [136] H. Liu, C. Song, L. Zhang, J. Zhang, H. Wang, and D.P. Wilkinson. "A review of anode catalysis in the direct methanol fuel cell." *Journal of Power Sources*, **2006**, *155*, 95-110. 10.1016/j.jpowsour.2006.01.030
- [137] K. Sasaki, H. Naohara, Y. Choi, Y. Cai, W.F. Chen, P. Liu, and R.R. Adzic. "Highly stable Pt monolayer on PdAu nanoparticle electrocatalysts for the oxygen reduction reaction." *Nat Commun*, **2012**, *3*, 1115. 10.1038/ncomms2124
- [138] E. Antolini. "Iridium As Catalyst and Cocatalyst for Oxygen Evolution/Reduction in Acidic Polymer Electrolyte Membrane Electrolyzers and Fuel Cells." *ACS Catalysis*, **2014**, *4*, 1426-1440. 10.1021/cs4011875
- [139] Z. Liu, G.S. Jackson, and B.W. Eichhorn. "PtSn intermetallic, core-shell, and alloy nanoparticles as CO-tolerant electrocatalysts for H₂ oxidation." *Angewandte Chemie, International Edition*, **2010**, *49*, 3173-3176. 10.1002/anie.200907019
- [140] Z. Liu, J.E. Hu, Q. Wang, K. Gaskell, A.I. Frenkel, G.S. Jackson, and B. Eichhorn. "PtMo Alloy and MoOx@Pt Core-Shell Nanoparticles as Highly CO-Tolerant Electrocatalysts." *Journal of the American Chemical Society*, **2009**, *131*, 6924-6925. 10.1021/ja901303d

- [141] L. Xiong, K.L. More, and T. He. "Syntheses, characterization, and catalytic oxygen electroreduction activities of carbon-supported PtW nanoparticle catalysts." *Journal of Power Sources*, **2010**, 195, 2570-2578. <http://dx.doi.org/10.1016/j.jpowsour.2009.11.013>
- [142] Y. Liu, T.G. Kelly, J.G. Chen, and W.E. Mustain. "Metal Carbides as Alternative Electrocatalyst Supports." **2013**
- [143] M. Nie, P.K. Shen, and Z. Wei. "Nanocrystalline tungsten carbide supported Au–Pd electrocatalyst for oxygen reduction." *Journal of Power Sources*, **2007**, 167, 69-73. [10.1016/j.jpowsour.2006.12.059](http://dx.doi.org/10.1016/j.jpowsour.2006.12.059)
- [144] D.J. Ham, C. Pak, G.H. Bae, S. Han, K. Kwon, S.A. Jin, H. Chang, S.H. Choi, and J.S. Lee. "Palladium-nickel alloys loaded on tungsten carbide as platinum-free anode electrocatalysts for polymer electrolyte membrane fuel cells." *Chem Commun (Camb)*, **2011**, 47, 5792-5794. [10.1039/c0cc03736b](http://dx.doi.org/10.1039/c0cc03736b)
- [145] D.J. Ham, S. Han, C. Pak, S.M. Ji, S.-A. Jin, H. Chang, and J.S. Lee. "High Electrochemical Performance and Stability of Co-Deposited Pd–Au on Phase-Pure Tungsten Carbide for Hydrogen Oxidation." *Topics in Catalysis*, **2012**, 55, 922-930. [10.1007/s11244-012-9875-2](http://dx.doi.org/10.1007/s11244-012-9875-2)
- [146] N.M. Schweitzer, J.A. Schaidle, O.K. Ezekoye, X. Pan, S. Linic, and L.T. Thompson. "High activity carbide supported catalysts for water gas shift." *Journal of the American Chemical Society*, **2011**, 133, 2378-2381. [10.1021/ja110705a](http://dx.doi.org/10.1021/ja110705a)
- [147] K. Lee, A. Ishihara, S. Mitsushima, N. Kamiya, and K.-i. Ota. "Stability and electrocatalytic activity for oxygen reduction in WC + Ta catalyst." *Electrochimica Acta*, **2004**, 49, 3479-3485. [10.1016/j.electacta.2004.03.018](http://dx.doi.org/10.1016/j.electacta.2004.03.018)
- [148] C.T. Campbell, S.C. Parker, and D.E. Starr. "The effect of size-dependent nanoparticle energetics on catalyst sintering." *Science*, **2002**, 298, 811-814. [10.1126/science.1075094](http://dx.doi.org/10.1126/science.1075094)
- [149] S. Wirth, F. Harnisch, M. Weinmann, and U. Schroder. "Comparative Study of IVB-VIB Transition Metal Compound Electrocatalysts for the Hydrogen Evolution Reaction." *Applied Catalysis B: Environmental*, **2012**, 126, 225-230. [doi:10.1016/j.apcatb.2012.07.023](http://dx.doi.org/10.1016/j.apcatb.2012.07.023)
- [150] Q. Sun, Q. Wang, P. Jena, and Y. Kawazoe. "Design of Janus Nanoparticles with Atomic Precision: Tungsten-Doped Gold Nanostructures." *ACS Nano*, **2008**, 2, 341-347. [10.1021/nn7002647](http://dx.doi.org/10.1021/nn7002647)
- [151] P.J. Cumpson, and M.P. Seah. "Elastic Scattering Corrections in AES and XPS. II. Estimating Attenuation Lengths and Conditions Required for their Valid Use in

Overlayer/Substrate Experiments." *Surface and Interface Analysis*, **1997**, 25, 430-446. 10.1002/(SICI)1096-9918(199706)25:6<430::AID-SIA254>3.0.CO;2-7

- [152] N. Toshima, and T. Yonezawa. "Bimetallic nanoparticles—novel materials for chemical and physical applications." *New Journal of Chemistry*, **1998**, 22, 1179-1201.
- [153] B. Ingham, C.D.A. Brady, G.T. Burstein, N. Gaston, and M.P. Ryan. "EXAFS Analysis of Electrocatalytic WC Materials." *The Journal of Physical Chemistry C*, **2009**, 113, 17407-17410. 10.1021/jp905283f
- [154] A.I. Frenkel, C.W. Hills, and R.G. Nuzzo. "A view from the inside: Complexity in the atomic scale ordering of supported metal nanoparticles." *Journal of Physical Chemistry B*, **2001**, 105, 12689-12703. 10.1021/Jp012769j
- [155] T. Haubold, W. Krauss, and H. Gleiter. "EXAFS studies on nanocrystalline tungsten." *Philosophical Magazine Letters*, **1991**, 63, 245-247.
- [156] B. Ravel, and M. Newville. "ATHENA, ARTEMIS, HEPHAESTUS: data analysis for X-ray absorption spectroscopy using IFEFFIT." *J Synchrotron Radiat*, **2005**, 12, 537-541. 10.1107/S0909049505012719
- [157] S. Calvin *XAFS for Everyone*; CRC Press, Taylor & Francis Group: Boca Raton, FL, **2013**.
- [158] S. Calvin, C.J. Riedel, E.E. Carpenter, S.A. Morrison, R.M. Stroud, and V.G. Harris. "Estimating Crystallite Size in Polydispersed Samples using EXAFS." *Physica Scripta*, **2005**, T115, 744-748.
- [159] A.I. Frenkel, C.W. Hills, and R.G. Nuzzo. "A View from the Inside: Complexity in the Atomic Scale Ordering of Supported Metal Nanoparticles." *The Journal of Physical Chemistry B*, **2001**, 105, 12689-12703. 10.1021/jp012769j
- [160] X. Fan, H. Zhou, and X. Guo. "WC Nanocrystals Grown on Vertically Aligned Carbon Nanotubes: An Efficient and Stable Electrocatalyst for Hydrogen Evolution Reaction." *ACS Nano*, **2015**. 10.1021/acsnano.5b00425
- [161] D. Dickertmann, J.W. Schultze, and K.J. Vetter. "Electrochemical formation and reduction of monomolecular oxide layers on (111) and (100) planes of gold single crystals." *Journal of Electroanalytical Chemistry and Interfacial Electrochemistry*, **1974**, 55, 429-443. 10.1016/S0022-0728(74)80437-7
- [162] A.T. Bell. "The impact of nanoscience on heterogeneous catalysis." *Science*, **2003**, 299, 1688-1691. 10.1126/science.1083671

- [163] G.A. Deluga, J.R. Salge, L.D. Schmidt, and X.E. Verykios. "Renewable Hydrogen from Ethanol by Autothermal Reforming." *Science*, **2004**, 303, 993-997.
- [164] J. Zhang, K. Sasaki, E. Sutter, and R.R. Adzic. "Stabilization of Platinum Oxygen-Reduction Electrocatalysts Using Gold Clusters." *Science*, **2007**, 315, 220-222.
- [165] Y. Zhai, D. Pierre, R. Si, W. Deng, P. Ferrin, A.U. Nilekar, G. Peng, J.A. Herron, D.C. Bell, H. Saltsburg, M. Mavrikakis, and M. Flytzani-Stephanopoulos. "Alkali-Stabilized Pt-OH_x Species Catalyze Low-Temperature Water-Gas Shift Reactions." *Science*, **2010**, 329, 1633-1636. 10.1126/science.1192449
- [166] J. Greeley, I.E.L. Stephens, a.S. Bondarenko, T.P. Johansson, H.a. Hansen, T.F. Jaramillo, J. Rossmeisl, I. Chorkendorff, and J.K. Nørskov. "Alloys of platinum and early transition metals as oxygen reduction electrocatalysts." *Nature Chemistry*, **2009**, 1, 552-556. 10.1038/nchem.367
- [167] D. Wang, H.L. Xin, R. Hovden, H. Wang, Y. Yu, D.A. Muller, F.J. DiSalvo, and H.D. Abruña. "Structurally ordered intermetallic platinum-cobalt core-shell nanoparticles with enhanced activity and stability as oxygen reduction electrocatalysts." *Nature Materials*, **2013**, 12, 81-87.
- [168] H. Yang. "Platinum-Based Electrocatalysts with Core-Shell Nanostructures." *Angewandte Chemie International Edition*, **2011**, 50, 2674-2676. 10.1002/anie.201005868
- [169] S. Guo, S. Zhang, and S. Sun. "Tuning Nanoparticle Catalysis for the Oxygen Reduction Reaction." *Angewandte Chemie International Edition*, **2013**, 52, 8526-8544. 10.1002/anie.201207186
- [170] F. Tao, M.E. Grass, Y. Zhang, D.R. Butcher, J.R. Renzas, Z. Liu, J.Y. Chung, B.S. Mun, M. Salmeron, and G.A. Somorjai. "Reaction-Driven Restructuring of Rh-Pd and Pt-Pd Core-Shell Nanoparticles." *Science*, **2008**, 322, 932-934. 10.1126/science.1164170
- [171] S. Alayoglu, A.U. Nilekar, M. Mavrikakis, and B. Eichhorn. "Ru-Pt core-shell nanoparticles for preferential oxidation of carbon monoxide in hydrogen." *Nature Materials*, **2008**, 7, 333-338.
- [172] C. Cui, L. Gan, M. Heggen, S. Rudi, and P. Strasser. "Compositional segregation in shaped Pt alloy nanoparticles and their structural behaviour during electrocatalysis." *Nature Materials*, **2013**, 12, 765-771. 10.1038/nmat3668

- [173] C. Wang, M. Chi, G. Wang, D. van der Vliet, D. Li, K. More, H.-H. Wang, J.A. Schlueter, N.M. Markovic, and V.R. Stamenkovic. "Correlation Between Surface Chemistry and Electrocatalytic Properties of Monodisperse Pt_xNi_{1-x} Nanoparticles." *Advanced Functional Materials*, **2011**, *21*, 147-152. 10.1002/adfm.201001138
- [174] K.A. Kuttiyiel, K. Sasaki, Y. Choi, D. Su, P. Liu, and R.R. Adzic. "Nitride Stabilized PtNi Core–Shell Nanocatalyst for high Oxygen Reduction Activity." *Nano Letters*, **2012**, *12*, 6266-6271. 10.1021/nl303362s
- [175] I.E. Stephens, A.S. Bondarenko, U. Grønbjerg, J. Rossmeisl, and I. Chorkendorff. "Understanding the electrocatalysis of oxygen reduction on platinum and its alloys." *Energy & Environmental Science*, **2012**, *5*, 6744-6762
- [176] J.A. Schaidle, N.M. Schweitzer, O.T. Ajenifujah, and L.T. Thompson. "On the preparation of molybdenum carbide-supported metal catalysts." *Journal of Catalysis*, **2012**. 10.1016/j.jcat.2012.02.012
- [177] T.G. Kelly, A.L. Stottlemeyer, H. Ren, and J.G. Chen. "Comparison of O–H, C–H, and C–O Bond Scission Sequence of Methanol on Tungsten Carbide Surfaces Modified by Ni, Rh, and Au." *The Journal of Physical Chemistry C*, **2011**, *115*, 6644-6650. 10.1021/jp112006v
- [178] M. Koenig, and J. Grant. "Signal-to-noise measurement in X-ray photoelectron spectroscopy." *Surface and Interface Analysis*, **1985**, *7*, 217-222.
- [179] E.J. Popczun, J.R. McKone, C.G. Read, A.J. Biacchi, A.M. Wiltrout, N.S. Lewis, and R.E. Schaak. "Nanostructured Nickel Phosphide as an Electrocatalyst for the Hydrogen Evolution Reaction." *Journal of the American Chemical Society*, **2013**, *135*, 9267-9270. 10.1021/ja403440e
- [180] E.J. Popczun, C.G. Read, C.W. Roske, N.S. Lewis, and R.E. Schaak. "Highly Active Electrocatalysis of the Hydrogen Evolution Reaction by Cobalt Phosphide Nanoparticles." *Angewandte Chemie International Edition*, **2014**, *53*, 5427-5430. 10.1002/anie.201402646
- [181] M. Caban-Acevedo, M.L. Stone, J.R. Schmidt, J.G. Thomas, Q. Ding, H.-C. Chang, M.-L. Tsai, J.-H. He, and S. Jin. "Efficient hydrogen evolution catalysis using ternary pyrite-type cobalt phosphosulphide." *Nature Materials*, **2015**, *14*, 1245-1251. 10.1038/nmat4410
- [182] P. Jiang, Q. Liu, Y. Liang, J. Tian, A.M. Asiri, and X. Sun. "A Cost-Effective 3D Hydrogen Evolution Cathode with High Catalytic Activity: FeP Nanowire Array as the Active Phase." *Angewandte Chemie International Edition*, **2014**, *53*, 12855-12859. 10.1002/anie.201406848

- [183] T.F. Jaramillo, K.P. Jørgensen, J. Bonde, J.H. Nielsen, S. Horch, and I. Chorkendorff. "Identification of active edge sites for electrochemical H₂ evolution from MoS₂ nanocatalysts." *Science*, **2007**, 317, 100-102. 10.1126/science.1141483
- [184] J.X. Wang, Y. Zhang, C.B. Capuano, and K.E. Ayers. "Ultralow charge-transfer resistance with ultralow Pt loading for hydrogen evolution and oxidation using Ru@Pt core-shell nanocatalysts." *Scientific Reports*, **2015**, 5, 1-8.
- [185] T.J. Schmidt, H.A. Gasteiger, G.D. Stab, P.M. Urban, D.M. Kolb, and R.J. Behm. "Characterization of High-Surface-Area Electrocatalysts Using a Rotating Disk Electrode Configuration 1." *Journal of the Electrochemical Society*, **1998**, 145, 2354-2358.
- [186] S. Trasatti, and O.A. Petrii. "Real surface area measurements in electrochemistry." *Pure and Applied Chemistry*, **1991**, 63, 711. 10.1351/pac199163050711
- [187] Z. Jusys, J. Kaiser, and R. Behm. "Composition and activity of high surface area PtRu catalysts towards adsorbed CO and methanol electrooxidation: A DEMS study." *Electrochimica Acta*, **2002**, 47, 3693-3706.
- [188] S. Rudi, C. Cui, L. Gan, and P. Strasser. "Comparative Study of the Electrocatalytically Active Surface Areas (ECSAs) of Pt Alloy Nanoparticles Evaluated by Hupd and CO-stripping voltammetry." *Electrocatalysis*, **2014**, 5, 408-418. 10.1007/s12678-014-0205-2
- [189] T. Binninger, E. Fabbri, R. Kötz, and T. Schmidt. "Determination of the electrochemically active surface area of metal-oxide supported platinum catalyst." *Journal of the Electrochemical Society*, **2014**, 161, H121-H128.
- [190] W. Schottky. "Über spontane Stromschwankungen in verschiedenen Elektrizitätsleitern." *Annalen der Physik*, **1918**, 362, 541-567.
- [191] T.J. Schmidt, H.A. Gasteiger, and R.J. Behm. "Methanol electrooxidation on a colloidal PtRu-alloy fuel-cell catalyst." *Electrochemistry Communications*, **1999**, 1, 1-4. 10.1016/S1388-2481(98)00004-6
- [192] A.K. Singh, and Q. Xu. "Synergistic catalysis over bimetallic alloy nanoparticles." *ChemCatChem*, **2013**, 5, 652-676.
- [193] J. Durst, C. Simon, F. Hasche, and H.A. Gasteiger. "Hydrogen Oxidation and Evolution Reaction Kinetics on Carbon Supported Pt, Ir, Rh, and Pd Electrocatalysts in Acidic Media." *Journal of the Electrochemical Society*, **2014**, 162, F190-F203. 10.1149/2.0981501jes

- [194] K. Elbert, J. Hu, Z. Ma, Y. Zhang, G. Chen, W. An, P. Liu, H.S. Isaacs, R.R. Adzic, and J.X. Wang. "Elucidating Hydrogen Oxidation/Evolution Kinetics in Base and Acid by Enhanced Activities at the Optimized Pt Shell Thickness on the Ru Core." *ACS Catalysis*, **2015**, *5*, 6764-6772.
- [195] C.C. McCrory, S. Jung, I.M. Ferrer, S.M. Chatman, J.C. Peters, and T.F. Jaramillo. "Benchmarking Hydrogen Evolving Reaction and Oxygen Evolving Reaction Electrocatalysts for Solar Water Splitting Devices." *Journal of the American Chemical Society*, **2015**, *137*, 4347-4357.
- [196] X. Huang, Z. Zhao, L. Cao, Y. Chen, E. Zhu, Z. Lin, M. Li, A. Yan, A. Zettl, Y.M. Wang, X. Duan, T. Mueller, and Y. Huang. "High-performance transition metal-doped Pt₃Ni octahedra for oxygen reduction reaction." *Science*, **2015**, *348*, 1230-1234.
- [197] K. Shinozaki, J.W. Zack, R.M. Richards, B.S. Pivovar, and S.S. Kocha. "Oxygen Reduction Reaction Measurements on Platinum Electrocatalysts Utilizing Rotating Disk Electrode Technique I. Impact of Impurities, Measurement Protocols and Applied Corrections." *Journal of the Electrochemical Society*, **2015**, *162*, F1144-F1158.
- [198] K. Shinozaki, J.W. Zack, S. Pylypenko, B.S. Pivovar, and S.S. Kocha. "Oxygen Reduction Reaction Measurements on Platinum Electrocatalysts Utilizing Rotating Disk Electrode Technique II. Influence of Ink Formulation, Catalyst Layer Uniformity and Thickness." *Journal of the Electrochemical Society*, **2015**, *162*, F1384-F1396.

Appendix A

List of Publications and Patents

Publications

S.T. Hunt, M. Milina, Z. Wang, Y. Román-Leshkov. “Activating Earth-Abundant Electrocatalysts for Inexpensive and Efficient Hydrogen Evolution and Oxidation: Atomically Dispersed Platinum on Carbide Nanoparticles.” **Submitted**, (2016).

C.H. Hendon, **S.T. Hunt**, M. Milina, A. Walsh, Y. Román-Leshkov. “Atomistic Origins of High-Performance Catalysis in Noble Metal-Coated Titanium Tungsten Carbide Nanoparticles.” **Submitted**, (2016).

S.T. Hunt, M. Milina, A.C. Alba-Rubio, C.H. Hendon, J.A. Dumesic, Y. Román-Leshkov. “Self-Assembly of Noble Metal Monolayers on Transition Metal Carbide Nanoparticle Catalysts.” **Science**, (2016). 10.1126/science.aad8471

S.T. Hunt, Y. Román-Leshkov “Reverse Microemulsion-Mediated Synthesis of Monometallic and Bimetallic Early Transition Metal Carbide and Nitride Nanoparticles.” **Journal of Visualized Experiments**, 105, (2015), e53147. 10.3791/53147

S.T. Hunt, T.M. Kokumai, D. Zanchet, Y. Román-Leshkov “Bimetallic Tantalum Tungsten Carbide Nanoparticles Exhibit High Hydrogen Evolution Activity and Increased Electrochemical Oxidation Resistance.” **Journal of Physical Chemistry C**, 119, (2015), 13691-13699. 10.1021/acs.jpcc.5b02922

S.T. Hunt, T. Nimmanwudipong, Y. Román-Leshkov “Engineering Non-Sintered, Metal-Terminated Tungsten Carbide Nanoparticles for Catalysis.” **Angewandte Chemie International Edition**, 53, (2014), 5131-5136. 10.1002/anie.201400294

Featured on the M.I.T. News homepage, <http://newsoffice.mit.edu/2014/engineering-earth-abundant-catalysts-mimic-platinum-renewable-energy-technologies>

T.G. Kelly[#], **S.T. Hunt**[#], D.V. Esposito, J.G. Chen "Monolayer palladium supported on molybdenum and tungsten carbide substrates as low-cost hydrogen evolution reaction (HER) electrocatalysts." **International Journal of Hydrogen Energy**, 38, (2013), 5638-5644. 10.1016/j.ijhydene.2013.02.116

[#]Co-1st Authors.

W.G. Gunther, Y. Wang, Y. Ji, V.K. Michaelis, **S.T. Hunt**, R.G. Griffin, Y. Román-Leshkov "Sn-Beta Zeolites with Borate Salts Catalyse the Epimerization of Carbohydrates via an Intramolecular Carbon Shift." **Nature Communications**, 3:1109, (2012), 1-8. 10.1038/ncomms2122

D.V. Esposito, **S.T. Hunt**, Y.C. Kimmel, J.G. Chen., "A New Class of Electrocatalysts for Hydrogen Production from Water Electrolysis: Metal Monolayers Supported on Low-Cost Transition Metal Carbides." **Journal of the American Chemical Society**, 134, (2012), 3025-3033. 10.1021/ja208656v

D.V. Esposito, **S.T. Hunt**, A.L. Stottlemyer, K.D. Dobson, B.E. McCandless, R.W. Birkmire, J.G. Chen "Low-Cost Hydrogen Evolution Catalysts Based on Monolayer Platinum on Tungsten Monocarbide (WC) Substrates." **Angewandte Chemie International Edition**, 49, (2010), 9859-9862. 10.1002/anie.201004718
(*Journal Cover*)

K. Douglass, **S. Hunt**, A. Teplyakov, R. Opila "Surface Cleaning Procedures for Thin Films of Indium Gallium Nitride Grown on Sapphire." **Applied Surface Science**, 257, (2010), 1469-1472. 10.1016/j.apsusc.2010.08.074

Patents

S.T. Hunt and Y. Román-Leshkov “Process for the Production of Non-Sintered Transition Metal Carbide and Nitride Nanoparticles.” US Patent Application 20150105241 A1, WIPO Application WO2015021177A1, 2015.

S.T. Hunt and Y. Román-Leshkov “Noble Metal Monolayer Shell Coatings on Transition Metal Ceramic Nanoparticle Cores.” US Patent Application 62/252,401, 2015.

Appendix B

List of Presentations

American Chemical Society (ACS) Spring Meeting 2016, San Diego, California

March 13th, 2016. Oral Presentation

“Engineering Heterometallic Carbide Nanoparticles for Electrocatalysis”

Sean T. Hunt, Maria Milina, Yuriy Román-Leshkov

American Chemical Society (ACS) Spring Meeting 2016, San Diego, California

March 14th, 2016. Poster Presentation

“Engineering Metal Carbide Nanoparticles Coated with Noble Metal Monolayers for Catalysis”

Sean T. Hunt, Maria Milina, Ana C. Alba-Rubio, Christopher H. Hendon, James A. Dumesic, Yuriy Román-Leshkov

North American Catalysis Society Meeting (NAM 24) 2015, Pittsburgh, Pennsylvania

June 19th, 2015. Oral Presentation

“Bimetallic Transition Metal Carbide Nanoparticle Electrocatalysts”

Sean T. Hunt, Yuriy Román-Leshkov

American Institute of Chemical Engineers (AIChE) 2014, Atlanta, Georgia

November 18th, 2014. Oral Presentation

“Engineering Non-Sintered, Metal-Terminated WC Nanoparticles for Electrocatalysis”

Sean T. Hunt, Tarit Nimmanwudipong, Yuriy Román-Leshkov

American Chemical Society (ACS) Fall Meeting 2014, San Francisco, California

August 14th, 2016. Oral Presentation

“Engineering Non-Sintered, Metal-Terminated WC Nanoparticles for Electrocatalysis”

Sean T. Hunt, Tarit Nimmanwudipong, Yuriy Román-Leshkov

New England Catalysis Society (NECS) Fall Meeting 2013, Worcester, Massachusetts
November 16th, 2013. Oral Presentation

“Engineering Tungsten Carbide (WC) Nanoparticles for Electrocatalysis”

Sean T. Hunt, Tarit Nimmanwudipong, Yuriy Román-Leshkov

Appendix C

About the Author

Name	Sean Thomas Hunt
Date of birth	April 20 th , 1989
Place of birth	West Chester, Pennsylvania
Nationality	United States of America

Education

August 2011 – June 2016	Ph.D. in Chemical Engineering, minor in Finance Massachusetts Institute of Technology (M.I.T.) Cambridge, Massachusetts, U.S.A. Thesis Advisor: Prof. Yuriy Román
August 2011 – February 2013	M.S. in Chemical Engineering Practice Massachusetts Institute of Technology (M.I.T.) Cambridge, Massachusetts, U.S.A.
August 2007 – May 2011	Honors B.ChE. in Chemical Engineering with distinction in research University of Delaware, Newark, Delaware, U.S.A. Thesis Advisor: Prof. Jinguang Chen
August 2007 – May 2011	Honors B.S. in Chemistry, minor in Materials Science University of Delaware, Newark, Delaware, U.S.A.

Honors and Awards

M.I.T. \$100K Competition Finalist	2016
American Chemical Society, Catalysis Division Registration Award	2016
Richard J. Kokes Award for the 24 th North American Catalysis Society Meeting	2015
National Science Foundation Graduate Research Fellowship	2011-2014
William C. Rousseau Award in Leadership and Ethics in Chemical Engineering Practice	2013
M.I.T. Research Support Committee Chang Award	2013
Charles and Hilda Roddey Graduate Fellowship	2011
University of Delaware Sharp Scholarship	2007-2011
Gene J. and Frances E. Schiavelli Undergraduate Research Fellowship	2011
Merck Engineering and Technology Fellowship	2009, 2010
Phi Beta Kappa Member	2010
Tau Beta Pi Record No. 555 Scholarship	2010
Joseph H. Noggle Undergraduate Award in Physical Chemistry	2010
Hypercube Undergraduate Scholar Award in Computational Chemistry	2010
Tau Beta Pi Member	2009
National Starch and Chemical Company Undergraduate Scholarship	2009
Eagle Scout, Silver Buckle Award, Order of the Arrow, Troop 149, Willistown, PA	2004

Hobbies

I enjoy snowboarding, skiing, scuba diving, snorkeling, sailing, mountain biking, hiking, camping, kayaking, white water rafting, impersonating Tony Clifton, water-skiing, taekwondo, turtles, exercising, exercising extreme sarcasm, skeet shooting, paintball, making bad puns, making good puns, building stuff, boogie boarding, art, rollercoasters, Pomeranians, traveling, fishing, tungsten carbide, mowing the lawn, indoor rock climbing, badminton, ping pong, sweatpants, mountain dew, comedy shows, pretending I know how to dance, arboretums, beer, pretending I can golf, the miracle that is the internet, karaoke, pretending I can play guitar, Cherry MX Blues, eating Ming's food, eating Indian food, video games, fine wood grain, very long sentences punctuated with commas, science, computers, astronomy, pointless gadgetry, devil sticks, torches, kendama, unicycling, cigar boxes, and diablo. But most of all, I enjoy juggling and hanging out with my wife, preferably at the same time:

